WARSAW UNIVERSITY OF TECHNOLOGY

Ph.D. Thesis

Natural Sciences
Physical Sciences

Jakub Zieliński, M.Sc.

Study of antiprotonic atoms and the limits of the nuclear and electromagnetic forces.

Supervisors:
dr hab. Georgy Kornakov, prof. PW
Prof. dr hab. inż. Adam Kisiel

WARSAW 2026

Dedicated to my lovely wife Marta,
who has always supported me,
sometimes,
even when I wasn't making any sense.

You must unlearn what you have learned...
Try not. Do. Or do not. There is not try.

MASTER YODA

Abstract

Study of antiprotonic atoms and the limits of the nuclear and electromagnetic forces.

Jakub Zieliński

Antiprotonic atoms are exotic systems in which one of the bound atomic electrons is replaced by an antiproton ($\overline{p}$), the antimatter counterpart of the proton. This substitution produces a highly excited atom, since the antiproton is approximately 2000 times more massive than an electron. The atom releases this energy via a combination of X-rays and Auger electron emission while the antiproton cascades to lower orbits. Eventually, the antiproton gets close enough to the nucleus and annihilates with one of the nucleons, a proton or a neutron.

The annihilation process leads to the emission of pions and occasionally kaons. This reaction can fragment the nucleus into smaller, often radioactive, isotopes. Alternatively, a single A-1 isotope may remain after the annihilation. Studying these remaining nuclei can provide insight into electromagnetic and nuclear interactions of $\overline{p}$s with nuclei, as well as the neutron and proton distributions of the target nucleus.

This thesis investigates a novel method for studying antiprotonic atoms by capturing their annihilation fragments in a Penning-Malmberg trap under ultra-high vacuum conditions. This included a detailed simulation using state-of-the-art Monte Carlo codes to model the interactions of antiprotons with target nuclei and the subsequent trapping of produced fragments as a function of the potentials applied to the trap electrodes. A model was developed to simulate time-of-flight (TOF) spectra, which, when combined with estimated yields, provides expectations for the experimental signal in the measurements.

The experiments have been conducted at CERN's Antiproton Decelerator (AD) facility at the *Antimatter Experiment: gravity, Interferometry, Spectroscopy* (AE$\overline{g}$IS) experiment. It provides the necessary infrastructure for testing the production method and evaluating the feasibility of trapping and identifying annihilation fragments. A series of experimental developments was conducted to produce antiprotonic atoms and subsequently trap annihilation fragments in a nested Penning-Malmberg trap configuration. The most significant of these was the development of a novel autonomous control system, called CIRCUS (*Computer Interface for Reliably Controlling, in an Unsupervised manner, Scientific experiments*).

Finally, experimental results on the trapping of cations produced as a result of the interaction of $\overline{p}$s with low-density ^{40}Ar gas within the Penning-Malmberg trap are described. Preliminary results suggest that the nested Penning-Malmberg trap was successfully implemented, and some positive ions were trapped directly after observation of antiproton annihilations. Furthermore, signals consistent with the predictions for annihilation fragments were observed, but due to the presence of residual gas background in the measurements and the limited amount of data collected, the results remain inconclusive. The thesis concludes by listing potential improvements, and future steps are suggested to consolidate the new techniques developed within this work.

Key words: antiprotonic atoms, antiprotons, antimatter, nuclear structure, control system, AE$\overline{g}$IS, CERN

Streszczenie

Badanie atomów antyprotonowych i granic oddziaływań jądrowych i elektromagnetycznych.

Jakub Zieliński

Atomy antyprotonowe to egzotyczne układy, w których jeden ze związanych elektronów atomowych zostaje zastąpiony antyprotonem ($\overline{\mathrm{p}}$), antycząstką protonu. Ta wymiana prowadzi do powstania silnie wzbudzonego atomu, ponieważ antyproton jest około 2000 razy masywniejszy od elektronu. Atom uwalnia tę energię poprzez kombinację promieniowania rentgenowskiego oraz emisji elektronów Augera, podczas gdy antyproton kaskadowo opada na niższe orbity. Ostatecznie antyproton znajduje się wystarczająco blisko jądra atomowego i anihiluje z jednym z nukleonów, protonem lub neutronem.

Proces anihilacji prowadzi do emisji pionów, a czasami kaonów. Ta reakcja może rozbić jądro na lżejsze, często radioaktywne, izotopy pierwiastków o mniejszej lub równej liczbie atomowej Z. Alternatywnie, po anihilacji może pozostać pojedynczy izotop o liczbie masowej $A-1$. Badanie jąder pozostałych po anihilacji atomów antyprotonowych może dostarczyć informacji na temat oddziaływań elektromagnetycznych i jądrowych między $\overline{\mathrm{p}}$ a jądrem atomowym, a także rozkładów neutronów i protonów w pierwotnym jądrze.

Niniejsza rozprawa rozważa nowatorską metodę badania atomów antyprotonowych poprzez wychwytywanie ich fragmentów anihilacji w pułapce Penninga-Malmberga w warunkach ultrawysokiej próżni. Obejmowała ona szczegółową symulację z wykorzystaniem najnowocześniejszych kodów Monte Carlo do modelowania oddziaływań antyprotonów z jądrami docelowymi i późniejszego uwięzienia wytworzonych fragmentów w kombinacji potencjałów przyłożonych do elektrod pułapki. Opracowano model symulujący widma czasu przelotu (TOF), który w połączeniu z oszacowanymi wydajnościami produkcji izotopów pozwala na przewidywanie sygnału eksperymentalnego w pomiarach.

Eksperymenty przeprowadzono w ośrodku CERN Antiproton Decelerator (AD) w ramach eksperymentu *Antimatter Experiment: Gravity, Interferometry, Spectroscopy* (AE$\overline{\mathrm{g}}$IS). Zapewnia on niezbędną infrastrukturę do testowania metody produkcji oraz oceny wykonalności wychwytywania i identyfikacji fragmentów anihilacyjnych. Przeprowadzono szereg usprawnień w eksperymencie w celu wytwarzania atomów antyprotonowych oraz uwięzienia fragmentów anihilacji w zagnieżdżonej konfiguracji pułapki Penninga-Malmberga. Najważniejszym z nich było

opracowanie nowatorskiego autonomicznego systemu sterowania o nazwie CIRCUS (*Computer Interface for Reliably Controlling, in an Unsupervised manner, Scientific experiments*).

Na koniec opisano wyniki eksperymentów dotyczących wychwytywania kationów powstałych w wyniku interakcji $\bar{p}$-ów z resztkowym gazem ^{40}Ar w pułapce Penninga-Malmberga. Wstępne wyniki sugerują, że zastosowanie zagnieżdżonej pułapki Penninga-Malmberga zakończyło się powodzeniem i jony dodatnie zostały uwięzione bezpośrednio po obserwacji anihilacji antyprotonów. Ponadto zauważono sygnały odpowiadające przewidywaniom dla fragmentów anihilacji, jednak ze względu na obecne tło gazu resztkowego w pomiarach oraz ograniczoną ilość zebranych danych, rezultaty pozostają niejednoznaczne. Praca kończy się listą potencjalnych usprawnień i propozycjami przyszłych działań mających na celu konsolidację nowych technik opracowanych w ramach tej pracy.

Słowa kluczowe: antyprotonowe atomy, antyprotony, antymateria, struktura jądra atomowego, system kontroli, AE$\bar{g}$IS, CERN

Preface

If you are reading this, it means I have successfully completed writing my thesis. It was a long and winding road, but it is finally over. As long as I can remember, writing hasn't been something I've enjoyed. I would often say that I prefer sciences like physics or maths because there isn't much writing involved and they don't require memorisation like history or biology. Furthermore, during my second year at the university in Warsaw, my friends were excited to hear about a possible opportunity of working at CERN, while I wasn't sure what it was. So I am not sure how I ended up doing a PhD in physics while working on antimatter at CERN. Nonetheless, I have always enjoyed physics, maths, programming, and solving problems, so pursuing a PhD always felt like a natural next step in my education/career.

Throughout the PhD process, I had to learn new skills. A significant part of the work undertaken in this PhD was the development of the control system for the AEgIS experiment. Here again, I started with hardly any practical experience in making control systems. And, like most students, I had no real love for LabVIEW™. However, with each VI "coded" and each µService made, I began to understand what LabVIEW™ is capable of and where it has limitations. Now I understand, at least I'd like to think I do, what the critical aspects of the control system are (definitely the graphics) and how to create a reliable system. Furthermore, I have improved my programming skills. I had a lot of fun learning about new concepts in programming, both in LabVIEW™ and Python, and then applying them in real-life scenarios, sometimes even without breaking anything (but making mistakes and fixing them is a part of the process).

One of the first memories of joining AEgIS was of the first week. I have just arrived, and I didn't know anyone. On the second day, Stefan, the technical coordinator, came to the desk where I was sitting and placed a controller on it. He said, "Make it work," and then left. It took me a week or two to go and ask what exactly I am supposed to do with it. Then I learned that it will operate an actuator which costs a couple of thousand euros, and that we don't have a spare. I managed to make it work; it took a while, and it was a gradual process of reaching small goals (and maybe breaking one power supply), but the work is now complete, and it has been used in the experiment. That's when I learned one of the most important lessons: sometimes you should just do. It is essential to take action and achieve a goal. Afterwards, you can determine if the initial plan was effective, if the implementation is working, and which areas can be improved upon. The project can be gradually improved upon. I applied a similar approach to most of my

simulations and modelling projects: start simple and then increase complexity.

Over the last four years, I have also experienced significant personal growth. A lot has changed, especially in my attitudes. Throughout the PhD process, I was exposed to numerous studies, presentations by other PhD students during seminars, and lectures by experts at conferences, among other experiences. As a result, I began exploring various fields of science, not just physics or mathematics. I began reading and listening to more philosophy, learning about experiments conducted in biology and chemistry, as well as findings in archaeology and various methods used in historical research. Although I may not have expertise in these fields, I can appreciate the work that other scientists do, and I am excited about the potential results that may come from their studies.

In retrospect, the PhD journey has been a lot of fun, except for writing, of course. I started with some knowledge about antimatter. Then I quickly realised that there was much more to it than I had thought. I had to understand what we know and what we still don't. And, to my surprise, there's a lot that we do. However, there is even more that we don't know. It's a bit paradoxical about physics. Our understanding is improving, but each breakthrough opens up another world of unknowns. It's hard to say if "physics will ever be complete," but I like the thought that I contributed, even in a small part, to pushing the frontier towards the possible finish line.

Acknowledgements

Finishing a PhD is a major milestone for anyone who decides to pursue an academic path. It took me much longer than I expected, and I wouldn't have reached this point without the help of many people.

First and foremost, I would like to express my deepest gratitude to my supervisors. To Prof. Adam Kisiel, for his vast knowledge of atomic and nuclear physics and for all the insights into the theoretical aspects of my work. Thank you for taking a chance on me and accepting me as your PhD student. To Dr. Georgy Kornakov, for his expertise in experimental approaches, especially within the AEGIS experiment. I am particularly grateful for your guidance throughout the entire PhD process and for maintaining a casually professional relationship that allowed me the freedom to work in my own style. I deeply appreciate the countless opportunities you opened for me to explore and discover what kind of scientist I want to become. And, from a "struggling" PhD student, thank you for all the dinners to which I was invited - they were always appreciated.

I would like to thank everyone I met and worked with in the AEgIS Collaboration. To the leading trio - Ruggero, Benji, and Gosia - who worked tirelessly to keep the experiment running while maintaining a lighthearted atmosphere, even during stressful times. I'm especially grateful for the trust you placed in me with many tasks, which taught me responsibility and a sense of leadership (though the stakes were never too high). To Stefan, thank you for showing me how to make things "physicist-proof" for integration into the experimental area and for your continuous teasing of my choice of words-or lack thereof-which surprisingly helped improve my social skills (a work still in progress). To all the others who battled for survival amid the chaos of the Control Room - Ashwin, Fredrik, Matthias, Riley, Saiva (especially for keeping the young AD community united and the CR clean), and Valts - thank you. Last but not least, to the person who sacrificed the most for me: Marco, thank you for sharing half your desk with me, for taking me on as your apprentice in the Dark Arts of LabVIEW™, and for your mentorship. As my powers grow stronger, I know I still have much to learn from my Master. I am also grateful to be part of the TALOS project and to contribute (occasionally) with my "smart" ideas.

I want to extend my heartfelt thanks to all the people who were there along the way - my fellow PhD students in the group: Kamila, Lidia, Maja, Shirajum, and Zuzia. Special thanks go to Wiola and Daniela for tolerating my Star Wars obsession and for the movie nights that kept me sane. You both set such a high bar with your theses and defences that it truly made me question

my life choices.

Thank you to all my friends. To those who made studying fun - Kasia (I didn't know to which section to include you, but I didn't make a section for enemies), Krystian, Mateusz, and Ola - it's your fault I ended up doing a PhD, so expect the therapist bill soon. To my childhood friends - Janek, Marcin, Piotrek, and the other Piotrek - thank you for sticking with me for the past fifteen years (for reasons I still can't explain). To the *DT* (those who know, know) Destiny 2 clan - later, Discord server - thank you. Gaming is a great escape from reality, and nothing says relax like a bunch of people screaming at each other. Furthermore, all the raids we did together have taught me two important skills that could be applied during the PhD journey: 1) you can stay till 5 a.m. struggling with a task, go to sleep for 3 hours, to just wake up and continue the struggle, 2) following simple commands ("Nie wbijamy flagi!"). Special thanks to my dream team for any competitive game - PureWater and Fenrir - with whom even losing was fun (not that we have ever lost).

I owe endless gratitude to my family - my parents, grandparents, aunts, and uncles - for supporting my pursuit of a PhD in physics, even if it didn't always make sense to them. To my brother, thank you for being the reasonable one among us and for challenging my arguments, which ultimately helped me become a better communicator.

Last but most certainly not least, I want to thank my wife, Marta, who has supported me through every step of this journey. You never stopped believing (or at least hid it well) that one day this PhD thesis would be finished. You continued encouraging the writing so we could finally travel and relax in peace (until it's your time for writing). Thank you for all the movie and bowling dates that became little vacations amid the stress, and for not making too much fun of how long the writing process took. Everything you do for me is greatly appreciated.

Contents

Chapter 1
Introduction

A fundamental asymmetry between matter and antimatter presents one of the outstanding problems in physics. The observable Universe consists primarily of matter, with very little antimatter present (approximately one antiproton per 10^4 protons travelling through the vacuum of space [1]). According to the Standard Model of particle physics (SM) and General Relativity (GR), the Big Bang should have produced equal amounts of matter and antimatter. Consequently, most particles should annihilate with their antiparticles, leaving mainly photons behind. Recent results from the ALICE Collaboration strengthen this notion. In their study of heavy-ion collisions at the LHC (Large Hadron Collider), which create states of matter similar to those theorised just a fraction of a second after the Big Bang, they showed that matter and antimatter are formed in equal quantities [2]. Despite over half a century of experiment-driven searches, the baryon-antibaryon asymmetry remains one of the open problems in physics.

To address this problem, Sakharov [3] introduced three conditions that must be met by any theory that tries to explain the baryon puzzle: (i) baryon-number violation, (ii) C&CP violation, and (iii) departure from the thermal equilibrium. Firstly, there must exist a process that violates the baryon-number (B) conservation. Secondly, the process must violate both charge (C) and charge-parity (CP) symmetries, otherwise the CP-symmetric counter-process would negate any asymmetry in the baryonic matter. Finally, the rate of the process must increase as the environment moves away from thermal equilibrium. This ensures a higher rate of the process in the early stages of the Universe and for matter to prevail after the Big Bang. These conditions are weakly included in the SM; however, the observed rates are insufficient to explain the baryon-antibaryon imbalance, so some beyond the SM (BSM) theory is required.

Studying bound-state antimatter, such as antihydrogen ($\overline{\mathrm{H}}$), positronium (Ps), or antiprotonic atoms ($\overline{\mathrm{p}}\mathrm{X}$), provides a direct probe of the fundamental symmetries and interactions. Improving our understanding of the differences between particles and antiparticles is necessary for solving the baryon puzzle.

In this thesis, I summarise the last four years of work towards establishing a new method for synthesising antiprotonic atoms directly inside a particle trap under vacuum conditions, and for trapping the annihilation fragments. Firstly, I give a brief overview of our current understanding

of the structure of matter in chapter 2, followed by a description of basic techniques of trapping charged particles in chapter 3. The new technique of producing antiprotonic atoms and trapping the annihilation fragments is described in chapter 4. Following, in chapter 5, I describe the AEgIS experimental setup. Chapter 6 provides detailed descriptions of the state-of-the-art Monte Carlo simulations that I performed for studying trapping of antiprotons and the annihilation fragments. Chapter 7 provides information about experimental sequences used during measurements. This is followed by the overview of the initial data analysis performed for simulations and detector-specific experimental data in chapter 8. The main results of the antiproton campaigns are presented in Chapter 9. A discussion of the results and next steps for the project is provided in Chapter 10. The conclusions of the thesis follow these.

Chapter 2

The structure of matter

2.1 The Standard Model of particle physics

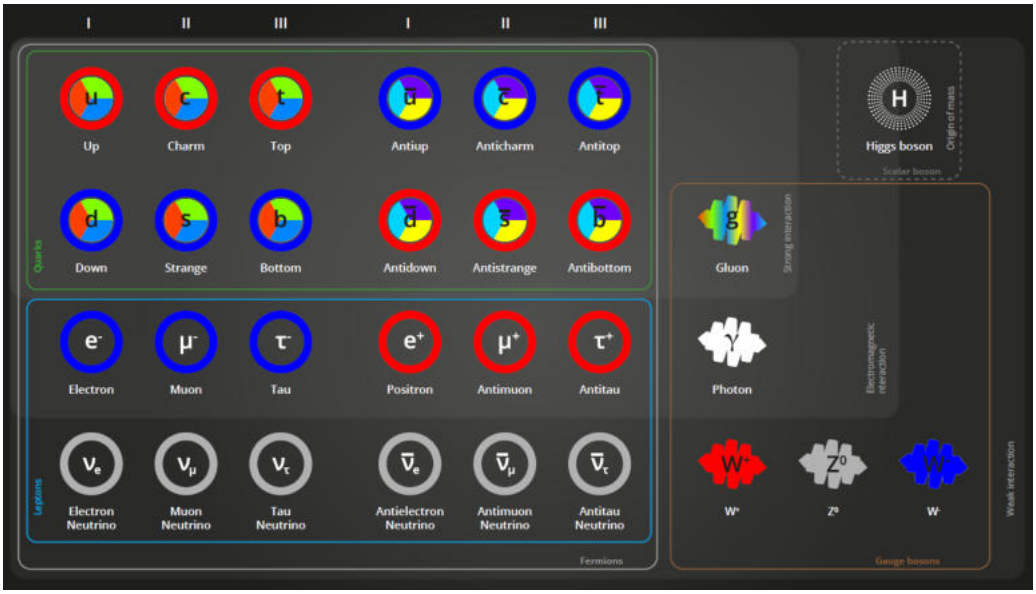

FIGURE 2.1: The summary of the elementary particles in the Standard Model of particle physics. On the left are shown three generations of fermions, along with their antimatter counterparts. On the right, gauge bosons are depicted. Particles with negative electric charge are highlighted in blue, while particles with positive electric charge are highlighted in red (credit: CERN).

The Standard Model of particle physics describes the fundamental particles that are the smallest known building blocks of matter [4]. It also describes three of the four fundamental interactions: electromagnetic, weak, and strong. The nature of the fourth interaction, gravity, and its relation to the SM are among the open problems in physics.

The particles of the SM, also known as the elementary particles, include both bosons and fermions. Bosons are particles with an integer spin, and they obey the Bose-Einstein statistics. SM includes five gauge bosons as the carriers of the fundamental interactions plus the Higgs boson, the latest confirmed particle of the SM [5], [6]. The fundamental forces described by the SM are: strong (gluons), weak (bosons Z^0, $W^{\pm}$), and electromagnetic (photons). Gravity is not yet

included in the SM; however, searches are underway for the theorised force carrier, the graviton. The fundamental forces and their characteristics are summarised in TABLE 2.1.

TABLE 2.1: The summary of the fundamental forces according to the SM and their fundamental properties. The graviton* is a hypothesised carrier for gravity; however, there is no experimental evidence for its existence.

	gravity	electromagnetic	weak	strong
carrier	graviton*	photon	$W^{\pm}$, Z^0	gluon
mass [GeV/c^2]	0	0	80.4, 91.2	0
range [m]	∞	∞	10^{-18}	10^{-15}
source	mass	electric charge (e)	weak charge (g)	color charge (g_s)
influence	everything	quarks, charged leptons, bosons $W^{\pm}$	quarks and leptons	quarks and gluons

Fermions are particles with a half-integer spin, and they obey the Fermi-Dirac statistics. The elementary fermions of the SM are divided into two groups: quarks and leptons. Together, they create the fundamental building blocks of matter in our Universe. There are three generations of quarks and leptons, with two quarks and two leptons per generation, resulting in a total of 6 quarks and six leptons. The summary of the elementary particles of the SM is shown in FIGURE 2.1.

Quarks are fermions that interact via the strong force due to their colour charge. According to QCD, there are three types of colour charges: red, green, and blue, where red + green + blue = white (neutral). Each quark can have any of the positive colour charges, while the antiquarks have negative colour charges. Quarks do not exist as free particles under standard conditions. Instead, they create composite particles called hadrons, which are colour-neutral. The simplest way of obtaining a colour-neutral hadron is by combining a quark and an antiquark, which creates a meson, e.g. $u\bar{d}$ is a positively charged pion (π^+) while $d\bar{u}$ is a negatively charged pion (π^-). Alternatively, three or more quarks can be combined to create baryons, for example, a proton (uup) or a neutron (ddu). In conditions of extreme pressure or temperature, quarks exhibit a quasi-free behaviour, which can be observed in Quark-Gluon Plasma achieved at high-energy heavy-ion collisions [7].

The second family of fermions, called leptons, are elementary particles which do not have a colour charge, and therefore, do not interact via the strong force. They can, however, have an electric charge, with electrons, muons, and tauons having a negative charge. For each charged

lepton, there is a neutral lepton called a neutrino (electron neutrino, muon neutrino, tauon neutrino), which is expected to have no mass; however, experimental results show that these particles have mass [8], creating another puzzle in modern physics. Contrary to quarks, leptons are free particles.

2.1.1 Antimatter

According to the SM, every particle has a counterpart with the same mass but opposite charge (baryon number, lepton number, electric charge, colour charge, etc.). These particles are called antiparticles (for example, up and anti-up quarks or electrons and positrons). As mentioned before, antiquarks can be used to form mesons. Furthermore, antiquarks can combine to form antibaryons. The antiproton is composed of two anti-up quarks and one anti-down quark. In this way, all existing particles have an antimatter counterpart. The antiparticle is usually denoted by a bar above the symbol ($\bar{u}$ for an up antiquark or $\overline{p}$ for antiproton).

Energy can be converted into matter according to the equation $E = mc^2$. Furthermore, according to conservation laws, any process that creates particles must conserve all quantum numbers. This is frequently realised through the simultaneous creation of a particle and an antiparticle. For example, when two photons collide with enough energy, a process called pair production occurs:

$$\gamma + \gamma \rightarrow e^- + e^+, \tag{2.1}$$

where a pair of electron (e^-) and positron (e^+), its antiparticle, is created. From the heavy-ion collisions, where a vast amount of energy converts to matter, in the form of tens of thousands of particles, we observe matter and antimatter being created in identical amounts [2]. This observation makes antimatter especially interesting, as we would expect to observe similar amounts of matter and antimatter in the Universe; however, this is not the case.

When a particle collides with its antiparticle, both are destroyed and converted into energy, which is then carried by new particles, typically bosons. This process is called annihilation. The most common annihilation channel for the electron-positron pair is:

$$e^+ + e^- \rightarrow \gamma + \gamma \tag{2.2}$$

where each produced photon (γ) receives kinetic energy equal to the rest mass of an electron/-positron, which is 511 keV. The annihilation process can also be considered in interactions between a baryon and an antibaryon. In the simplest picture for that interaction, the process is described as the rearrangement of quarks between a proton and an antiproton [9]. This process

is dominated by emission of pions ($\pi^{\pm}$ and π^{0}) and sometimes kaons ($K^{\pm}$ or K^{0}). Production of kaons contradicts the quark rearrangement model, as kaons contain a strange quark, which isn't present in either a proton or an antiproton. On average, five pions are produced, of which three are charged. The characteristics of distributions of produced pions were experimentally measured and can be recreated by existing statistical models [10].

The annihilation process can be used to explain why we don't observe abundant amounts of antimatter. However, the current understanding of the creation and annihilation mechanisms doesn't explain the dominance of matter particles over antimatter in the Universe, a phenomenon known as the baryon puzzle. Baryogenesis [11]–[13] tries to address this puzzle by suggesting that there should be processes that favour the production of matter over antimatter, while breaking charge-parity symmetry. Some evidence for these processes has already been observed [14]; however, the measured asymmetries aren't sufficient to explain the imbalance between matter and antimatter in the Universe.

2.2 Atomic structure

An atom is built of a positively charged nucleus, consisting of protons and neutrons, and an electron cloud. Most of the mass of the atom is concentrated in the nucleus, which has a radius of approximately 10^{-14} m, while the size of atoms is in the range of 10^{-10} m. The simplest quantum model of an atom is the Bohr model [15], which considers both electrons and the nucleus as point particles. It introduces circular orbits having well-defined radii and discrete energy levels. Even though it is not an accurate description of the atom, it is helpful to introduce the basic concepts and constants. Furthermore, it still provides a satisfactory description of systems that include two charged point-like particles travelling at non-relativistic velocities with respect to each other, as well as systems such as positronium (a bound state of an electron and a positron) or any atom in a Rydberg state. The Rydberg state refers to an atom in a highly excited state, with sufficiently large principal quantum number n, where the excited atom will have similar characteristics to those of a hydrogen atom.

The radius of the electron orbit in the hydrogen atom with the principal quantum number n can be described as:

$$r_n = \frac{\hbar^2}{k_e e^2} \frac{n^2}{\mu}, \tag{2.3}$$

where $\mu = \frac{m_0 M_A}{m_0 + M_A}$ is the reduced mass of a particle with mass m_0 ($m_0 = m_e$ for hydrogen) orbiting nucleus of mass M_A ($M_A = m_p$ for hydrogen), k_e is the Coulomb constant, and e is the

elementary charge. The energy of the electron is then:

$$E_n = -\frac{Zk_e e^2}{2}\frac{1}{r_n} = -\frac{k_e^2 e^4}{2\hbar^2}\frac{\mu}{n^2}, \tag{2.4}$$

with $Z = 1$ for hydrogen. We can introduce the Rydberg constant assuming an electron orbiting an infinitely heavy nucleus:

$$R_\infty = \frac{m_e e^4}{8\epsilon_0^2 h^3 c}, \tag{2.5}$$

where ϵ_0 is the permittivity of free space, h is the Planck constant, and c is the speed of light in vacuum. This is useful, as $R_E = hcR_\infty = m_e c^2 \alpha^2/2$, where α is the fine-structure constant, is a Rydberg unit of energy which can be used to describe the energy levels in hydrogen atoms:

$$E_n = -R_E \frac{\mu}{m_e}\frac{Z^2}{n^2}, \tag{2.6}$$

with $Z = 1$ for hydrogen. The equation 2.6 can also be used to calculate a rough approximation for energy levels of atoms other than hydrogen, by assuming the nucleus has charge $q = Ze$.

The Bohr model is a simplification for a single electron orbiting a positive nucleus. It correctly describes the energies but not the intensities of hydrogen spectral lines and can be used as an approximation for hydrogen-like atoms. When the quantum nature of the electron is considered via the Schrödinger equation, the atomic structure is better described by the shell (orbital) model. It postulates five primary shells (orbits) that electrons can occupy: K, L, M, N, and O, which depend on the primary quantum number $n = 1, 2, 3, 4, 5, \ldots$. Higher orbits are available; however, they aren't present for atoms in the ground state. Each shell is split into smaller subshells based on the primary quantum number n and azimuthal quantum number l, where l is an integer and $0 \leq l < n$ for each shell. The subshells are denoted s, p, d, f, g, h, …, which correspond to consecutive values of l, starting at 0. In an atom in a ground state, electrons occupy subshells with lower energy levels first, that is, those with lower $n + l$ values. The magnetic quantum number m defines available orbitals for electrons in a subshell with quantum number l, where m is an integer and $|m| \leq l$. Furthermore, each orbital can accommodate up to two electrons, one with spin $+1/2$ and the other with spin $-1/2$. Therefore, each subshell can accommodate $4l + 2$ electrons, while each shell can be occupied by at most $2n^2$ electrons. For example, the L-shell ($n = 2$) has two subshells called $2s$ ($l = 0$ with $4 \times 0 + 2 = 2$ electrons) and $2p$ ($l = 1$ with $4 \times 1 + 2 = 6$ electrons), with a total of $2 + 6 = 2 \times 2^2 = 8$ electrons. The model was improved by including corrections, such as the charge screening for many-electron atoms. Furthermore, to obtain more precise energy levels for electrons, the relativistic nature of electrons needs to be

included, as described by the Dirac equation [16].

2.3 Nuclear structure

When considering the movement of electrons in the atom, the nucleus can be thought of as a single particle with charge Z, assuming a uniform charge distribution inside the nucleus. However, the nucleus is composed of Z protons and $N = A - Z$ neutrons, where Z is the atomic number and A is the atomic mass number of the atom.

Some nuclear properties, such as size and binding energies, are well estimated by a simple liquid-drop model. This model treats the nucleus as a single drop of nuclear matter with uniform density, which falls to zero at the surface. The binding energy E_B is described by the semi-empirical mass formula [17]:

$$E_B = a_V A - a_S A^{2/3} - a_C \frac{Z\left(Z-1\right)}{A^{1/3}} - a_A \frac{\left(N-Z\right)^2}{A} + \delta\left(N,Z\right), \qquad \delta\left(N,Z\right) = \begin{cases} 33.6A^{-3/4} & \text{when } N \text{ and } Z \text{ even,} \\ -33.6A^{-3/4} & \text{when } N \text{ and } Z \text{ odd,} \\ 0 & A \text{ is odd.} \end{cases} \tag{2.7}$$

The parameters of the model a_V, a_S, a_C, and a_A are related to the volume, the surface area, the charge (Coulomb), and the asymmetry of the nucleus. For heavier nuclei ($A > 20$), the average binding energy per nucleon is $\sim$ 8 MeV. According to the model, the volume of a nucleus is proportional to the atomic mass number A. From that follows $R_A \sim A^{1/3}$ ($\sim$ 1–10 fm).

The formula 2.7 shows that nuclei with an even number of protons and an even number of neutrons have higher binding energy, while having an odd number of protons and an odd number of neutrons lowers the binding energy in the nucleus. This can be explained with a Fermi gas model, which describes a nucleus as a gas of non-interacting fermions inside a potential well. Both protons and neutrons occupy the lowest available energy levels within their respective potential wells, in accordance with the Pauli exclusion principle. Because of the Coulomb repulsion, the potential well of protons is shallower than the potential well of neutrons. However, the energy is minimised when the maximum occupied energy levels of protons and neutrons are equal. Thus, the number of neutrons increases progressively faster than the number of protons in stable nuclei.

Moreover, atoms that have Z and/or N equal to a magic number (2, 8, 20, 28, 50, 82, 126) also experience higher binding energies. To address the magic numbers, the shell nuclear model [18],

[19] can be used, which postulates that protons and neutrons occupy discrete quantised energy levels.

This model successfully explains the structure of nuclear excitation spectra visible during nuclear spectroscopy. Nucleons fill available energy levels starting from the lowest, yielding the most stable nuclei when all lower shells are completely occupied. Transitions of nucleons to higher energy levels result in excited nuclear states, which are called isomers. These states tend to be unstable, and the nucleus de-excites into a lower energy state by releasing the excess energy via gamma emission. However, when the half-life of the excited state exceeds a timescale of approximately one picosecond, the isomer is considered metastable. An example of a metastable isomer is the 2424.95 keV state of ^{93}Mo with a half-life $T_{1/2} = 6.85$ h [20].

2.3.1 Nucleon distributions inside nuclei

Nuclei consist of nucleons, i.e. protons and neutrons, bound together with the strong force. The distributions of the nucleons inside a nucleus can provide information about the strong force itself. The attractive potential inside a nucleus needs to be greater than the repulsion between protons. The complicated interplay between the short-ranged strong interaction between nucleons and the weaker, but infinitely-ranged, Coulomb interaction between protons results in the binding energies of MeV. Furthermore, the size of a nucleus originates from the short-range nature of the strong interaction, and as a result, the size depends on the number of nucleons (atomic mass number A) [21].

Two radii for any nucleus can be defined. The first one, called the charge radius, depends on the distribution of positive charges, specifically protons. The charge radius can be experimentally measured through the Coulomb interactions, for example, with scattering of electrons on a nucleus [22]. The second radius, sometimes referred to as the nuclear or matter radius, depends on the distribution of nucleons, both protons and neutrons, inside the nucleus. This radius can be determined from scattering experiments where hadrons, such as alpha [23], interact with the nucleus. These radii enable us to estimate the distributions of protons and nucleons inside nuclei. The neutron distribution can be inferred as the difference between the nucleon and proton distributions.

In light nuclei, the numbers of protons and neutrons are approximately equal, whereas heavy nuclei typically contain about 1.5 times as many neutrons as protons. For such nuclei, the nuclear radius exceeds the charge radius, implying the presence of a neutron-rich peripheral region, commonly referred to as a neutron skin [24], [25]. In certain cases, nuclei display a neutron halo, a region of extended, low-density neutron distribution located far from the nuclear core [26], [27].

These structural features offer valuable insights into the underlying nuclear forces. One effective experimental approach to probe such features involves the use of exotic systems, particularly antiprotonic atoms.

2.4 Exotic matter

An ordinary atom consists of electrons and a nucleus with protons and neutrons. However, any of these particles can be replaced by a different particle but having the same charge as one of the constituents[1,2], forming a new bound state, exotic matter [30]. For example, an electron can be replaced with a muon, a heavier lepton from the second generation of elementary particles. This bound system is called a muonic atom. Many other particles have been used to form exotic atoms, like: pions (pionic atoms) [31], kaons (kaonic atoms) [32], [33], antiprotons (antiprotonic atoms) [34], or sigma baryon (sigma hyperonic atoms) [35]. Most of the particles used to form exotic atoms are unstable (except for antiprotons); therefore, the lifetime of such an atom depends on the decay of the particle used, which results in the lifetime of the atom in the order of μs.

Exotic atoms can also include positronium (Ps), an electron and a positron orbiting each other, and its proton or antiproton equivalent, protonium, a proton and an antiproton orbiting each other. The positronium is the lightest exotic atom that can be formed. It is a fully leptonic state, which means it doesn't contain any gluons as opposed to $\overline{\mathrm{H}}$. Therefore, positronium is considered for an alternative approach towards direct measurements of gravity on antimatter [36]. Protonium, on the other hand, allows for investigation of the long-range part of the strong interaction between a proton and an antiproton [37].

TABLE 2.2: Properties of particles and associated exotic atoms as described by a simple Bohr Model. The table is inspired by Table 1 from [30] with updated properties of particles based on [38].

Particle	Type	Mass [MeV]	Mean life [s]	Bohr energy [keV]	Bohr radius [fm]
μ^-	Lepton	105.658	2.197×10^{-6}	$2.8Z^2$	$256/Z$
π^-	Meson	139.570	2.603×10^{-8}	$3.7Z^2$	$194/Z$
K^-	Meson	493.677	1.238×10^{-8}	$13.1Z^2$	$54.7/Z$
$\bar{p}$	Baryon	938.272	∞	$25.0Z^2$	$28.8/Z$
Σ^-	Hyperon	1189.37	0.802×10^{-10}	$31.8Z^2$	$24.6/Z$

[1]Replacing an electron creates an exotic atom, while replacing a neutron or proton inside the nucleus creates exotic nuclei.

[2]There is evidence for existence of the bound state of "K^-pp" created by replacing a neutron in the nucleus [28], [29]; however, it's not clear if this state can be considered as a nucleus.

The exotic atom can be described by applying a simple Bohr model of the hydrogen atom [35]. The energy E_n of the atomic level corresponding to the principle quantum number n for any exotic atom can be estimated from equation 2.6, where Z is the charge of the nucleus, and $\mu = \frac{m_0 M_A}{m_0 + M_A}$ is the reduced mass of a particle with mass m_0 orbiting nucleus of mass M_A. Similarly, the radius for the particle can be estimated from equation 2.3. With this simple description, we get the transition energies in the keV to MeV range. Furthermore, the Bohr radii in the ground state are comparable to the nuclear radius for medium-heavy muonic atoms.

2.4.1 Antiprotonic atoms

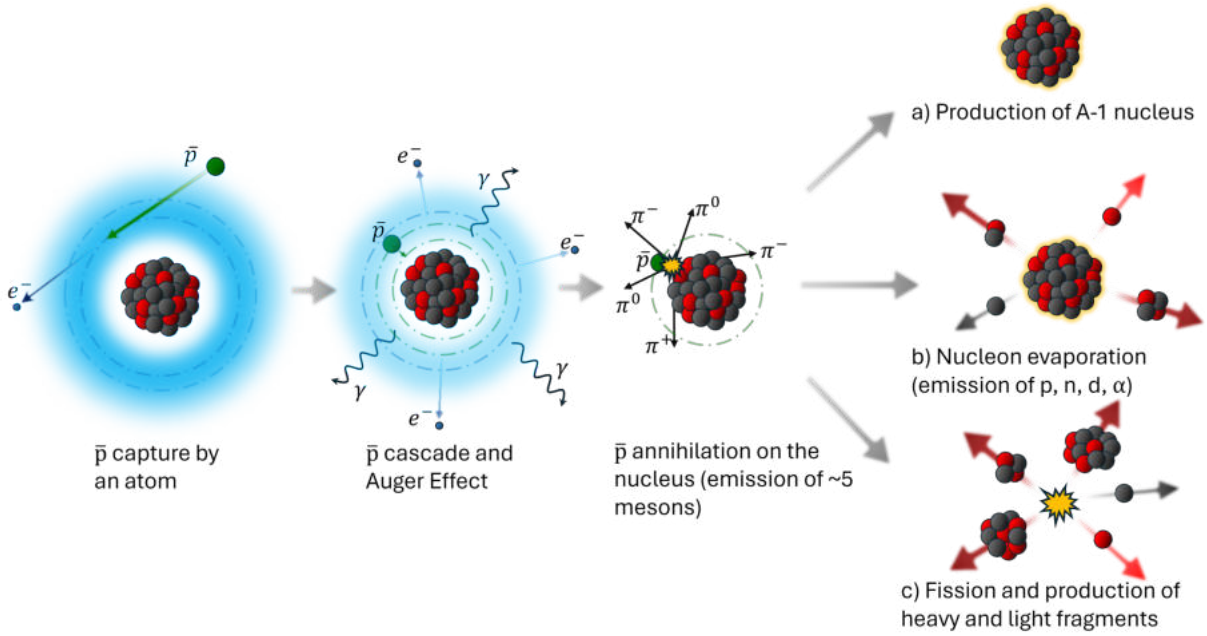

FIGURE 2.2: Diagram of the production and lifecycle of the antiprotonic atoms from capture to final products.

The antiprotonic atom ($\overline{\text{p}}$X) is an exotic matter in which one of the electrons is replaced by an antiproton [34], [39].

With a mass approximately 1836 times larger than that of an electron, $\overline{\text{p}}$ occupies high-Rydberg levels ($n \approx 38$) with a much smaller orbital radius. The excited atom releases the excess energy via a combination of X-rays and Auger electron emission. During this process, $\overline{\text{p}}$ cascades to lower orbits. Eventually, $\overline{\text{p}}$ annihilates when in proximity to the nucleus [40]. The annihilation results in the release of energy carried by ∼5 mesons. These mesons can subsequently be absorbed by the nucleus, which can lead to excitations, nucleon evaporation, or even fission. In

some events, when annihilation happens at the far periphery, the mesons have a high chance of missing the nucleus, with a single $A-1$ ion remaining after the annihilation. The schematic view of the lifecycle of $\overline{\text{p}}$X is shown in FIGURE 2.2.

Antiprotonic atoms can be used as a probe for fundamental physics, including QCD, QED, atomic and nuclear physics, and the proton-antiproton annihilation process [41]. Furthermore, they are excellent probes for neutron halo studies [27], [42], [43]. They can also be used as a means of production of short-lived, radioactive atoms in the highly-charged ion (HCI) state [44], which is explored as the primary goal of this thesis.

Antiprotonic atoms were initially studied during the Low Energy Antiproton Ring (LEAR) era at CERN. The experiments were performed using high-energy antiprotons in a beam-on-target configuration (solid, liquid, or gas). Studies on antiprotonic atoms are continued, with antiprotonic helium [45] at the Antiproton Decelerator (AD) facility at CERN. Currently, CERN is the only place in the world with access to low-energy antiprotons, where experiments routinely trap millions of antiprotons that can be used for studies of antiprotonic atoms at lower energies.

Chapter 3

Techniques for trapping charged particles

There are two main techniques for trapping charged particles. They are traps with dynamic electric fields, called Paul traps, and traps with static magnetic fields, called Penning traps. Most, if not all, of the existing trapping techniques for charged particles can be defined as one or the other type, often requiring the use of both techniques combined.

The overview of the particle trapping methods is well described in [46], and the overview of different applications for particle traps can be found in [47], [48]. The following subsections give a brief introduction to Penning and Paul traps.

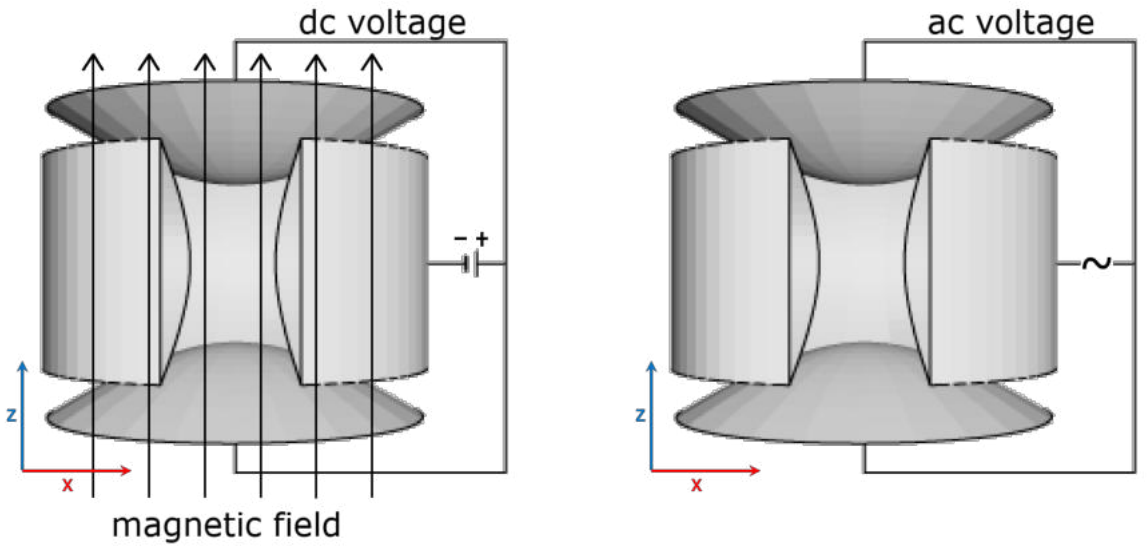

(A) The Penning trap uses a static potential on the electrodes for confinement in the z-axis (axial) direction. Confinement in the radial direction is achieved through an external, uniform magnetic field.

(B) The Paul trap uses an oscillating electric potential applied between the electrodes of the trap.

FIGURE 3.1: Schematic arrangement of the two common types of particle traps (from [46]). A light grey shape indicates a ring electrode. Both traps are closed with the endcap electrodes, depicted as dark grey, parabolic shapes.

3.1 Penning trap

The Penning trap is a combination of static electric and magnetic fields that create a confinement for charged particles. A force acting on a particle with mass M and charge Q, moving through the electromagnetic field $\mathbf{E}$ and $\mathbf{B}$ with velocity $\mathbf{v} = (v_x, v_y, v_z)$ is described as:

$$\mathbf{F} = Q\left(\mathbf{v} \times \mathbf{B} + \mathbf{E}\right). \tag{3.1}$$

The ideal Penning trap uses a homogenous magnetic field $\mathbf{B} = (0, 0, B)$ and an electric field $\mathbf{E} = -\nabla\Phi$, where the potential Φ is described as:

$$\Phi = \frac{U_0}{2d^2}\left(2z^2 - x^2 - y^2\right), d = \sqrt{\frac{1}{2}r_0^2 + z_0^2} \tag{3.2}$$

This potential is established with a cylindrical electrode of length $2z_0$ and radius r_0, and two hyperbolic endcap electrodes following the equations:

$$r^2 - 2z^2 = r_0^2$$
$$r^2 - 2z^2 = -2z_0^2;$$

however, a potential near the centre of the trap, as described by equation 3.2, can be created with simple plane endcap electrodes. The potential U_0 is applied between the endcaps and the circular electrode. The basic arrangement of electrodes is shown in FIGURE 3.1a.

The axial confinement of a particle is done by applying a potential on the endcaps of U_0. The radial confinement is established via the applied magnetic field. The ion with atomic mass A and charge Q and velocity $v_\perp$ perpendicular to the magnetic B field has motion with radius:

$$r = \frac{m_n \cdot v_\perp}{\frac{Q}{A} \cdot B}, \tag{3.3}$$

where m_n is the mass of a nucleon.

The Penning trap can be simplified by changing the hyperbolic electrodes to axisymmetric ring electrodes. By adding more cylindrical electrodes, it is possible to ensure a reasonable trapping volume while simplifying the manufacturing process. Furthermore, the additional electrodes enable further manipulation of plasmas within the trap and the creation of more complex trapping potentials.

3.2 Paul trap

The confinement in a Paul trap is achieved by applying an oscillating electric potential, which can be accompanied by a static component, between the main ring and two end caps electrodes. The basic arrangement of electrodes is shown in FIGURE 3.1b. The Paul trap doesn't require the use of an external magnetic field. The potential used can therefore be expressed, by modifying the equation 3.2, as:

$$\Phi = \frac{U_0 + V_0 \cos \Omega t}{2d^2} \left(2z^2 - x^2 - y^2\right), d = \sqrt{\frac{1}{2} r_0^2 + z_0^2} \tag{3.4}$$

where $\Omega = 2\pi/T$ is the frequency of the oscillating electric potential with period of T. The shape of the potential at two instants differing by half of the oscillation period and for $y = 0$ is shown in FIGURE 3.2.

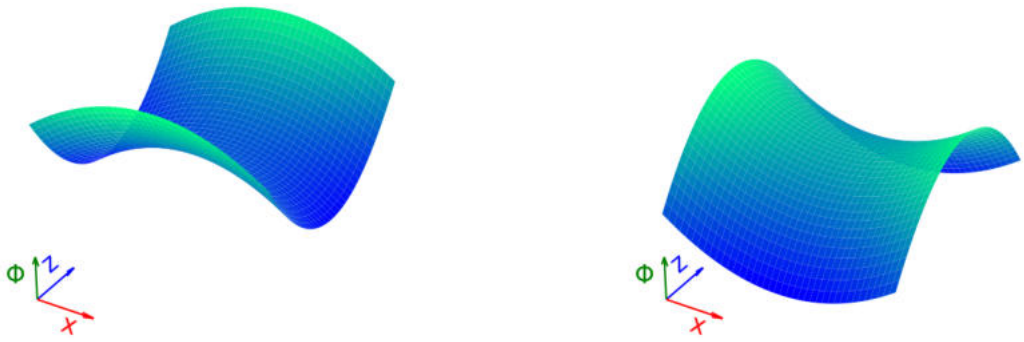

(A) $t = 0$ (B) $t = \frac{T}{2} = \frac{\pi}{\Omega}$

FIGURE 3.2: Oscillation of the electric potential of a Paul trap with period T. The potential can be thought of as rotating about the Φ axis.

The potential creates a saddle point for a particle where it is convergent in one direction while divergent in the perpendicular direction. An appropriate choice of field amplitude and frequency enables the achievement of a time-averaged force in all three directions towards regions of the weak field at the centre of the trap. This force confines the particle inside the trap.

Chapter 4
Novel production method of antiprotonic atoms

One of the main goals of this thesis is to showcase the novel production scheme for antiprotonic atoms, as shown in [44]. The scheme is based on the charge-exchange reaction performed between co-trapped cold antiprotons and ions. Ions and antiprotons are trapped in a single Penning-Malmberg trap, where the ions can be excited to Rydberg states. After excitation, the exchange of an electron for an antiproton in a given ion is highly likely, creating an antiprotonic atom. Details of the scheme are presented in the section 4.1.

So far, the only way to produce antiprotonic atoms was available by directing a beam of antiprotons (usually with the kinetic energy of antiprotons in the order of MeV [34], or recently achieved <100 keV for antiprotonic-helium [45] with theoretical possibility for <1 keV [49]) into either a bulk target or high pressure gas. The antiprotons slow down within the target material through numerous Coulomb interactions and are randomly captured by target atoms, forming antiprotonic atoms before undergoing annihilation. The antiprotonic atoms are then studied either via gamma-ray spectroscopy (studies of the atomic antiproton transition energies) or via radiochemistry, where effects from the radioactive decay of the produced fragments can be observed (studies of the neutron halo of different nuclei [27]).

The production scheme proposed in this thesis has three main advantages.

- The production is performed with cold (potentially temperatures of sub-Kelvin) antiprotons and ions. Hence, the majority of the energy during production and subsequent annihilation comes from the annihilation itself. This fact can be used to study in isolation the details of the formation process of antiprotonic atoms and the interactions between antiprotons and nuclei.

- The production is performed directly inside a particle trap, which opens up the possibility of trapping the fragments produced during the annihilation of the antiprotonic atom. The information about different residual nuclei formed during the annihilation process is essential for validating and developing models of antiproton-nucleus interaction and the nuclear periphery [41].

- The production is done in a controlled manner. With the co-trapping scheme, it is possible to separate antiprotons from ions and combine them with nanosecond precision via trap manipulation. Having access to the precise time of the atom formation is crucial to eliminate signals due to other interactions, for example, annihilation of the antiprotons on the rest-gas inside the trap or the walls of the apparatus, and more importantly, to be able to probe short-lived states immediately after production, opening the possibility for conducting spectroscopy of short-lived isotopes and isomers.

4.1 The production scheme

One of the production methods of antihydrogen atoms is based on an induced charge-exchange reaction between Rydberg positronium and an antiproton [50]. An antiprotonic atom can be created similarly when a positronium atom is replaced with any other atom. This principle is at the core of the proposed production method for antiprotonic atoms. In contrast to antihydrogen production, the initial atoms have long lifetimes and can be easily co-trapped with antiprotons. The reaction can be described as:

$$\bar{p} + A^* \rightarrow \bar{p}A^* + e^-, \tag{4.1}$$

where the A^* is the target atom in the Rydberg state, and the $\bar{p}A^*$ is the corresponding antiprotonic atom formed in the Rydberg state.

To trap atoms with antiprotons, the atoms need to either gain or lose an electron to become ionised. Both cations and anions can be used in this method; however, anions have the same electric charge as antiprotons, which makes it easier to mix the two species within a single particle trap. An ionised gas of target atoms is then co-trapped with antiprotons inside the same particle trap. By maintaining a high vacuum and low pressure of the target gas, the annihilation process can be suppressed.

The charge-exchange reaction is then induced with three laser pulses with nanosecond duration. The first pulse is the infrared laser used for photo-detachment of the excess electron from the anion, making the atom electrically neutral. The second and the third laser pulses (of ultraviolet and visible light, respectively) are used for the sequential excitation of the atom into the high-n Rydberg state. The cross section for the charge-exchange process between an atom and an antiproton increases as a function of the excitation level of the atom (for the charge exchange between Ps and antiproton, the cross section scales with the principal quantum number of Ps in the fourth power, $\sigma \propto n_{Ps}^4$ [51]). The lifetime of the Rydberg antiprotonic atom is on the order of

10 ns. At that time, the antiproton initiates the cascade, and the atom loses energy through electron emission, via the Auger process, and gamma emission. An additional advantage of using the Rydberg excited state for the antiprotonic atoms is the initial orbit of the antiproton in the atom. With the excited atom, the antiproton is expected to be implanted outside the electron cloud, thereby increasing the probability of complete electron stripping. The entire process concludes with the annihilation of the antiproton in the periphery of the nucleus, where the nucleon density is less than 10% of the central density [52]. The schematic overview of the production scheme is shown in FIGURE 4.1.

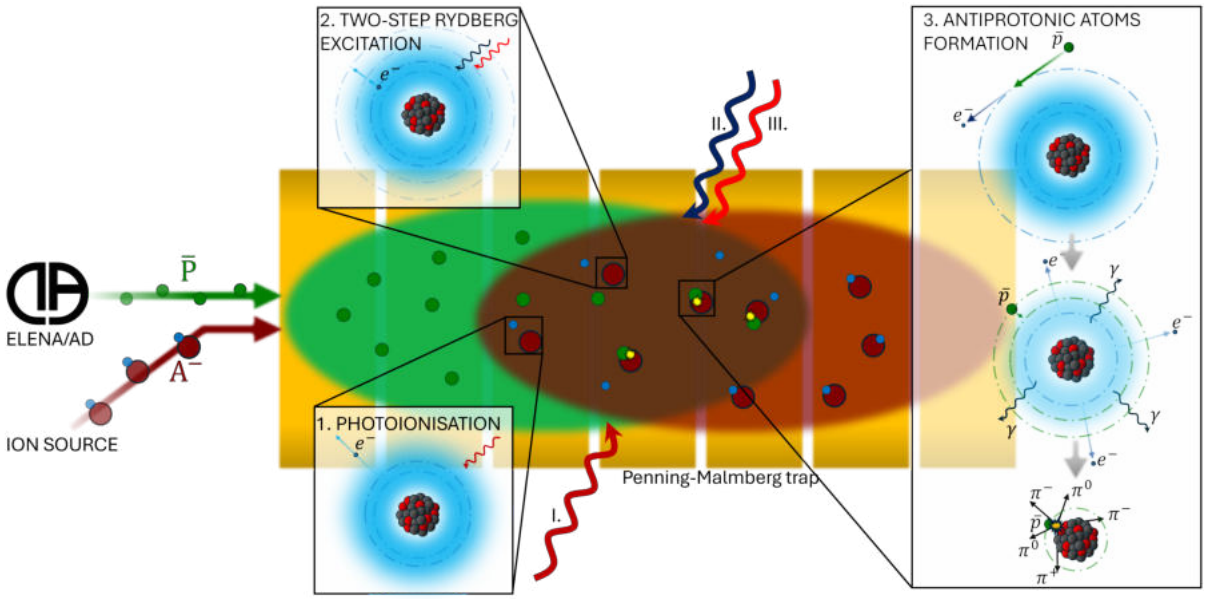

FIGURE 4.1: The overview of the production scheme for the antiprotonic atoms inside a particle trap. The blue circles represent electrons, the red circles represent atoms, and the green circles represent antiprotons. Firstly, antiprotons and anions are co-trapped inside the same Penning-Malmberg trap. Then, a series of three laser pulses (indicated by I, II, and III), each with a nanosecond duration, is used. The first laser induces the photoionisation, creating a neutral atom. The second and third pulses bring the atoms to the Rydberg state via the two-step Rydberg excitation. Finally, the antiproton is captured by the Rydberg excited atom, and the antiprotonic atom is formed.

There can be three outcomes of the annihilation. Let's assume that we start with a target atom with a mass number of A_{target}. In the first possibility, the annihilation removes one of the nucleons and no subsequent reactions happen, producing one nucleus with a mass number of $A_{target} - 1$, usually in an excited state. In the second possibility, the annihilation can leave one heavier nucleus with an atomic mass of $A_{target} - 1 - k$ and several light fragments (protons, neutrons, alphas, and/or lithium nuclei) where $k = \sum A_{p,n,He,Li}$. The third option

is a nuclear fission induced by the pions from the annihilation. The target nucleus splits into X and Y nuclei, with atomic masses of A_X and A_Y respectively, and some light fragments where $A_{target} - 1 - k = A_X + A_Y$. All fragments are expected to be created as entirely stripped of electrons, meaning they will mainly consist of positively charged nuclei and neutrons. Therefore, the products of the annihilation can be trapped inside the particle trap either by creating a nested trap or by coincidentally switching the trap polarisation to accommodate positively charged particles.

4.1.1 Multi process path

After establishing the controlled production and trapping of the fragments, a possible expansion of the procedure is theorised. It involves repeating the charge exchange process for trapped fragments. This is a more complex technique and is only possible after the primary method has been established. The procedure begins after trapping the fragments resulting from the annihilation of antiprotons with a specific target isotope. Additional selection can be made on the fragments to limit them to only one species inside the trap. For Paul-like traps, a radiofrequency technique can be applied [53]. For Penning-like traps, a multi-reflection time-of-flight method can be used [54], [55].

The trapped fragments are expected to be in the entirely stripped state; therefore, a reattachment of the electron needs to be performed before the charge-exchange reaction can be initiated. Alternatively, the plasma of antiprotons and the highly-charged ions could be mixed without control, with ns precision, over the formation of subsequent antiprotonic atoms. After the annihilation, the fragments produced are trapped in the same trap.

This method could provide further details on the annihilation and fragmentation processes. Furthermore, it opens up the possibility of using shorter-lived isotopes (with lifetimes of minutes) as targets for antiproton-induced fission.

Chapter 5
Experimental setup

I declare that I was actively involved in the operation of the AEgIS apparatus since 2021. Details of the most significant upgrades to the setup of AEgIS can be found in reports of AEgIS to the SPC (Scientific Policy Committee) Committee at CERN [56]–[59]. My most significant contribution to the apparatus is the new control system, introduced in [60] and [61], to which I am a contributing author. I was also involved in hardware upgrades of the apparatus. My biggest contribution was in performing the following tasks:

- *I was involved in the installation of the degrader ladder actuator.*
- *I designed and installed controls for motors used for the operation of the degrader ladder/rotation of the MCP detector.*
  - *I was responsible for connecting the controller to the stepper motor. After the retirement of the degrader ladder in 2023, the controller setup was refurbished for the operation of the rotation of the MCP detector in the* HedgeHog *region of the beamline.*
  - *I created a dedicated µService called* Degrader Ladder Manager
- *I created an interface between software used at UMK (University of Mikołaj Kopernik in Toruń) and ARTIQ for operation of the new ion source provided by UMK.*
- *I integrated several new valves into the apparatus (both physical connection and software implementation).*

Furthermore, since 2024, I was part of the cryogenics team at AEgIS responsible for refilling the cryostats. This work is necessary for keeping the magnetic field on at AEgIS. I was also responsible for overseeing the warm-up and subsequent cooling procedures in August 2025.

Moreover, I declare that I am one of the co-developers of the CIRCUS control system of AEgIS. I created multiple µServices used in the experiment, some of which are described in the Appendix D. Furthermore, I am one of the two co-developers of the underlying framework TALOS along with its creator, Dr Marco Volponi [62].

I have taken part in the development of the custom ARTIQ-based library, of which Dr Saiva Huck is the principal author and developer [63]. I was personally responsible for:

- *Development of the procedure for squeezing plasma by manipulating potentials on trap electrodes.*
- *Implementation of messages between ARTIQ and various µServices in CIRCUS.*

- *Implementation of labels for sync-check timestamps.*
- *Development of functions for creating a nested-trap setup.*
- *Development of functions for controlling correctors in the beamline provided by the ELENA infrastructure.*

Furthermore, I was heavily involved in multiple code consolidations.

In development of TALOS, I was personally responsible for:

- *Development of the Config class and its implementation into the Father of All Detectors class.*
- *Development of the chain for executing a series of experimental scripts, which includes:*
  - *Development of utility classes for defining a series of experimental scripts (schedules) and performing operations on them.*
  - *Development of core µServices; Scheduler, Monkey, Kasli Wrapper.*
  - *Development of the internal logic (flow of messages) between the µServices to ensure safe processing of the schedules.*
  - *Implementation of support for using multiple FPGAs in parallel*
- *Addition of interfaces to TALOS, opening the framework to experiment-based implementation of DAQ, Analysis Framework, and FPGA controls.*
- *Various quality-of-life improvements and code consolidation.*
- *Active participation in deciding on the future perspective of TALOS.*

Furthermore, I implemented graphics for Monkey and Tamer µService. Together with Dr M. Volponi, we created the logo for CIRCUS and the special version of the logo for AEḡIS experiment. I created alternative versions of the logo for some holiday periods. All graphics are summarised in A.

In development of CIRCUS, I was personally responsible for:

- *Development of Degrader Ladder µService for controlling one of the actuators.*
- *Adaptation of the old control software for pulser and rotating-wall controllers to µServices.*
- *Development of Captorius µService for controlling LeCroy oscilloscopes.*
- *Development of a µService for controlling one of the cryo-motors inside the experiment.*
- *Implementation of the interface for ALPACA, the analysis framework of AEḡIS.*
- *Implementation of the interface for Kasli, the FPGA of AEḡIS.*
- *Implementation of the beam-steering with direct access to all 10 correctors provided by the ELENA accelerator.*
- *Adaptation of the DAQ control into an implementation of the DAQ interface for AEḡIS.*
- *Supervision of development of various µService.*

The production method of antiprotonic atoms and subsequent trapping of the fragments from the antiproton-induced fission requires unique equipment. Currently, the only place in the world where cold antiprotons are produced is the Antimatter Factory at CERN. Furthermore, the

AEgIS experiment at the Antimatter Factory has successfully implemented the charge-exchange scheme for the pulsed production of an antihydrogen beam. Taking all this into account, the AEgIS experiment provides the most suitable environment for testing the novel production method of cold antiprotonic atoms directly inside a particle trap.

This chapter gives an overview of the experimental setup used for testing the production method. The section 5.1 gives an introduction to CERN's accelerator complex and the production scheme for antiprotons. Section 5.2 explains the main components of the AEgIS apparatus, focusing on the main components needed for establishing the controlled production of antiprotonic atoms.

5.1 CERN

The European Organization for Nuclear Research (CERN) is home to the world's largest particle accelerator, known as the Large Hadron Collider (LHC), which spans a circumference of 27 km. The LHC is used to collide protons and ions at tremendous energies, achieving up to 14 TeV for proton-proton collisions. To reach the desired energies, CERN uses past colliders as pre-accelerators and injectors to the LHC. TABLE 5.1 states the energies reached by the protons during the acceleration. The entire accelerator complex is depicted in FIGURE 5.1.

TABLE 5.1: The kinetic energy of protons reached in the different stages of acceleration at CERN. The corresponding speed is presented as the percentage of the speed of light.

Accelerator	Kinetic energy of proton	Speed [% c]
Linac 4	160 MeV	52
PS Booster	2 GeV	94.8
PS	25 GeV	99.93
SPS	450 GeV	99.9998
LHC	7 TeV	99.999 999 1

The experiments at CERN aren't limited to the LHC alone. Super-Proton Synchrotron (SPS) delivers beams to experiments in CERN's North Area, where experiments like NA61/SHINE [65] and NA62 [66] study fixed target collisions. Protons from the Proton-Synchrotron Booster (PS Booster) are delivered to the Isotope Mass Separator On-Line facility (ISOLDE) [67], where the low-energy beams of radioactive nuclides can be created. Furthermore, the Proton-Synchrotron is used to create antiprotons for the Antimatter Factory, where various experiments can study the unique properties of antiprotons.

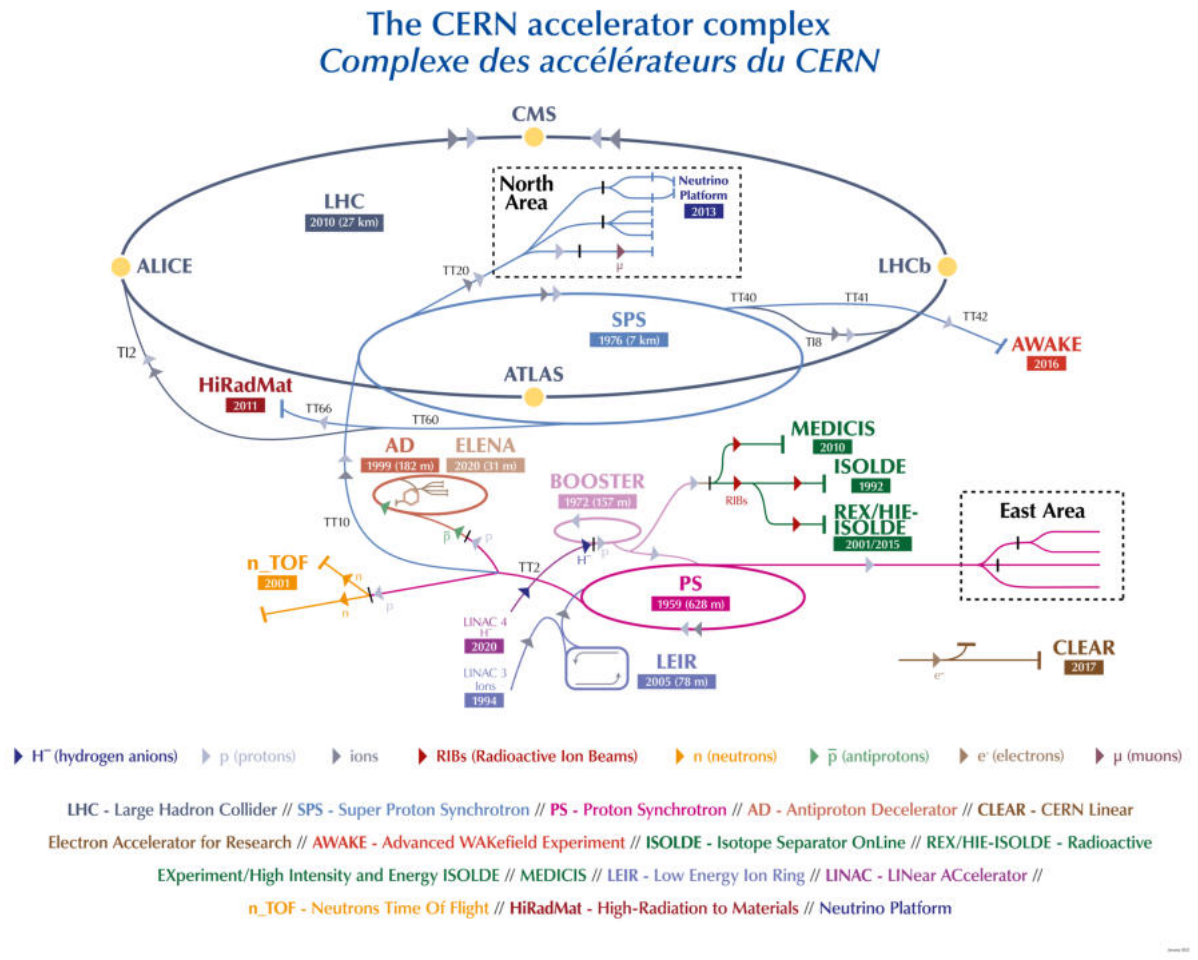

FIGURE 5.1: The CERN accelerator complex [64]. AD and ELENA are the only accelerators that slow down, and not speed up, particles, making them decelerators; ELENA is the newest addition to CERN's accelerator complex.

5.1.1 AD

The Antimatter Factory is the only place in the world with access to cold antiprotons. It's home to six experiments: AEgIS [68], ALPHA [69], ASACUSA [70], BASE [71], GBar [72], and PUMA [73]. Each experiment aims to answer some fundamental questions about antimatter by utilising trapped antiprotons.

The primary device that allows for all the science at the Antimatter Factory is the Antiproton Decelerator (AD) [74], [75]. It is a synchrotron that is used to slow down (instead of speeding up) antiprotons. The antiprotons are created from the high-energy collision of protons from PS with an iridium target. During the collision, part of the beam energy is converted into new particles.

The antiprotons are created according to the equation:

$$p(beam) + p(target) \rightarrow p + \bar{p} + p + p, \tag{5.1}$$

when a proton from the beam interacts with a proton in the target, and according to the equation:

$$p(beam) + n(target) \rightarrow n + \bar{p} + p + p, \tag{5.2}$$

when the target's neutron is involved instead. To produce antiprotons, the kinetic energy of the proton beam needs to be at least 6 GeV, which creates antiprotons with energy of $E \sim 1$ GeV on average. The PS provides protons with kinetic energy around 26 GeV. As a result, produced $\overline{\text{p}}$ have higher energies ($E \sim 3.6$ GeV) and are boosted in the forward direction to improve subsequent focusing by the magnetic horn. Furthermore, the production yield of $\overline{\text{p}}$ is increased. This energy of produced $\overline{\text{p}}$ is too high for any efficient trapping; therefore, the AD is used to slow down antiprotons to energies of 5.3 MeV.

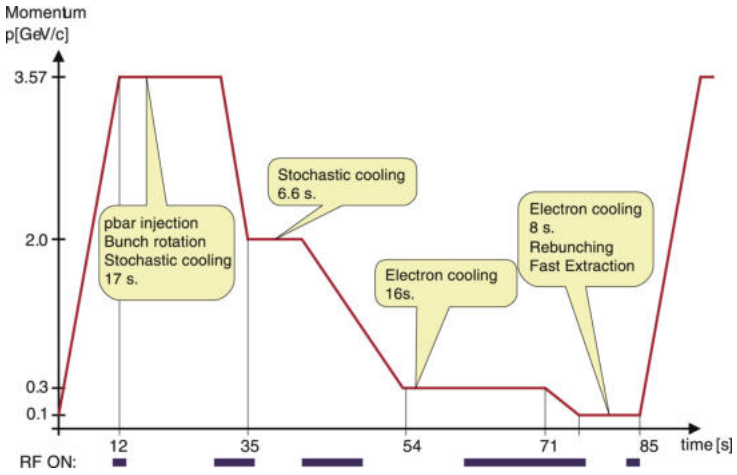

FIGURE 5.2: Momentum of $\overline{\text{p}}$ as a function of time over a typical cycle in the AD (taken from [75]).

The cooling (reduction of the phase-space while increasing density) and decrease of the energy of antiprotons is achieved within a 100 s cycle. AD uses radiofrequency (RF) cavities to decrease the energy of antiprotons. There are two techniques for cooling antiprotons: stochastic cooling and electron cooling. The momentum over time of $\overline{\text{p}}$ during a single cycle is shown in FIGURE 5.2. The complete antiproton cycle in AD is described below.

Firstly, a bunch, consisting of $\sim 6 \times 10^7$ $\overline{\text{p}}$ with energy $E \sim 3.6$ GeV and momentum spread of $\frac{\Delta p}{p} \sim 6$ %, is injected into the AD. Then, the bunch is stretched from a length of 30 m to 190 m

by RF fields which decreases the momentum spread to $\frac{\Delta p}{p} \sim 1.5\,\%$. At this point, the stochastic cooling is performed. A series of pickup electrodes along the AD ring detects deviations in momenta and transverse positions of subgroups of $\overline{\text{p}}$, with respect to the mean values of all orbiting $\overline{\text{p}}$. These values are sent to the steering electrodes located on the opposite side of AD. The electrodes apply correction to the orbit of the subgroup based on received signals. By applying repeated corrections the momentum spread decreases to $\frac{\Delta p}{p} \sim 0.07\,\%$. This is followed by RF deceleration to $p = 2$ GeV/c. The stochastic cooling is repeated once again, and $\overline{\text{p}}$ are decelerated to $p = 300$ MeV/c. The electron cooling is applied in the second half of the deceleration cycle. Electrons, with velocities matched to that of $\overline{\text{p}}$, are injected in a collinear configuration into $\overline{\text{p}}$ beam. As a result, $\overline{\text{p}}$ are bathed in a stationary cloud of "cold" electrons. The antiprotons collide with electrons through Coulomb interactions, losing a portion of their energy and effectively cooling the antiproton beam. Then $\overline{\text{p}}$ are decelerated to $p = 100$ MeV/c, followed by electron cooling and the final deceleration stage. Finally, the beam of energy 5.3 MeV and momentum spread $\frac{\Delta p}{p} \sim 0.01\,\%$ is then ejected from AD and injected into the second decelerator called Extra Low ENergy Antiproton ring (ELENA).

5.1.2 ELENA

To improve the trapping efficiency of experiments at the AD hall, the secondary deceleration cycle was introduced in 2020 [76]. It is the smallest working synchrotron at CERN with a diameter of only 10 m. The 5.3 MeV antiprotons from AD are cooled and decelerated by another factor of 50, reaching energies of 100 keV. The ELENA cycle is similar to that of AD [77]; however, it utilises electron cooling as its sole cooling mechanism. $\overline{\text{p}}$ with momentum of 100 MeV/c are injected into ELENA and decelerated to intermediate momentum in the range 35–40 MeV/c. At that time, the electron cooling is applied. The second deceleration period brings momentum of $\overline{\text{p}}$ to 13.7 MeV/c and the second stage of the electron cooling follows. Ultimately, the beam is bunched into four bunches and ejected to experiments with a final energy of 100 keV.

Before the introduction of ELENA, all experiments at the Antimatter Factory worked in a shift mode, where one experiment at a time would receive a beam of $\overline{\text{p}}$. The combination of AD and ELENA allows for simultaneously cycling up to 4 bunches of $\sim 1.2 \times 10^7$ $\overline{\text{p}}$ every 120 s working all day long without any interruption. This means that up to 4 experiments can receive antiprotons for their studies at once, which is an overall improvement. To take full advantage of the beam provided by ELENA requires physicists to oversee their experiment 24 hours every day of the week. For smaller collaborations, this poses a challenge, as they might not have enough people to support shift work.

5.2 AEgIS experiment

The Antimatter Experiment: Gravity, Interferometry, Spectroscopy, or AEgIS for short, is one of the six experiments in the AD hall at CERN. Its main goal is to perform a precise measurement of the gravitational interaction of a horizontal beam of $\overline{H}$ [78].

In 2018, AEgIS has demonstrated the pulsed production of antihydrogen [79]. The charge-exchange reaction between Rydberg-excited positronium atoms and the antiprotons was used to create $\overline{H}$ atoms. This marked the end of Phase 1 of AEgIS. Phase 2 started in 2019, coinciding with Long Shutdown 2 (LS2) at CERN. In this phase, the experiment expects to improve the pulsed production of $\overline{H}$ by at least two orders of magnitude, achieving a production rate of 1 to 10 $\overline{H}$ per ELENA cycle. This is crucial to achieve the required precision of 1 percent by the end of Phase 2 in 2026, at the beginning of LS3 at CERN.

AEgIS has three physics programs [80]: Antihydrogen Physics, Positronium Physics, and Antiprotonic Atoms Physics. The primary focus of the experiment is the gravity measurement; however, other programs are given dedicated times to perform necessary measurements, e.g. a recent publication about the achieved positronium laser cooling performed at AEgIS [81]. The antiprotonic atoms program is the latest addition to the physics at AEgIS, and the recent developments in this program are the subject of this thesis.

5.2.1 The apparatus overview

The AEgIS experiment is built as a combination of multiple subsystems. The antiprotons for the experiment arrive from ELENA via the beam transfer line. Along the line, a series of chambers allows for the injection of other particle species, the ejection of cold antiprotons, and the placement of diagnostic equipment (see section 5.2.2). The antiprotons travel via the beamline, passing through degraders until they reach the main body of the experiment, where two cryostats host electromagnets and a series of electrodes needed to realise the Penning-Malmberg traps. Inside the traps, detailed studies of trapped particles and the pulsed production of antihydrogen can be performed. After the cryostats, another beamline is prepared for performing measurements of the interaction of the $\overline{H}$ beam with gravity.

Outside the main body of the experiment, a dedicated system is in place to produce positrons, which are used to create positronium within the main cryostat. Additionally, a dedicated laser system provides laser pulses necessary for Rydberg excitation of positronium.

There are ongoing works to expand the existing apparatus. One of them is to introduce an ion source to the injection beamline that can be used for developing controlled formation of

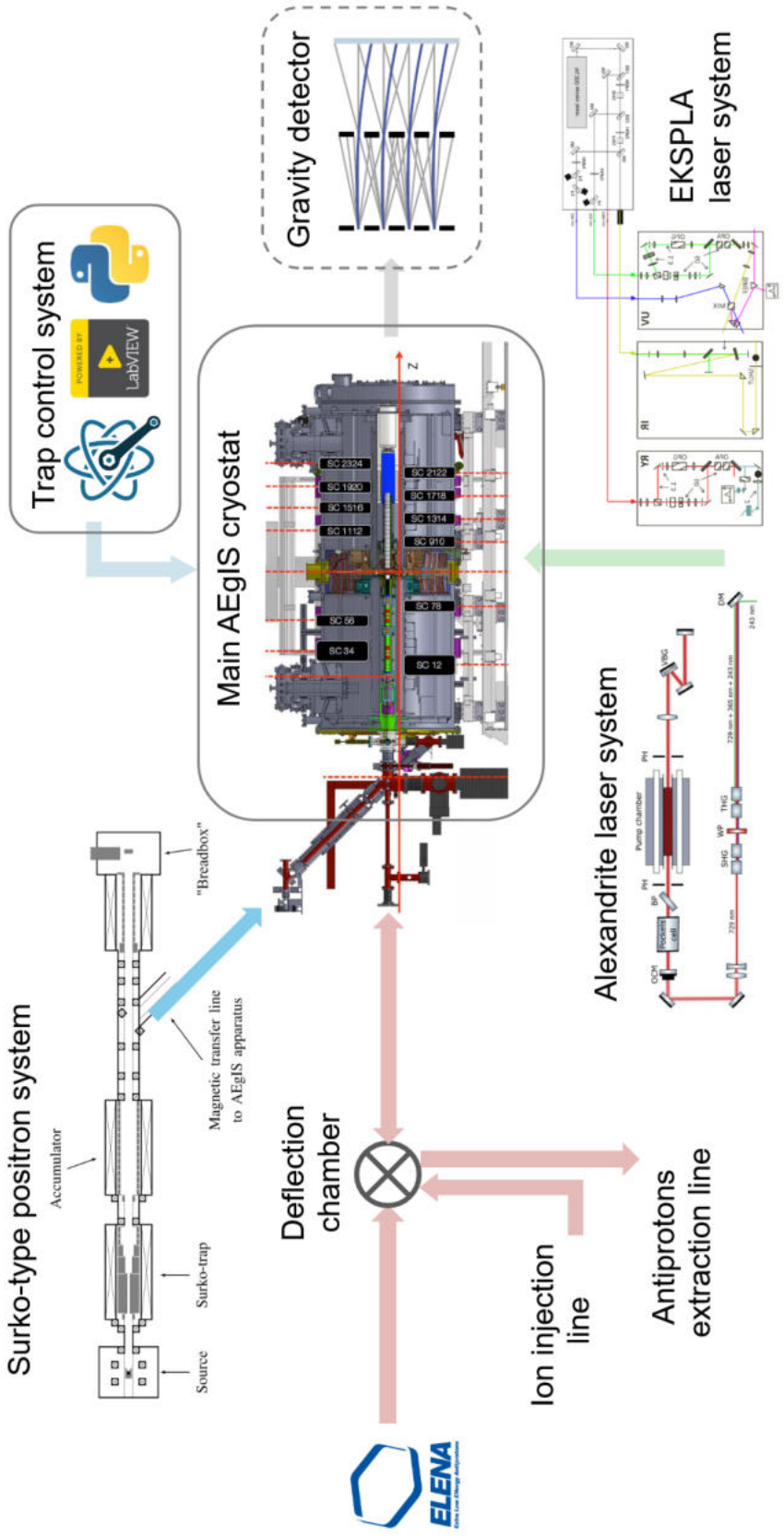

FIGURE 5.3: The overview of the AEgIS experiment with all the subsystems.

antiprotonic atoms. A parallel effort is attempting to achieve a backwards ejection of antiprotons (in the opposite direction to the injection line) for trapping antiprotons within external traps.

The schematic overview of the experiment is shown in FIGURE 5.3.

5.2.2 The beamline

ELENA and the main body of AEgIS experiment are connected via a beamline. This beamline comprises multiple ports and chambers designed to accommodate various detectors or manipulators for steering and observing the $\bar{p}$ beam.

One of the upgrades of the AEgIS apparatus to accommodate ions in the experiment was a new chamber for the injection of ions. This chamber, colloquially referred to as "STARSHIP" due to its distinctive appearance, features two injection ports and is equipped with two bending electrodes. It is shown in FIGURE 5.3 as the "Deflection chamber". FIGURE 5.4 shows the schematic overview of the chamber (on the left) and a picture of the chamber installed in the beamline (on the right).

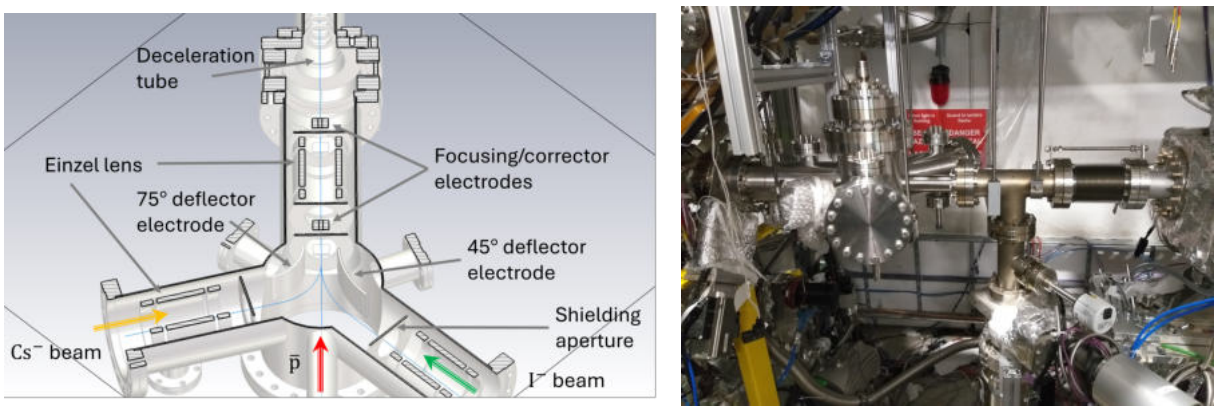

FIGURE 5.4: The schematic overview of the chamber [82] (on the left) and the chamber installed in the beamline [58] (on the right).

The whole chamber has four entrances. The two concentric ones are used as the main entrance and exit of the uninhibited antiproton beam from ELENA. The two other entrances (at $75°$ and $45°$) can be used for either ion injection or antiproton ejection. There are three Einzel lenses (electrostatic lens), in two ion injection regions and the exit line towards the central AEgIS apparatus. These can be used to focus the particle beam after the bending electrodes. Inside the main chamber, two bending electrodes can be used to steer the beam into or out of the exit ports. A detailed simulation was performed to validate the design [82]. The results of the simulation are shown in FIGURE 5.5. It shows that a beam of 2 keV iodine ions can be successfully steered by either of the bending electrodes in the direction of the AEgIS experiment.

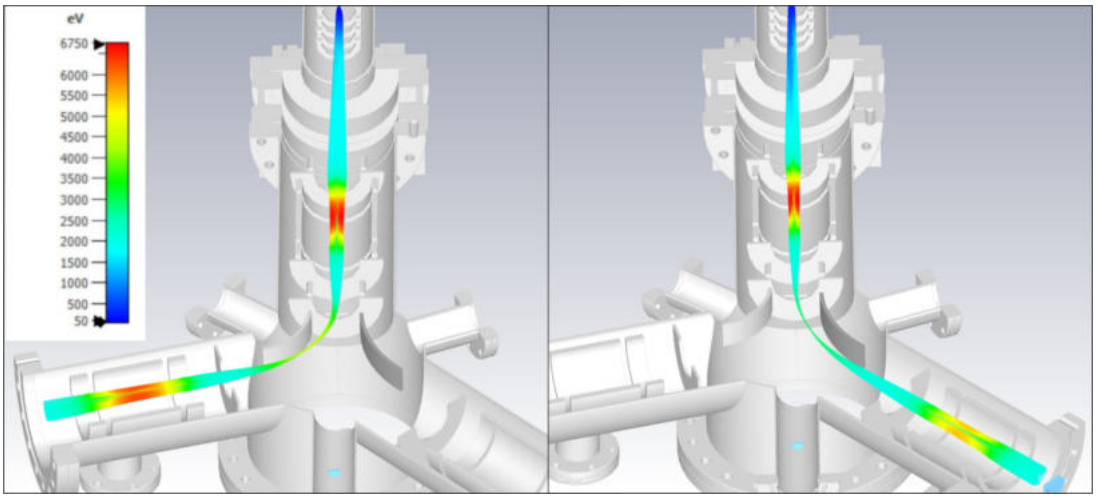

FIGURE 5.5: CST simulation of a 2 keV I- beam with a radius of 10 mm (from [82]).

Between the "STARSHIP" and the cryostat, there are two more chambers on the beamline. First, called *HedgeHog* (HH) is used as the injection point for positrons to the main AEgIS cryostat. It also hosts a rotatable actuator which can be used to insert one of the Microchannel Plate (MCP) detectors into the beamline. The second chamber, located directly at the entrance to the main cryostat, is called *SUN* and hosts a series of actuators used to insert and remove diagnostic equipment from the antiproton beam path. This is where the electron gun, used for delivering electrons for electron cooling, can be inserted. Moreover, the actuator housing the degrader ladder with thin degrader foils was placed in this chamber.

5.2.3 Ion sources

The crucial element needed for the controlled formation of antiprotonic atoms is a source of ions into the AEgIS experiment. There are two sources: the iodine source developed by the University of Mikołaj Kopernik in Toruń, and the Borealis source.

5.2.3.1 Iodine source

The source consists of a molecular beam source, an electron gun, and a linear Paul trap. The ions are produced via electron dissociative attachment in electron-molecule collisions. The electrons from the electron gun are shot onto the beam of molecules. Via collisions, an electron can be attached to a molecule, causing it to dissociate into two or more fragments. Some of the fragments can be negatively charged. The molecule that was selected as the initial target is I_2. There

are two dissociation processes for that molecule:

$$I_2 + e^- \rightarrow I^- + I, \tag{5.3}$$

$$I_2 + e^- \rightarrow I^- + I^+ + e. \tag{5.4}$$

The negatively charged ions are then trapped in the Paul trap, which serves as an ion accumulator. Subsequently, the trap can be opened with a trigger, and the ions will be moved via the beamline to the main body of the experiment.

The group from KL-FAMO/UMK in Toruń built the source system for the AEgIS experiment, and it was transported to CERN at the end of 2024. The control system for the source is currently under development, and the source is being prepared for connection to the beamline.

5.2.3.2 Borealis

The *Borealis* project at AEgIS was implemented to demonstrate the laser cooling of negative ions [83]. The setup of Borealis uses an Even-Lavie supersonic expansion valve [84] to produce neutral molecules from a gas mixture of 92 % He, 5 % C_2H_3, and 3 % CO_2. These molecules are later ionised with a dielectric barrier discharge to produce anions. A Wien filter, which uses an electromagnetic field to select the desired mass-to-charge ratio, is used to limit the produced anions to $C_2{}^-$.

In 2024, this setup was moved to the AEgIS zone and connected with the I^- *beam* injection line on the "STARSHIP," as a temporary ion source, before the iodine source is ready for commissioning.

5.2.4 Magnetic field

Two sets of superconducting magnets generate the magnetic field of the Penning-Malmberg trap at AEgIS. Each magnet is a solenoid made from Niobium-Titanium alloy (Nb:Ti). The magnets are kept at <9 K using a liquid helium bath. Furthermore, each magnet has an additional set of 10 correction coils that ensure field homogeneity of 10^{-5} and sharper field termination at the magnet's endcaps.

The two magnets generate fields of different strengths. The first region, closer to ELENA, is 5 T, while the second field has a strength of 1 T. The field strength is also used as the name of the two sections of the experiment: 5T and 1T, respectively.

The dual-field design was chosen to address two aspects of the antihydrogen production [78]. Firstly, a high magnetic field is desired for efficient trapping and further electron cooling of

antiprotons. Secondly, a low magnetic field is necessary in the $\overline{H}$ formation region. The magnetic field is further described in the section 6.2.2 in the context of the simulation of the degrader foil effects.

5.2.5 Cryogenics

The superconducting magnets that are used to create the magnetic field of AEgIS operate in the cryogenic temperatures of <9 K. That's why they need to be submerged in a bath of liquid helium (lHe), which has a boiling temperature of 4.2 K. A complex cryogenic structure surrounds the magnets to maintain low temperatures while minimising liquid helium consumption. Additionally, keeping the trapping region at low temperatures provides a cryogenic-pumping (cryo-pumping for short) of the surfaces [85], that is, absorption of molecules on the apparatus walls, which enables access to extremely-high vacuum (EHV) necessary for long lifetimes of antiprotons.

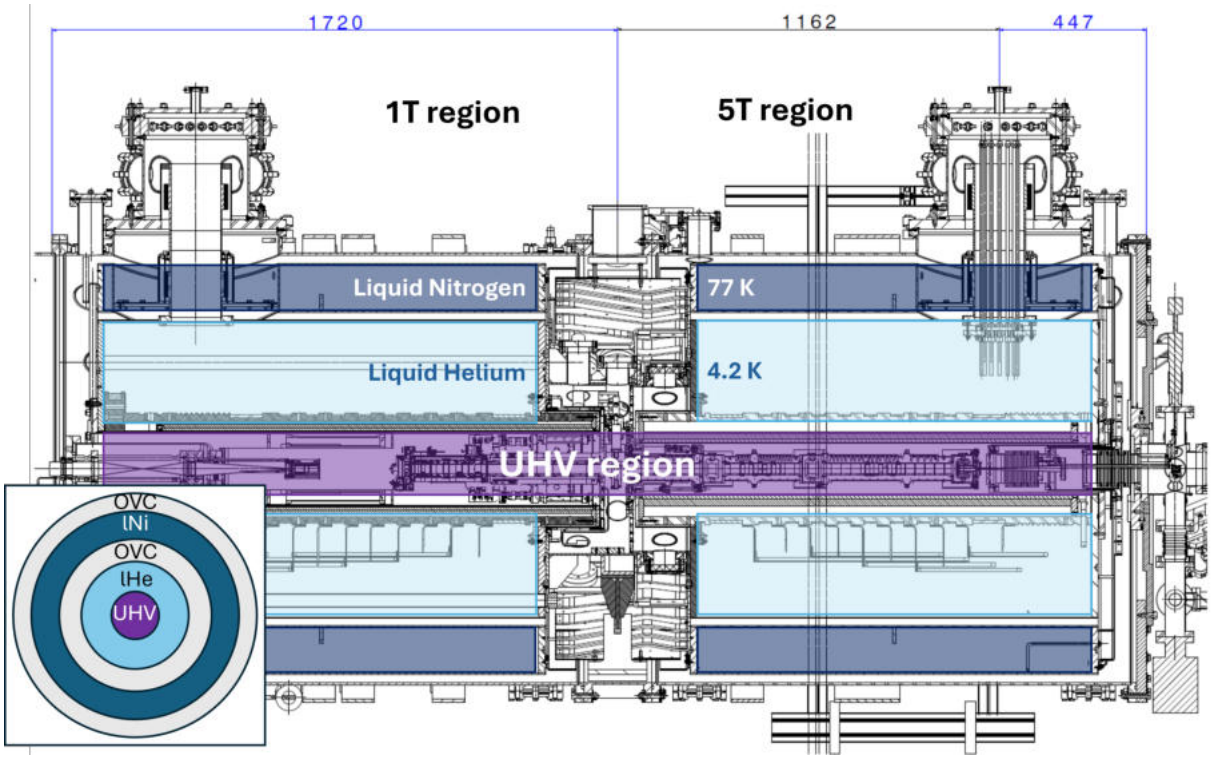

FIGURE 5.6: A cut view of the cryostat of AEgIS. The 1T region is depicted on the left and the 5T on the right, together with the *SUN* entrance region. The dark blue colour indicates the region cooled with liquid nitrogen (T $\sim$ 77 K). The light-blue colour indicates the region cooled with liquid helium (T $\sim$ 4.2 K). The purple region indicates the UHV inside the AEgIS apparatus. The inset shows a diagram of the front-view cut.

The cryostat consists of concentric cylindrical chambers. The cut-view of the cryostat is shown in FIGURE 5.6. The innermost region is the ultra-high vacuum (UHV) environment and hosts the experiment's traps. This is placed inside a second cylinder that hosts the magnets and is filled with liquid helium. This is enclosed by the outer vacuum chamber (OVC). The OVC is "divided"[1] into two sections, between which there's another chamber filled with liquid nitrogen. The boiling temperature of liquid nitrogen is 77.4 K. Liquid nitrogen is more readily available than liquid helium. Furthermore, a layer of liquid nitrogen works as a heat shield for the liquid helium inside. This optimises the experiment's operation by limiting liquid helium consumption while reducing the time required for cooling of the experiment. Both liquid helium and liquid nitrogen vessels are covered with multi-layer insulation blankets, with 30 and 10 layers, respectively, which further shield the liquids from external heat.

5.2.6 Vacuum

One of the characteristic interactions between matter and antimatter is annihilation. Because of this, it is essential to keep antimatter and matter as separate as possible. This is achieved by conducting experiments within a vacuum environment. A vacuum environment can be classified by the maximum pressure, which is directly correlated to the amount of matter inside the system. TABLE 5.2 shows the common pressure ranges for different vacuum environments.

TABLE 5.2: Vacuum ranges for different types of environments.

Vacuum	Pressure range [mbar]
high	$10^{-7} - 10^{-3}$
ultra-high (UHV)	$10^{-12} - 10^{-7}$
extremely-high (EHV)	$< 10^{-12}$

Obtaining the pressures of $<10^{-12}$ mbar is a stepwise process involving different vacuum technologies. The vacuum system of AEgIS includes a series of backing pumps that are used for the fore-vacuum. This provides an initial vacuum of $\approx 10^{-3}$ mbar. At that stage, turbomolecular pumps (or turbo pumps for short) can be used to reach $\approx 10^{-7}$ mbar. Turbo pumps are capable of reaching lower pressures; however, their effectiveness is limited due to the large size of the entire vacuum volume at AEgIS. The lower pressures can be achieved by a combination of getter pumps, reaching the levels of 10^{-9} mbar in the OVC region. For the simplicity of the system, the UHV is maintained only in a small section of the experiment, where the traps are located. The pressures of $<10^{-12}$ mbar are achieved thanks to the ion pumps and the cryogenic environment.

[1] Both cryostats and the central region share the same insulation vacuum.

At pressures of UHV, the particles of the gas seldom interact with each other and more often interact with the walls of the chamber. Maintaining the chamber walls at cryogenic temperatures enables the entire chamber to function as a cryopump, as particles that come into contact with the walls adhere to them, thereby effectively removing these particles from the main volume.

To improve the pumping of the apparatus, a thermal-treatment process called "baking" is performed to eliminate the possibility of later out-gassing, that is, the release of small quantities of gas trapped inside solid material, which would pollute the environment over time. To maintain a stable vacuum, a series of sensors and valves is used to monitor the current vacuum status. Interlock is programmed in the control system to automatically close specific valves whenever the vacuum readout exceeds a predefined threshold. This allows us to separate sections with a worse vacuum, maintaining a fairly good vacuum for the experiment.

Furthermore, there are specific pressure requirements for opening the beamline between AEgIS and ELENA. This protects the ELENA vacuum, and by extension, other experiments from the potential contamination of a single experiment at the AD hall.

5.2.7 Trapping system

The main trapping system of the AEgIS experiment uses the Penning-Malmberg design. The trap consists of ≈ 1620 mm of 65 circular electrodes. The electrodes have various lengths and support different voltages; however, all electrodes have the same diameter of 30 mm.

The entire ensemble is divided into two separate sets of electrodes, 5T and 1T, which are axially aligned and placed inside the UHV region with a gap of 6.8 mm between the two sets. Schematic overviews of the electrodes used as 1T and 5T traps are shown in Figure 5.7 and Figure 5.8 respectively. The positions of the electrodes are given in the AEgIS coordinate system, which defines $z = 0$ mm at the half-point between 1T and 5T magnets, which corresponds to the centre along the beam axis of the B0 electrode. The first part, mounted in the 5T region of the experiment, is used for trapping and cooling of antiprotons. The trap has 3 high-voltage (HV) electrodes capable of reaching −15 kV potentials. These electrodes are used to trap the moderated $\overline{p}$ leaving the degraders, thin foils used to reduce the energy of the $\overline{p}$ beam (see section 5.2.8 for more details), after they are delivered by ELENA. The electrodes are grouped into smaller traps called "C" (for catch), "P" (for positron), and "T" (for transfer)[2]. These electrodes support the potentials of ±200 V, which is sufficient for the plasma manipulation. The middle electrodes in sections "C" and "P" consist of two segmented electrodes that are used for the rotating wall

[2]The names refer to the original purpose for each section. Since then, the traps have often been used interchangeably for different tasks, and their names no longer fully reflect their intended purpose.

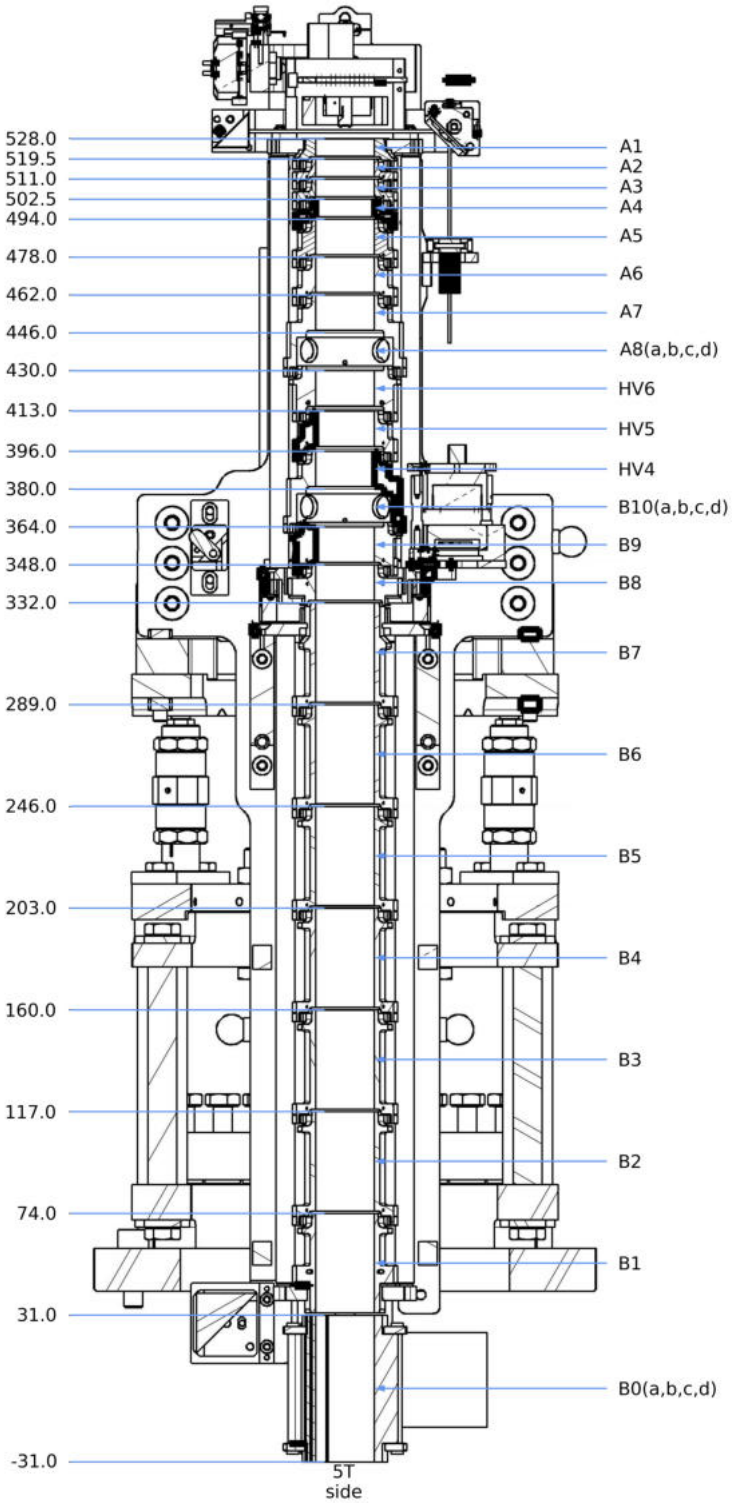

FIGURE 5.7: The schematic overview of the electrodes comprising the 1T. The positions of the electrodes are given in the AEgIS coordinate system, which defines $z = 0$ mm at the half-point between 1T and 5T magnets. "B" electrodes create an extension of the transfer region from the 5T to the 1T trap. "A" electrodes define a region where $\bar{H}$ is formed.

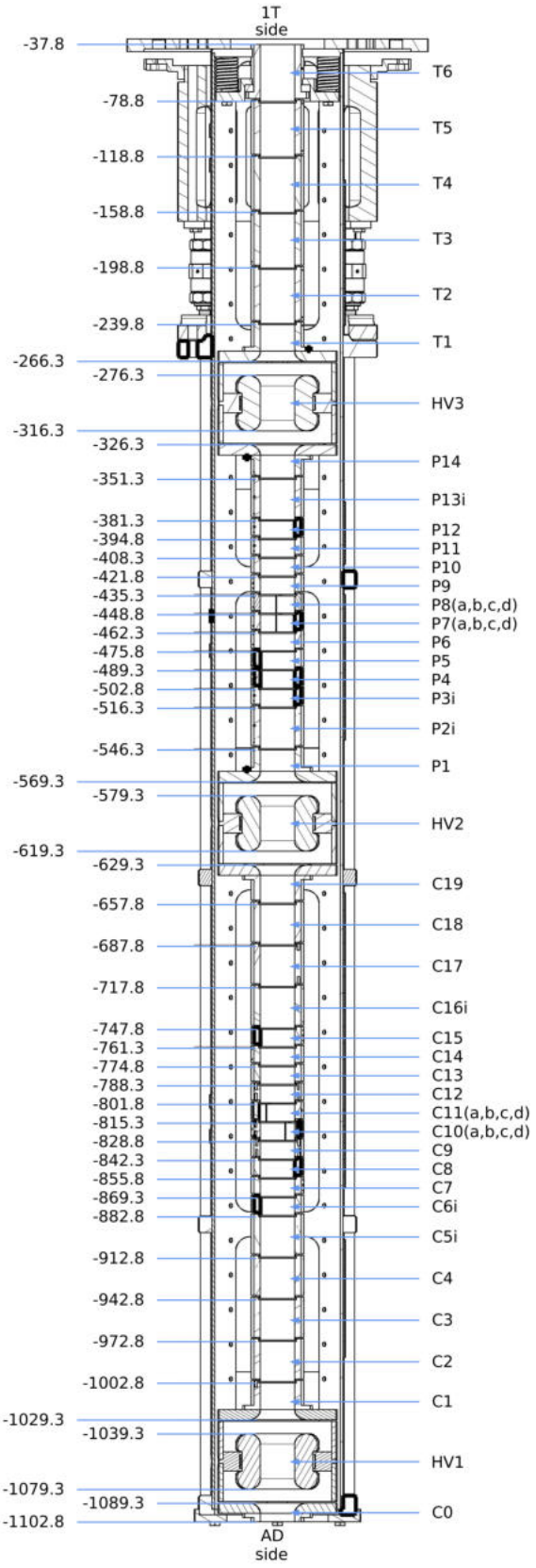

FIGURE 5.8: The schematic overview of the electrodes comprising the 5T. The positions of the electrodes are given in the AEgIS coordinate system, which defines $z = 0$ mm at the half-point between 1T and 5T magnets. HV1-HV3 electrodes are used for trapping high-energy $\bar{p}$. "C" (catch) electrodes are used for initial trapping of electrons for electron cooling. "P" (positron) electrodes are used for electron cooling of $\bar{p}$. "T" (transfer) electrodes are used for transferring plasma between 5T and 1T traps. C10, C11, P7, and P8 are segmented electrodes used for compression of plasma via the rotating wall technique.

technique [86]. The technique enables plasma confinement (either compression or expansion) through the use of rotating electric fields. The "T" section is used for moving plasmas through the magnetic field gradient between two sections of the experiment (1T and 5T).

At the centre of the experiment is another sectorised electrode, called B0. This electrode enables greater control over the plasma in the region between the two magnets in the experiment by establishing an electric field gradient.

The 1T trap electrodes are also grouped into smaller traps. Section "B" defines an extension of the transfer region that is located at the end of the 5T trap. The second section, marked as "A", defines a region where antihydrogen formation occurs in the AEgIS experiment. These electrodes support potentials of ±200 V, the same as the electrodes of the 5T trap. Between the two sections, there are three HV electrodes capable of achieving potentials of 5 kV, which can be used for the recapture of plasma from 5T and 1T regions with higher launching potentials[3]. Furthermore, the electrodes of each section closest to the HV region are replaced with the segmented electrodes that can also be used for the rotating wall technique.

All electrodes can be used simultaneously to create more complex traps, i.e., a nested trap, a setup in which a potential well with one polarity is created within a longer potential well with opposite polarity. The nested trap enables the simultaneous trapping of particles with opposite electric charges within a single confinement region, which is necessary for the production of antiprotonic atoms and the subsequent trapping of the produced fragments. The electrodes from both 1T and 5T are used to define a parabola (ranging from the P10 electrode in the 5T region to the A1 electrode in the 1T region), which is crucial for the forward-boosted production of antihydrogen that is the cornerstone of the gravity measurement at AEgIS [63].

The 1T ensemble is equipped with additional features shown in FIGURE 5.9. The entire trap is connected to the centre region of the experiment; however, the addition of cryogenic piezoelectric motors allows for fine alignment of the trap inside the apparatus in the cryogenic environment. Moreover, the structure houses two rotary actuators, one with a positronium target holder and the other with an ionisation grid, i.e. a wire grid that can be polarised to some potential to increase or decrease the energy of incoming particles. This allows for inserting the grid and/or target, depending on the experiment's needs, thereby limiting the restriction on the path for antiprotons inside the experiment.

[3] Higher launch potential mitigates losses of particles during the transfer between two trapping regions.

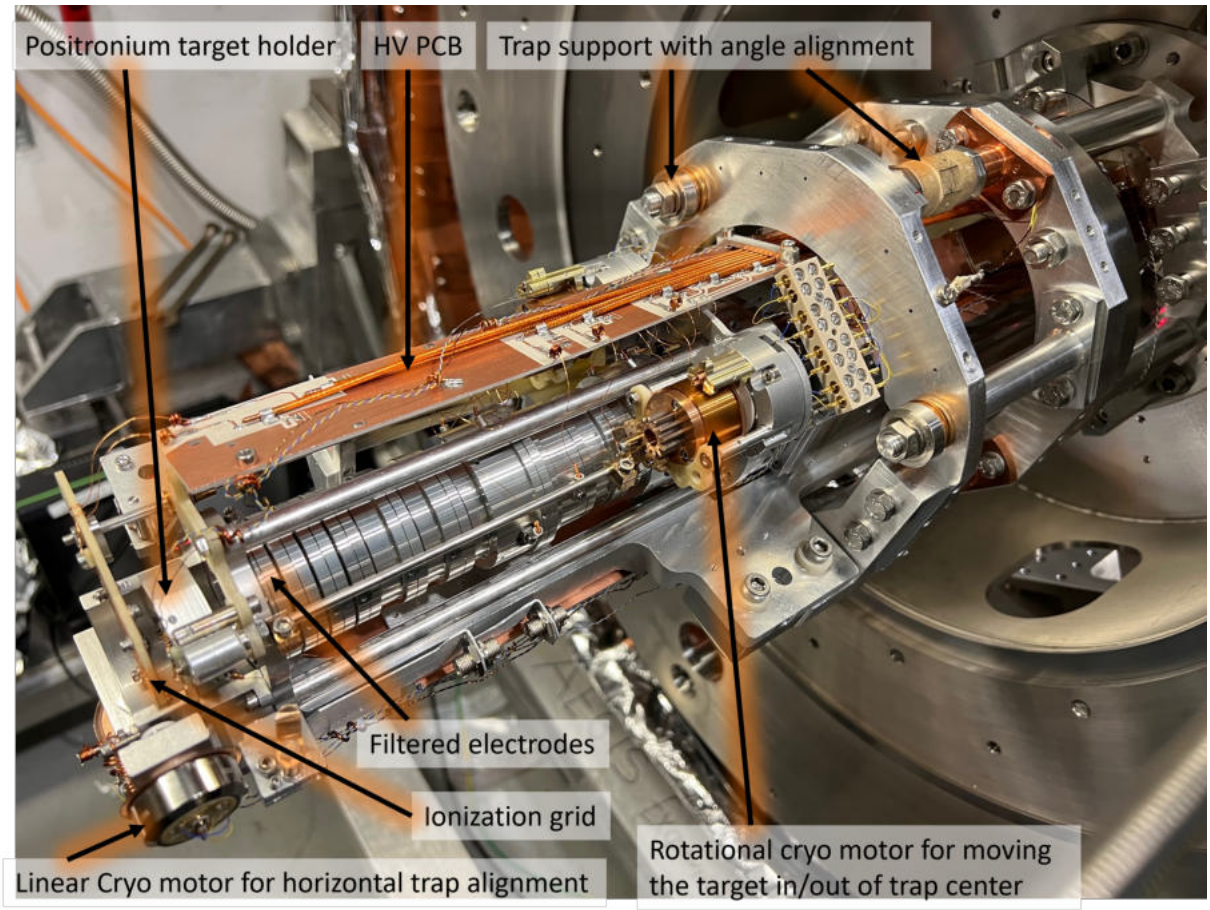

FIGURE 5.9: The picture of the 1T trap in the AEgIS experiment (taken from [57]). There are two linear cryo motors (one visible for horizontal alignment) used for the horizontal and vertical alignment of the trap after the experiment is closed. Two additional rotational cryo motors (visible only the target rotation motor) are used for inserting an ionisation grid and positronium target into the trap centre.

5.2.8 Degrading system

To obtain the best trapping efficiency of antiprotons, it is crucial to optimise all aspects of the trapping process. The antiprotons that are delivered to experiments by the AD/ELENA complex have an energy of 100 keV. This means that a potential of roughly 100 kV is required on the end-cap electrodes of a trap to have high enough stopping power for all particles. To avoid electrical discharge, in practice, the supplied voltage is limited to <20 keV. Different methods can be implemented to further decrease the energy of the incoming $\bar{p}$ beam. The simplest method involves inserting a degrader, a thin foil or gas mixture (usually SF_6 /He [87]), that moderates the energy of $\bar{p}$ through atomic collisions. In general, the longer the path of $\bar{p}$ in the degrader (the thickness of the foil), the higher the decrease in the energy. At the same time, the cross section of the

annihilation of $\overline{p}$ in the foil increases with lower energy. Therefore, the optimal thickness of the foil used as the degrader depends on the material used and the initial energy of the incoming $\overline{p}$ beam. Alternatively, an RF quadrupole decelerator (RFQD) [88] can be used. It works by applying RF to decelerate $\overline{p}$ while simultaneously applying a magnetic field from a quadrupole magnet to focus the beam. RFQD is more efficient than a simple degrader in moderating the energy of $\overline{p}$; however, implementing a foil as the degrader is much simpler.

At the AEgIS experiment, two sets of degraders are used. The main degrader has an effective thickness of 1400 nm consisting of two Mylar foils and is positioned at the entrance to the 5T trap. The two foils have thicknesses of 900 nm and 500 nm Mylar. The first, thicker foil is coated with a four-fold segmented 10 nm aluminium (see FIGURE 5.10a). The segments are separated by 1 mm gap. The antiprotons passing through the foil can be either in one of the four metallised segments or passing through the uncoated cross. This leaves a signal via the charge deposition, which can be used as a rough beam position monitor. The second foil is fully metallised with the same aluminium thickness (see FIGURE 5.10b). Via the same mechanism, it can therefore be used to estimate the integrated beam intensity.

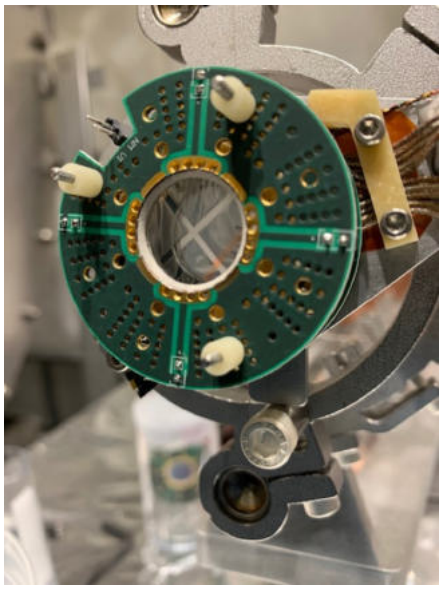

(A) The foil with segmented metallisation (10 nm Al), facing the ELENA.

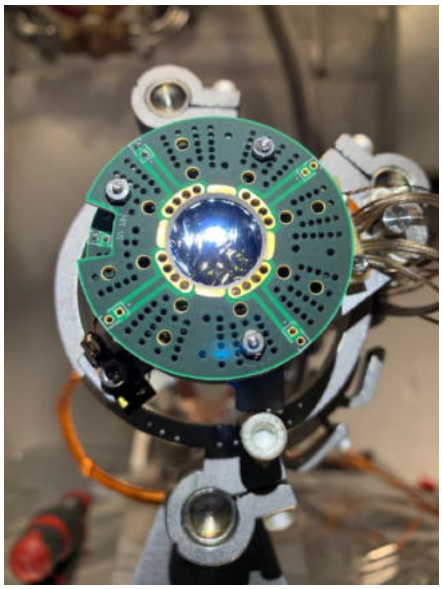

(B) The foil facing the 5T trap with full metallisation (10 nm Al) for beam monitoring

FIGURE 5.10: The main degrader holder of the AEgIS experiment. In the picture, the foils used are 1500 nm Parylene N on the left and the 100 nm Parylene N on the right. The material was later replaced after careful considerations of the GEANT4 simulations (see sections 6.2 and 9.3). Pictures taken from [56].

The second degrader is a movable actuator with five slots for different foils. This is used to

study different combinations of the degrader foil thicknesses and their effects on the trapping efficiency. The holder of the foils is shown in FIGURE 5.11. The actuator is placed just in front of the 5T cryostat (also known as the *SUN*), making it effectively the first degrader for the antiprotons. The thin degraders can be entirely removed, and the main degrader can be used as the sole degrader.

FIGURE 5.11: The degrader ladder with five different foils mounted. Each foil is either 100 nm or 200 nm of Parylene N. For this configuration, the effective thickness of each degrading stack is: 400 nm ($\mathbf{2}\times$ 200 nm), 300 nm (200 nm + 100 nm), 200 nm, 200 nm, 100 nm. Picture taken from [56].

The thickness of the degraders at AEgIS was studied with detailed simulations in GEANT4. The simulation setup is presented in section 6.2. The comparison of the simulated results with experimental measurements is presented in section 9.3.

5.2.8.1 Actuator control

The degrader ladder is mounted on the linear actuator. The foils on the ladder, as shown in FIGURE 5.11, are 21 mm in diameter with 28 mm distance between their centres. It is mounted on a 400 mm long actuator, which has an Oriental PKP268MD28B stepper motor attached to it. The motor has a basic step of 0.9° (corresponding to 7.5 µm linear movement) and is controlled by a Trinamic TMCM-1311 closed-loop stepper motor controller module. The controller allows for 256 microsteps per full step of the motor, which means that the smallest movement of the actuator that can be achieved is about 30 nm. The actuator is also equipped with two limit switches along the linear shaft, which are connected to the controller. The controller supports directional limit switches, which means that movement in one direction (turning right or left) can be interrupted when the directional switch (right or left, respectively) is tripped. This allows for the definition

of the upper and lower limits for the actuator position, utilising physical stoppers. Moreover, the limit switch can be used as a reference point for the software calibration of the device (which was implemented in the μService of the controller).

Details of the controller setup are described in the documentation for the TMCM-controller-based rotation control attached to this thesis in Appendix E, while the details of the μService are described in the section D.1.

5.2.9 The electron gun

Electrons play a crucial role in experiments at AEgIS. They provide an additional cooling mechanism, stochastic electron cooling, and allow testing, to some extent, the plasma manipulation operations without the need for antiprotons. The electron plasma is generated via the electron gun that can be inserted into the beam axis with the help of a linear actuator installed in the *SUN* entrance.

The electron gun works on the principle of the thermal effects of metals. Electrons are extracted by heating a metal to a high enough temperature. In the process, a fraction of electrons in the material receive enough thermal energy to overcome the work function for the metal and escape the material. Afterwards, electrons are accelerated by an electric field to extract them from the device, creating a forward boosted, continuous current of electrons.

The electron gun at AEgIS consists of a thin barium oxide filament. The filament is heated with a 1130(1) mA current supplied by a custom power supply that can be current-regulated. The filament can be biased up to −200 V with respect to the electron gun case. The device typically operates with a bias of −40 V.

The current of electrons extracted from the electron gun is around 10 μA. This can be experimentally measured with the help of the micro-channel plate (MCP) plate detector located at the end of the 1T region.

5.2.10 Source of positrons

The production of an antihydrogen atom requires positrons. At the AEgIS experiment, positrons are created via the β^+ decay of ^{22}Na source. The sodium source is placed on a tantalum plate that acts as the positron reflector. The source is placed inside a copper holder that is kept at a temperature of 7 K inside the vacuum. The low temperature allows for the formation of an ice layer of neon (inserted into the vacuum as a gas), which serves as a moderator for positrons. The positrons are then accelerated to 8 eV and collected inside a Surko-trap [89]. This type of trap is

a variation on the Penning trap. The trap is filled with a gas used for cooling the particles through inelastic collisions between the particles and the gas. The cold positrons from the Surko-trap are accumulated inside an accumulator.

The positrons can then be transported into the main body of the experiment via a special beam line that accelerates positrons to 2.5 keV and brings them on the axis of the traps inside 5T and 1T regions.

5.3 Detection systems at AEgIS

The AEgIS experimental apparatus is a complicated device that can be used for many tasks. It is also equipped with multiple detectors. However, in the context of this thesis, only two detectors are considered.

5.3.1 External Scintillating Detector Array

One of the most essential detectors used in AEgIS is a series of twelve curved scintillators that are placed around the main cryostat, called the External Scintillating Detector Array (ESDA). They are used as the primary detection of pions from the annihilation of antiprotons and photons from the annihilation of positrons inside the apparatus.

Each scintillator is an arc-shaped slab of plastic (polystyrene doped with POPOP wavelength shifter) that is 1 cm thick, about 150 cm long, and 20 cm (two scintillators nearest to the degrader) or 10 cm wide. The location of the scintillators is shown in FIGURE 5.12. The scintillators are placed in contact with the cryostat (about 70 cm from the trap axis) to maximise the solid angle ($\sim 20\,\%$ of 4π) for the detection of annihilations of antiprotons inside the antihydrogen production trap.

Each slab of the scintillator is connected with a photomultiplier tube (PMT), mostly XP2020 with some Thorn-EMI 9954B phototubes, that boost the signal from the scintillator. Using two PMTs (one at each end of the detector) also allows for collecting data in coincidence within a window of 50 ns, which can significantly decrease the background from unwanted events.

The scintillators react to high-energy charged particles. The particle moving through the active material of the detector ionises it. The ionised material relaxes via emission of photons that travel via the plastic to the PMTs at the end. Photons are then converted to photoelectrons by a photocathode PMT. Furthermore, this signal is then multiplied with the help of multiple dynodes (a structure that creates secondary electrons when hit by a primary charged particle). The voltage at the dynodes can be optimised for different applications, which results in a clean and

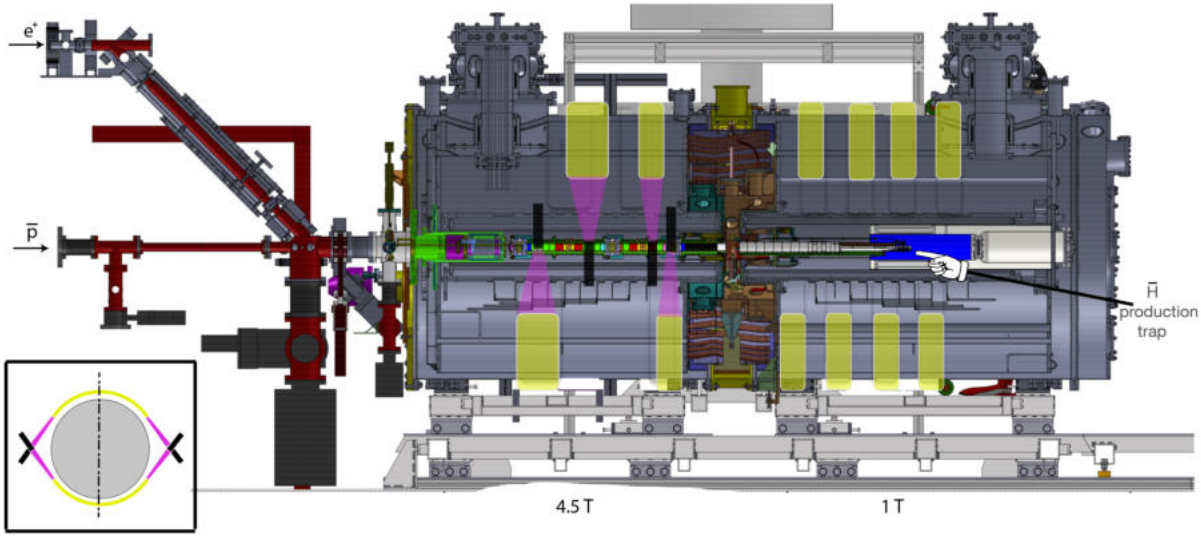

FIGURE 5.12: The position of the scintillators on top of the lateral view of the AEḡIS experiment. Scintillators are shown in light yellow. A sketch of the front view is presented in the inset in the bottom left corner (Taken from [90]).

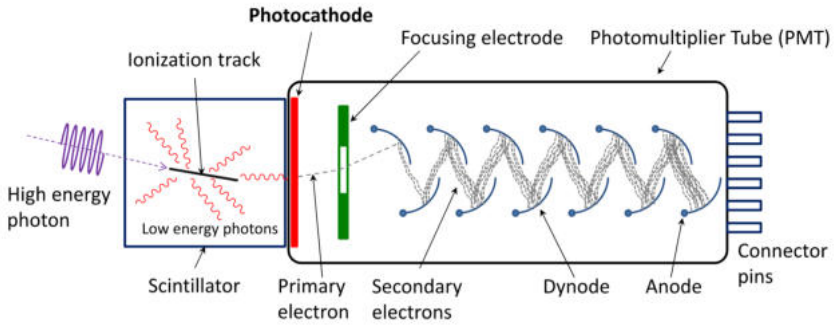

FIGURE 5.13: A schematic overview of the inner-workings of a PMT (taken from [91]).

strong signal. The schematic overview of the conversion process inside a PMT is shown in FIGURE 5.13.

5.3.2 Micro-channel plate detector

A micro-channel plate (MCP) detector consists of an array of micrometre-scale channels. The channels function as photomultiplier tubes; each particle striking the channel's wall triggers the emission of secondary electrons, which are accelerated by the electric field applied between the two faces of the detector [92]. This leads to a cascade effect, increasing the signal by up to a factor of a thousand. The channels in the MCP are tilted $\sim 8\,\%$ with respect to the normal of the detector surface to limit the possibility of a particle passing through the detector without

interacting with any channel. This means that the signal of the MCP can be further increased by stacking two plates on top of each other with the second rotated by 180°. This is referred to as "chevron" configuration [93]. The electrons are then converted to photons by passing through a phosphor screen, creating a photoluminescence effect. The light from the phosphor screen is then captured by a digital camera. At the same time, the current deposited by the particles hitting the MCP is recorded with an oscilloscope.

The MCP detectors are perfect for detecting low-intensity signals. Moreover, they provide high spatial resolution thanks to the dense channel configuration and have a rapid response time in measuring the current on the screen.

In the AEgIS experiment, several MCP detectors can be used to monitor the beam quality, detecting the antihydrogen produced, or can be used together with an oscilloscope to provide information about the charge deposition in time as a time-of-flight detector.

The central MCP detector is positioned about 30 cm from the end of the formation trap in the 1T region. It is a Hamamatsu F2223 MCP, coupled with a P67 phosphor screen and imaged with an ORCA-Flash4.0 V2 CMOS camera. The second MCP can be inserted into the beamline at the entrance to the experiment (the *SUN*).

5.3.2.1 Oscilloscopes

Oscilloscopes are the most common devices that can be found in any physics laboratory. They enable the analysis of signals over time. The AEgIS has two main types of oscilloscopes that can be used to collect the data: the NI 5152 and LeCroy HDO6105 oscilloscopes.

The NI 5152 is an NI oscilloscope module designed for high-frequency signal acquisition. The oscilloscope has a bandwidth of 300 MHz with a maximum sampling rate of two GS s^{-1} (giga-samples per second). The amplitude of the signal can be within the range of $\pm$ 10 V. Thanks to a four-channel multiplexer, the device can sample up to four different sources during the same measurement.

The Teledyne LeCroy HDO6105 oscilloscope (referred to as "Captorius" in AEgIS) is a high-definition, 12-bit device that has a bandwidth of 1000 MHz with a maximum sampling rate of 2.5 GS s^{-1}. The oscilloscope supports four concurrent channels and can be triggered by one of the channels or an external trigger. This device has additional internal memory that allows it to store the data before the device is triggered. Currently, there are two instances of this oscilloscope at AEgIS. A dedicated µService was created for controlling the device (see section D.2).

By combining the oscilloscope with the MCP detector, it is possible to obtain the time-of-flight measurements at AEgIS. The phosphor screen of the MCP serves as the Faraday cup, measuring the intensity of charged particles striking the MCP. The oscilloscope measurements display signals as a function of time with nanosecond resolution. By synchronising the trigger to the oscilloscope with the lowering of the potential wall of the trap, it is possible to obtain the time it takes particles to travel between the trapping region and the detector. Further analysis can be used to decouple the particle species from the signal.

5.3.3 Triggering system

Many operations performed during a single measurement at AEgIS require a high level of synchronisation between different processes, from starting the measurement, to plasma manipulation, to triggering of the detectors. All time-sensitive operations are triggered by the low-level hardware of AEgIS control system, handled by ARTIQ/Sinara ecosystem, which is introduced in more detail in the next chapter.

Furthermore, AD/ELENA sends a series of triggers[4] to experiments requesting a $\overline{p}$ beam. These triggers are adapted to the individual needs of each experiment. Timings of these triggers for AEgIS experiment, as time before ejection of antiprotons from ELENA, are summarised in Table 5.3. The first trigger (*Injection in AD*) is sent at the injection of $\overline{p}$ into AD, which is approximately 110 s before antiprotons will be delivered to the experiment. This trigger is used at AEgIS to start actions that require longer preparation times, e.g. preparation of the Field Programmable Gate Array (FPGA) setup for operation of traps. The second trigger (*Injection in ELENA*) is sent at the injection of $\overline{p}$ beam into ELENA. This marks T− 20 s for the arrival of $\overline{p}$. It is used to initiate semi-long actions at AEgIS, e.g., powering up high-voltage power supplies for the trap or trigger detectors that require longer preparation times, such as some cameras. The third trigger (*ELENA Ejection T− 20 µs*[5]) is sent at about 395 µs before the ejection of antiprotons from ELENA. The final trigger (*ELENA Ejection*) arrives 35 µs after the third trigger, at 360 µs before the ejection of antiprotons from ELENA. The last two signals can be used to trigger fast detectors and start the final sequence of ns-precise operations for trapping antiprotons. In 2024 and 2025, the third trigger wasn't used.

[4] Each experiment can decide which triggers it needs.
[5] This is the name of the trigger for historical reasons.

TABLE 5.3: Summary of triggers sent by AD/ELENA to AEgIS together with the time of ejection of antiprotons from ELENA. It takes around 7 µs for $\bar{p}$ to arrive at the AEgIS experiment after it is ejected from ELENA.

Trigger	Time before $\bar{p}$ ejection from ELENA
Injection in AD	∼ 110 s
Injection in ELENA	∼ 20 s
ELENA "Ejection−20 µs"	395 µs
ELENA Ejection	360 µs

5.4 Analysis framework of AEgIS

Evolution of the AEgIS Collaboration and moving towards autonomous operation of the experiment required a new way of handling the data and subsequent analysis. This prompted the creation of the All Python Analyses Code of AEgIS (ALPACA). It is a Python package created by Tassilo Rauschendorfer as the analysis framework for the experiment.

The package is used to process the raw data from the detectors and create user-friendly formats for further analyses. The data flow through the ALPACA framework is based on a pipeline architecture that processes the data. The schematic flow is depicted in FIGURE 5.14. The underlying rule of the architecture is to expand and never delete.

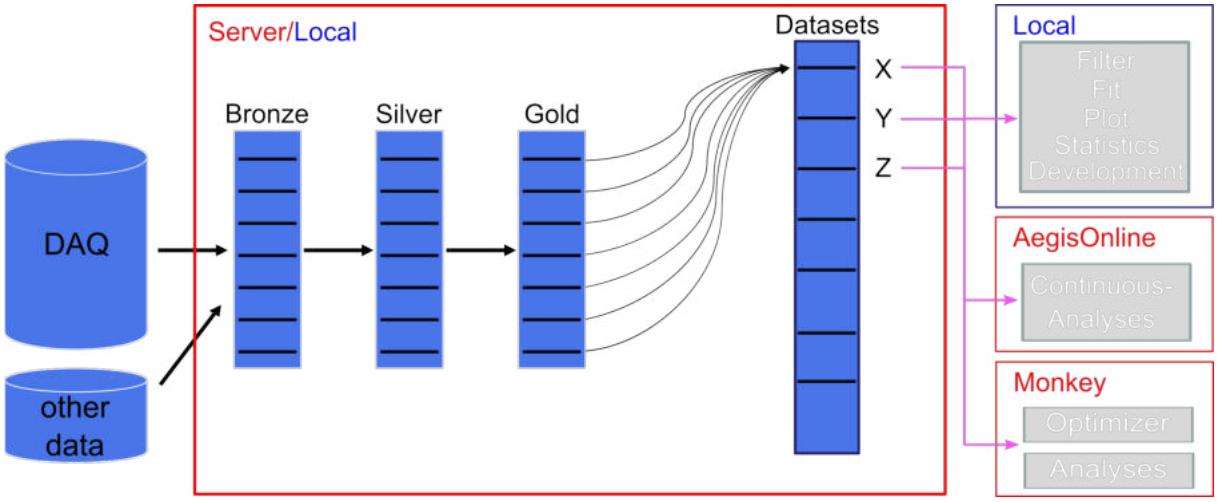

FIGURE 5.14: The data flow through the ALPACA framework. In the *Bronze*, all the data of interest is collected from the DAQ system. The *Silver* expands the data by introducing unified formatting and units. In the *Gold*, the set is expanded by observables of interest which are extracted from the data (i.e. peak positions, intensities, etc.). The final dataset concatenates the *Gold* sets from all selected runs, which can be used later in further analysis.

Firstly, the data from the DAQ and other sources is collected and combined into a uniform instance called *Bronze*. At this stage, the raw data from different forms (JSON, txt, ROOT, PNG, etc.) is connected in a single Python dictionary.

At the second stage (*Bronze-to-Silver pipeline*), the data is refined, creating the *Silver* data. The formatting is unified, and additional information has been added. For example, the signal from the oscilloscope is saved in a single column, where the first couple of rows are used as the configuration file (with the initial time value, time interval, etc.), and the subsequent rows contain the observed voltages. The ALPACA interprets the data and creates the accessible variables (in the oscilloscope example, this will be the initial time, the list of times, the list of voltages, etc.). At this stage, ALPACA also unifies the units used based on the detector configuration files. This simplifies the analysis process by eliminating the need to understand the formatting of each detector's data.

At the third stage (*Silver-to-Gold pipeline*), the observables for each detector are calculated and appended, creating the *Gold* data. The observables are specific information that can be retrieved from the data. For example, a number of antiprotons can be estimated based on the signals from the scintillators. The number of counts in the given scintillator is proportional to the number of annihilations happening. Each scintillator contributes with a different coefficient to the final count. One detector can also lead to multiple observables. For example, images from the MCP are normalised, and the background is calculated in that stage. Then, the background is subtracted, and the sum, mean, and standard deviation of all pixels are calculated as new observables.

Ultimately, a user-specified dataset is created that collects the specified observables and values from multiple runs. This dataset can be further analysed or plotted. In this scheme, the user can download a portion of the data necessary for analysis without needing to store all the data that is not relevant at this time.

ALPACA implements numerous features available to the end-user, including plotting, fitting, data visualisation with supersets, and more. Some of the features were designed to be utilised by the control system to perform complex tasks. One of the features is the Bayesian optimiser (see section C.5.2 for its implementation in the control system).

5.4.1 Bayesian optimiser

Optimisation tasks can be defined as a set of problems which aim to find the maximum[6] of a function $f : \mathcal{X} \to \mathbb{R}$ that is defined on some domain $\mathcal{X}$, which may, or may not, be comprised

[6] The minimum can be obtained by considering problem with $-f$.

of complex structured objects. The optimisation problem is then [94]:

$$x^* \in \arg\max_{x \in \mathcal{X}} f(x); \quad f^* = \max_{x \in \mathcal{X}} f(x) = f(x^*), \tag{5.5}$$

where $x*$ is a point at which function f reaches globally maximal value. There exist many ways of finding a maximum (minimum) of a given function. In general, they all follow the same pattern.

1. Start with an initial dataset $\mathcal{D}$ of pairs of location x and observed results y. This dataset can be empty.
2. Define an optimisation policy for selecting a new location x (e.g., a grid spanning the entire parameter space) from the available parameter space.
3. Select a new location x based on the policy (e.g. next point in predefined list of points to evaluate).
4. Observe the result y at the new location.
5. Append the result $\{x, y\}$ to the dataset $\mathcal{D}$.
6. Check the termination condition (e.g. number of iterations, minimal y value reached). If the condition is not reached, repeat from step 3.
7. x corresponding to the pair with the highest y in $\mathcal{D}$ is the solution to the optimisation problem.

With many approaches, observation of y at x becomes simply $y = f(x)$, and choosing the proper function f for the optimisation is crucial for reaching the solution. These methods assume that the objective function f is known and/or the evaluation of $f(x)$ is cheap. This often isn't the case. E.g. during optimisation of the trapping of $\overline{\text{p}}$ at AE$\overline{\text{g}}$IS, a set of parameters x can be checked, at the fastest, once every 110 s, because of the AD cycle.

Bayesian optimisation [95] is a powerful tool that can be used to address such problems. It is beneficial for problems where the objective function:

- is costly to compute,
- has no defined form (can be considered as "black box"),
- is inherently noisy and cannot be evaluated exactly,
- has no means to evaluate its gradient.

Most of the optimisation problems encountered in physics experiments, such as those related to AE$\overline{\text{g}}$IS, match at least one of the stated conditions.

The Bayesian optimisation method is a family of algorithms that are based on the principle of Bayesian inference [94], which means that the optimisation policy is guided by the probabilities of a beneficial outcome based on prior expectations and already evaluated data from $\mathcal{D}$. According to Bayes' theorem, the posterior probability distribution of an inferred value of the objective

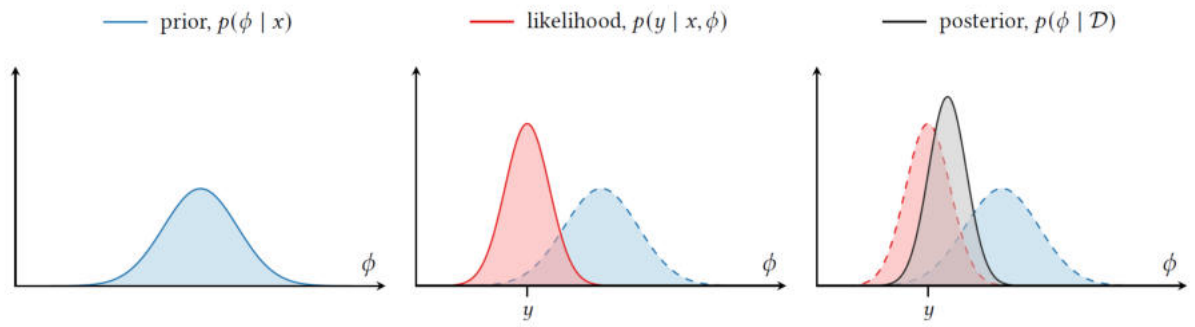

FIGURE 5.15: Bayesian inference for an unknown function value $\phi = f(x)$ (taken from [94]). A prior distribution of ϕ is shown in blue. The likelihood of the observation y assuming some Gaussian noise for observations is shown in red. The posterior distribution, given the observation and the prior, is shown in black.

function $\phi = f(x)$ at some point x given observation of value y at x can be expressed as:

$$p(\phi|x, y) = \frac{p(\phi|x)p(y|x, \phi)}{p(y|x)}. \tag{5.6}$$

Here, $p(\phi|x)$ is the *prior*, a probability distribution of ϕ, before observation of the data. $p(y|x, \phi)$ is the *likelihood* function, which describes the probability distribution of the observed value y in terms of the value of interest ϕ. $p(y|x)$ is a probability distribution of observation at location x and ensures normalisation, as it is a constant with respect to ϕ:

$$p(y|x) = \int p(y|x, \phi)\, p(\phi|x) d\phi. \tag{5.7}$$

In this approach, all unknown quantities are treated as random variables, and their corresponding probability distributions are calculated. The *prior* is first guessed (with some assumptions). After taking a measurement, the *likelihood* is calculated. With the *prior* and the *likelihood*, the posterior distribution can be calculated. The process repeats, with the *posterior* becoming the *prior* in the next iteration, accumulating measurements and increasing the likelihood, thereby converging on the optimal value. The visualisation of the calculation process of *posterior* is shown in FIGURE 5.15.

The Bayesian optimiser can find a solution to the optimisation problem with complex, multidimensional parameter landscapes, where humans struggle to visualise and understand the relationships between the parameters. Furthermore, the Bayesian optimiser is more efficient than a simple linear scan approach when dealing with a parameter space with 15–20 dimensions [96]. This is a significant advantage when performing multidimensional optimisation (the

beam steering of the antiprotons into the AEgIS experiment is an example of an 8D optimisation problem).

The Bayesian optimiser implemented in the ALPACA package is supplied via the scikit-optimize Python module [97]. ALPACA provides functionalities that can be called from the control system of AEgIS to perform complex optimisation tasks of the real system. More information about the interface between ALPACA and the control system is provided in section C.5.2 in Appendix C.

5.5 Control system of AEgIS

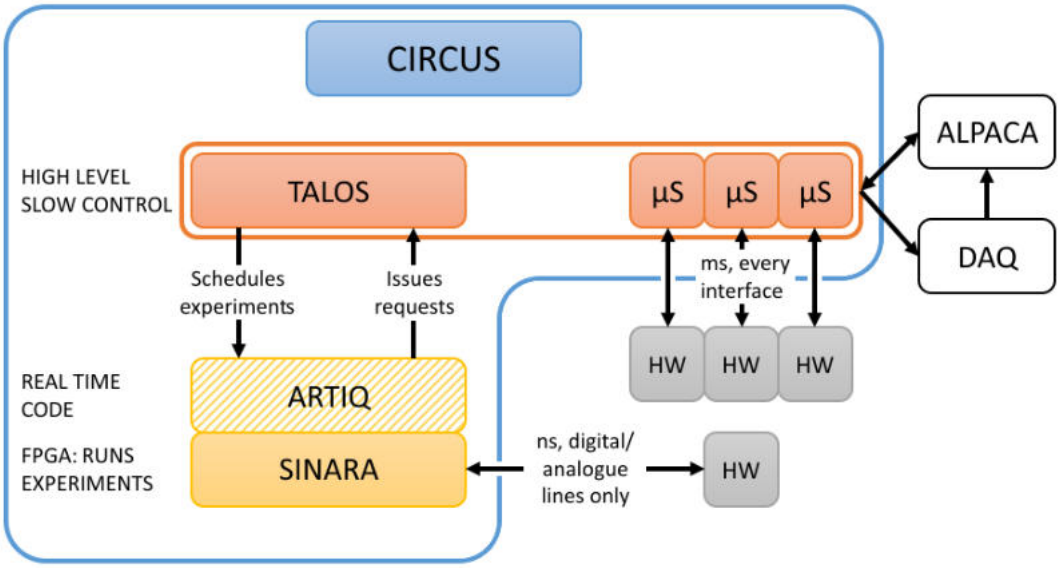

FIGURE 5.16: Schematic of the CIRCUS control system and its constituent parts (ARTIQ/Sinara and TALOS, with various MicroServices (µServices)), together with its relationship with other software and hardware subsystems (e.g. ALPACA) (from [60]).

In 2021, AEgIS showed the pulsed production of $\overline{H}$ [79]. To achieve this goal, a coordinated operation of multiple devices was necessary. Often, the controls for different subsystems were developed separately to expedite the development process. This approach resulted in highly complicated control of the entire experiment. The achieved yield of $\overline{H}$ beam needed to be improved by a factor of at least 100. Moreover, in 2020, a new decelerator was added to the AD complex, called Extra Low ENergy Antiproton ring (ELENA) [76], which changed the operation scheme for experiments at the AD Hall at CERN. The previous operation, which involved 8 hours of beam time shifts for a specific experiment, was modified to deliver antiprotons continuously to each experiment every 2 minutes. All these resulted in a decision by the AEgIS Collaboration

to create a new control system that could address all the requirements of the evolving experiment. This is how the CIRCUS (Computer Interface for Reliably Controlling, in an Unsupervised manner, Scientific experiments)[60] was born.

CIRCUS consists of TALOS (Total Automation of LabVIEW™ Operation for Science) that provides the framework for the system and FPGA (Field Programmable Gate Array) Interface template, which can be implemented by the User to integrate carriers for the FPGA chips specific to the experiment. TALOS ships with the implemented interface for the "Kasli" FPGA carrier from Sinara. Microservices, or µServices for short, are responsible for the slow control of the experiment, while the FPGA system is used to obtain operation with nanosecond timing resolution and sub-microsecond latency required for experiments. In the case of the AEgIS experiment, the FPGA Interface is established via ARTIQ (Advanced Real-Time Infrastructure for Quantum physics) [98], [99] control systems. Each computer in CIRCUS starts a Guardian, a singleton actor, which is the central process of the system. It monitors and distributes all µServices started on the computer. Each Guardian continuously exchanges messages with other Guardians in the system via the TCP protocol, which unifies the computers into a single system. The system can be further expanded with the addition of the analysis interface. Via this interface, CIRCUS can be equipped with online run quality checks and automatic parameter optimisation. The overview of the CIRCUS with its constituent parts is shown in Figure 5.16. Details about the TALOS framework and the core µServices of the framework are provided in Appendix C.

5.5.1 ARTIQ

The core of the control system at AEgIS is developed based on the Advanced Real-Time Infrastructure for Quantum physics (ARTIQ) control system [98]. ARTIQ is an open-source environment created with quantum information experiments in mind. The environment provides a high-level programming language based on Python that allows for human readability while maintaining the nanosecond capabilities of an FPGA via the provided compiler. It supplies specialised functions for communicating with hardware. Experiments in ARTIQ are controlled via a series of scripts with nanosecond resolution and microsecond latency.

The ARTIQ code is divided into two types of parts that can be used together. The first consists of regular Python code that is executed on the host machine. This includes preparation before experiments, pre-calculations, and any time-consuming operations that do not require direct access to hardware devices. The second part, called ARTIQ kernel, is executed directly on the FPGA of the core device. This code is pre-compiled before execution to meet the requirements of real-time programming.

All programmed input and output events create a timeline that keeps the synchronisation of the experimental routines. Output events are set with a given timestamp and are executed when the timestamp matches the internal, high-resolution clock. The input events are recorded with a timestamp of the internal clock. By default, the system assumes that the FPGA carrier, known as "Kasli," is being used. This carrier contains an internal clock with a frequency of 125 MHz; however, an external clock can be supplied with a higher frequency.

The ARTIQ environment allows for observing a given input TTL channel and register rising or falling edge events that can be further used as triggers for subsequent events, i.e. setting voltage on a dedicated digital-analogue-converter (DAC) channel. Furthermore, the environment allows for scripting events in parallel, i.e. two events with the same timestamp. For more complex operations that require ns-resolution, it is possible to pre-record the series of events on the core device by utilising the direct-memory-access (DMA) recording feature of the environment.

A custom library based on the ARTIQ environment was created for the AEgIS experiment. A quick introduction into the library is given in Appendix B with more details available in [63].

5.5.2 Sinara

The first instances of the ARTIQ systems were developed with hardware built in-house by physicists. To increase the reproducibility and scalability of the systems, a dedicated hardware was designed for compatibility with ARTIQ. This system is called Sinara [99]. The hardware is created as an open-hardware project, with all designs shared online [100] under CERN OHL v1.2 licence.

FIGURE 5.17: One of the Sinara crates used at AEgIS. It consists of 10 modules. From left: power module, Kasli carrier, two DDS-based frequency synthesisers ("Urukul"), 16-channel digital I/O unit, 8-channel analogue-to-digital converter ("Sampler"), 32-channel digital-to-analogue converter ("Fastino"), 32-channel HV amplifier, HD86-IDC adapter, IDC-MCX adapter.

The core device in the Sinara family is the 1124 Carrier called "Kasli". It hosts the Artix-7 100T FPGA, DDR3 SDRAM. The controller can pilot up to 12 cards. The Sinara family also includes some commonly used hardware like: digital-to-analogue converters called Fastino and Zotino, analogue-to-digital converter called "Sampler", DDS-based frequency synthesisers called "Urukul,"[7] and more. An example crate fitted with some Sinara modules is shown in FIGURE 5.17. This crate is used for controlling early production and trapping, using a Paul trap, of ions for the AEgIS experiment.

The open-source nature of Sinara systems allows for easier development and integration of custom modules. An example of that is a "HV_AMP_8CH," [101] an 8 channel, HV amplifier that can output in range of ±200 V. This module was developed specifically for particle traps in AEgIS.

5.5.3 Scheduling and sequencing experiments with CIRCUS

AEgIS operates as a series of measurements, each consisting of a set of operations that need to be performed in a specific order with precise timing. These operations include preparing the traps, manipulating plasmas, triggering detectors, and acquiring data. A series of timed operations that need to be performed is defined in a single ARTIQ script, referred to as a Run Instance. To manage these operations, CIRCUS utilises a scheduling and sequencing system that allows for the definition and execution of multiple series of these scripts. It provides functionality for defining schedules for multidimensional parameter scans and solving optimisation problems. A detailed description of the scheduling system is provided in section C.4.2 in Appendix C.

5.5.4 Autonomous operation

CIRCUS allows for autonomous operation where the system can execute a predefined series of experiments without any supervision. It is implemented via a close cooperation of core µServices, that is, Tamer, Monkey, FPGA (Kasli) Wrapper, and the Error Manager together with the Sinara system controlled by ARTIQ. Details about the implementation of these µServices are provided in section C.4 in Appendix C. The system operates in a master-slave scheme, where roles are switched throughout the execution.

At the beginning, the role of the master is taken by TALOS. The run session starts with Schedules, prepared in the Scheduler µService, sent to Tamer µService. It checks what FPGA is required by the Schedules and starts corresponding Monkey and FPGA Wrapper µServices. Afterwards, a series of checks is performed where the system checks:

[7] Initially, modules were called with names of lakes in Russia. This was abandoned at some point; however, this name stayed.

- check that all computers are online and can communicate with each other;
- check that each computer has the necessary μServices running;
- check that all μServices are ready for operation.

After all checks are passed, the Schedules are distributed to each Monkey responsible for executing one, and autonomous operation begins. Monkey sequentially executes each script in the Schedule by sending it to the FPGA Wrapper μService. At this point, control of the system is given to the FPGA, which can request the operation of each μService in the system via TCP messages from the running script. Throughout the execution, the Error Manager monitors the system's status and updates Tamer with all errors that occur. After the script is finished, the control is returned to TALOS and Monkey decides whether the script was finished successfully or not and takes appropriate action (see section C.4.4 in Appendix C for more details).

Furthermore, TALOS implements features which utilise the analysis framework. Firstly, after each run is executed, the system can check if the collected data fulfils a predefined condition. This is called the *quality of run check*. The second feature that utilises the analysis framework is the optimisation of run parameters. In this process, the Monkey asks the analysis framework to estimate a specified observable, which is used in the objective function of the optimisation problem. Afterwards, a second call to the analysis framework is performed to retrieve a new set of parameter values for the run. More details about the implementation of the optimisation cycle can be found in section C.5.2 in Appendix C.

The run session ends when there are no more runs left in the Schedule. At this point system becomes idle; however, TALOS continues monitoring the status of all μServices.

5.5.5 Multi-FPGA operation

It is common to use multiple FPGAs in a single experiment. This is the case for the AEgIS experiment, where different Kaslis control the two trap regions (1T and 5T). A single Sinara crate doesn't have enough space to accommodate all the necessary modules for controlling both trapping regions. This can be solved by having two crates, with additional crates working as "satellites," which effectively extend the first crate with modules from the second. This, however, introduces a delay for modules in the "satellite" crates, which is caused by signal propagation via a cable connecting two crates. Furthermore, a single Kasli is limited in the number of parallel operations it can perform. Therefore, two regions are controlled by two different Kaslis, making both areas fully parallel.

TALOS was designed so that it is possible to control multiple FPGAs. There are three modes of operation: sequential, parallel asynchronous, and parallel synchronous. The mode of operation is defined in the Scheduler µService when creating the Schedule.

The sequential mode is the default operation. A single schedule is defined, which can be filled with runs for any FPGA. The Tamer will start a single Monkey µService and an FPGA Wrapper for each FPGA that is used in the Schedule. The Monkey will send the run to the correct FPGA Wrapper based on the run in the Schedule. At the end of the run, the acknowledgement message, called `BANANA` (*Basic quAlity Notification After the eNd of an Action*), is received by the Tamer, which directly forwards it to the Monkey. The Monkey then continues according to internal logic (see FIGURE C.6). In this operation mode, the Tamer is used in minimal capacity. The flow of messages between µServices for the sequential operation is shown in FIGURE 5.18.

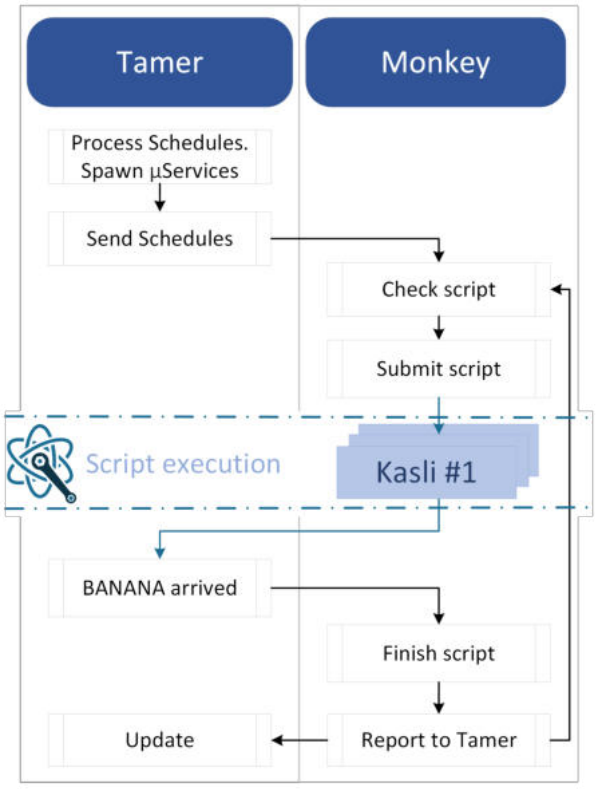

FIGURE 5.18: The flow of cooperation of Tamer and Monkey during execution of a schedule in sequential mode.

In parallel mode, the system can run multiple FPGAs simultaneously. It is up to the User to ensure that the FPGAs don't request the same resources (messages to µServices) when working in parallel. For the parallel operation, a separate schedule is defined for each FPGA. This means that each Schedule consists of the scripts for a dedicated FPGA. There is also a *synchronisation*

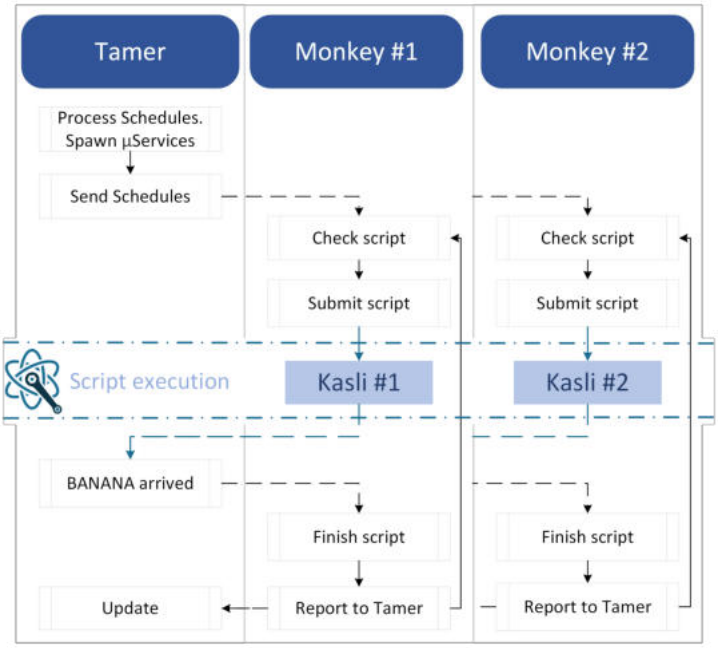

(A) Asynchronous operation.

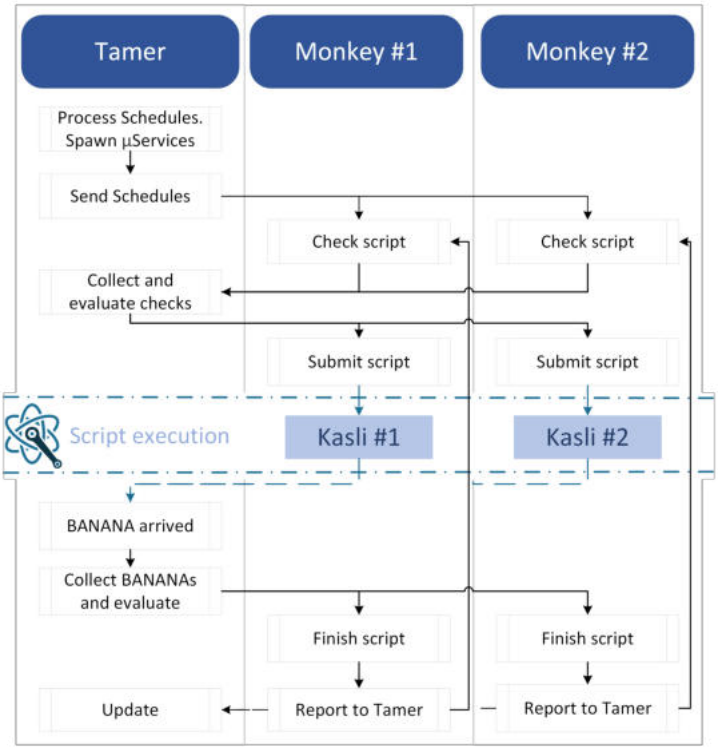

(B) Synchronous operation.

FIGURE 5.19: The flow of cooperation of Tamer and Monkey during execution of a schedule in parallel mode. Dashed lines indicate messages between two µServices that are asynchronous.

mask that can be defined in the Scheduler. This map defines which FPGAs should be used for synchronous (True value in the mask) and asynchronous (False value in the mask) operations. In the asynchronous operation, all schedules are considered as individual instances. In contrast, scripts in the same position in synchronised schedules are considered as a single experimental sequence. Therefore, each script in synchronised schedules is started at similar time instances in the synchronous operation, introducing a "slow" synchronisation between two FPGAs. This synchronisation can be improved by implementing hardware triggers between devices.

In the parallel operation, the Tamer will create a pair of a Monkey and an FPGA Wrapper for each FPGA. Each Monkey receives a Schedule dedicated for its dedicated FPGA. Each Monkey will execute its Schedule according to their internal logic.

In asynchronous parallel operation, the operation of Monkeys works in the same way as it does for sequential operation. The Tamer works as a message distributor. It receives the `BANANA` messages from the FPGAs, which are then forwarded directly to the Monkey responsible for the FPGA. The flow of the messages is shown in Figure 5.19a.

In the synchronous parallel operation, Monkeys start each run at the same time. Furthermore, to maintain the synchronisation of the schedules, they must perform the same action for each run (i.e., skip or retry the script). This requirement is implemented by using the Tamer as the evaluator. Firstly, all synchronous Monkeys check the script and send the result to the Tamer. The Tamer waits for all the checks, then evaluates them and selects the following action for the Monkey. If at least one Monkey fails the script check, the cell will be skipped in all schedules. The Monkey then continues according to its internal logic. At the end of the run, each FPGA sends the `BANANA` message to the Tamer. The Tamer collects all the `BANANA` messages. Only when the Tamer receives a `BANANA` from all synchronous FPGAs does it evaluate the responses. The highest value of the collected `BANANA` messages is used as a typical `BANANA` for the FPGAs. Each Monkey receives the same message, which guarantees the same decision by the µService. The flow of the messages in the synchronous parallel operation is shown in Figure 5.19b.

This implementation of the synchronisation decouples the Monkey's internal logic (which is already complicated) from the synchronisation. Furthermore, it makes the Tamer µService the global coordinator, simplifying communication within the system µServices (FPGA Wrappers and the Error Manager always send messages to the Tamer). Moreover, the system can operate in a hybrid mode, with some FPGAs running synchronously while others run asynchronously, as defined by the synchronisation mask.

This implementation enables fully parallel operation across multiple FPGAs, regardless of any limitations in parallel operation within the FPGAs themselves. Unfortunately, the current version of TALOS supports a single DAQ run present, which means that in the parallel asynchronous

operation, the DAQ is not used. DAQ will be started for any synchronous operation. Therefore, a single FPGA can be started in synchronous mode to work as the DAQ manager, while the other FPGAs are started in asynchronous mode. This mode is used at AE$\overline{g}$IS during $\overline{H}$ production, with one Kasli in 5T running in asynchronicity, constantly trapping $\overline{p}$. The production of $\overline{H}$ is triggered by scripts executed by 1T Kasli, which sends messages to 5T to request transfer of $\overline{p}$. The two Kaslis are connected with TTL lines to provide triggers necessary for synchronisation to ns level.

5.5.5.1 Synchronisation

A dedicated measurement was performed to test the synchronisation capabilities of the parallel mode in TALOS. Ensuring that two scripts in a parallel operation execute within a reasonable time delay allows proper implementation of timeout functions in the ARTIQ scripts, which is especially important when working with scripts of different durations. The synchronisation should maintain a constant delay between scripts, independent of the scripts' durations.

The measurement uses five dummy FPGAs (*Dummy_1-5*), each executing a Python script. The test script prints the time when it starts and then waits for a specified number of seconds, which can be set as a parameter. Then it prints a goodbye message before finishing the script. In the first test, the wait duration is fixed at 2 s for all Dummy FPGAs. In the second test, the duration varies between the FPGAs. The value increases by 2 s for successive FPGA starting at 0 s for *Dummy_1* to 8 s for *Dummy_5*. Each test consists of 50 runs for each Dummy FPGA. Moreover, it was performed in parallel with FPGAs in complete synchronicity or full asynchronicity. It is expected that the delay between scripts in the same position in the Schedule from different *Dummies* will remain constant in synchronous operation, whether the scripts have the same duration or not. In the asynchronous operation, the delay between scripts should increase linearly with the script's position in the Schedule across different *Dummies* with varying script durations.

Two values are calculated from the collected data to evaluate the performance. The δT is defined as the difference between the starting time of the i-th script for two neighbouring *Dummies* (that is, between *Dummy_1* and *Dummy_2*, *Dummy_2* and *Dummy_3*, etc.). The ΔT is the difference between the first and last *Dummy*, the earliest and the latest start time of the i-th script in the schedules. The FPGAs are stored in an alphabetic order, which defines the starting order of FPGAs by the *Tamer* µService.

The calculated δT and ΔT from the tests are shown in FIGURE 5.20 and FIGURE 5.21, respectively. Each plot is accompanied by the average value across the 50 runs. In asynchronous operations with scripts of varying durations, the data is fitted with a linear trend line, and the average

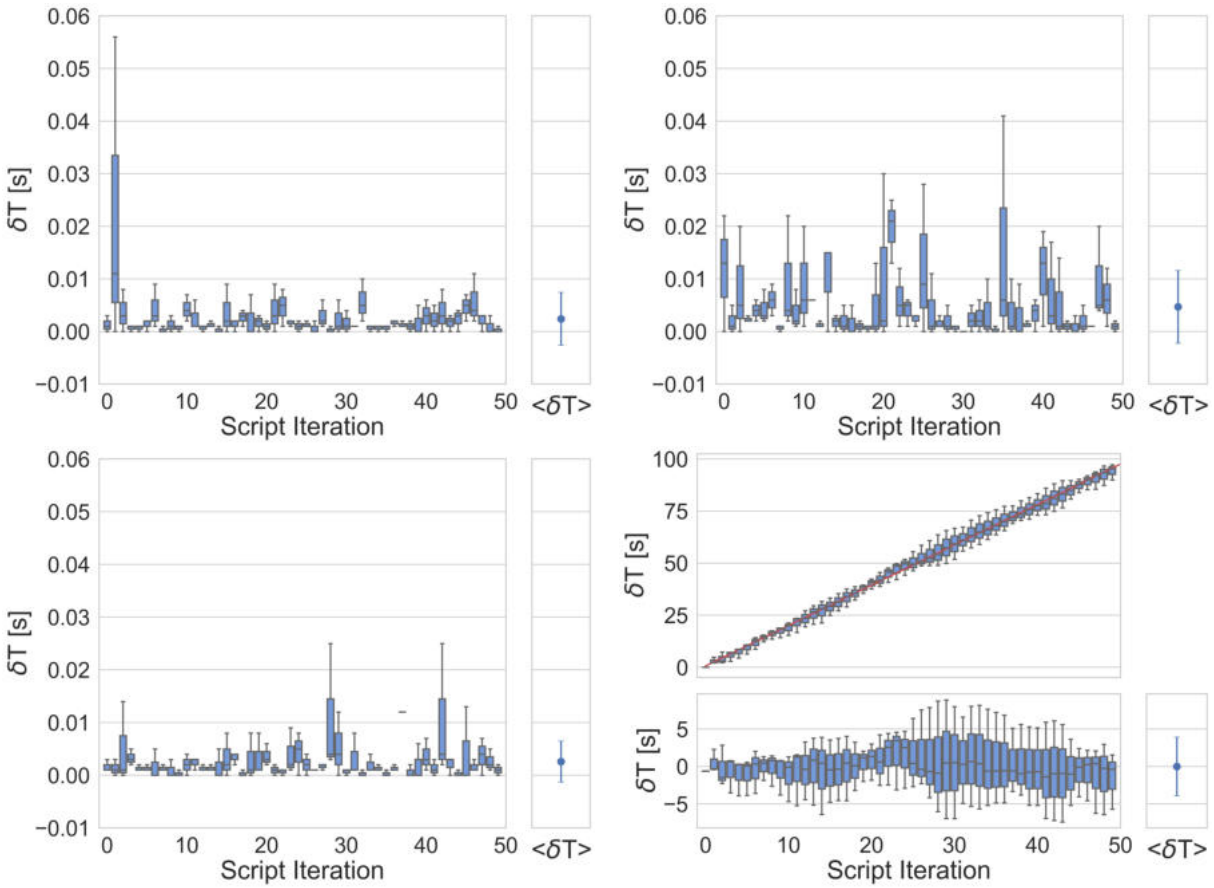

FIGURE 5.20: The δT for the asynchronous (right) and synchronous (left) operation, and for the scripts with a constant (top) and varying (bottom) duration.

is then calculated as the average of the differences between the trend line and the value for each run.

The average delays between scripts are summarised in TABLE 5.4. Both δT and ΔT stay constant when using synchronised operation, even when using scripts with varying duration in different FPGAs. This effect does not occur when asynchronous parallel mode is used, which demonstrates that the synchronicity of the schedules is effective, with the capability of slow synchronisation of 15 ms between FPGAs. In FIGURE 5.21 in asynchronous operation with varying script duration (bottom right plot), the ΔT value seems to oscillate along the linear trend line. These are unexpected results. It may be a systematic effect due to the definition of ΔT. The value is defined as the difference between the earliest and the latest start times of a script in the schedules. Given that the script duration changes between FPGAs by a constant amount, it is possible that all scripts finish at the same time, which results in a later submission of the i-th script for a later FPGA.

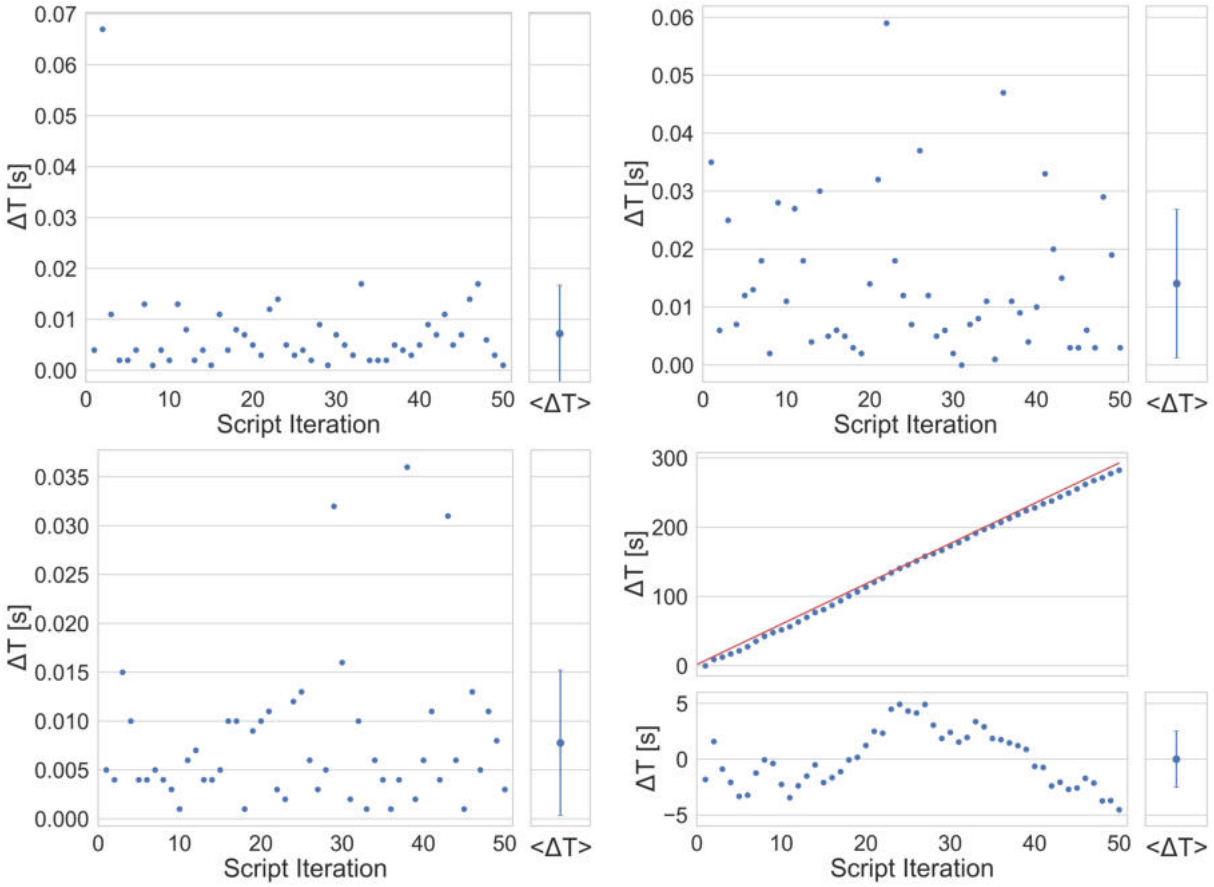

FIGURE 5.21: The ΔT for the asynchronous (right) and synchronous (left) operation, and for the scripts with a constant (top) and varying (bottom) duration.

TABLE 5.4: Results of slow synchronisation measurements for schedules of 50. Runs executed on 5 dummy FPGAs with either the same duration runs between FPGAs or varying duration in synchronised or asynchronised parallel operation.

	$\langle \delta T \rangle$		$\langle \Delta T \rangle$	
	synchronous	asynchronous	synchronous	asynchronous
constant duration	2(5) ms	5(7) ms	7(9) ms	14(12) ms
varying duration	2(4) ms	0(4) s	8(7) ms	0(2) s

Chapter 6
Simulations

I declare that the work presented in this chapter is the result of simulations and analysis performed by me for this thesis.

For simulating the full chain process, from capture of $\overline{p}$ by an atom to the time-of-flight spectrum of produced fragments, I performed the following tasks:

- *I performed a detailed* GEANT4 *simulation to estimate the best combination for the efficient antiproton capture. The best configuration was also experimentally tested with a combination of the main degrader (*1400 nm *Mylar)* + 100 nm-500 nm *Parylene N foils.*
  - *All code is available in a public GitHub repository [102].*
- *I created a program based on* GEANT4 *toolkit for simulating $\overline{p}$ with $E = 1$ keV inside a thin sphere of material for studying the residual nuclei produced in $\overline{p}$-nucleus interactions.*
  - *All code is available in a public GitHub repository [103].*
- *I re-created the program based on FLUKA toolkit.*
- *I compared various physics lists within* GEANT4 *toolkit in the context of secondary nuclei created from the antiproton-capture-at-rest process.*
- *I performed a comparison of* GEANT4 *and FLUKA toolkits.*
- *I simulated the interaction of antiprotons with over 3000 different isotopes as the target material (using a program based on* GEANT4*).*
- *I calculated yields of different fragments from the annihilation of antiprotonic atoms for various trapping conditions.*
- *I calculated the expected neutron-skin factor for specific isotopes based on the trapping conditions.*
- *I calculated optimal paths for various isotopes, assuming subsequent annihilation on produced fragments.*
- *I created a model for simulating the TOF signals for measurements with trapped fragments.*
  - *I performed validation of the model by comparing the simulated signals with TOF measurements obtained with trapped, cold antiprotons in AE$\overline{g}$IS traps.*
  - *All code for the simulation is available in a public GitHub repository [104].*

One of the first steps in designing a new experiment is to calculate the expected results based on current theoretical knowledge. Given the complexity of modern theories, it is often hard to

perform detailed calculations. It is especially true in particle physics, where statistical and systematic effects play a crucial role in determining experimental results. This can be overcome by using simulations and Monte Carlo methods.

In this chapter, an overview of the available simulation toolkits is provided, along with the details of the two main simulations created for this study.

6.1 Toolkits

There exist many software toolkits designed to simulate different physical phenomena. In the context of this thesis, the interactions of particles, particularly antiprotons, with various types of matter are of interest. There are two main tools used in particle physics for simulating particle interactions with different materials: GEANT4 [105]–[107] and FLUKA [108], [109]. However, both toolkits were developed with high-energy physics in mind. The following is a short overview of these toolkits, with special emphasis on the antiproton interaction.

6.1.1 GEANT4

GEANT4 is a software package which provides tools for accurately simulating the passage of particles through material. It utilises data-driven models to simulate the interactions between particles and their environment, as well as the entire chain of producing secondary particles at each interaction point. Each step of the simulation is saved and can be accessed later, allowing for the recreation of particles' tracks through the material and detailed event-by-event studies of interactions. Furthermore, it allows for creating a whole geometry of detectors and different devices used in physics experiments. Materials for each component can be selected from a predefined list of materials or by defining a custom material type. This feature enables the accurate simulation of detectors' responses, energy depositions, radiation levels, and other key aspects considered when developing or using any detector or device. Thanks to all these features, GEANT4 is used beyond High-Energy Physics experiments, e.g. Space and Radiation science or Medical Physics.

GEANT4 comes equipped with a plethora of different physics models. FIGURE 6.1 shows the mapping of interaction and the corresponding model used in GEANT4. Details about implementation of the models are available in the Physics Reference Manual of GEANT4 [110]. When creating a new simulation, it is up to the user to decide which models to include. This definition is done by creating *Physics Lists*. They allow for further tailoring of the simulation to the specific needs of the problem, as some models may require more computational time without being

beneficial to the final result. GEANT4 comes with several default physics lists that have been optimised for different purposes. It is highly recommended to use these lists; however, it is possible to define custom lists if some specific interactions are to be considered.

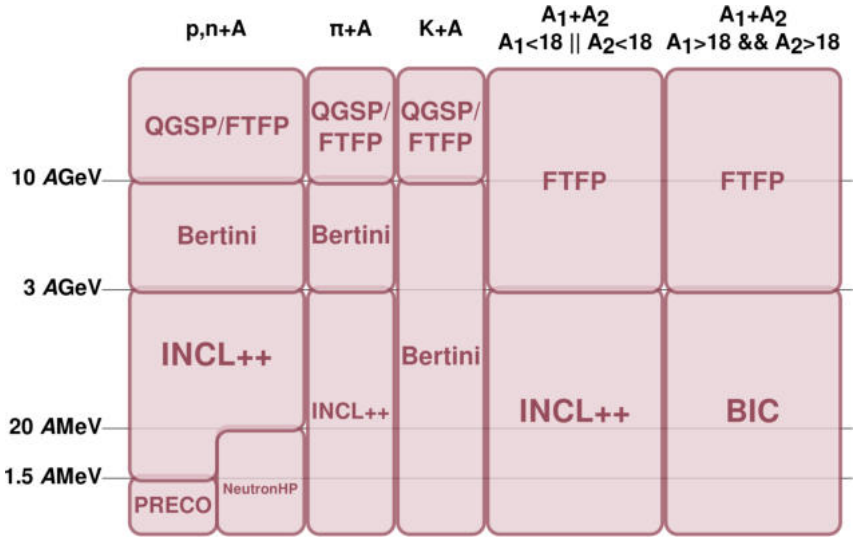

FIGURE 6.1: Overview of the used models for the different types of interactions and energy ranges in case of including the `INCL++` model in GEANT4.

The elastic interactions of antiprotons with matter are interesting for studying energy losses of antiprotons as they move through specific materials. The example of this is the study of the degrading foils for the AEgIS experiment (see section 6.2). The inelastic interaction, however, is more interesting for this thesis. These models will describe processes such as capture at rest, annihilations, and nuclear de-excitation. In particular, in the context of antiprotonic atoms, the simulation should include initial capture of the antiproton by the nucleus, the annihilation, the intranuclear cascade of the antiproton and pions produced from the annihilation, the excitation of the nucleus, and the de-excitation, which can result in the fragmentation of the nucleus.

Fritiof model (`FTF`) [111] is used for simulation of the following interactions when considered in the simulation:

- hadron-nucleus interactions at momenta $P_{LAB} > 3$–4 GeV c^{-1},
- nucleus-nucleus interactions at $P_{LAB} > 2$–3 GeV/c/nucleon,
- antibaryon-nucleus interactions at any energies,
- antinucleus-nucleus interactions at any energies.

It considers all hadron-hadron interactions as binary reactions, where the excited hadron, which can result from a reaction, is a QCD string. Therefore, the decay of excited hadrons is done using a Lund-string fragmentation model. Furthermore, it can be coupled with the Precompound model (creating `FTFP`), a hadron kinetic model. This allows for a continuous transition between

the kinetic stage of the reaction, which the hadron kinetic model describes, and the equilibrium stage of the reaction, described by the subsequent equilibrium de-excitation models.

GEANT4 provides many models for simulating intranuclear cascades (INC). There are two components to inelastic particle-nucleus collisions. The first, fast 10^{-23}–10^{-22} s, component results in highly excited nucleus. This can lead to a fission or a pre-equilibrium emission. The second, slow 10^{-18}–10^{-16} s, is responsible for evaporation, i.e. emission of nucleons from the nucleus.

The Bertini model (`BERT`) [105], [112] solves, on average, the Boltzmann equation, which describes the collision process. This model is implemented together with a pre-equilibrium model, a nucleus explosion model, a fission model, and an evaporation model in GEANT4.

The Binary Cascade model (`BIC`) [113], [114] is an alternative INC model in GEANT4. Instead of solving the Boltzmann equation, it assumes that the cascade is a series of interactions between the particle (primary or secondary) and individual nucleons in the nucleus. At low energies, this assumption breaks down, and the evaporation and pre-equilibrium models are called.

The Liège Intranuclear Cascade model (`INCL++` or `INCLXX` in GEANT4) [115]–[117] is yet another INC model available in GEANT4. This model focuses on the spallation reactions[1] of different particles, including antibaryons and light ions, on nuclei. It can reasonably simulate reactions with energies from 10 AMeV to 20 AGeV. The GEANT4 implementation is coupled with a statistical de-excitation model.

A more advanced de-excitation model called `ABLA++` [118], [119] can be used in GEANT4. In principle, it can be coupled with all INC models. A combination of `INCL++` and `ABLA++` is considered as one of the most accurate models for predicting residuals from spallation reactions [120].

The annihilation of an antiproton in interactions with a nucleus was simulated using the CHiral Invariant Phase Space (`CHIPS`) model, until it was removed in version v10.0 [121]. Afterwards, the `FTF` was the only available model for simulating annihilations. However, in version v11.2 [122], the implementation of `INCL++` was expanded also to handle antibaryon-nucleus interactions.

6.1.2 FLUKA

FLUKA [108], [109], [123], [124]is a tool for simulating particle transport via a material. It covers a wide range of applications, including beam accelerator shielding, target design, calorimetry, dosimetry, radiotherapy, and other related fields. Furthermore, it provides tools for defining

[1] Results of an impact of a particle on a nucleus.

complex geometries.

It aims to implement sound and modern physical models. It allows for simulating interaction between matter and about 60 different particles, including antiprotons. Hadrons can be simulated with energies up to 20 TeV. Experimental data is used to guarantee the most accurate results. Predictivity is provided whenever data is not available.

FLUKA adopts microscopic models whenever possible, with consistency ensured between different models. Conservation laws are enforced at each step of the simulation, with results being checked against experimental data. The hadron-nucleon interactions are modelled with resonance production and decay below a few GeV and on the Dual Parton model above [125]. All nuclear effects are treated by the PEANUT model [126]. The annihilation of $\overline{\mathrm{p}}$ occurs inside the nucleus at a depth, which is taken as a function of the atomic number of the nucleus. The interaction is more peripheral as the nuclear mass increases.

6.2 Efficient antiproton trapping studies

One of the simulations made for this thesis was the study of the degrader thickness material used at the AE$\bar{\mathrm{g}}$IS experiment to slow down antiprotons. The goal of this study was to determine the optimal combination of available foils to achieve the highest trapping fraction of antiprotons with the available high-voltage electrode.

6.2.1 Geometry

The degrader system of AE$\bar{\mathrm{g}}$IS is described in the section 5.2.8. The simulation implements a simplified geometry where each degrader is considered as a single foil (a cylinder). The thickness of the foil can be changed via the configuration file. Each foil has an additional 10 nm of aluminium layer attached to it. This layer is a metallization layer that is present in thin foils from the manufacturing process (the real foils are created by coating a nanometer-thick aluminium layer with a specified material). Furthermore, the first foil can be removed, allowing for a simulation of the degrading effects of a single material to be studied. Both foils are placed inside a cylinder that defines the magnetic field.

FIGURE 6.2 shows a visualisation of the geometry in GEANT4, together with the magnetic field as arrows and the tracks of the antiprotons as red lines.

The simulation was performed with various combinations of foil thickness and material. There were two main materials considered: Mylar ($C_{10}H_8O_4$ with density of $\rho = 1.4\,\mathrm{g\,cm^{-3}}$) and Parylene ($C_{16}H_6$ with density $\rho = 1.145\,\mathrm{g\,cm^{-3}}$). For each material, a simulation was performed with a

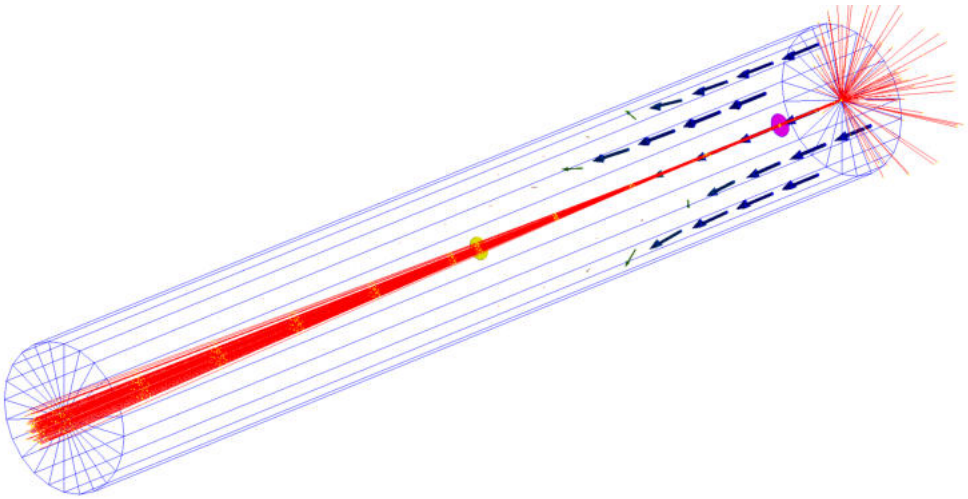

FIGURE 6.2: Visualisation of 100 antiprotons passing through two degrader foils inside the magnetic field. The beam of antiprotons is focused when travelling through the magnetic field, but it diverges after it exits the magnetic field. Arrows represent the strength of the magnetic field.

single degrading foil in the position of the main degrader. The thickness was ranging from 100 nm to 3000 nm in steps of 20 nm. Furthermore, a combination of two foils was also simulated. The first foil of Parylene was placed at the position of the degrader ladder, and its thickness ranged from 100 nm to 500 nm in steps of 100 nm. The second foil of Mylar, placed at the position of the main degrader, ranged from 1300 nm to 1500 nm with steps of 20 nm.

6.2.2 Magnetic field map

A crucial aspect of the Penning-Malmberg trap is the magnetic field, which provides radial confinement. The magnetic field is essential for using the degrader foils correctly. The antiprotons passing through a degrader are subjected to multiple elastic collisions within the material, resulting in a lower energy but also introducing a divergence in the beam. Thanks to the magnetic field, the antiprotons leaving the first degrader are still expected to hit the second degrader. This effect can be seen in FIGURE 6.2, where antiprotons entering the magnetic field have a radial spread bigger than the radius of the degrader. All the antiprotons pass through both degraders. The divergence effect can be observed when the antiprotons exit the magnetic field[2].

[2]The magnetic field is cropped in the simulation for simplification reasons. The experimental field extends to the end of the experiment.

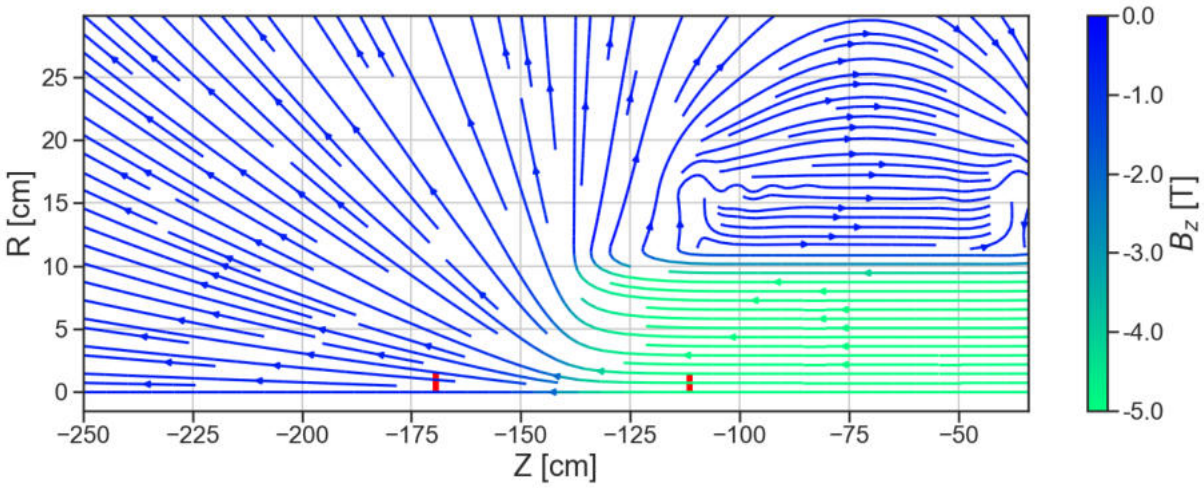

FIGURE 6.3: Visualisation of the magnetic field at the entrance of the AEgIS experiment. The z position is in the AEgIS coordinate system (with zero at the centre of the experiment). The red markings show the position of the degrader ladder (at ≈ −170 cm) and the main degrader (at ≈ −111.9 cm).

A map of the magnetic field at AEgIS was added to the simulation. The field is saved as:

$$B(r,z) = \begin{pmatrix} B_R(r,z) \\ B_Z(r,z) \end{pmatrix} \tag{6.1}$$

where B_R, B_Z are the strengths of the magnetic field in the radial (r) and axial (z) direction, respectively. The z component of the magnetic field that was used in the simulation is shown in FIGURE 6.3.

The magnetic field at the entrance to the experiment also works as a focusing lens. FIGURE 6.4 shows the transverse distribution of antiprotons sent into the magnetic field in the simulation (left) and the distribution after they leave the second degrader (right). The plots clearly show that the focusing due to the magnetic field is stronger than the divergence due to the degraders. This focusing effect is significant as the antiproton beam diverges after passing through a foil due to the multiple scatterings that occur within the material.

6.2.3 Degrading efficiency

The main goal of the simulation is to estimate the trapping efficiency of the degrader setup used in AEgIS. The trapping potential that can be used at AEgIS is limited by the HV electrodes. Currently, the safe limit is −14 kV; however, the electrodes can support higher voltages, but this requires an update of the HV switch necessary for trapping of antiprotons.

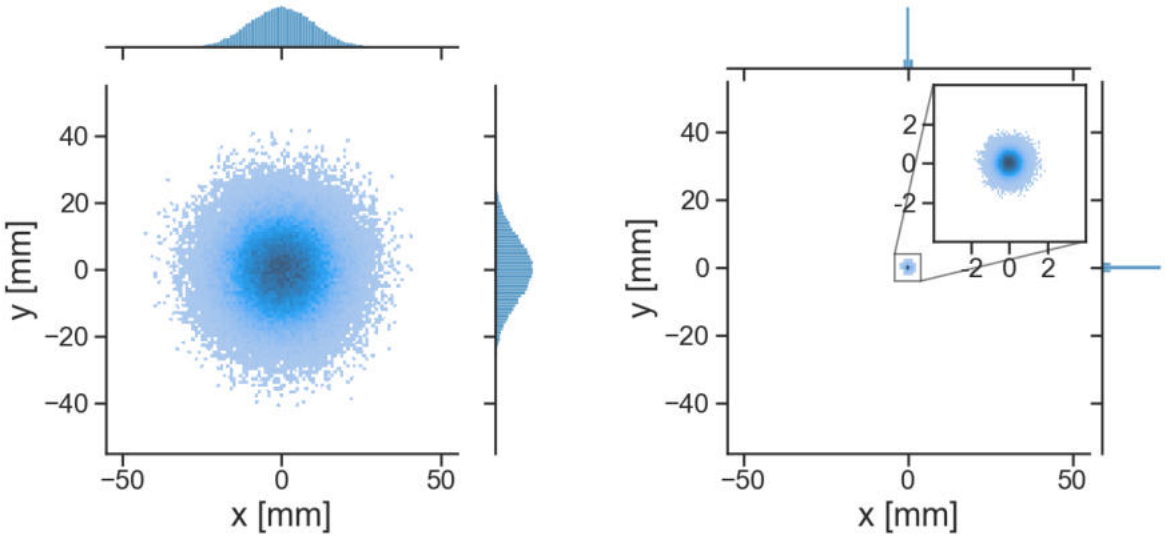

FIGURE 6.4: Spatial beam distribution before (left) entering the magnetic field and after (right) leaving the second degrader. In the simulation, a two-degraders setup was used with 500 nm Parylene and 1400 nm Mylar foils.

The degrader is used to decrease the kinetic energy of the antiproton beam. This reduction is achieved via the scattering of antiprotons inside a thin foil of a material. Because of this, the thicker the degrader, the higher the energy loss for antiprotons. At the same time, increasing the thickness of the degrader increases the possibility for antiprotons to annihilate inside the material. Therefore, two observables were studied: the fraction of antiprotons lost on the foil due to annihilation and the fraction of moderated antiprotons, i.e. antiprotons that have passed through the degrader(s), that can be trapped.

The fraction of antiprotons that annihilate inside the degrader is shown in FIGURE 6.5a. The dashed line indicates the foil of 1400 nm thickness, which is the total Mylar thickness used for the main degrader in AEgIS. The plot shows that the number of annihilations increases with the thickness of the degrader. The highest increase of annihilations is seen in the region between 1600 nm and 2160 nm, where the percentage of antiprotons lost due to annihilations increases from 10 % to 90 % respectively. For the thickness of 1400 nm Mylar, the fraction lost due to annihilation is 2.2(8) % according to the simulation.

The fraction of trappable antiprotons is defined as the antiprotons with axial momentum p_z less than the potential on high-voltage electrodes HV. The absolute fraction of trappable antiprotons is shown in FIGURE 6.6a and, as expected, the fraction of antiprotons that can be trapped increases with the trapping potential. The fraction is calculated based on the total number of simulated antiprotons impinging on the degrader setup; therefore, each degrading stack

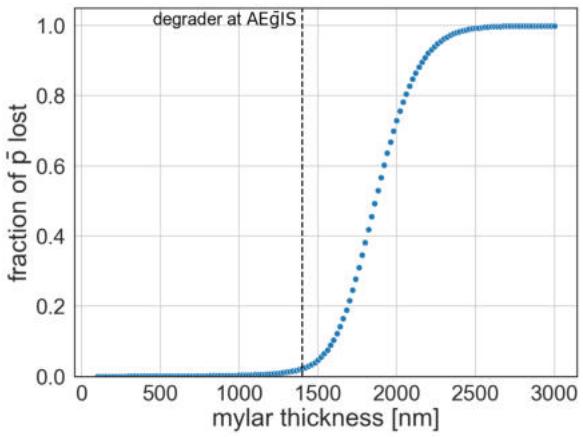

(A) Fraction of antiprotons lost due to annihilation on the Mylar foil for different thicknesses of the material.

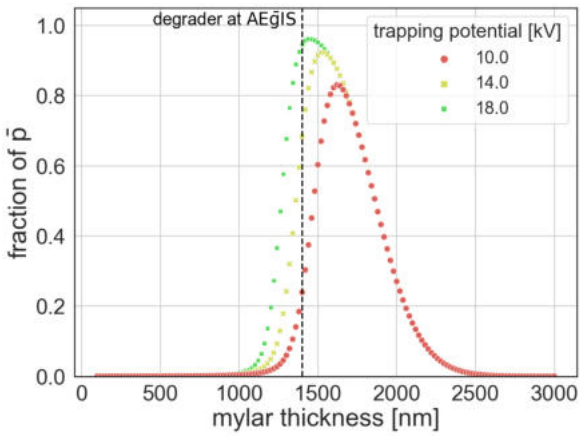

(B) Fraction of antiprotons that can be trapped (with axial momentum $p_z < \text{trapping potential}$) as a function of the thickness of the Mylar foil for three trapping potentials (10 kV, 14 kV and 18 kV).

FIGURE 6.5: The efficiency of the Mylar foil as a degrader for antiprotons.

has a unique maximum fraction that can be reached. Similarly, FIGURE 6.6b shows the fraction of moderated antiprotons, i.e. antiprotons that passed through the degrader, that cannot be trapped with the given potential. As the moderated fraction is based on the number of antiprotons that pass through the degrader, the fractions don't directly reflect the total number of antiprotons trapped; however, these values are easier to validate experimentally, because it eliminates the uncertainty of the total number of antiprotons received from ELENA, which can oscillate from bunch to bunch by $\sim 2\,\%$.

Both fractions, represented as percentages, are compared in TABLE 6.1. For the trapping potential of 14 kV (a safe high limit for the electrodes at AEgIS), the highest fraction is reached by the 100 nm Parylene with 1400 nm Mylar. At this point, the setups with thicker Parylene foils have already reached their maximum trappable fraction. Moreover, the degrader of only 1400 nm Mylar foil reaches a trappable fraction of $\approx 68\,\%$, which is lower than the setups with Parylene foils of thickness up to 300 nm. To achieve a trapping efficiency similar to that of Mylar+Parylene, the trapping potential needs to reach at least 18 kV.

From the simulation, it can be concluded that for the optimal trapping of antiprotons, a combination of 1400 nm Mylar with 100 nm Parylene is required when using 14 kV trapping potential. This setup allows for a trapping efficiency of over 90 %. Limiting to only 1400 nm Mylar simplifies the degrader setup while lowering the efficiency to $\sim 68\,\%$. When considering a single degrader of Mylar, it is possible to achieve trapping efficiency of over 90 % with upgrades of the trapping potentials to at least 18 kV. The experimental trapping efficiency accounts for additional losses,

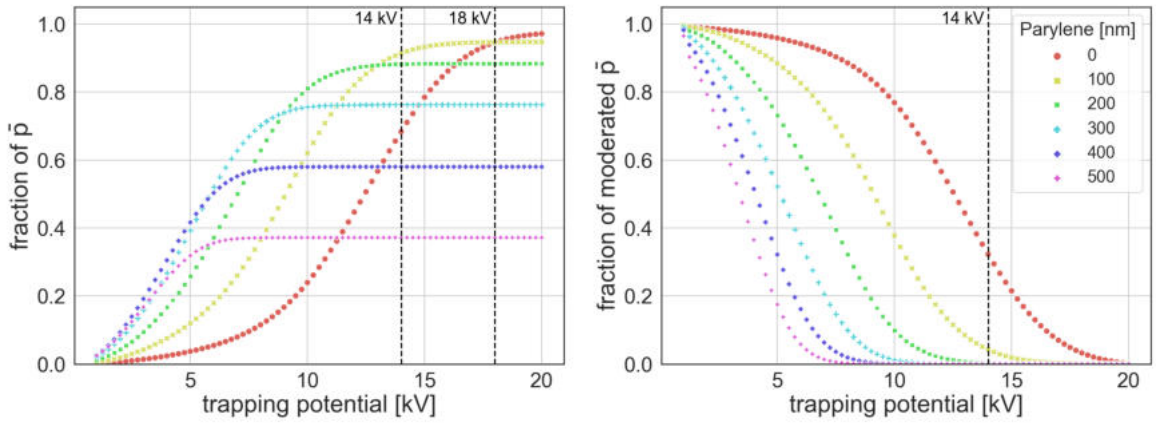

(A) The absolute fraction of the antiprotons with $p_z \leq$ HV.

(B) Fraction of moderated antiprotons with $p_z >$ HV.

FIGURE 6.6: The trapping efficiency of different degrader setups as a function of the trapping potential HV.

such as those due to the trap's closing time, which were not considered in these simulations.

6.3 Studies of the antiproton-nucleus annihilations

The novel synthesis of antiprotonic atoms and the subsequent trapping of their annihilation remnants are the main subjects of this thesis. A dedicated simulation using GEANT4 was performed to evaluate the yields of different nuclei and study the annihilation processes in antiproton-nucleus interactions.

The simulation was performed using GEANT4 version v11.1 with `FTFP_BERT_HP` physics list. A study of the effects of different physics lists on the results of the nuclei was initially performed with version v10.7 and later repeated with versions v11.1 and 11.2, after `INCL++` model was introduced for $\overline{\text{p}}$ annihilation. The comparison is shown in section 6.3.2.

6.3.1 Geometry

A simple geometry was employed in the simulation to investigate nuclear evaporation and fragmentation in antiproton-nucleus interactions. It consists of a single hollow sphere of 500 nm thickness. The antiprotons are created in the centre of the sphere with an initial energy of 1 keV. With this geometry, antiprotons can either enter the material and annihilate or bounce from the

TABLE 6.1: Absolute percentage of antiprotons that can be trapped with a specified trapping potential for a combination of 1400 nm Mylar degrader with Parylene foils of various thicknesses. The table also contains the percentage of moderated antiprotons lost (with $p_z > \mathrm{HV}$).

Parylene [nm]	12 kV	14 kV	16 kV	18 kV
	absolute trappable %			
0	44.67(8)	68.35(8)	86.18(8)	94.64(8)
100	82.07(8)	91.41(8)	94.16(8)	94.66(8)
200	87.10(9)	88.26(9)	88.40(9)	88.42(9)
300	76.25(9)	76.30(9)	76.30(9)	76.30(9)
400	58.00(9)	58.00(9)	58.00(9)	58.00(9)
500	37.18(9)	37.18(9)	37.18(9)	37.18(9)
	moderated losses %			
0	56.62(8)	32.30(8)	12.96(8)	3.24(8)
100	15.27(9)	4.22(9)	0.74(9)	0.08(9)
200	1.87(9)	0.24(9)	0.02(9)	0.00(9)
300	0.10(10)	0.01(10)	0.00(10)	0.00(10)
400	0.00(12)	0.00(12)	0.00(12)	0.00(12)
500	0.00(15)	0.00(15)	0.00(15)	0.00(15)

material and hit it again in a different place of the sphere, making sure that the antiproton annihilates within the material. The visualisation of the simulation is shown in FIGURE 6.7 with an example annihilation event for $\overline{\mathrm{p}}^{197}$Au.

The simulation of 10^6 antiprotons annihilating on a target was conducted for all known isotopes with atomic number Z <100. Atoms with Z >99 (Es) are highly radioactive and have short lifetimes. Furthermore, many do not occur naturally and must be produced. These factors make them highly unlikely to be considered as the initial target for the production of any isotopes via aptiproton-induced fragmentation. At the same time, californium (Cf) with Z =98 is widely available and used as a radioactive source, making it an interesting candidate for use as the target material.

6.3.2 Comparison of the simulation models

As described in section 6.1, different toolkits and models exist that can be used to simulate the capture-at-rest process in antiproton-nucleus interactions. A simple comparison of GEANT4 and FLUKA models was performed to understand the differences. In GEANT4, the following physics lists were used:

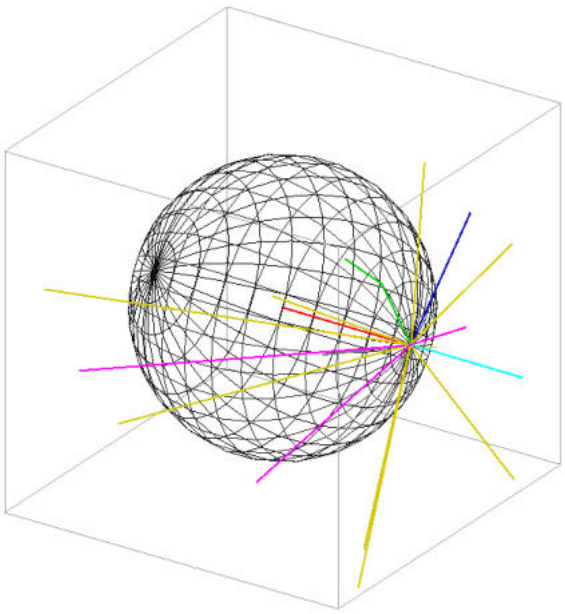

FIGURE 6.7: Visualisation of the simulated sphere with antiproton track (red) from the centre of the sphere until it annihilates on the surface of the sphere. This annihilation produced pions (magenta), gammas (yellow), protons (cyan), electrons (green), neutrons (blue), and heavy nuclei (grey).

- `FTFP_BERT_HP`[3],
- `FTFP_INCLXX_HP`,
- `QGSP_BIC_HP`,
- `QGSP_INCLXX_HP`.
- `QGSP_BERT_HP`.

The comparison of models in GEANT4 v11.1 and FLUKA is shown in FIGURE 6.8 as distributions of fragments as a function of the atomic number (left plot) and the atomic mass (right plot). The outcome from GEANT4 is the same except when using the `QGSP_BIC_HP` list (green). This difference is to be expected, as the capture-at-rest in GEANT4 v11.1 is handled only by `FTF` model. Therefore, the only difference between the two lists is in the INC implementation, with `BIC` being used in the `QGSP_BIC_HP` and `BERT` in all the rest, as `INCL++` wasn't yet implemented for $\overline{\mathrm{p}}$ reactions in this version. There are two distinct regions, one at $A = 45$ and $Z = 15$, and the second at $A = 170$ and $Z = 70$, where neither of the models produced any remnants from the annihilations. This effect is shown as a straight line without any points. Nevertheless, the differences are negligible, especially in the fission region (middle of plots, where the nucleus is split into two nuclei of similar sizes).

[3]The `HP` means that the High-Precision Neutron model for low energy neutron is included.

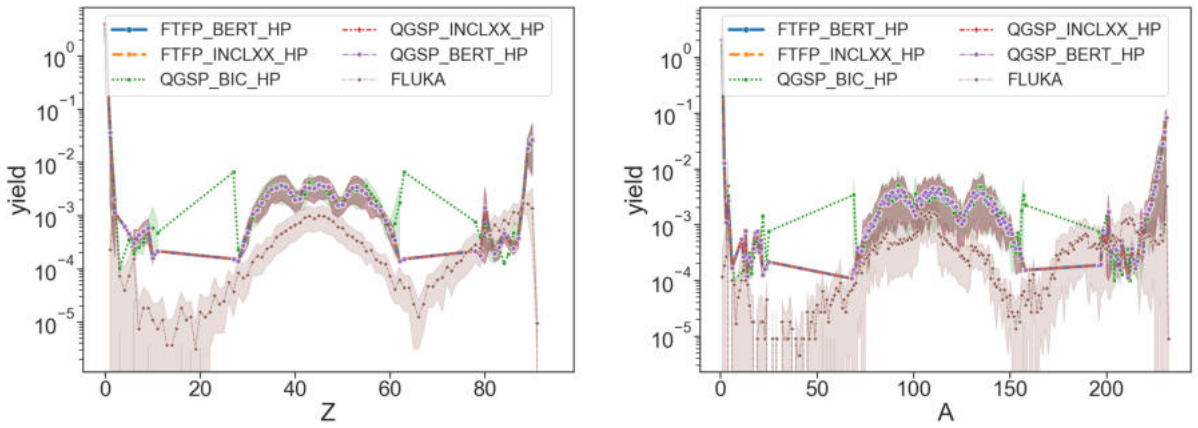

(A) Distribution of fragments as a function of the number of protons (atomic number)

(B) Distribution of fragments as a function of the atomic mass.

FIGURE 6.8: Distribution of fragments from 10^4 $\overline{\text{p}}^{232}$Th annihilations as functions of number of protons and neutrons in the final nuclei (with GEANT4 v11.1 and FLUKA).

The distributions obtained from FLUKA (brown) are different from the ones obtained from GEANT4. The distributions from FLUKA lack complex structure (three peaks) for the nuclei from the fission process. This formation suggests that the fine structure of nuclei was taken into account during pion-induced excitation and subsequent de-excitation. Therefore, the model used in FLUKA might be a simplified approach compared to the model used in GEANT4. Furthermore, the yields in FLUKA are obtained by using the RESNUCLEI card, which calculates yields of nuclear residuals as fractions and doesn't provide direct access to the energy of fragments. Moreover, the yields from FLUKA are consistently lower than from GEANT4.

Models in GEANT4 seem to be better equipped for simulating the antiproton-nucleus interactions. The slight differences between the models in GEANT4 itself are negligible; therefore, the `FTFP_BERT_HP` physics list has been chosen for all simulations of antiproton-nucleus interactions. However, this conclusion isn't based on any benchmark against experimentally measured yields of fragments from antiproton-nucleus interaction, due to a lack of direct experimental measurements.

In the later versions of GEANT4 (version v11.2), the `INCL++` model was expanded to handle the antiproton capture-at-rest reaction. FIGURE 6.9 shows the comparison between the same models as in FIGURE 6.8 when using GEANT4 v11.2. The physics lists based on the `INCL++` model (red and orange) produce identical distributions. In these lists, the `INCL++` model is used for both the capture of an antiproton by the nucleus and the INC. Therefore, any physics list based on the `INCL++` should produce the same result. The approach used in `INCL++` (coupled with the `ABLA++` de-excitation model) yields a distribution that lacks the complex structures visible

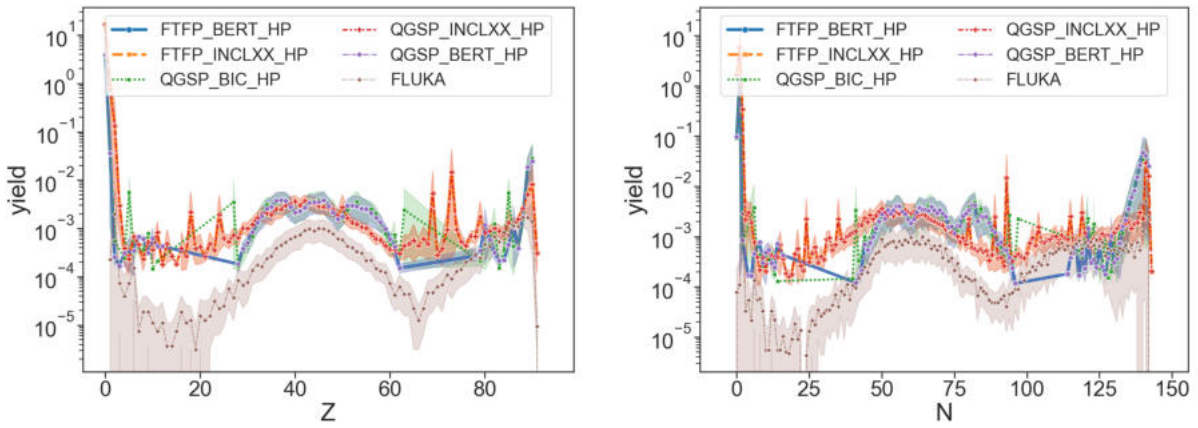

(A) Distribution of fragments as a function of the number of protons (atomic number).

(B) Distribution of fragments as a function of the number of neutrons.

FIGURE 6.9: Distribution of fragments from 10^4 $\overline{\text{p}}^{232}$Th annihilations as functions of number of protons and neutrons in the final nuclei (with GEANT4 v11.2 and FLUKA).

in the FTFP lists for the fission fragments. These distributions are more similar in shape to those obtained from FLUKA; however, with higher yields in the case of GEANT4.

It is worth noting that the ASACUSA Collaboration conducted a more in-depth comparison of the antiproton annihilation models [127]. In the paper, FLUKA is presented as having the best model for replicating the multiplicities of the minimal-ionising particles (MIPs) from the annihilations of antiprotons in some solid targets. However, the primary interest of this thesis is on the heavier fragments, either A−1 or the fragments coming from the fission. It is also stated that the model accounting for all the features observed from the annihilations of antiprotons on nuclei is missing.

6.3.3 Isotopes yields

The example plot showing the yields of all nuclei produced from the annihilations of antiprotons on nuclei of ^{232}Th is shown in FIGURE 6.10. As mentioned in section 4.1, the results can be grouped into three different outcomes: annihilation, evaporation, and fission. The plot shows three distinct regions. First region for $N < 20$ and $Z < 20$ contains light fragments that are produced from the evaporation process. This process also produced the second region with $N > 110$ and $Z > 70$ values, which correspond to heavy nuclei that remain after evaporation. The third region contains fragments produced in the fission process. In this process, the initial nucleus is split into two fragments with similar mass.

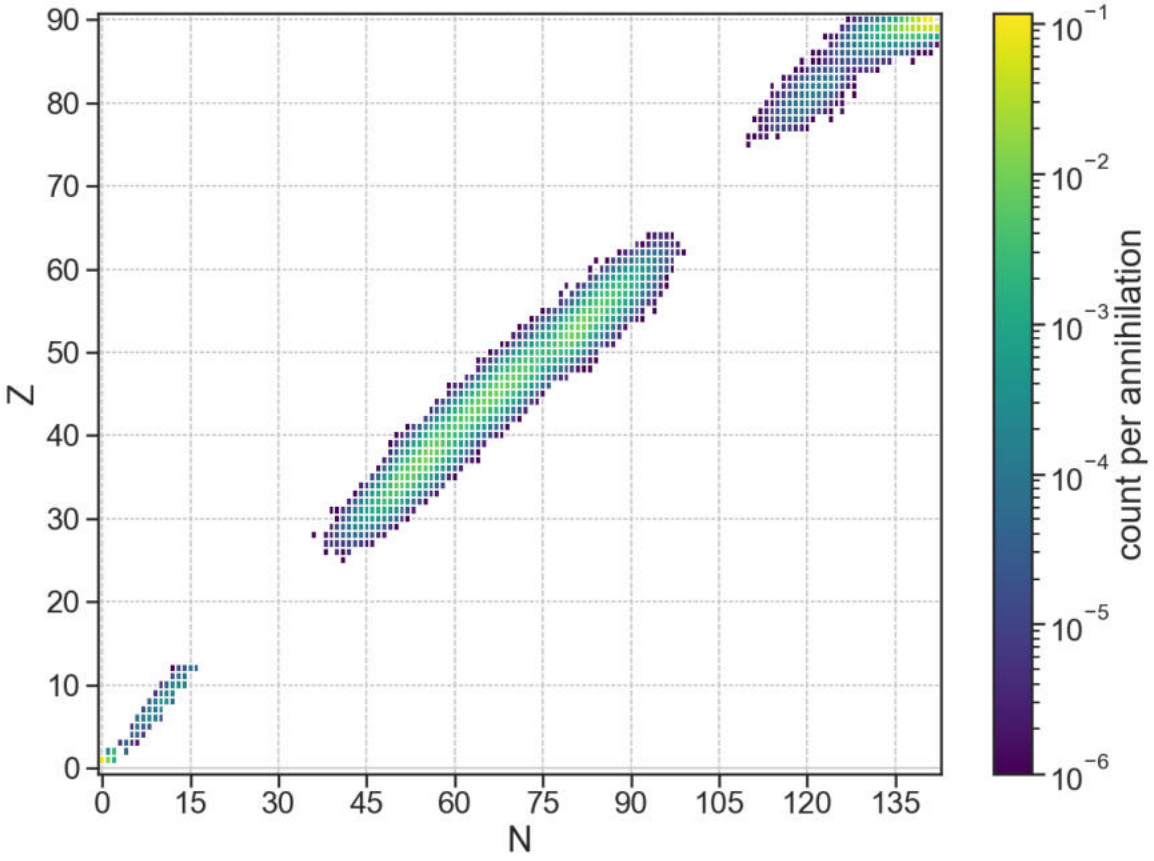

FIGURE 6.10: The yields of nuclei from $\bar{p}^{232}$Th as modelled by GEANT4.

The highest yields of heavier fragments are achieved via a sole annihilation process, which produced fragments A-1. The evaporation process produces a high number of free protons. Similarly, protons can be released in the fission process, which contributes to the high yield of protons from the antiproton-nucleus interaction.

Comparing the total energy might not be appropriate in the context of electromagnetic traps. Therefore, the energy of the produced fragments is scaled by the charge of the fragment E/Q ($Q =$ Z as we assume production of entirely stripped fragments). The average $\langle E/Q \rangle$ is shown in FIGURE 6.11. FIGURE 6.11b shows the $\langle E/Q \rangle$ as a function of the neutron number N and the atomic number Z of fragments from $\bar{p}^{232}$Th. It can be concluded that $\langle E/Q \rangle$ decreases with the higher atomic mass (A) of the produced fragment. As a result, the lighter fragments have much higher $\langle E/Q \rangle$, which means that these fragments will be more difficult to trap with an electric potential. This behaviour is independent of the target isotope. The trend is shown in FIGURE 6.11a for four different target isotopes.

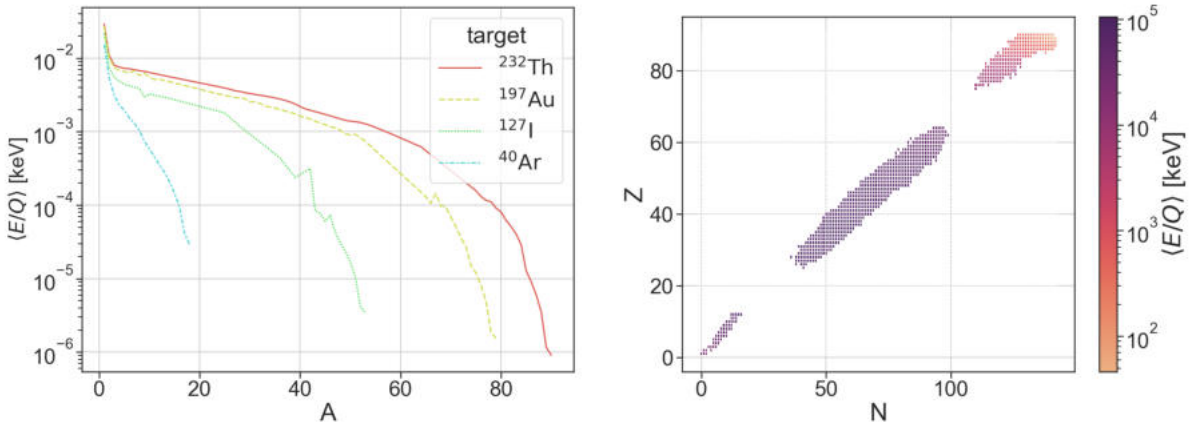

(A) The distribution for fragments from a few example targets as a function of atomic mass (A) of the fragment.

(B) The distribution for fragments from $\overline{\mathrm{p}}^{232}$Th.

FIGURE 6.11: The distribution of average energy scaled by the charge of nuclei $\langle E/Q \rangle$ of fragments from antiproton-nucleus interaction as modelled by GEANT4.

The methods for trapping and studying different isotopes, such as Penning or Paul traps in combination with TOF or RF measurements, usually depend on the mass-to-charge m/Q of the fragments. The distribution of the m/Q for fragments is shown in FIGURE 6.12. The fragments with lower atomic number Z have a higher spread of the m/Q values with a mean around 2 u/e (atomic mass unit per elementary charge). This distribution is due to the structure of the nuclei in which the number of protons and neutrons is similar for lighter elements. With the higher atomic number Z, the nucleus tends to have a greater number of neutrons than protons, which is seen by the average m/Q getting closer to 2.5 u/e for fragments with higher Z.

The isotopes used as the example targets, that is ^{232}Th, ^{197}Au, ^{127}I, and ^{40}Ar, were chosen to cover a range of different atomic masses and nuclear structures. Moreover, ^{40}Ar was used in the form of a gaseous target at the AE$\bar{\text{g}}$IS experiment, and ^{127}I is considered as the isotope for the ion source developed for AE$\bar{\text{g}}$IS to be used in the first controlled production of antiprotonic atoms.

6.3.4 Trapping of fragments

Calculating the exact number of trapped fragments produced from the $\overline{\mathrm{p}}$-nucleus interaction requires solving equations of motion for each remnant produced. These values can be estimated to the leading order with different approaches. The simple method is to consider that all fragments with kinetic energy E_{kin} (in keV) and charge Q (in units of elementary charge) which meet

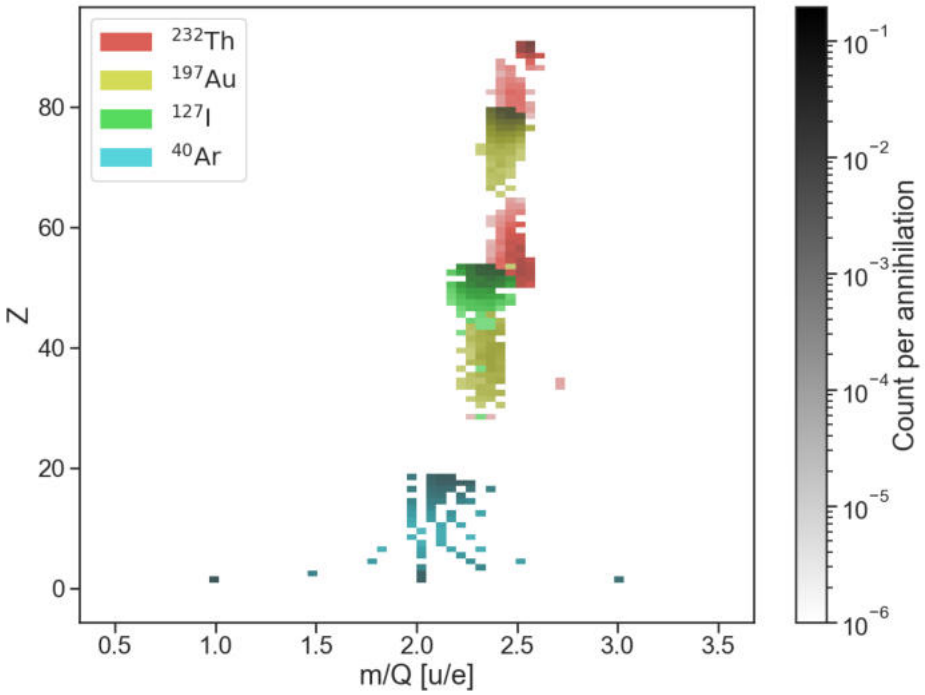

FIGURE 6.12: The distribution of fragments produced from different targets as their m/Q and Z, as modelled by GEANT4.

the condition $E_{kin} < Q \times V$ can be trapped by the potential V (in kV). This simple approach yields a trappable value, assuming a spherical electric potential.

The second approach is to consider the type of trap in the calculations, either a Penning-like or a Paul-like trap. In the context of this thesis, a Penning-like trap is considered. As described in section 3.1, the trapping inside a Penning trap is done via a combination of the confinement by the electric potential in the axial direction and by the magnetic field in the radial direction. Let's consider a fragment that is produced inside a trap with radius R, magnetic field B, and moving at an angle θ from the z-axis. From $E_{kin} = mv^2/2$ we have that:

$$v_T = \sqrt{\frac{2E_{kin}}{m}} \sin\theta, \quad v_Z = \sqrt{\frac{2E_{kin}}{m}} \cos\theta, \tag{6.2}$$

where v_T and v_Z are the velocities in the transverse and axial directions, respectively. The trapping in the axial direction is done via the electric potential of the electrodes V, which gives the condition:

$$\frac{E_{kin}}{Q} \cos^2(\theta) < V. \tag{6.3}$$

The trapping condition in the radial direction is determined by the radius of the electrodes in the

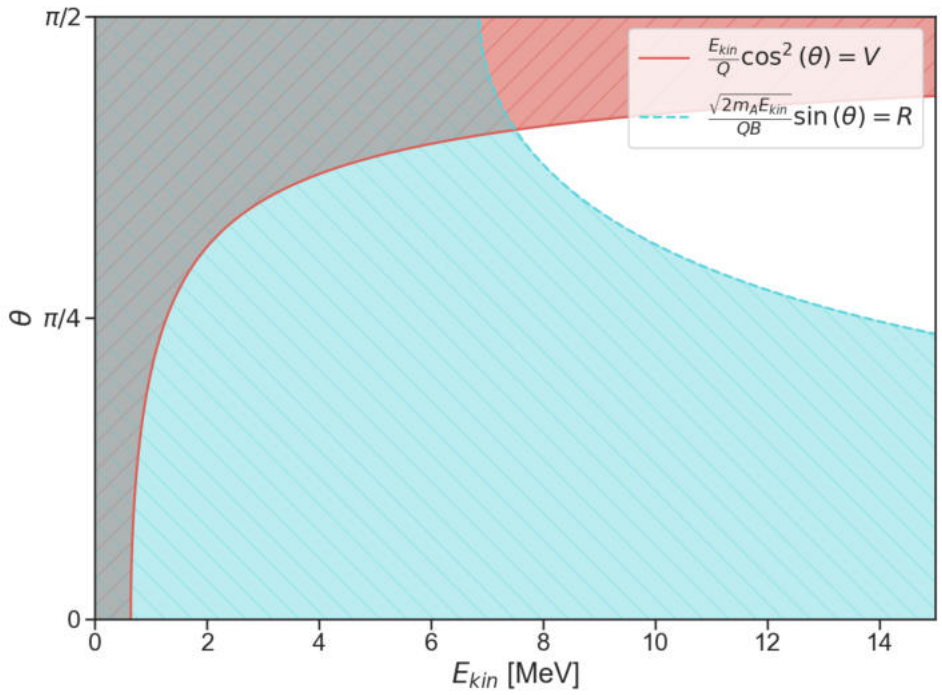

FIGURE 6.13: Trapping conditions for θ and kinetic energy of the ^{162}Gd isotope. The red (//) region indicates values for which the isotope can be trapped by potential $V = 10$ kV. The blue (\\) region indicates values for which the isotope can be trapped inside a trap with radius $R = 15$ mm and magnetic field $B = 5$ T.

Penning-Malmberg trap. From equation 3.3 for the radius of a particle inside a magnetic field, we get:

$$\frac{\sqrt{2m_A E_{kin}}}{QB}\sin(\theta) < R, \tag{6.4}$$

where m_A is the mass of the fragment. FIGURE 6.13 shows the two conditions for $^{Gd}162$ as a fragment inside a Penning trap with $R = 15$ mm, $B = 5$ T, and $V = 10$ kV. It is reasonable to assume that the fragments from annihilation-induced fragmentation are produced isotropically in 4π angle. Because of the rotational symmetry about the z-axis and the mirror symmetry about the transverse plane going through the centre of the trap, the θ angle can be limited to $\left[0, \frac{\pi}{2}\right]$. From the two conditions 6.3 and 6.4, we can calculate the trappable fraction for each fragment for a specific kinetic energy. FIGURE 6.13 shows that a Penning trap is capable of trapping fragments with greater energy than the energy cut of QV assumed in a simple approach, granting that more energetic fragments are only trappable for a specified emittance angle range and would require some cooling mechanisms to keep the fragments trapped for more extended periods. The total yield is then estimated as the sum of all the fractions.

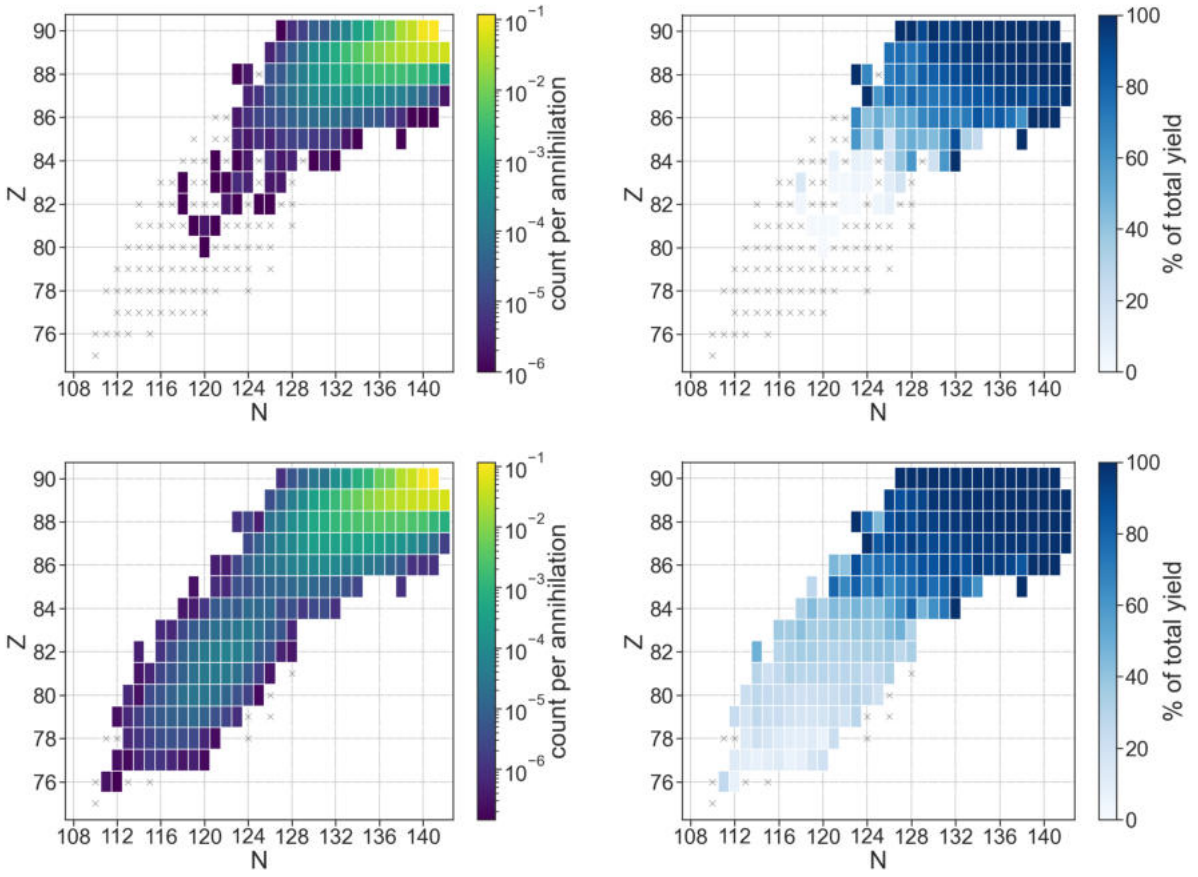

FIGURE 6.14: Comparison of the yields of trappable fragments (left) assuming a simple energy cut with $V = 10$ kV (top) or a Penning-Malmberg trap with $R = 15$ mm, $B = 5$ T (bottom). Parameters for the Penning-Malmberg trap were chosen in accordance with traps used in the AE$\bar{g}$IS experiment. The percentage of the total yield that can be trapped is shown on the right. The yields calculated for $\bar{p}^{232}$Th. Fragments that are produced and not trapped are indicated as "X" markers on the plots.

The yields of trappable fragments using both techniques are shown in FIGURE 6.14 for the fragments from $\bar{p}^{232}$Th. The left plots show the estimated yields assuming axial trapping by the electric potential only (top) and assuming trapping inside a Penning-Malmberg. The "X" markers indicate the fragments that were produced but cannot be trapped with a given method. The right plots show the yield as the percentage of the total yield of the given fragment. The Penning-Malmberg traps are capable of trapping a greater range of fragments and provide access to most of the heavier fragments produced in the antiproton-induced fragmentation. The calculations of yields were performed assuming a trapping potential of V=10 kV for both methods and R=15 mm with B=5 T for the Penning-Malmberg trap. These values are based on the

parameters of the Penning-Malmberg trap used in the AEgIS experiment.

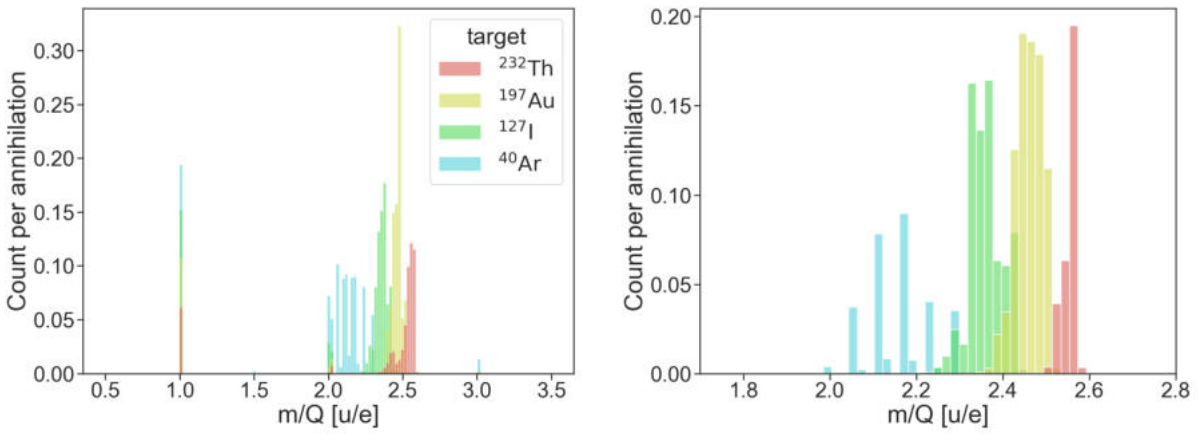

(A) Distribution for all fragments.

(B) The distribution for trappable fragments assuming a Penning-Malmberg trap with $R = 15$ mm, $B = 5$ T and $V = 10$ kV as used in the AEgIS experiment.

FIGURE 6.15: The distribution of m/Q and Z for fragments produced from different targets as modelled by GEANT4.

The trapping conditions inside a Penning-Malmberg trap depend on both the mass of the fragment m and the charge Q. In all calculations, it is assumed that produced fragments are in the entirely stripped state, because atoms lose all electrons during $\overline{\text{p}}$ cascade in the antiprotonic atoms [128], [129], with few electrons remaining in atoms with higher binding energy than $\overline{\text{p}}$ Kr. Therefore, the charge of the produced ion is $Q = Z$. FIGURE 6.15 shows the distribution of the mass-to-charge ratio m/Q of all produced fragments (on the left) and the fragments trappable inside a Penning trap. Due to the limitation of trapping, lighter fragments cannot be trapped, as is directly evident from the m/Q distribution. The trapped fragments are grouped around values 2 u/e$< m/Q <$ 2.5 u/e. Furthermore, the average m/Q increases for heavier targets. The m/Q is binned in bins of size 0.02 u/e. For lighter targets, it is possible to see unique peaks; however, the heavier fragments produce a continuous distribution, due to a higher number of unique fragments produced, which is skewed to the left.

6.3.5 Estimation of the neutron halo factor

The neutron halo factor is a ratio between $\bar{p}n$ and $\bar{p}p$ annihilation reactions in antiprotonic atoms [42]. This ratio provides information about the density distribution of protons and neutrons inside the nucleus. Annihilation of $\overline{\text{p}}$ with a single nucleon in a nucleus is not the only possible reaction. Pontecorvo first suggested these reactions, where an antiproton annihilates with more

nucleons involved in [130]. Furthermore, production of neutral strange-particles observed in [131] points to other $\overline{\text{p}}$-nucleus annihilation processes with multiple nucleons involved [132]. The type of annihilation can provide information about the annihilation process itself, as well as about the parton distribution inside the nucleus, especially the neutron halo.

The ratio between the number of annihilations with neutrons $N(\bar{p}n)$ and annihilations with protons $N(\bar{p}p)$ depends on the nuclear structure of the isotope. The annihilations with neutrons are more common in nuclei with a thicker neutron skin. Similarly, the neutron halo increases the probability of $\bar{p}n$ and production of $A-1$ fragments.

One of the first studies of the neutron halo in heavier nuclei was performed in the early 1970s at Brookhaven National Laboratory (BNL) [42]. A similar study was later performed with antiprotons at CERN [27]. Two experiments calculate the halo factor according to the same formula:

$$f_{halo} = \frac{N(\bar{p}n)Z_t}{N(\bar{p}p)N_t}; \tag{6.5}$$

however, the two experiments use different methods to determine the $N(\bar{p}n)$ and $N(\bar{p}p)$. The team from BNL used the total charge of pions produced from the annihilations to determine the number of annihilations with neutrons and protons. In this way, all annihilations of antiprotons were taken into consideration. The team at CERN used a gamma spectroscopy to determine the number of fragments with $A-1$, which probes the more peripheral region of the halo; therefore, the factor is denoted as f_{halo}^{periph}. In the [42] paper, the authors normalise the neutron halo factor by the $N\left(\bar{p}n\right)/N\left(\bar{p}p\right) = 0.632$ ratio measured for ^{12}C target. This value is later used in a theoretical paper that tries to describe the neutron halo from antiproton absorption [43] and subsequently by the authors of the [27] paper. The justification for using this normalisation is that there is no good evidence for the proton halo.

TABLE 6.2: Comparison between the simulated neutron halo factors calculated using two different methods.

Target	N_t/Z_t	f_{halo}	f_{halo}^{periph}
^{12}C	1.0	1.0001(2)	0.9461(4)
^{14}N	1.0	1.0124(2)	0.5385(3)
^{40}Ar	1.22	1.065(2)	1.331(6)
^{127}I	1.40	1.221(3)	1.063(5)
^{197}Au	1.49	1.339(3)	1.201(5)
^{232}Th	1.58	1.390(3)	1.442(8)

Calculation of both factors was performed based on the simulated results. The comparison

of the neutron halo factors calculated from the simulation is shown in TABLE 6.2. In the calculation, the formula from equation 6.5 was used; however, the normalisation factor of 0.632 was ignored. The calculated f_{halo} for ^{12}C is equal to 1.0 as expected. The peripheral halo for ^{12}C and ^{14}N suggests the existence of some peripheral proton halo. Therefore, a further experimental study is required to validate and/or develop the existing models and our understanding of the nuclear structures.

Trapping of the fragments can be used as another method to study the neutron halo. The trapping provides direct access to the number of $A-1$ atoms produced from the annihilation. One method that can be used to determine the number of $A-1$ atoms is the time-of-flight measurement of trapped fragments, which provides information about the m/Q of the fragments. This method, however, requires determination of m/Q to a precision of 10^{-6} u/e to distinguish between all m/Q. Precision of 10^{-4} u/e[4] is sufficient to discriminate between the $A-1, Z$ and $A-1, Z-1$ fragments. This precision is achievable even with a simple setup that can be realised in AEgIS after an upgrade of high-voltage power supplies for trapping electrodes.

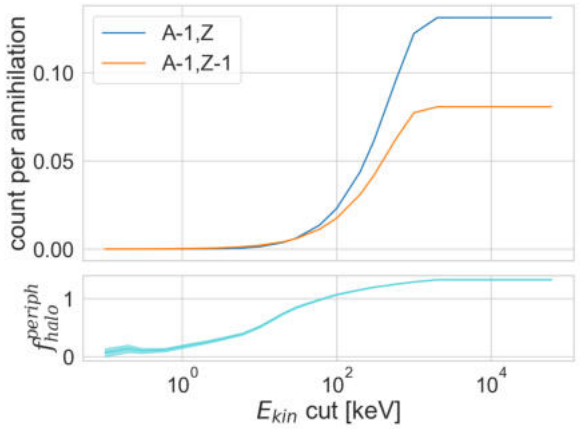

(A) The total number of $A-1, Z$ and $A-1, Z-1$ for $\bar{p}^{40}$Ar with kinetic energy below the energy cut (top). The calculated peripheral neutron halo below the energy cut (bottom).

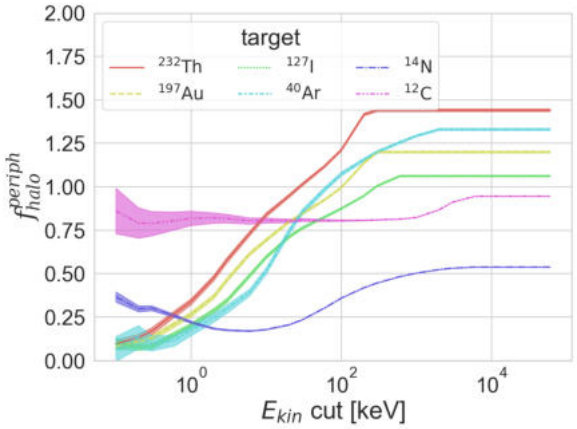

(B) Peripheral neutron halo as a function of kinetic energy cut for different targets.

FIGURE 6.16: Peripheral neutron halo as calculated from GEANT4 simulations.

FIGURE 6.16 shows how the total number of $A-1, Z-1$ and $A-1, Z$ depend on the cut on the kinetic energy of the fragments. From this, it can be concluded that the neutron halo factor measured with the trapped fragments depends on the trapping conditions. This dependence is especially relevant for lighter targets. The peripheral neutron halo factors for ^{12}C, ^{14}N, ^{40}Ar, ^{127}I, ^{197}Au, ^{232}Th are summarised in TABLE 6.3. The second column contains the value calculated

[4]For Launch potential of 1 kV and the distance of 1 m this corresponds to resolution in TOF of about 10 ns.

TABLE 6.3: The simulated values for the peripheral neutron halo factor and the value that can be estimated based on different trapping potentials. The trapping is simulated as a Penning trap with 30 mm diameter and 5 T magnetic field with trapping potentials of 5 kV, 10 kV, 20 kV and 100 kV.

Target	f_{halo}^{periph}	Trapping potential			
		5 kV	10 kV	20 kV	100 kV
^{12}C	0.9461(4)	1.251(3)	1.248(3)	1.244(2)	1.2238(13)
^{14}N	0.5385(3)	0.5366(9)	0.5507(8)	0.5653(7)	0.5905(5)
^{40}Ar	1.331(6)	1.263(8)	1.287(7)	1.307(7)	1.331(6)
^{127}I	1.063(5)	1.043(4)	1.063(5)	1.063(5)	1.063(5)
^{197}Au	1.201(5)	1.201(5)	1.201(5)	1.201(5)	1.201(5)
^{232}Th	1.442(8)	1.442(8)	1.442(8)	1.442(8)	1.442(8)

without any cuts on the data. The last four columns contain the values calculated for different trapping potentials (5 kV, 10 kV, 20 kV and 100 kV) inside a Penning trap with radius R=15 mm and magnetic field B=5 T.

Experimentally measuring the exact number of $\bar{p}n$ and $\bar{p}p$ isn't trivial. When relying on the charged meson count, as used in [42], the final neutron factor depends on the number of positive and negative pions measured. However, pions from the annihilation can be absorbed by the material, especially with solid targets. Furthermore, the count depends on the solid angle coverage of the detector. When relying on the radiochemistry to determine the $A-1, Z-1$ and $A-1, Z$ remnants, as used in [27], the neutron halo depends on the precision to detect the gamma rays produced by the radioactive fragments. This method cannot be applied to targets when one of the fragments with atomic mass $A-1$ is stable. The direct measurement of the fragments produced presents several challenges that need to be addressed. Firstly, the trapping of the fragments depends on the available potentials and the recoil energy of the produced fragments. By applying a high enough potential and a cooling technique for trapped fragments, virtually all fragments could be trapped. Secondly, some of the trapped ions might not come from the annihilation. Secondary reactions, like pion absorption or ionisation, could create a background signal. While fragments from ionisation should be easy to identify, as they are ions of the target atom, the pion absorption might be more challenging. Finally, after the fragments are trapped, a reliable method for identifying trapped ion species is needed. A TOF method with sufficient resolution can be implemented to distinguish between different species.

6.3.6 Successive annihilation path

Antiprotonic atoms can be used as a source of exotic isotopes. Therefore, it is necessary to be able to find the highest yield of any isotope of interest. Direct high-yield production of all the known isotopes starting from a stable element is not always possible using antiprotons. To increase the number of reachable isotopes using the technique, a multi-step process can be prepared, where capture and annihilation occur multiple times until the chain reaches the desired production target. Therefore, the highest experimentally possible yield for exotic isotopes might require a multi-step scheme.

We have investigated the optimal path to produce a trappable arbitrary isotope following the antiproton annihilation scheme. As described in section 4.1.1, the fragments created from the primary annihilation of an antiproton on the target nucleus can be used as a secondary target for subsequent reaction with antiprotons. This leads to a secondary annihilation event, which can result in the fragmentation of the secondary target.

To find the optimal path for a specific isotope (y_X), a simple algorithm is applied as follows. Firstly, the sources are limited to only targets with a lifetime of at least 10 min. Next, the primary yields are calculated. Then, for each target, the same process is repeated (load sources, limit to semi-stable isotopes only, calculate the yields). This produces a chain of isotope 1 $\rightarrow$ isotope 2 $\rightarrow \cdots \rightarrow$ desired isotope. The yield is calculated as:

$$y_X = \prod_{i=1}^{N-1} y_i,$$

where y_i is the yield of going from isotope X_i to X_{i+1} and N is the number of isotopes in the chain.

This process can be continued until there are no more semi-stable sources; however, the total yield y_X decreases with each step. Therefore, the calculations are limited to include a maximum of three annihilation steps in a path. The paths are further limited to the stable isotope as the initial target. TABLE 6.4 contains the paths with the highest yield of ^{220}Th. The highest yield is achieved for the direct production form ^{237}Cm, and the best 2-step path achieves yields over two times lower. The 3-step process lowers the yield by another factor of 2; however, the yields are still in the order of 10^{-7}. This process is more critical for the isotopes that don't have a direct production from a stable target, like ^{100}Sn, for which the best achievable yield is from the 2-step process of ^{112}Sn $\rightarrow$ ^{108}Sn $\rightarrow$ ^{100}Sn with yield of 3.4(4) $\times$ 10^{-8} per annihilation chain.

Furthermore, the annihilation produces isotopes in different energy states depending on the target. Therefore, different paths can be considered to obtain a specific isomer with an increased

TABLE 6.4: The ten paths with the highest yields of ^{220}Th which start from a stable isotope.

Path	yield [10^{-9}]
^{237}Cm $\rightarrow$ ^{220}Th	491(98)
^{241}U $\rightarrow$ ^{232}Pa $\rightarrow$ ^{220}Th	231(46)
^{241}U $\rightarrow$ ^{233}Pa $\rightarrow$ ^{220}Th	217(43)
^{241}U $\rightarrow$ ^{234}Pa $\rightarrow$ ^{220}Th	211(42)
^{241}U $\rightarrow$ ^{228}Th $\rightarrow$ ^{220}Th	205(41)
^{241}U $\rightarrow$ ^{230}Th $\rightarrow$ ^{220}Th	201(40)
^{241}U $\rightarrow$ ^{231}Pa $\rightarrow$ ^{220}Th	188(37)
^{241}U $\rightarrow$ ^{229}Th $\rightarrow$ ^{220}Th	161(32)
^{241}U $\rightarrow$ ^{235}Pa $\rightarrow$ ^{228}Th $\rightarrow$ ^{220}Th	140(28)
^{241}U $\rightarrow$ ^{235}Pa $\rightarrow$ ^{228}Th $\rightarrow$ ^{220}Th	140(28)

TABLE 6.5: The ten paths with the highest yields of ^{100}Sn which start from a stable isotope.

Path	yield [10^{-9}]
^{112}Sn $\rightarrow$ ^{108}Sn $\rightarrow$ ^{100}Sn	33(7)
^{112}Sn $\rightarrow$ ^{110}Sn $\rightarrow$ ^{108}Sn $\rightarrow$ ^{100}Sn	15(3)
^{112}Sn $\rightarrow$ ^{109}Sn $\rightarrow$ ^{108}Sn $\rightarrow$ ^{100}Sn	12(2)
^{112}Sn $\rightarrow$ ^{111}Sn $\rightarrow$ ^{108}Sn $\rightarrow$ ^{100}Sn	10(2)
^{114}Sn $\rightarrow$ ^{108}Sn $\rightarrow$ ^{100}Sn	6.7(1.3)
^{114}Sn $\rightarrow$ ^{110}Sn $\rightarrow$ ^{108}Sn $\rightarrow$ ^{100}Sn	6.1(1.2)
^{114}Sn $\rightarrow$ ^{111}Sn $\rightarrow$ ^{108}Sn $\rightarrow$ ^{100}Sn	5.2(1.0)
^{114}Sn $\rightarrow$ ^{112}Sn $\rightarrow$ ^{108}Sn $\rightarrow$ ^{100}Sn	4.4(8)
^{122}Ce $\rightarrow$ ^{108}Sn $\rightarrow$ ^{100}Sn	3.5(7)
^{114}Sn $\rightarrow$ ^{109}Sn $\rightarrow$ ^{108}Sn $\rightarrow$ ^{100}Sn	3.3(7)

yield, One of the uses for isomers is as qubits in quantum computers. In the paper [133], we looked for different candidates that can be produced with antiproton annihilation. The best candidates that we selected were ^{93}Mo in 2425 keV isomer state and ^{92}Nb in 135 keV isomer state. The isomers of ^{93}Mo can be achieved directly from stable isotopes. The yields of the ^{93}Mo reach up to 0.145; however, the yields for 2425 keV isomers drop to below 0.02 per annihilation. There are no direct paths of obtaining ^{92}Nb in the 135 keV state according to the GEANT4 simulation. However, all the states 225.8 keV, 285.7 keV, 389.8 keV and 975.0 keV decay exclusively to the 135 keV state with a halftime of less than 10 µs [134]. Therefore, we can consider all of these isomers as practically being the isomer with 135 keV excitation energy. From this, we can calculate the highest yield for ^{92}Nb in the 135 keV state to be 0.09 per annihilation. The calculated yields for the two isomers are summarised in TABLE 6.6.

TABLE 6.6: Simulated yields of the product isomers from the annihilation of one antiproton with the target nucleus. For each product, the total isotope yield in all energy states is reported together with the isomer yield corresponding to the isomer with excitation energy E. The yields for ^{92}Nb (denoted with "*") are calculated as the sum of yields of all isomer states below 1 MeV that decay exclusively to the 135 keV. Table taken from [133].

Target	Product	Isotope yield [%]	E [keV]	Isomer yield [%]
^{94}Mo	^{93}Mo	14.5	2425	1.7
^{94}Mo	^{92}Nb	8.7	135	5.2*
^{95}Mo	^{93}Mo	13.0	2425	1.5
^{95}Mo	^{92}Nb	7.7	135	4.6*
^{94}Tc	^{93}Mo	10.3	2425	1.2
^{94}Tc	^{92}Nb	0.5	135	0.3*
^{93}Nb	^{92}Nb	12.7	135	9*
^{94}Nb	^{92}Nb	11.6	135	6.8*
^{95}Nb	^{92}Nb	9.4	135	5.5*

6.3.7 Modeling of time-of-flight spectrum of fragments and ions

One of the methods used to estimate the species of particles inside a Penning-Malmberg trap is a time-of-flight (TOF) spectrometry. This is achieved by elevating the trap (raising the trap's floor) to some initial launch potential V_{launch}, and releasing particles with a quick pulse (order of ns), which serves as the start t_{launch} for the TOF measurement, of one of the trap walls to 0 V. Particles travel a distance L between the trap and a detector that measures the time of arrival of the particles. Assuming that initial velocities, starting times, and flight distances are constant between different particles[5], it is possible to estimate the mass-to-charge ratio (m/Q) of the trapped fragments based on the time of arrival in the detector, which provides the stop signal t_{detect}. The time between the opening of the trap and detection can be calculated as:

$$\Delta t = t_{detect} - t_{launch} = \frac{L}{v}, \tag{6.6}$$

assuming that the particle travels with a constant velocity v between the trap and the detector, which is a valid first-order approximation. The velocity of the particle can be calculated from its kinetic energy:

$$E_{kin} = \frac{mv^2}{2} \rightarrow v = \sqrt{\frac{2E_{kin}}{m}} \tag{6.7}$$

[5]All these values depend on the distribution of particles in the trapping region.

where m is the mass of the particle. The kinetic energy used in TOF spectrometry isn't in the relativistic region; therefore, the relativistic corrections can be ignored. Substituting equation 6.7 to equation 6.6 we get:

$$\Delta t = \sqrt{\frac{mL^2}{2E_{kin}}}, \tag{6.8}$$

where L is the distance travelled by the particle.

In the case of particles released from a Penning-Malmberg trap, we can assume, as the first-order approximation, that the kinetic energy of the particle comes fully from the electric potential of the trap:

$$E_{kin} = U_E = QV_{launch} \tag{6.9}$$

where U_E is the potential energy of the particle with electric charge Q (in case of fragments, we can assume full stripping, which gives $Q = Z \times e$, with e being the elementary charge) inside a trap with floor potential V_{launch}. Combining equations 6.8 and 6.9 we get:

$$\Delta t \left(\frac{m}{Q}\right) = \sqrt{\frac{L^2}{2V_{launch}}}\sqrt{\frac{m}{Q}}. \tag{6.10}$$

As equation 6.10 shows, the TOF depends on the mass-to-charge ratio. Therefore, the resolving power of TOF measurements for different species is limited by the resolution to determine Δt of each species.

The yields of different fragments per annihilation of $\overline{\text{p}}^{40}$Ar were calculated via the simulation done in GEANT4 to estimate the content of the trap in experiments with ^{40}Ar in AE$\overline{\text{g}}$IS. From the equation 6.10, the Δt for each fragment can be calculated. However, m/Q of fragments falls mostly in the range from 2.0 u/e to 2.5 u/e[6]. Therefore, a high resolution of the TOF signal is required to differentiate between two fragments. In the TOF spectrum, especially at low resolution, two or more signals can overlap, resulting in a superposition.

Therefore, a model of TOF measurement is required to simulate the expected spectra for fragments based on the experimental conditions. This simulation, however, is far from trivial. One of the primary challenges lies in calculating the density, momentum, and energy equations for non-neutral plasma. Non-neutral plasma is a group of charged particles whose equilibrium thermodynamics is dominated by the long-distance interactions. Calculation of non-neutral plasma, consisting of a single-species particles, is an extensively studied problem in plasma physics,

[6]For ^{40}Ar there are 44 fragments in that range with an average m/Q difference between two peak positions being 0.008 u/e.

known as *autoconsistent plasma potential* [135], [136]. The distribution can be solved numerically, albeit at high computational costs. This problem was explored in more detail in [137]. Particles inside a Penning-Malmberg trap in an equilibrium state can be considered as *rigid rotor* with plasma rotation gyro-frequency ω on the axis of symmetry of the trap. The analytical spatial distribution can be described as [137]:

$$n\left(r,z\right)=n_0\left(\frac{m}{2\pi k_B T}\right)^{3/2}\exp\left[-\frac{1}{k_B T}\left(-q\phi\left(r,z\right)-\frac{m}{2}\omega\left(\omega_c+\omega\right)r^2\right)\right] \tag{6.11}$$

where n_0 is the particle density at the center of the distribution and $\omega_c = QB/m$ is the cyclotron frequency of particles with electric charge q and mass m inside a uniform external magnetic field $\vec{B}$, while $\phi\left(r,z\right)$ is the total potential felt by the plasma which is a sum of potentials due to trapping electrodes $\phi^{tr}\left(r,z\right)$ and the potential due to the plasma itself $\phi^{pl}\left(r,z\right)$:

$$\phi\left(r,z\right)=\phi^{tr}\left(r,z\right)+\phi^{pl}\left(r,z\right). \tag{6.12}$$

As $\phi^{pl}\left(r,z\right)$ depends on $n\left(r,z\right)$ obtaining a solution to this equation is challenging. Furthermore, when considering multi-species plasma, the problem becomes more complicated as the final distribution is a product of distributions from each of the species [138], [139].

The goal of this exercise was to recreate experimentally observed TOF signals without explicitly solving the *problem of the autoconsistent non-neutral plasma potential* for plasma consisting of fragments from the annihilation of antiprotonic atoms. The model is based on the following assumptions and simplifications:

- Assume that the radial distribution of the plasma does not affect the TOF signal. This assumption allows us to simplify the potential geometry to only z-direction, effectively making the problem one-dimensional instead of three.
- Particles along the z-direction are distributed according to a generalised Gaussian function $f(z)=\frac{\beta}{2\Gamma(1/\beta)}\exp\left(-|z|^{\beta}\right)$, where β defines the shape of the distribution ($\beta=1$ is identical to Laplace distribution and $\beta=2$ is similar to normal distribution with $\sigma=1/\sqrt{2}$). The model uses $\beta=10$ to assume that particles are thermalised to low temperature inside the trap and $\beta=2$ to assume that particles are in some hot state.
- Particles are uniformly distributed inside the trapping potential between two values called *spacecharge_min_V* and *spacecharge_max_V*.

The TOF signal is calculated in the following steps:

1. *Calculate the trapping potential shape as a function of z-position* for $t < t_{launch}$ and $t = t_{launch}$, where t_{launch} is the moment of pulsing one of the endcap electrodes. For the AEgIS

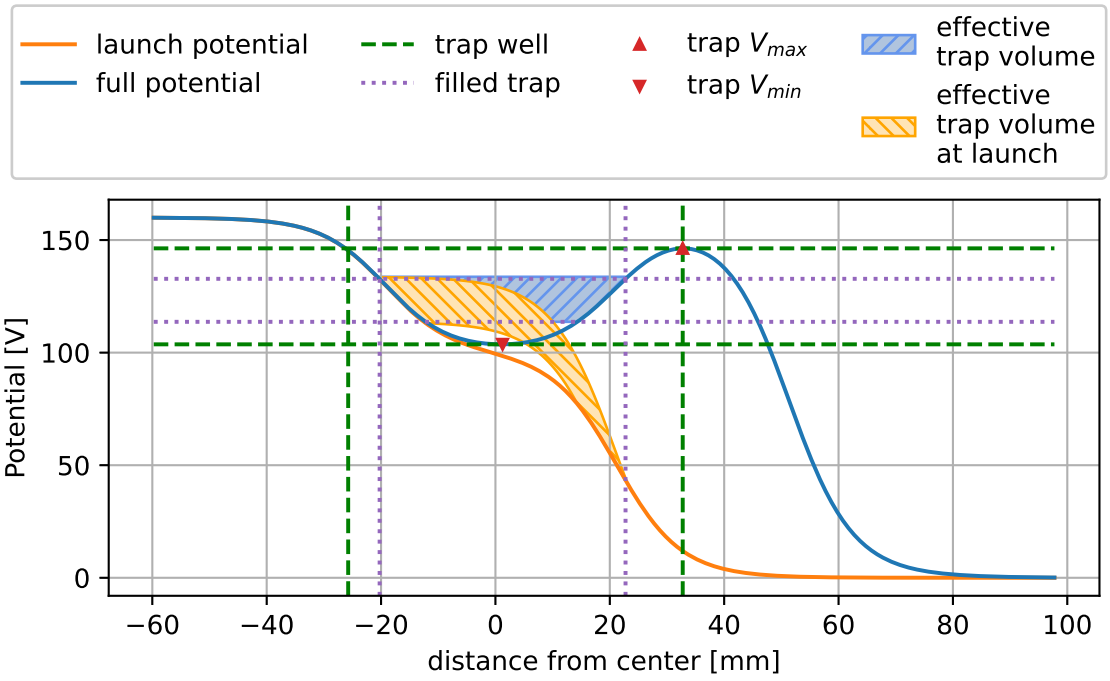

	wall [V]	floor [V]	full depth [V]	spacecharge [eV]
Set trap	160	100	60	10.00-30.00

	depth [V]	min [V]	max [V]	width [mm]	from [mm]	to [mm]
Full trap	42.63	103.68	146.31	58.50	-25.75	32.75
Filled trap	29.10	103.68	132.78	43.00	-20.25	22.75

FIGURE 6.17: Example potentials in the "ready to launch" and "launch" configuration of Penning trap.

experiment, this is achieved by defining the electrodes used in the TOF measurement and utilising a matrix that describes the contribution of each electrode to the potential as a function of position z with a step size of 0.5 mm.

2. Find effective trapping volume. In this step, the limits on z and V are calculated based on the given parameters. It includes finding the real maximum V_{max} and minimum V_{min} potentials of the trapping region.

3. Limit trapping region to one filled with particles based on values of *spacecharge_min_V* and *spacecharge_max_V*. If the maximum value of spacecharge exceeds the maximum trapping potential, the region is limited by the maximum trapping potential instead.

FIGURE 6.17 shows the potential shape of the trapping region at $t < t_{launch}$ in as blue line and at the $t = t_{launch}$ with orange curve with $V_{floor} = 100\,\text{V}$ and $V_{wall} = 160\,\text{V}$[7]. Furthermore, the calculated maximum and minimum of the trapping potential are indicated with red triangles.

[7] These values are used to demonstrate the main features of the potential shapes.

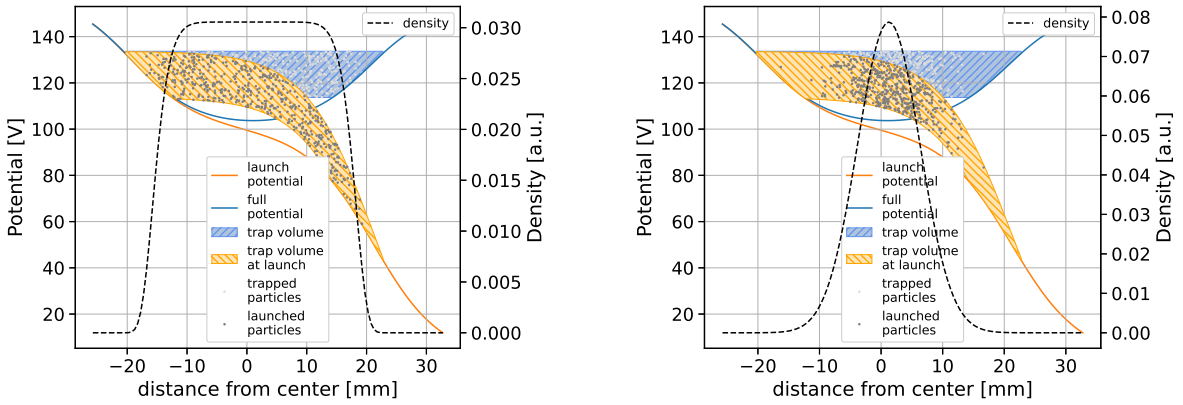

(A) Assuming distribution consistent with thermalised plasma.

(B) Assuming distribution consistent with not thermalised plasma.

FIGURE 6.18: A random sample of initial conditions of single species particles inside the trapping potential at $t < t_{launch}$ (light grey points) and at $t = t_{launch}$ (dark grey points). The shape of the particle density function used for generating initial conditions is shown as the dashed back line.

The dashed green lines show the whole available trapping region, while dotted purple lines indicate the area limited by selecting *spacecharge_min_V* = 10 and *spacecharge_min_V* = 30. The shaded areas indicate regions available as initial conditions for trapped particles (in blue) and particles at launch (in orange).

4. Generate initial conditions for particles. Using a generalised Gaussian distribution, generate $N_{iterations} \times N_{particles}$ random z-position. And, according to uniform distribution, generate $N_{iterations} \times N_{particles}$ random initial potential values based on the potential at $t = t_{launch}$.

FIGURE 6.18 shows samples of initial conditions calculated for particles assuming *thermalised* (left) and *not thermalised* distributions. The shape of the density distribution function used for generating a random sample in the z-direction is shown as dashed lines.

5. Calculate velocities as a function of z-position. For each particle, its velocities are calculated along the distance between its initial position z_i and the detector. Velocity $v_{z_i}(z)$ of a particle with initial conditions $(z_i, V|_{z_i})$ is calculated based on equation 6.9:

$$\frac{1}{2}mv^2 = q\Delta V \rightarrow v(z)|_{z_i} = \sqrt{\frac{2q\Delta V(z)|_{z_i}}{m}} \tag{6.13}$$

where

$$\Delta V(z)|_{z_i} = V|_{z_i} - V_{launch}(z). \tag{6.14}$$

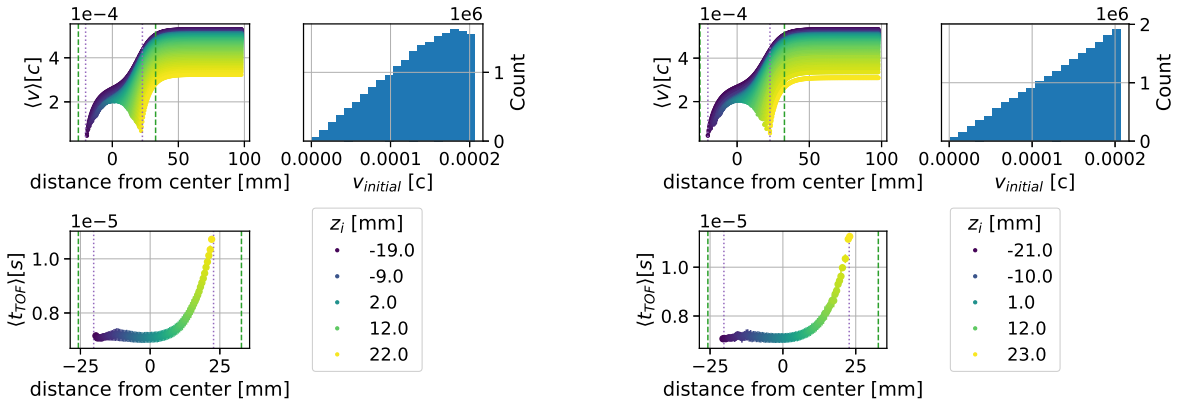

(A) Assuming distribution consistent with thermalised plasma.

(B) Assuming distribution consistent with not thermalised plasma.

FIGURE 6.19: Calculated average velocities (top) and TOF times (bottom) as functions of the distance from the MCP.

6. Calculate t_{TOF} for each particle. For each calculated velocity $v(z)|_{z_i}$ I calculate the step-time dt from

$$dt(z)|_{z_i} = ds/v(z)|_{z_i}, \tag{6.15}$$

where ds is the small distance the particle travels in the z-direction in a single step. $ds = 0.5$ mm was used in all calculations in this thesis. The total time $t_{TOF}|_{z_i}$ is then calculated as:

$$t_{TOF}|_{z_i} = \sum_z dt(z)|_{z_i} \tag{6.16}$$

7. Calculate the TOF signal by binning t_{TOF}. The final step is to create the signal based on the arrival times of the particles at the detector. All $t_{TOF}|_{z_i}$ for a single iteration are grouped into bins of size *tof_dt* (it is a parameter of the program). For this thesis, *tof_dt* of 1 ns was used. The signal for each bin is calculated as the average number of entries in the bin over all iterations ($N_{iterations}$) divided by the number of particles in each iteration ($N_{particles}$). The uncertainty of the signal is calculated as the standard deviation of the count divided by $\sqrt{N_{iterations}}$.

FIGURE 6.20 shows final simulated TOF signals for $\overline{\text{p}}$ released from a trap with $V_{floor} = 100$ V and $V_{wall} = 160$ V with either *thermalised* (left) or *not thermalised* (right) distribution in z-direction.

8. Sum signals from multiple species. Steps 4-7 are repeated for each particle species in the trap. The final signal is then calculated as the sum of the signals from each species scaled by a weight describing how much a given species contributed to the overall signal (in the case of fragments obtained from the GEANT4 simulations, the fragment's trappable yield is used as its

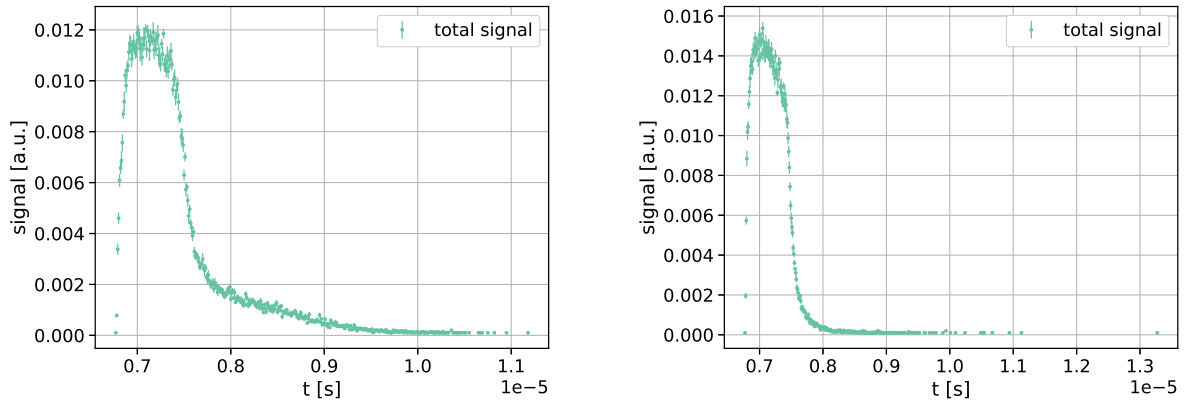

(A) Assuming distribution consistent with thermalised plasma.

(B) Assuming distribution consistent with not thermalised plasma.

FIGURE 6.20: Example simulated TOF signal of $\overline{\mathrm{p}}$ assuming $V_{floor} = 100\,\mathrm{V}$ and $V_{wall} = 160\,\mathrm{V}$ and *thermalised* (left) and *not thermalised* (right) trapped fragments. The *not thermalised* TOF spectrum is narrower (the distribution reaches higher signal values). There is a more evident tail in the *thermalised* signal, which suggests that slower particles are present.

weight):

$$S_{total}\left(t\right) = \sum_{i}^{N} W_{X_i} \cdot S_{X_i}\left(t\right), \tag{6.17}$$

where N is the number of different fragments, $S_{X_i}\left(t\right)$ is the signal at t from fragment X_i, and W_{X_i} is the fragment's weight.

Initial validation of the model was done against the experimentally measured TOF signals for electron-cooled antiprotons (the validation results are available in Appendix H). It was demonstrated that the primary characteristics of the spectra (the maximum position and the peak width) can be accurately reproduced using this model. However, the shapes don't perfectly match experimental data. This result can be attributed to severe assumptions made, likely due to the 1-D nature of the model, and the estimated spatial and potential distributions used for calculating the initial condition of particles, which are the two most significant factors. The model can be improved by expanding it to a full 3D description of the electric potential, which will allow for the calculation of the distribution of real particles inside the trap, assuming a specific initial temperature of the plasma.

FIGURE 6.21 shows simulated TOF signals for trappable fragments from annihilation of $\overline{\mathrm{p}}^{40}$Ar with *thermalised* (left) or *not thermalised* (right) distribution. Different values of the minimum of the spacecharge are also compared, where the values of *spacecharge_min_V* were varied between rows in the figure, while the maximum trapping potential was used as *spacecharge_max_V*

parameter. When using higher *spacecharge_min_V*, the peaks became easier to distinguish. However, when using the *not thermalised* distribution, the contribution of some fragments is more pronounced in the total spectra. This sharpness of spectrum suggests that the distribution used for *not thermalised* fragments doesn't reflect reality.

More experimental data are needed to benchmark this model, along with a good understanding of the distribution of species inside the trap and their thermodynamics. Another approach to testing the model would be to calculate the distribution under different assumptions analytically.

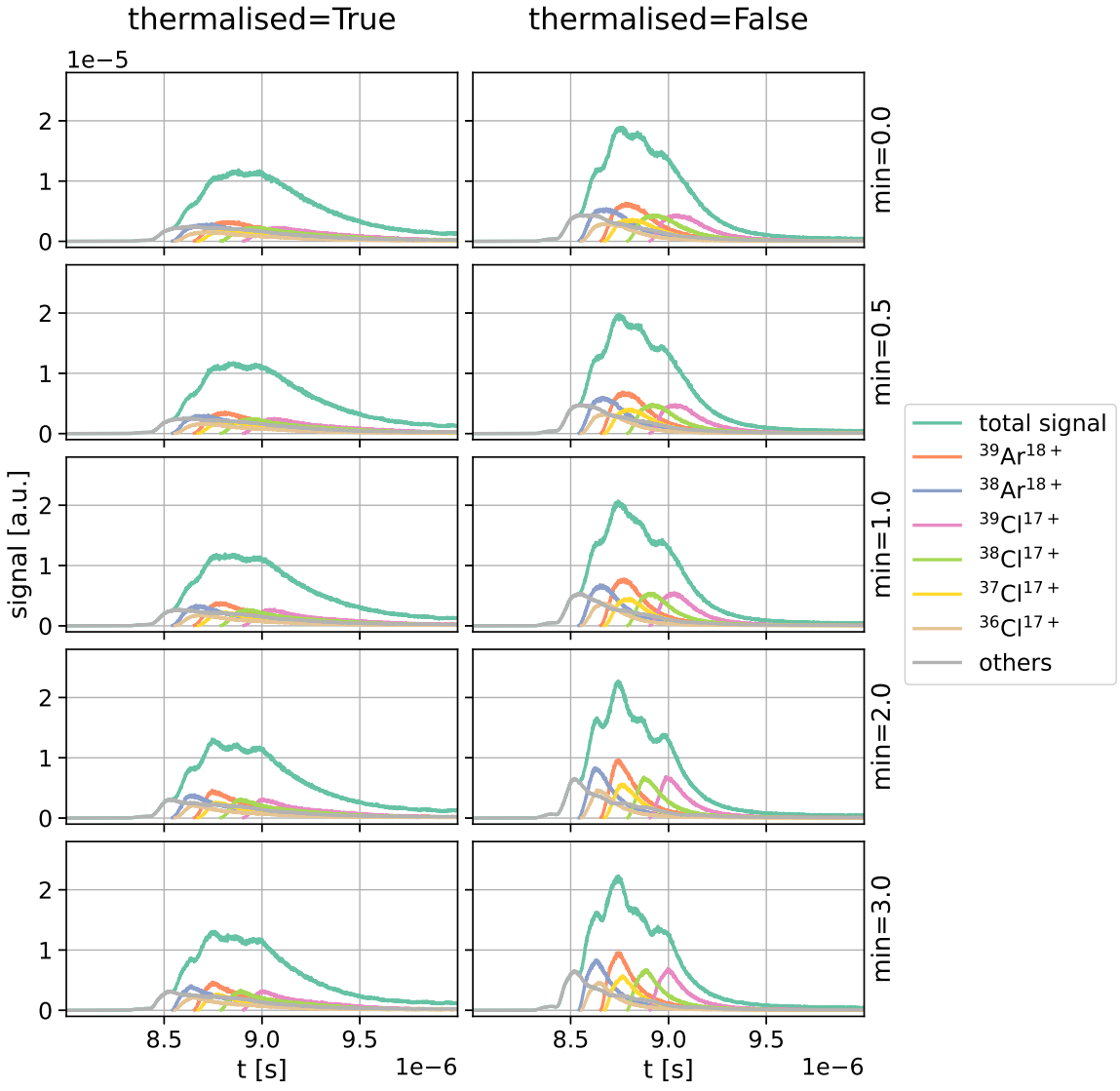

FIGURE 6.21: Total simulated TOF signal, as a sum of signals from all fragments, from $\overline{p}^{40}Ar$ is shown as a teal curve. The TOF signal of 5 fragments with the highest yields is shown as different colour lines, while the grey curve shows the TOF signal from the remaining fragments as a sum of the signals. Different signals are shown as obtained with the *thermalised* flag True or False as columns and different minimums of *spacecharge* used as rows.

Chapter 7
Experimental control and sequencing

The following chapter describes procedures used at AEgIS for plasma manipulation that are related to experiments reported in this thesis. I performed the following tasks related to the plasma manipulation:

- *Development of communication between AEgIS and ELENA for steering of all correctors in the beamline.*
- *Development of the plasma squeezing procedure.*
- *Development, alongside Dr M. Volponi and Dr S. Huck, of the nested-trap trap procedure.*
- *Implementation of some trapping configurations for the nested-trap experiments.*
- *Implementation, alongside Dr M. Volponi, of the TOF technique for HCI experiments at AEgIS.*
- *Development of the HV scan procedure for measuring the energy of positive ions trapped in the nested-trap experiments.*

The AEgIS apparatus is a versatile experimental environment that enables the execution of various experiments using antiprotons and positrons. Each experiment is defined as a single ARTIQ script. The scripts define a sequence of different operations, including moving actuators, preparing detectors, controlling valves, and operating particle traps for plasma operation.

This chapter explains the most important sequences that were used at AEgIS to perform various measurements. The first section focuses on the primary operations that include the whole experiment. These basic functions can be expanded for more complex experiments by adding particle manipulation of the trap potentials. The second section provides a more detailed description of some of the trap operations that can be performed with the AEgIS setup.

7.1 Standard antiproton operations

7.1.1 Beam steering

The ELENA decelerator complex provides access to fine-tuning the steering of the antiproton bunch into the experimental area. In the AEgIS, the parameters can be set directly from the experimental script. The steering is performed with 20 electrostatic correctors. There are 6 pairs of dipole (3 for horizontal and 3 for vertical deflection), and 4 pairs of quadrupole correctors.

The dipole correctors can have potentials of ± 1500 V, where each pair, either right and left for horizontal or top and bottom for vertical, accepts the same value but with opposite sign. The quadrupole corrector works with potentials ± 6000 V. The pairs are made of correctors with positive and negative potentials. Therefore, the beam steering can be defined with 10 parameters that set the potentials on 20 correctors.

7.1.2 Passthrough

The most standard operation that can be performed with antiprotons is the *Passthrough*, which lets the antiprotons pass through the experiment. This procedure is used to determine the status of the antiproton beam inside the experiment.

The standard operation of the *Passthrough* is as follows. Firstly, the parameters for the beam steering are set. Next, the actuators are moved to correct positions. This process involves removing the electron gun and any other actuator that could collide with the degrader, and then inserting the degrader(s) as required. Next, the detectors are set up. The PMTs of the scintillators are turned on to measure any annihilations of antiprotons in the experiment. The MCP detector at the experiment's exit (in the 1T region) is prepared to measure the spatial distribution of antiprotons passing through it. The oscilloscopes connected to the MCP and the degrader are configured to measure the charge deposition in time. After all the detectors are configured, a high-voltage potential can be set on the HV3 electrode (with up to −15 kV). This electrode works as a deflector for the antiprotons. With the MCP placed after the electrode, it is possible to estimate the number of antiprotons with energy higher than the used potential. After all the preparatory actions are finished, the experiment waits for the first trigger from ELENA. This trigger arrives approximately 30 s before the bunch is delivered to the experiment. At this point, voltages for some detectors are turned on to minimise the time high-voltage is present on the delicate equipment. The experiment waits for the second trigger to arrive. This trigger arrives together with the antiproton bunch. At this point, all the previously set detectors are triggered, and the experiment is finished. In the closure procedure, all the high voltages are turned off.

7.1.3 Catch&Dump

The *Catch&Dump* procedure is similar to the *Passthrough*. However, in this procedure, the high voltage on the HV3 electrode is prepared in advance (before the first trigger arrives). The HV1 electrode is connected to a fast high-voltage switch that allows for applying the potential from 0 V to −15 kV in tens of nanoseconds. The switch is triggered with some delay after the second trigger

from the ELENA. After antiprotons enter the experiment, they are deflected by the HV3. Then, after the HV1 is raised and the antiprotons are reflected again, trapping them between the two high-voltage potentials. The delay was experimentally measured (with the help of the optimiser, see sections 5.4.1 and 9.1.1) for the highest antiproton capture rate. The 1T MCP is triggered at the arrival of antiprotons. This detection provides additional monitoring for the losses of antiprotons during capture due to the too high energy of particles.

After the trapping is established, the antiprotons are stored in the trap for some time. This time is referred to as *hot storage* because no active cooling is provided for the antiproton plasma. After the hot storing is complete, the antiprotons are released from the trap. The dumping of antiprotons from the trap is performed via a slow ramping down of the HV1 electrode (the operation takes approximately 12 s to ramp down to zero from a −15 kV potential). This operation is called "slow hot dump[1]." The antiprotons are released on the degrader, where they annihilate. The signal of the annihilations is captured by the scintillators, which provides an estimate of the number of antiprotons in the trap. After the ramping is done, the HV3 electrode is also ramped down. The slow extraction of antiprotons limits the possibility of overexposure of scintillators.

7.2 Trap sequences

7.2.1 Antiproton electron cooling

Electron cooling is a process in which plasma of antiprotons and electrons is trapped together and mixed, leading to the cooling of the antiproton plasma via the elastic collisions between antiprotons and electrons [140]. The electrons can be kept at temperatures near 4 K. When $\overline{\mathrm{p}}$ cloud overlaps the electrons, particles of the two species collide, reaching thermal equilibrium at some intermediate temperature.

To perform the electron cooling of antiprotons, electrons are first loaded into the trap. A small potential well is created between electrodes P4 and P8 with a positive potential of 150 V. Furthermore, the downstream electrodes P9-P11 are set to −180 V to create a potential barrier for incoming electrons. The electrons are inserted from the electron gun [63]. They are reflected from the potential barrier and lose energy by colliding with incoming electrons. The electrons that lose enough energy are then trapped inside the potential well. This process takes about 14 s, which fills the well up to the space-charge limit for electrons, containing approximately 10^7 particles. FIGURE 7.1 shows the trapping potential for the electron loading procedure.

[1] It's slow because the HV electrode is ramped down over seconds, while hot refers to lack of cooling for trapped $\overline{\mathrm{p}}$ s

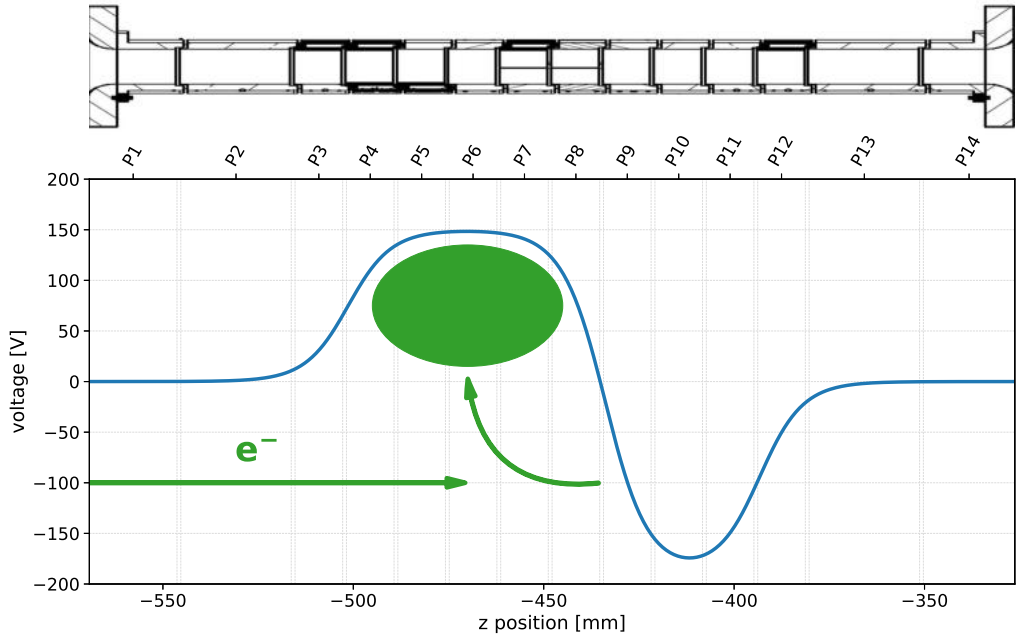

FIGURE 7.1: Potential shape used for loading electrons to the P-section of the 5T trap at AEgIS. The schematic overview of the electrodes (from FIGURE 5.8) used in the procedure is shown at the top.

Afterwards, the antiprotons are captured, as described in the *Catch&Dump* procedure in the previous section, between the high-voltage electrodes HV1 and HV3. The electrons sympathetically cool the antiprotons via the elastic collisions between the particles. The cooled antiprotons fall into the same potential well as electrons. The schematic overview of the cooling procedure is shown in FIGURE 7.2. After about 30 s[2] of cooling time, the high-voltage electrodes are ramped down, removing any uncooled antiprotons (the cooling between particles happens only in the overlapping region between two plasmas). At this step, the rotating wall technique [86] can be applied to compress the $\overline{p}$ plasma.

The last step is to "raise" the trap. The electrodes P3 and P9 (which create the walls of the potential well) are raised to −180 V potential, and the trap floor (electrodes P4-P8) is raised to −10 V. This configuration is referred to as "ready to dump." With this setup, the particles experience the same trapping potential; however, by simply lowering one of the walls, the particles experience a gradient from slightly negative to zero, which forces particles to leave the trap. In this way, the particles can be launched and measured on one of the detectors.

[2] This value can be specified as a parameter to the script.

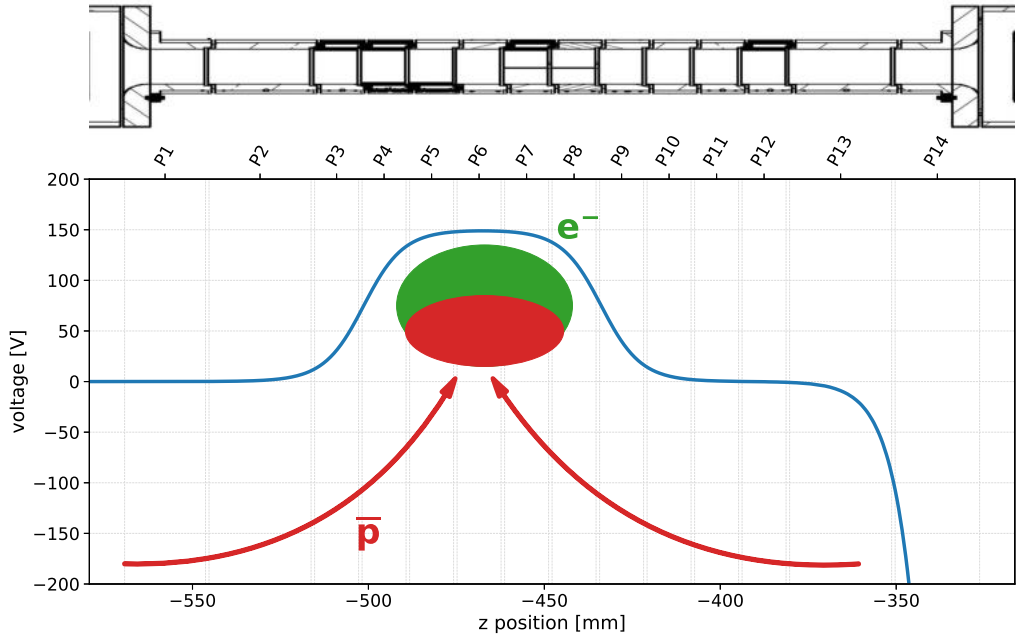

FIGURE 7.2: Potential shape used for electron cooling of antiprotons in the 5T trap at AEgIS. The antiprotons are trapped between the HV1 and HV3 electrodes, which are positioned in the P-section of the 5T trap. Cold antiprotons are trapped together with electrons in the P-section. The schematic overview of the electrodes (from FIGURE 5.8) used for accumulating cold antiprotons is shown at the top.

7.2.2 Nested trap for antiprotonic atoms

The antiprotons and electrons have the same electric charge, which means that the same trap can be used to confine both species. However, fragments produced in the antiproton-induced fission are positively charged. Therefore, a special configuration needs to be created to trap the resulting fragments. This configuration is referred to as the "nested trap," as it creates a positive potential well for positive fragments within the negative potential well for antiprotons. The potential of this configuration is shown in FIGURE 7.3. This configuration is used to trap the fragments produced from the interactions of antiprotons with the rest gas inside the trapping region. The method for controlling the formation of antiprotonic atoms and subsequently trapping the fission fragments is under development.

The production of highly-charged ions (HCIs), as described in chapter 4, starts with trapping of cations or anions inside a trap. Alternatively, the trap can be filled with neutral atoms (rest gas). This approach allows for the establishment of trapping the produced fragments with a more straightforward method; however, the production of antiprotonic atoms becomes random, due to interactions of $\overline{p}$ with the residual gas. The initial experiments performed in AEgIS were done

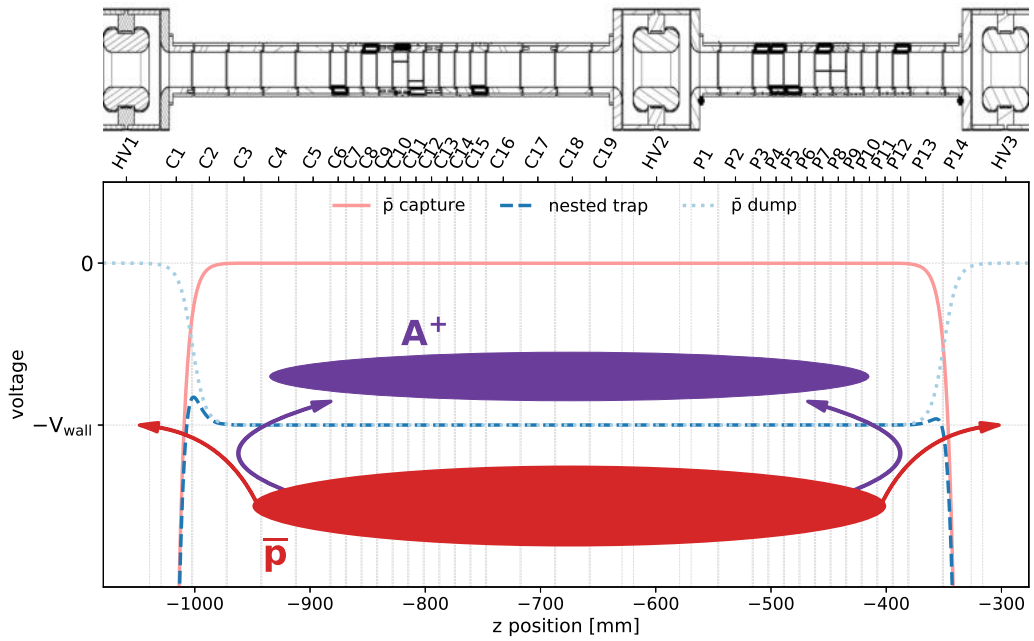

FIGURE 7.3: The potential for the nested trap configuration. Antiprotons are trapped by the HV potential applied on HV1 and HV3 electrodes (red line). Afterwards, the nested trap is created by setting all in between electrodes to -V_{wall} potential (dashed, blue line). Some cations A^+ produced from annihilations of antiprotons are trapped in the middle potential. Finally, antiprotons are released by lowering the HV electrodes (dotted blue line). The schematic overview of the electrodes (from FIGURE 5.8) used for the tested trap configuration is shown at the top.

with the rest gas setup, and the nested trap procedure was developed for this purpose.

The nested trap starts with the trapping of the antiprotons between the HV1 and HV3 electrodes. Given the presence of the rest gas inside the trap, the antiprotons are expected to undergo annihilations with the rest gas. Antiprotons interact with the gas through elastic collisions. The antiprotons lose energy, which leads to the capture of the antiproton by the nuclei of the gas, which ends with the annihilation and the possible fission of the nucleus.

The lifetime of the trapped antiprotons [3] is estimated experimentally by trapping antiprotons for long periods and measuring annihilation rates until all antiprotons are gone. The time corresponding to the maximum annihilation rate observed is taken as the lifetime of $\overline{p}$ s in the trap. This lifetime depends on the vacuum conditions inside the trap. When the trap is filled with a rest gas, such as nitrogen or argon, the lifetime decreases in proportion to the pressure of the introduced gas. Antiprotons are stored between HV electrodes for the duration of *pbar_cooling_time*,

[3] The average time for an antiproton before it annihilates on the gas inside the trap.

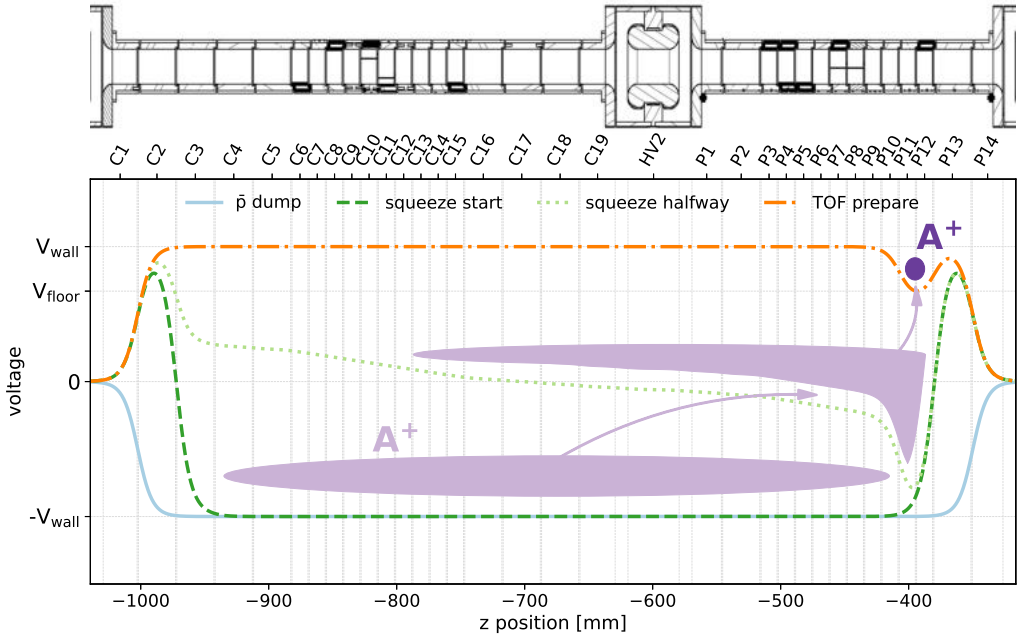

FIGURE 7.4: The potential sequence for preparing trapped cations for TOF measurement. Cations A^+ are squeezed into a smaller trap in the Ptrap section of the 5T trap. The schematic overview of electrodes (from FIGURE 5.8) used in the squeezing procedure is shown at the top.

which should be similar to, or slightly less than, the estimated lifetime of trapped antiprotons. Subsequently, the nested trap is formed by raising the potential on electrodes between the HV1 and HV3 to −190 V. This configuration remains for the duration called *ion_accumulation_time*. During this time, antiprotons annihilate with the gas and the produced fragments are trapped in the potential well. Then the high-voltage electrodes are lowered to release all the antiprotons that didn't annihilate. Next, the two end electrodes of the nested trap (C2 and P13) are raised to positive potential up to 195 V. Then the trap is squeezed, moving the ions to a smaller trap between electrodes P9 and P13. This process is shown in FIGURE 7.4. Then the floor of the trap (electrodes P10, P11, and P12) is all raised from −190 V to some positive potential that is called "launch potential" as it defines the potential used for the time of flight measurements (see section 7.2.3). The final potential for the ion trapping is shown in FIGURE 7.5.

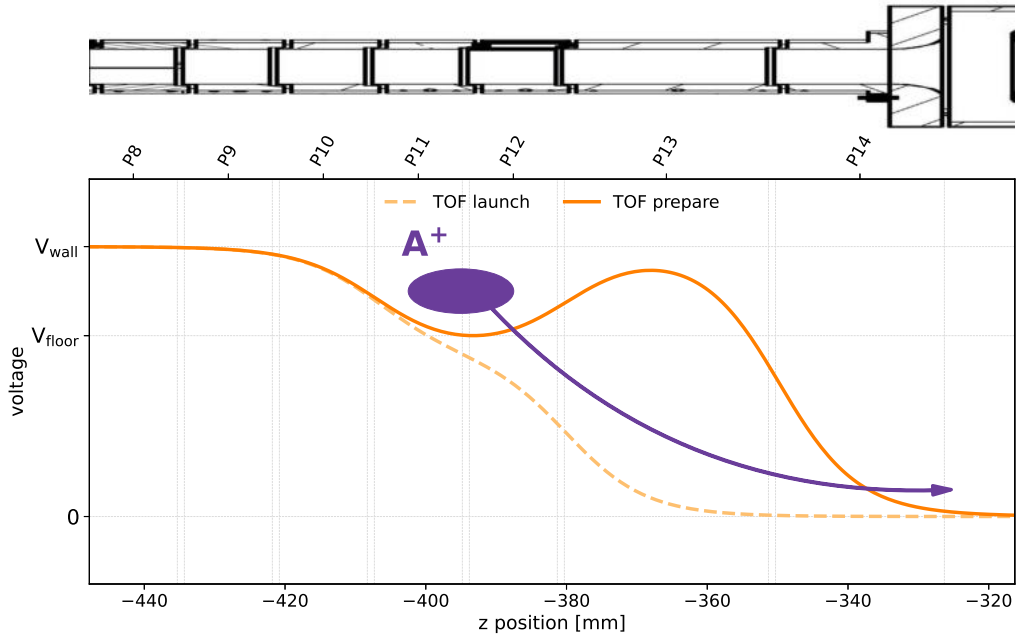

FIGURE 7.5: The potential sequence for performing TOF measurement. Cations A^+ are released from the trap by a quick pulse of *P13* electrode and travel towards the MCP detector. The schematic overview of the electrodes (from FIGURE 5.8) used in the TOF measurement is shown at the top.

7.2.3 Time of flight measurement

To perform the TOF measurement at AEgIS, a trap with potential is defined such that one of the endcaps is realised by electrodes that are connected to the pulser[4]. The particles are released from the trap by pulsing the endcap electrode, causing them to be released towards one of the MCP detectors. The detector is connected to a "Captorius" oscilloscope (via a readout circuit between the phosphor screen and the scope), which is triggered simultaneously with the pulsing of the electrodes. The particles hitting the MCP are measured as the charge deposition on the phosphor screen of the MCP, and the TOF signal is then acquired using one of the oscilloscopes.

Several factors influence the TOF signal. Firstly, as equation 6.9 states, the floor potential V_{floor} plays a leading role. This potential defines the expected velocity for each fragment. Secondly, the length of the trapping region is essential. As the TOF depends on the distance travelled to the detector, the longer the trap, the bigger the uncertainty in the TOF signal. Finally, the initial velocity distribution of fragments inside the trap must be considered. The time for fragments leaving the trap in equation 6.9 assumes that particles start from the trap with velocity $v_0 = 0$.

[4]At the time of writing this thesis, these electrodes were: C5, C6, C16, P2, P3, and P13.

However, the fragments are expected to have non-zero initial kinetic energy. The temperature of the trapped fragments gives an estimate of their kinetic energy. That's why it is essential to apply cooling mechanisms to the fragments inside the trap to achieve better resolution of the TOF spectra. When taking into consideration the initial kinetic energy E_i of fragments, the equation 6.9 becomes:

$$t = l\sqrt{\frac{M}{E_i + 2V_{floor}Ze}} \tag{7.1}$$

where l is the distance between the centre of the trapping region and the MCP detector. During measurements with a nested-trap setup, this distance was estimated to be $l = 1.05(1)$ m, which was experimentally verified from TOF measurements performed with $\overline{\text{p}}$.

Chapter 8
Data analysis

The following chapter describes the data structure and processing of the data from the simulations and experimental measurements. I was responsible for the following tasks:

- *Preparation and formatting of the data from simulations of degrader efficiency.*
- *Preparation and formatting of the data from simulations of antiproton-nucleus interactions.*

This chapter describes the pre-processing performed on the data to establish a standard format and estimate the uncertainties. The bronze-to-silver pipeline in the ALPACA handles these processes for the experimental data. Initial data formatting from the simulations was performed with ROOT [141] to access the data returned by GEANT4 [105]–[107]. The final data analysis performed in this thesis utilises Python tools. In particular, three packages were used: seaborn [142], scipy [143], and polars [144].

8.1 Data processing of results from simulations

8.1.1 Degrader efficiency

Each simulation returns a single ROOT file that includes three ROOT branches:

- *fPosition* (x^i, y^i, z^i) - position in mm of the i-th antiproton leaving the second degrader foil.
- *fMomentum* (p_x^i, p_y^i, p_z^i) - momentum in keV of the i-th antiproton leaving the second degrader foil.
- *fRunSummary*:
  - annihilation_events - total number of antiprotons annihilating on the foils.
  - normal_events - total number of antiprotons moving through the degrading system.
  - killed_events - total number of events that were stopped by the simulation due to errors.

All the results were combined into two parquet files. The first file contained the x and y positions and the momentum vector for all antiprotons leaving the second foil, along with the thickness of the Mylar and Parylene foils. The position of the foil can be inferred from the thicknesses.

Mylar foils were used only at the position of the main degrader. Table 8.1 shows the data type for each of the columns in the event-based parquet file.

Table 8.1: Formatting of the simulation results file.

Event based antiproton file						
mylar_nm	parylene_nm	x_mm	y_mm	px_keV	py_keV	pz_keV
uint16	uint16	float64	float64	float64	float64	float64

The second file contains the general statistics of the simulated foil combinations, including a summary of the simulated events and information about the number of different types of events (normal, annihilation, and killed). This information enables a detailed study of antiproton losses and trapping capabilities with various combinations of degrader foils and trapping potentials. Table 8.2 shows the data type for each column in the summary parquet file.

Table 8.2: Formatting of the degrader simulation summary file.

Summary file			
mylar_nm	parylene_nm	annihilation_events	normal_events
uint16	uint16	uint32	uint32

Each simulation was performed with 1.5×10^6 primary antiprotons shot into the magnetic field. Some of the antiprotons experienced unphysical behaviours due to the rough implementation of the magnetic field, which were considered wrong events and marked as *killed_events* by the simulation. These events include antiprotons being stuck in the magnetic field, i.e. moving perpendicular to the z-axis for over 50 steps, or antiprotons changing direction in z-axis to negative values (moving backwards) inside the magnetic field itself. Events in which the direction of motion was changed due to interactions of antiprotons with the foil were considered as normal events, as there is experimental evidence for the reflection of antiprotons by a solid material [145].

On average, the number of killed events for single foil simulations was 0.88(2) %, while for two foil simulations was 15(6) %. The increased number of killed events in the two foil simulations might be a result of antiprotons' transport through the first foil. An antiproton moving inside the foil undergoes scattering, which leads to a change in the direction of its velocity vector. After the antiproton exits the foil, the scattering stops as it moves inside a vacuum, and only the magnetic field influences its path. The first foil (thin degrader) is placed in a region of a weaker and non-homogeneous magnetic field. Therefore, the gradients in the field might change too abruptly between the steps of the simulation, which can result in the antiproton changing its direction of

motion by 180°. These events, however, aren't fully understood; therefore, they were marked as killed events and excluded from the analysis.

Two main quantities are of interest from this simulation. First is the percentage of antiprotons lost due to annihilations on the foils. The number of annihilations is expected to increase with the thickness of the foil(s). The second is the percentage of antiprotons that can be theoretically trapped, assuming a specific potential on the endcaps of the Penning-Malmberg trap. The goal of using the degrader is to decrease the energy of antiprotons so that they can be trapped inside the Penning-Malmberg trap. As the efficiency of the degrader increases with its thickness (to some limit), the number of antiprotons that can be trapped with a given potential should increase.

The two values estimated from the simulation are crucial for determining the optimal trapping conditions for antiprotons originating from ELENA. Both percentages are calculated as a ratio with respect to the total number of good events, that is *normal_events* + *annihilation_events*.

8.1.2 Fragmentation

The goal of the fragmentation simulation is to understand which nuclei can be accessed via the antiproton-induced fission. Furthermore, it is used to understand the existing models for simulating the process, and it provides means to validate and improve the models by comparing the results with the data.

Over 3000 different isotopes with atomic number $Z < 100$ were used as a target material in the simulation. Each simulation creates a single file with the fragments produced during the annihilation of antiprotons. The files are firstly created as the ROOT files with two[1] ROOT trees:

- *counter* - this tree saves information about the number of particles (*Nparticles*) produced by the antiproton capture-at-rest and the number of particles (*Nnuclei*) that are nuclei.
- *nuclei* - this tree saves information for each nucleus that was produced from the antiproton-induced fission. The information saved is:
  - *Z* - number of protons in the nucleus (atomic number),
  - *A* - number of nucleons in the nucleus (atomic mass),
  - *N* - number of neutrons in the nucleus,
  - *E* - kinetic energy of the nucleus in keV,
  - *EoverQ* - kinetic energy of the nucleus divided by the charge of the nucleus (the charge is assumed as the fully stripped ion)
  - *T* - lifetime of the nucleus as saved by the GEANT4

[1] The simulation can either save information about the nuclei or the particles produced from the annihilation

- *particles* - this tree saves information for each particle that is produced as a secondary of the antiproton capture-at-rest process (including nuclei). The information saved is:
  - *Name* - the name of the particle as defined in GEANT4,
  - *PDGEncoding* - the particle code as defined by Particle Data Group (PDG),
  - *PDGCharge* - the charge of the particle as defined by PDG,
  - *PDGMass* - the mass of the particle (in MeV) as defined by the PDG,
  - *PDGLifeTime* - the lifetime of the particle as defined by PDG,
  - *Energy* - the kinetic energy of the particle,
  - *LeptonNumber* - the lepton number of the particle,
  - *BaryonNumber* - the baryon number of the particle

The *counter* tree enables event-based analysis by saving information on how many entries from the *particles* and *nuclei* trees belong to each annihilation. The *particles* tree is used to perform comparisons of different values estimated from models, such as the number of pions produced from annihilation.

The *nuclei* tree is converted to a parquet file for simplicity of further analysis. The structure of the file is described in TABLE 8.3. The data is expanded so that each file contains two columns with information about the atomic number and mass of the target used in the simulation. This format enables a quick and straightforward analysis, as the files can be concatenated with each other. Furthermore, for each isotope, a reverse file was created to define the sources of the isotope of interest. The format of the sources file is the same as for fragments. All the columns have the same meaning as shown in TABLE 8.3. The files with sources are obtained by loading all the simulation results and selecting the entries with fragment columns that match the desired isotope. The algorithm is shown in the 8.1.2 code snippet. When using the files of sources, the event column is ignored. Furthermore, the lifetime column is replaced with the values corresponding to the lifetimes of the target isotope instead of the fragments [2].

```
import polars as pl
(pl.scan_parquet("*_fragments.parquet")
   .filter(pl.col("fragmentA").eq(197),
           pl.col("fragmentZ").eq(79))
   .collect()
   .write_parquet("Au197_sources.parquet"))
```

LISTING 8.1: The algorithm used to create the sources files for the ^{197}Au isotopes.

[2] The fragment columns in the sources file of any specific isotope are constant. Similarly, the target columns in the fragments file are constant.

TABLE 8.3: Formatting of the parquet file with results from the simulation of fragments. The same formatting is used for the file with the sources of the specified isotope.

Column name	Description	Value format
event	Id of the event for the target	uint32
targetA	Atomic mass of the target	uint16
targetZ	Atomic number of the target	uint8
fragmentA	Atomic mass of the produced fragment	uint16
fragmentZ	Atomic number of the produced fragment	uint8
energy_keV	Kinetic energy of the produced fragment	float64
energyOverQ_keV	Kinetic energy of the produced fragment divided by the electric charge of the ion, assuming full stripping	float64
excitation_keV	Excitation energy state of the produced isotope	float64
lifetime_s	Half-life of the isotope	float64

In all analyses of the fragments, the half-life and mass of the isotope are taken from the International Atomic Energy Agency - Nuclear Data Service (IAEA-NDS), obtained via their API [146]. The code used to download the data is shown in Appendix G. For the isotopes obtained from the simulation that are missing in the IAEA-NDS database, the half-time from GEANT4 is used, while the mass is calculated as $m = A \langle m_n \rangle$, where A is the atomic mass number of the isotope and $m_n = (938272.08816 + 939565.42052)/2$ keV c^{-2} is the average mass of a nucleon. Using the average nucleon mass adds an error to the calculated mass in the order of 1 % compared to using the atomic mass unit. This difference is negligible compared to the energy transferred to the nucleus from the annihilation of the antiprotonic atom. Moreover, there are 747 out of 4104 possible isotopes with missing mass in the database. Most of these are very unstable isotopes, laying on the peripheries of the nuclear stability landscape. Only five of these isotopes have a half-life of greater than 10^{-12} seconds. Therefore, the value used for the missing mass doesn't influence the conclusions and results obtained from simulations.

8.1.2.1 Uncertainty in isotope yields

The yields of specified isotopes are calculated as the number of isotopes produced divided by the total number of annihilation events simulated. The simulation is based on the Monte Carlo model for de-excitation of the nucleus after the capture-at-rest of antiprotons. The uncertainty of the count is calculated as $\sqrt{N_{isotope}}$, where $N_{isotope}$ is the count of the isotope. Furthermore, the models used for de-excitation are data-based; however, the experimental data for antiproton-induced nuclear fragmentation are scarce, especially for the heavier fragments. Therefore, the

additional 10 % uncertainty is added as the model-based error. The final error is calculated as:

$$\Delta N_{isotope} = \sqrt{(0.1 \cdot N_{isotope})^2 + \left(\sqrt{N_{isotope}}\right)^2}. \tag{8.1}$$

The count of isotopes is divided by the total number of annihilation events, which gives the uncertainty for the yield to be:

$$\Delta\text{yield} = \frac{\Delta N_{isotope}}{N_{events}}. \tag{8.2}$$

8.1.2.2 Uncertainty in neutron ratio and halo

The peripheral neutron halo factor is calculated based on the equation 6.5 [43]. The uncertainty of the halo factor is then:

$$\Delta f_{halo}^{periph} = \sqrt{\left(\frac{\sqrt{N(\bar{p},n)}Z_t}{N(\bar{p},p)N_t}\right)^2 + \left(\frac{\sqrt{N(\bar{p},p)}N(\bar{p},n)Z_t}{N^2(\bar{p},p)N_t}\right)^2} \tag{8.3}$$

Assuming that all produced fragments can be trapped, it is possible to calculate the ratio between the number of $\bar{p}p$ and $\bar{p}n$ annihilations for all events. The ratio can be calculated according to the equation 6.5, where $N(\bar{p},n)$ and $N(\bar{p},p)$ are events in which an antiproton annihilated with a neutron or proton, respectively. Experimentally, these values can be estimated by calculating the total charge of the fragments in each annihilation event. This value provides information about the total probability of the annihilation of an antiproton with a proton or neutron.

8.1.2.3 Optimal path for specified isotope

In section 4.1.1, an extension of the antiprotonic atom formation was described, which allows for using fragments of antiproton-induced fission as the target for subsequent fission. Given this method, it is essential to consider yields for different isotopes resulting from the multi-annihilation process.

The uncertainty for the yields is calculated as a simple sum of the uncertainties for each yield in the chain, with an additional 20 % of the final yield. This approach overestimates the uncertainties; however, given the complexity of the method, this approach to uncertainty is reasonable.

8.2 Experimental data

The data read by the detectors differs from the data that can be accessed via the simulations. Moreover, a single detector can be used for multiple observables and depending on the experiment performed, the meaning of the data changes. The following is a detailed explanation of the two main detectors and how the experimental data are handled.

8.2.1 ESDA

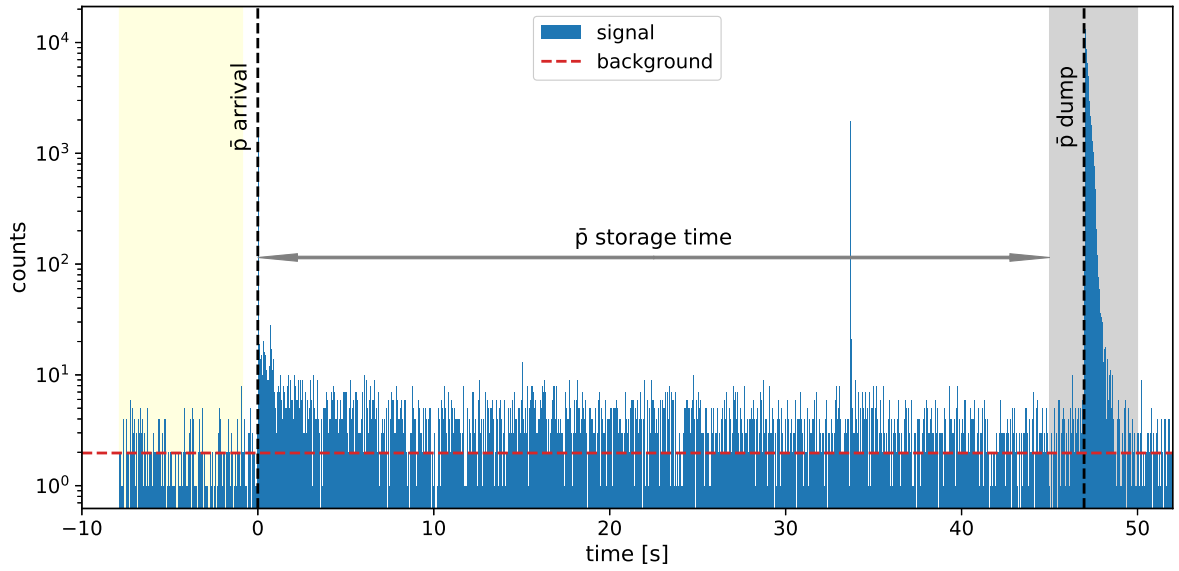

FIGURE 8.1: Example scintillator signal from SC56 in the form of a histogram (in blue). The grey region indicates the window for the signal coming from the dump of antiprotons on the degrader. The window starts after the $\overline{\text{p}}$ storage time since $\overline{\text{p}}$ arrival timestamp, and it has a fixed length of 5 s. The timestamps for $\overline{\text{p}}$ arrival and start of the $\overline{\text{p}}$ dump procedure are indicated with vertical, dashed, black lines. The background rate is calculated based on the first 7 s of acquired signal (guaranteed to be before $\overline{\text{p}}$ arrival timestamp). A yellow-shaded region indicates the background window. The background rate is indicated with a dashed, horizontal, red line.

Data from each scintillator in the ESDA detector is saved as a list of timestamps for the coincidence events in the PMTs of the scintillator. The scintillator signal is then binned into intervals of fixed time width. The uncertainty is then calculated for each bin as $\sqrt{N_i}$, where N is the number of entries in the given bin. The scintillator signal provides information about annihilation events that occur during the experiment.

Along with the scintillator data, a series of timestamps is saved. These timestamps are referred to as "sync checks" and record the precise times of specific operations within the experimental script (for example, the start of the script, the start of trap manipulation, opening the trap, etc.). These values are essential for analysing the scintillator data as they divide the data into segments that can be correlated to specific operations.

The AD is a source of constant background for the scintillators, as there are continuous annihilations of antiprotons all around the AD hall. Furthermore, the injection of antiprotons into the AD and then into ELENA creates massive spikes in the signal for the scintillators, as these events are sources of high-energy pions from the losses of antiprotons on the apparatus. The background for each scintillator is calculated as the first 7 seconds of the signal. As in that window, no operation is performed. The background can be calculated as:

$$bcg = \frac{\sum_{t=0}^{7\,s} N\left(t\right)}{7\,s}$$

which gives a rate in counts per second. The detector signal is then decreased by $bcg \times \Delta T$, where ΔT defines the time window in which the signal is calculated.

8.2.1.1 Estimation of number of trapped antiprotons

To estimate the number of antiprotons inside a trap using scintillators, a dedicated procedure called "slow cold dump" is used (see section 7.1.3). The antiprotons are dumped onto the main degrader of AE$\bar{g}$IS and annihilate. The beginning of the procedure is timestamped by one of the "sync check" signals. This time marks the beginning of the 20 s window, during which the sum of the events is calculated. This value is then corrected for the background. To convert this value to the estimate of antiprotons, a special conversion is used. The conversion is based on the GEANT4 simulation and was calculated for one of the scintillators called SC56[3], which is equal to 36.5 annihilations per count in the scintillator. To obtain the number of annihilations based on the other scintillators, a ratio of signals between scintillators SC34, SC1112, SC1516, and SC1920 was experimentally measured. TABLE 8.4 shows the measured ratios. The estimation from the SC is then calculated as:

$$N_{\bar{p}} \approx S_{SCX} \cdot C_{56} \cdot R_{SC56}^{SCX} = S_{SCX} \cdot 36.5 \cdot R_{SC56}^{SCX}$$

[3]The SC refers to the scintillator. The numbers refer to the two PMTs connected to the scintillator (in this case PMT 5 and PMT 6, similarly, SC1112 is connected to PMT 11 and PMT 12).

where the S_{SCX} is the signal from the scintillator of interest SCX, the C_{56} is the conversion factor calculated for the scintillator SC56 from GEANT4, and R_{SC56}^{SCX} is the experimentally measured ratio of the signals between SCX and SC56.

TABLE 8.4: Experimentally measured ratios of signals between the different scintillators and the scintillator SC56.

SCX	R_{SC56}^{SCX}
SC34	7.61
SC1112	10.10
SC1516	20.76
SC1920	19.44

8.2.2 MCP

The MCP signal is saved as an image of the phosphor screen. Moreover, the current on the phosphor screen can be recorded using an oscilloscope (see section 8.2.2.1). This image is saved as an intensity of the pixels in a 2D array. The intensity of the pixel is proportional to the charge deposition on the phosphor screen. The picture of the MCP is bigger than the active area of the MCP, which is useful, as it allows for subtracting the background of the image. Firstly, the signal is normalised by subtracting the minimum intensity value from the entire image. Then, the background is calculated as the average intensity on the edges of the picture. Then the image is normalised according to the formula:

$$px_{norm} = \frac{px - bcg_{mean}}{bcg_{mean}},$$

where the bcg_{mean} is the mean background of the image and the px is the intensity of the pixel.

The total signal of the MCP can then be calculated as the sum of the intensities of pixels over the entire image. Similarly, a portion of the signal can be defined by limiting the summing region.

8.2.2.1 Captorius

The data from the oscilloscope is saved as two arrays of voltages and times. The size of the arrays depends on the sampling rate used in the configuration. Then the data is binned into small time intervals dt. For the analysis of the HCIs, the time interval was equal to 100 µs, and the sampling rate was 100 000 points. This results in a resolution of 1 ns for measured signals. Subsequently, the data is binned into small time intervals dt. For nested-trap analysis, a standard bin size was

$dt = 10$ ns, which corresponds to 10 points per bin. The value for the point is calculated as the mean of the points, and the error is calculated as the standard deviation.

8.2.2.2 Analysis of TOF spectra of HCIs

The TOF spectra are used to estimate the mass-to-charge ratio of the trapped species. The background signal in the oscilloscope primarily originates from the impedance of the MCP's readout circuit, creating a sinusoidal background that is removed from the signal. Furthermore, the signals are represented as the absolute values, as all species have the same sign of the electric charge. The HCI spectrum consists of multiple peaks. After removing the background, each peak is fitted with the exponentially-modified Gaussian (EMG) function that is defined as:

$$f(x;\mu,\sigma,\lambda) = A\exp\left(\frac{\lambda^2\sigma^2}{2} - \lambda\left(x-\mu\right)\right)\mathrm{erfc}\left(\frac{\mu+\lambda\sigma^2-x}{\sqrt{2}\sigma}\right),$$

where μ and σ are, respectively, the mean and variance of the Gaussian distribution, and λ is the rate of the exponential component. Furthermore,

$$erfc\left(x\right) = 1 - erf\left(x\right) = \frac{2}{\sqrt{\pi}}\int_{\pi}^{\mathrm{inf}} e^{-t^2}dt$$

is the complementary error function. FIGURE 8.2 shows fitting of one of the peaks that later was identified as the He^+. After fitting each peak individually, the entire spectrum is re-fitted with a function which is a sum of EMG functions. FIGURE 8.3 shows the averaged signal of four HCI spectra (as blue points) with the final fitted function (in red). The maximum of each peak is then used as the TOF value, which is subsequently used to determine the $\frac{m}{Q}$ fraction.

8.2.3 TOF calibration

To determine the $\frac{m}{Q}$ fraction for each TOF value, a reference value is required. This value was initially obtained by performing the TOF measurement on electron-cooled antiprotons launched from a potential with $V_{floor} = 120$ V and $V_{wall} = 150$ V. However, for the final HCI spectrum, the TOF of the second peak, identified as He^+, is used as the reference. The mass-to-charge of the trapped ions is calculated from the reference as:

$$\frac{m}{Q}|_i = \left(\frac{T_i}{T_{ref}}\right)^2 \frac{V_i}{V_{ref.}}\frac{m}{Q}|_{ref}, \tag{8.4}$$

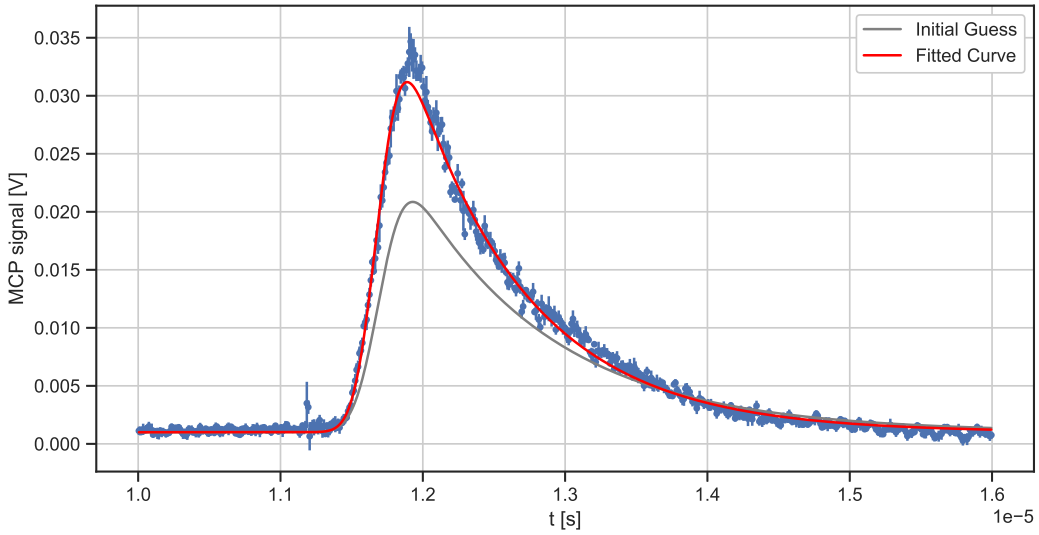

FIGURE 8.2: Example fit of a single peak from the HCI TOF spectrum of an average of 4 runs from antiprotons interacting with argon gas inside the Penning-Malmberg trap. The positive ions were launched from a potential with $V_{floor} = 180$ V and $V_{wall} = 190$ V. The data (in blue) is fitted with the Exponentially Modified Gaussian function. The final fit is shown as the red curve.

where T_i is the time measured i-th peak position on of the TOF spectrum, the V_i is the launch potential used in the measurement, V_{ref} is the potential used in the reference measurements, and $\frac{m}{Q}|_{ref}$ is the $\frac{m}{Q}$ of the reference particle ($\frac{m}{Q}|_{\bar{p}} = 1.00728$ u/e for antiprotons and $\frac{m}{Q}|_{\bar{p}} = 4.00260$ u/e for He^+). The measured reference TOF is $t_{TOF(\bar{p})} = 6.49(4)$ µs for antiprotons and $t_{TOF(He^+)} = 11.911(7)$ µs for He^+.

The uncertainty is separated into systemic and statistical components and is calculated as relative errors. The statistical uncertainty is calculated from the uncertainties in fitting the data and is defined as:

$$\frac{\Delta_{stat}\frac{m}{Q}|_i}{\frac{m}{Q}|_i} = \sqrt{\left(2\frac{\Delta T_i}{T_i}\right)^2 + \left(2\frac{\Delta T_{ref.}}{T_{ref.}}\right)^2}$$

where the ΔT_i and ΔT_{ref} are the uncertainties of the TOF for the i^{th} peak and the reference peak, respectively.

Similarly, the systematic uncertainty is calculated from the possible fluctuations in the potentials used for trapping. The error in potentials is assumed to be equal to ± 5 V. The systematic

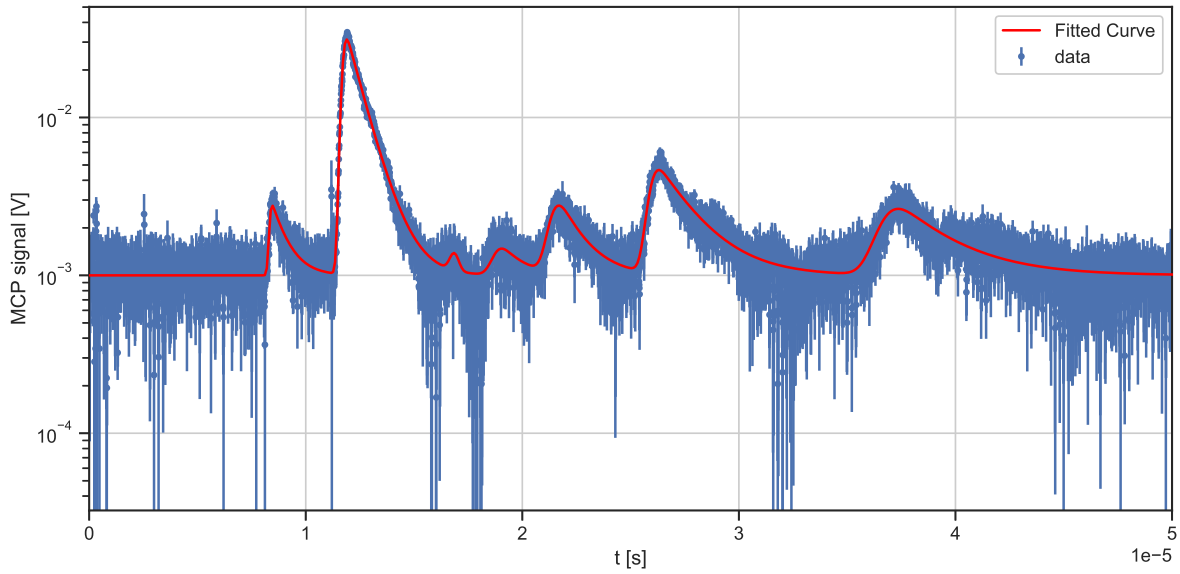

FIGURE 8.3: Example fit of a single peak from the HCI TOF spectrum of an average of 4 runs from antiprotons interacting with argon gas inside the Penning trap. The positive ions were launched from a potential with $V_{floor} = 180$ V and $V_{wall} = 190$ V. The data (in blue) is fitted with the Exponentially Modified Gaussian function. The final fit is shown as the red curve.

uncertainty is calculated from:

$$\frac{\Delta_{sys}\frac{m}{Q}|_i}{\frac{m}{Q}|_i} = \sqrt{\left(2\frac{\Delta V_i}{V_i}\right)^2 + \left(2\frac{\Delta V_{\bar{p}}}{V_{\bar{p}}}\right)^2}$$

with V_i and $V_{\bar{p}}$ are the potentials used for the TOF of fragments and the antiprotons, respectively.

Chapter 9
Results

The following chapter shows experimental results gathered by the AE$\overline{g}$IS Collaboration. All results presented in this chapter were obtained using the new control system, CIRCUS, which enabled reliable and stable operation of the experiment without significant downtime during the data-taking periods, and sometimes even in fully autonomous operation. Therefore, the new control system, of which I am one of the primary developers, has served as the basis for achieving these results. Furthermore, I actively participated in the data-taking process, often being responsible for creating and overseeing schedules of planned measurements.

Moreover, I developed trapping sequences used in both $\overline{H}$ production and HCI experiments. With the latter, I was also responsible for developing a comprehensive experimental script used for conducting experiments with a nested-trap setup.

I was responsible for performing the following analyses:

- *I characterised the degrading efficiency of different degradation stacks by comparing experimental measurements with predictions from simulations.*
- *Analysis of measurements from $\overline{p}$ interactions with the rest gas inside the Penning-Malmberg trap. In particular:*
  - *I estimated the cooling effects the Ar gas has on trapped antiprotons;*
  - *I compared the obtained TOF spectra with simulated prediction and characterised the trapped species captured in the nested trap experiments.*

The following chapter presents the experimental results collected by the AE$\overline{g}$IS Collaboration during the period covered in this thesis. Results are divided into three main sections. The first section describes the performance of the control system. Highlights of physics results from the AE$\overline{g}$IS Collaboration are showcased in the second part. The final section is related to the study of the interactions of antiprotons with the ^{40}Ar nuclei.

9.1 Control system performance

The new control system of AEgIS proved to be a capable tool when the experiment started using it back in 2021 during the development stage of the system. Thanks to the modular structure of the system, it could be used in the beginning with only a handful of µServices, including Scheduler and a single Monkey with a Kasli Wrapper. Since then, the system grew with many new µServices, but also new features.

One of the first tasks that the control system of AEgIS experiment must be capable of is trapping antiprotons. In this regard, the system performed exceptionally well. Thanks to the parameter-scan feature of the Scheduler, good parameters could be found for reliably trapping antiprotons from ELENA. Furthermore, in the following year, the trapping of antiprotons was established already on the first day of taking the beam, which proves the reproducibility of procedures of the CIRCUS system. Establishing $\overline{\mathrm{p}}$ trapping with the previous system would typically require over a week of intense work, with people working in shifts.

The most important feature of the system is its autonomous operation, which allows for performing experiments and collecting data over nights and weekends without constant supervision. Dr M. Volponi estimated the performance of the system in his thesis [62]. During the antihydrogen production campaign of 2023, which spanned 69 days, AEgIS acquired data for a total of 894.2 hours (about 54 % of the total beam time) in full autonomy thanks to CIRCUS. Furthermore, CIRCUS encountered 17 757 errors, which were correctly identified and handled. It was estimated that CIRCUS has saved over 280 hours of data-taking time and human interventions to address the errors.

9.1.1 Optimisation

The optimiser of the experimental sequences is done in AEgIS thanks to the new control system. The first optimiser test was performed on the beam steering of the antiprotons from ELENA into AEgIS. The maximum number of trapped antiprotons, as measured with the *Catch&Dump* procedure, was used as the optimisation goal. The optimiser controlled the 4 steering parameters accessible from ELENA: horizontal and vertical offsets and angles of the delivered beam of $\overline{\mathrm{p}}$. The results from the optimisation are shown in the FIGURE 9.1. The yellow region highlights the initial 30 exploration runs in which the parameters were randomly selected. A convergence criterion was defined to better illustrate the capabilities of the optimiser. It can be described as:

$$\left| \frac{\sigma_{10\ \mathrm{best}}}{\mu_{10\ \mathrm{best}}} \right| < \delta, \tag{9.1}$$

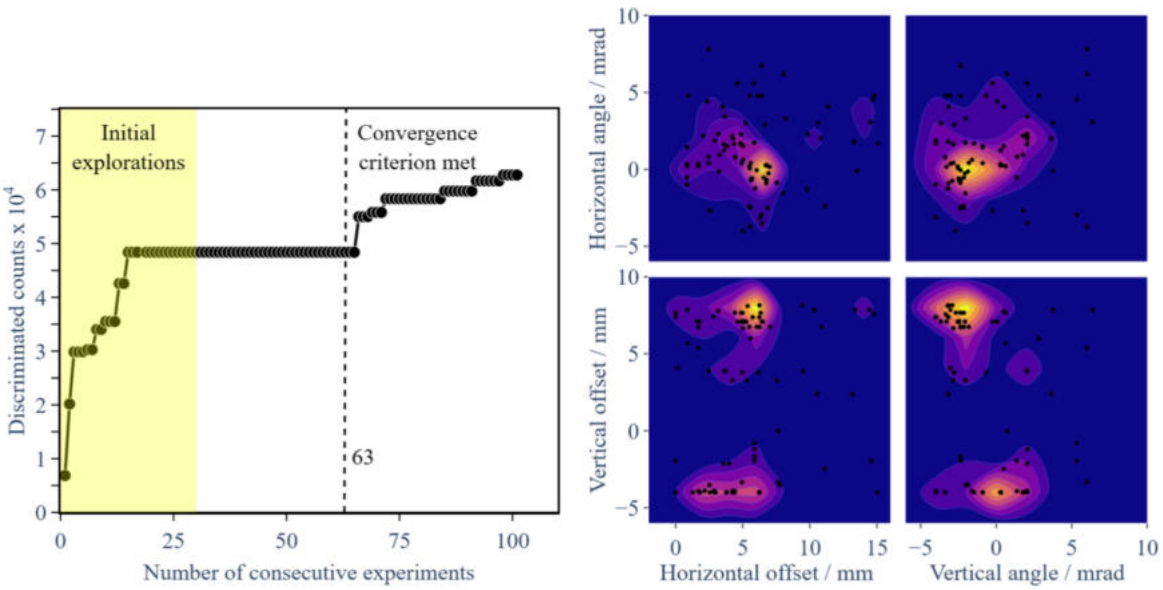

(A) The number of annihilations counted after

(B) Beam steering parameter landscape.

FIGURE 9.1: Results of the beam steering optimisation performed in AEgIS (taken from [62]).

where μ and σ are the mean and standard deviation of the 10 runs with the best optimisation score, and the δ is a threshold defined by the user. For the optimisation of the beam steering, the threshold was set to $\delta = 0.05$

In the shown example, the optimiser reached the convergence criterion after 63 total runs (including 30 explorations). After the criterion was met, the optimiser improved on the obtained values in the following 38 runs by ~ 23 %. This result shows that the criterion for the optimal beam steering could be stricter; however, the intensity of the antiproton beam provided by ELENA varied from bunch to bunch by up to 10 % at the time of optimisation, which could be a source of errors in the evaluation of the criterion.

The values obtained by the optimiser were in good agreement with the values obtained by performing the scan over the entire parameter space in previous years. To perform the scan, the parameters were restricted to values within the ranges −3 mm to 3 mm for offsets and −3 mrad to 3 mrad for angles. The parameters were scanned with a step of 2 mm for offsets and 2 mrad for angles, which provides 4 points per parameter. This scan required 256 runs. Afterwards, a second scan was performed around the best values from the first scan. Already with the course (first) scan, it is evident that the optimiser performs more efficiently.

However, performing a parameter scan over the whole parameter space is challenging for the beam steering. The four values provided by ELENA, which experiments can set to steer the

beam, in fact, control 20 electrostatic correctors placed along the beamline towards the experiment. A complex relationship between the four parameters and voltages on the correctors limits the effectiveness of the steering, as the four parameters aren't independent (changing a single parameter updates many correctors, which can be rejected whenever a value on the corrector exceeds allowed limits). Because the optimiser proved to be time-efficient, it was decided to use the parameters of the correctors, effectively creating a 10-dimensional optimisation problem (correctors are steered in pairs, where one potential is positive and the other has the same magnitude with negative polarisation). Similar results were obtained in trapping efficiency by using the 10-D optimiser; however, the optimisation of the beam steering is regularly repeated to improve the beam steering and keep it optimised for $\overline{\mathrm{p}}$ trapping.

Since the optimiser is a reliable and efficient tool, it can be used in other applications. One example is optimising the trapping delay between HV electrodes, which is crucial whenever a new degrader system is introduced or the trapping potential is increased. Another task would be the optimisation of the pulse duration and delay of the laser for the positronium formation.

9.2 Main experimental results

All the hardware and software updates of the AE$\bar{\mathrm{g}}$IS apparatus throughout the last 5 years lead to many experimental results. All upgrades and results were reported in three technical reports at CERN [57]–[59] and two PhD theses [62], [63]. It is essential to note that the new control system, which was partially developed as part of this thesis's technical component, played a crucial role in achieving these results. Following, the main experimental results of AE$\bar{\mathrm{g}}$IS Collaboration are highlighted.

9.2.1 Positronium cooling

The most significant achievement of the AE$\bar{\mathrm{g}}$IS Collaboration in the last 5 years is the first-time demonstration of the laser cooling of the positronium [81]. The positronium was cooled by using a system of lasers to force the $1^3\mathrm{S} - 2^3\mathrm{P}$ transition. In the paper it has been shown that the cloud of positronium was effectively cooled by $\Delta T \approx 210(20)$ K, from initial temperature of $\sim 380(20)$ K to final temperature of $\sim 170(20)$ K. To achieve this cooling effect, a total of 11 cooling cycles were used within 70-ns-laser-Ps interaction.

To reliably perform the experiment, the nanosecond synchronisation provided by Sinara was crucial. Furthermore, the experiment required repeating experimental procedures with different sets of parameters, which often took hundreds of runs. CIRCUS played a crucial role in enabling

the physicist to execute the procedures efficiently, with special emphasis on the Scheduler and Kasli Wrapper.

This result was the first experimentally demonstrated laser cooling of positronium. The significance of the result was highlighted by its inclusion in the list of *Top 10 Breakthroughs of the Year in physics for 2024* by *Physics World* magazine [147].

9.2.2 Antihydrogen production

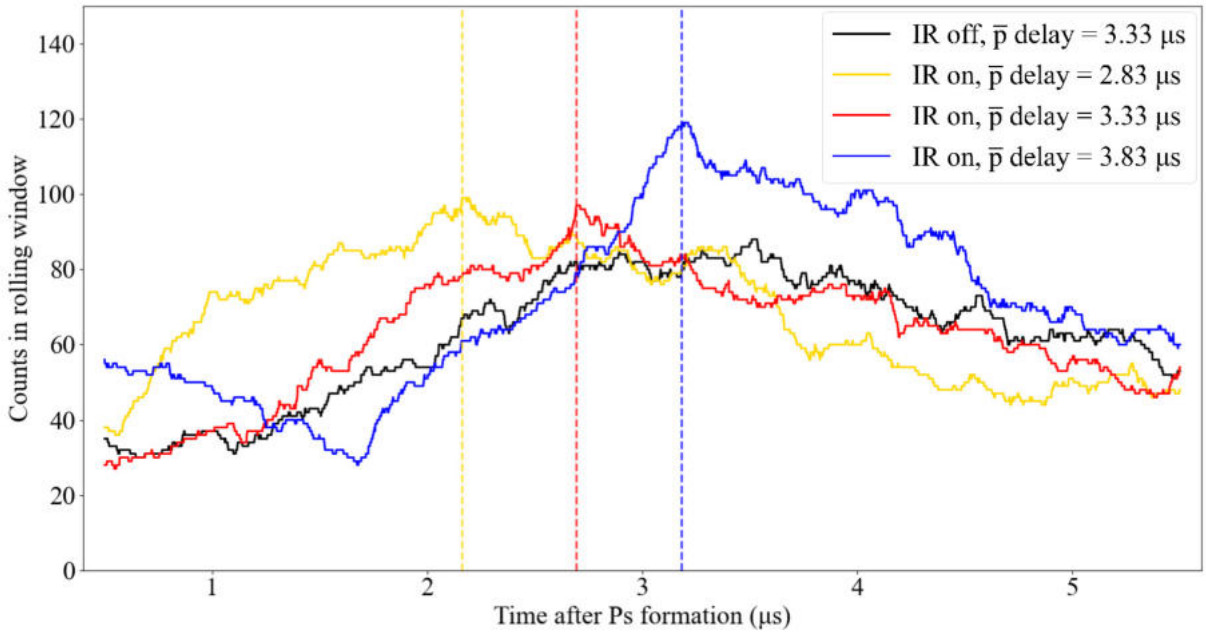

FIGURE 9.2: Coincidence counts treated as candidates for the $\overline{H}$ signal. The black lines were obtained from datasets where the Ps-Rydberg excitation laser wasn't present. The coloured lines were obtained from measurements with different synchronisation timings between antiprotons and positronium (yellow is 2.83 μs, red is 3.33 μs, and blue is 3.83 μs). The time difference between three excesses matches the time difference between synchronisations of antiprotons and positronium. Plot taken from [63].

The AEgIS experiment was the first experiment to produce $\overline{H}$ atoms in a pulsed beam scheme [79], which was achieved for the first time during the 2018 antiproton campaign at AEgIS. After changes to the antiproton delivery scheme in AD (with the introduction of ELENA) and the upgrades to the experiment, AEgIS began recommissioning of the antihydrogen production.

The steps taken towards recommissioning of the $\overline{H}$ production are outlined in the thesis of Dr M. Volponi [62]. The year 2023 was the first time the pulsed production of antihydrogen in the new scheme (with collinear positronium production) was tried at AEgIS. Furthermore, it was the

first time the production was tried with the use of CIRCUS. By the end of the 2023 $\overline{\text{p}}$ campaign, it was not possible to conclusively state any rate of production; however, with a refined data analysis process[1] prepared for the 2024 $\overline{\text{p}}$ campaign, the production of $\overline{\text{H}}$ in AE$\overline{\text{g}}$IS in 2023 was confirmed. FIGURE 9.2 shows the main evidence for production of $\overline{\text{H}}$ in 2023 datasets.

The 2023 dataset comprises approximately 1000 antihydrogen formation runs. The signals were corroborated with the preliminary analysis of 60 runs from the 2024 dataset. The preliminary analysis estimates a yield of ≈ 2 $\overline{\text{H}}$ per run. This result shows already an improvement in yield by a factor of 40 compared to the yields obtained during the demonstration of the method in 2018 [79]. This rate can be further improved by upgrading to a newer positron source with higher activity, which should provide an additional order of magnitude in $\overline{\text{H}}$ production.

The control system played a crucial role in the recommissioning of the $\overline{\text{H}}$ production at AE$\overline{\text{g}}$IS. Especially the introduction of the optimiser, which enabled higher efficiency in trapping antiprotons. Furthermore, the autonomous data collection performed by CIRCUS allowed for more time to be spent refining the analysis pipeline.

9.3 Efficient trapping of antiprotons

According to the GEANT4 simulation (see section 6.2.3), the best trapping efficiency is achieved with 1400 nm Mylar foil as the main degrader and additional foil of 100 nm Parylene. To test the predictions by GEANT4, the degrader ladder was introduced into the AE$\overline{\text{g}}$IS apparatus in 2022 [57] (see section 5.2.8). This device allowed the total thickness of the degrading stack to be varied by inserting one of five Parylene foils with different thicknesses before the main degrader.

All the foils used in the degrader setup of AE$\overline{\text{g}}$IS have uncertainty in their thickness of 10 %. Which means that the main degrader is 1400(140) nm. To validate the thickness of the foils, the *PassThrough* experiments (see 7.1.2) were performed in which the antiprotons pass through the degrader, fly through both 1T and 5T regions and are recorded on the MCP. By only raising a single HV electrode, the number of antiprotons can be limited to $p_z > |HV|$. It is assumed that the integrated signal of MCP is proportional to the number of $\overline{\text{p}}$ hitting the detector $I_{MCP} \sim N(\bar{p})$. Therefore, the signal recorded with the $HV = 0$ kV corresponds to the number of $\overline{\text{p}}$ that passed through the degrader.

FIGURE 9.3 shows the MCP signal (black dots) as a fraction of the average measured signal for $HV > -0.25$ kV[2]. The data is compared with the fraction of $\overline{\text{p}}$ with energy greater than the trapping potential, normalised to the total number of antiprotons that passed through the

[1] The scintillator-based detection system, rather than the MCP-based image analysis.
[2] The reading of the voltage on the high-voltage electrodes fluctuates.

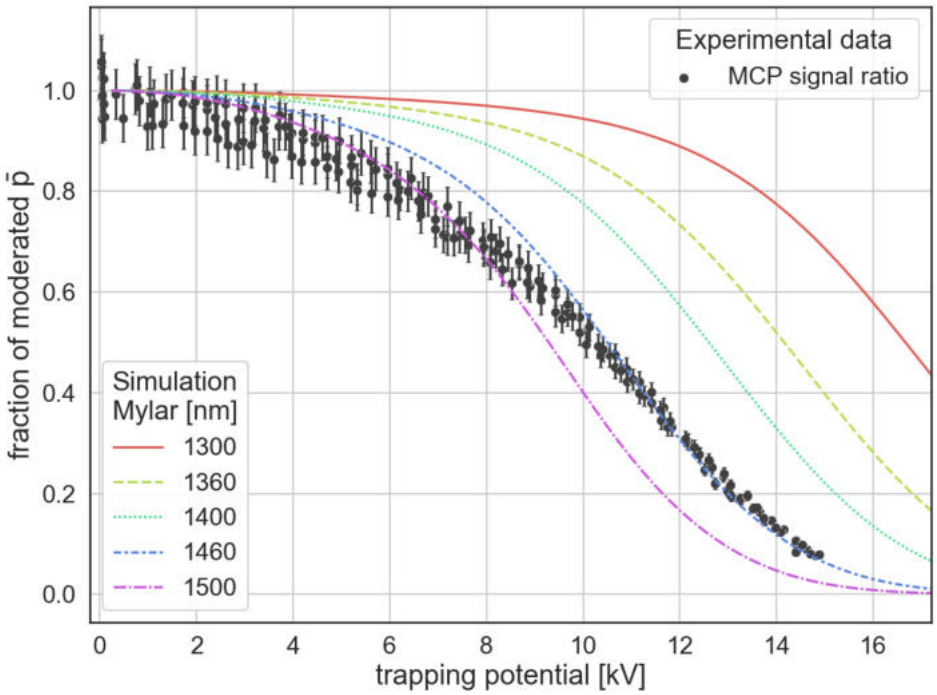

FIGURE 9.3: The ratio of antiprotons with energy higher than the trapping potential. Experimental data (black points) measured with the MCP positioned after the Penning trap and normalised to the measured value for trapping potential <0.5 kV. The simulation was normalised to the total number of antiprotons that passed through the degraders.

degrader. The results from the simulation are shown as a line plot in FIGURE 9.3, with different line styles corresponding to a different thickness of the Mylar foil used in the simulation. From FIGURE 9.3 it can be seen that the experiment data is in better agreement with simulated 1460 nm Mylar than expected 1400 nm Mylar used at AE$\bar{g}$IS; however, the experimental and simulated data diverge as the trapping potential is decreased. Moreover, the spread of the experimentally measured values increases with the lower trapping potential. The value of 1460 nm is within the expected degrader thickness of 1400(140) nm. The experimentally measured data suggest that the MCP signal is not necessarily linearly dependent on the number of particles. With the lower trapping potential, the expected number of $\bar{p}$ increases. Moreover, the particles hitting the detector have a higher energy spread, which can also play a factor in the measurements.

In the second test, $\bar{p}$ are trapped with *Catch&Dump* procedure (see 7.1.3). The antiprotons

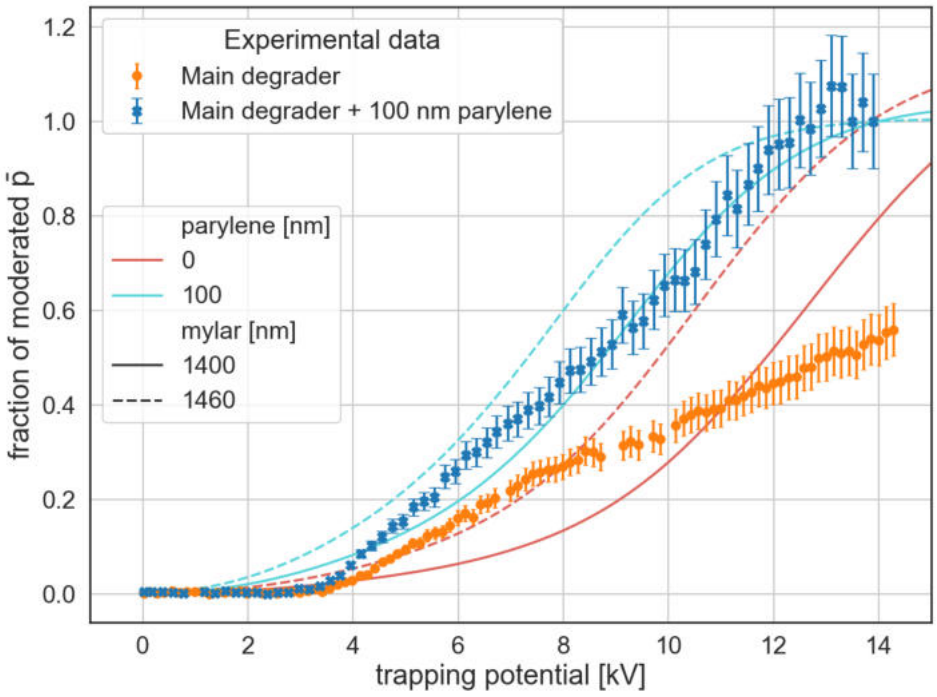

FIGURE 9.4: The fraction of $\overline{\mathrm{p}}$ captured in the Penning trap with specific trapping voltage HV (represented as the absolute value for simplicity). The experimental data are presented as orange circles (for energy moderation with the main degrader only) and blue crosses (for energy moderation with the main degrader and an additional thin foil degrader). The data is scaled as a fraction of the maximum signal, which was achieved for $HV \sim -14\,\mathrm{kV}$. The expected signal according to the GEANT4 simulation is shown as solid, dashed, and dotted lines for different thicknesses of the main degrader. The colours indicate the thickness of additional foil in the simulation. The simulated data was scaled as a fraction of values calculated for $|HV| = 14\,\mathrm{kV}$ to compare with the experimental results.

are dumped from the trap on the main degrader, where they annihilate. The number of antiprotons trapped is estimated based on the scintillator signals. The trapped fraction from the simulation was calculated by dividing number of antiprotons with $p_z < |HV|$ by the total number of antiprotons with $p_z < 14\,\mathrm{kV}$ when using the main degrader in combination with 100 nm Parylene foil. Similarly, the experimentally trapped fraction was calculated as a ratio of the estimated number of antiprotons trapped to the estimated number of antiprotons trapped while using $HV = -14\,\mathrm{kV}$ and both degrading foils.

The comparison of the simulated fractions with experimental results is shown in FIGURE 9.4. The simulated data for 100 nm Parylene and 1400 nm Mylar degrading stack (solid cyan line) is in reasonable agreement with experimentally estimated fractions when using the main degrader

with 100 nm thin foil (blue points). The experimentally measured fractions, obtained by using only the main degrader (orange points), are in agreement with the simulation (red lines) only until $HV = -8$ kV, after which the experimental data continue in a linear trend.

Both results are somewhat puzzling. The shape of experimentally measured fractions doesn't exactly resemble shapes from the simulation. This result may be due to several aspects of trapping that were not taken into consideration when calculating fractions from the simulation. For example, the delay for raising the potential on the second HV electrode. This delay was optimised for use with −12 kV, as this was the default trapping configuration at the time. As the energy of antiprotons after passing through the foil isn't a uniform distribution, using a lower trapping potential might increase the number of particles that are cut off by this delay. Additionally, this delay is coupled to the energy of antiprotons after the degrading stack. Therefore, by adding/removing the Parylene foil, the energy profile changes, and so, the delay should be adjusted accordingly. Moreover, the beam steering of antiprotons into the experiment was optimised for a single trapping condition, and the simulation didn't explore the beam angle at the time of measurements.

The experimental data for 100 nm Parylene shows a closer match to the main degrader of 1400 nm Mylar in the simulation. At the same time, the *PassThrough* experiment showed data closer to 1460 nm Mylar. This result might be due to 10 % uncertainty in the manufacturing of the Parylene foils.

From the preliminary estimates, the trapping efficiency achieved at AEḡIS is of the order of 64–74 % [63], which is in agreement with estimates from the simulations.

9.4 Formation of antiprotonic atoms at AEḡIS

During the 2023 and 2024 antiproton campaigns at AEḡIS, the first study could be conducted of trapping the positively charged secondaries produced in the antiprotons reacting with a rest gas inside a trap. There were two HCI campaigns in total at AEḡIS. The campaigns were limited, however, to only a couple of weeks before the end of the $\overline{\mathrm{p}}$ beam time at AD and the subsequent warm-up of the experiment. This timeline resulted from the nature of the HCI measurements. The HCI measurements performed in AEḡIS ($\overline{\mathrm{p}}$-nucleus interactions in a rest gas) require that the trap volume be filled with a gas. Given that pumps have different efficiencies for various gases, introducing gas into the apparatus meant that a background from that gas remains inside the trap. This effect is especially prominent with gases such as helium or argon. To avoid the background, it would be necessary to flash the entire system by warming up the apparatus and

then cooling it again. This operation takes around two weeks for the AEgIS experiment. The main results of the HCI campaigns were summarised in a publication released on arXiv [148].

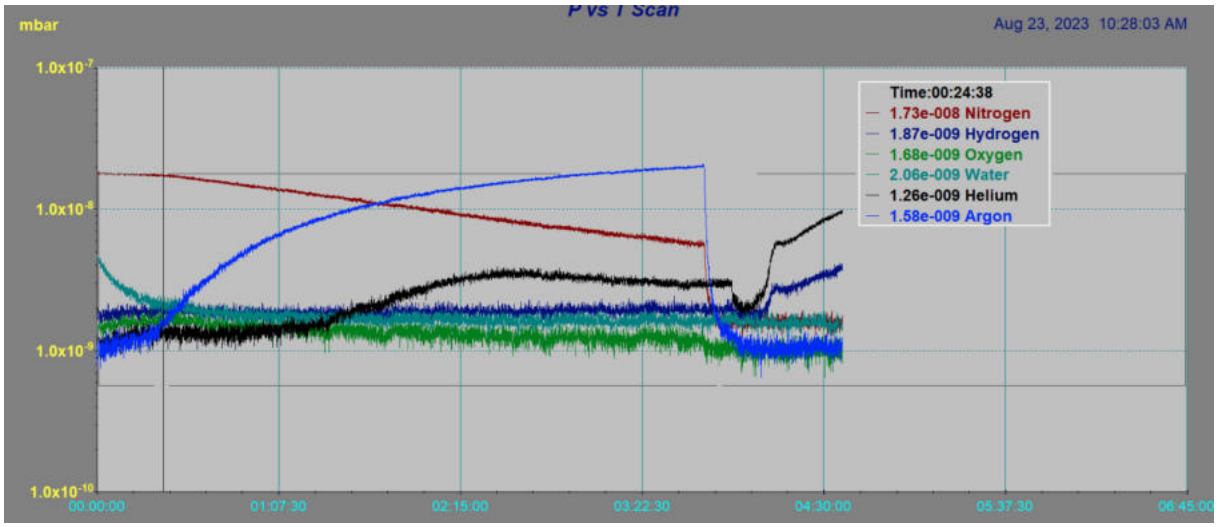

FIGURE 9.5: Screenshot of the pressure vs time RGA measurement performed at the start of the warm-up of the experiment after ending nitrogen runs. Nitrogen is present from the beginning, while the amounts of argon and helium increase with time as the cryo-surfaces warm up.

9.4.1 HCI runs of 2023

Initially, gas was introduced into the trap via a leak in the SUN region of the apparatus. After localising the region containing the leak, it was covered with a vacuum jacket that could then be filled with nitrogen, helium or argon gases[3]. At the end of the campaign, coinciding with the start of the experiment's warm-up, a rest gas analysis (RGA) measurement was performed. A screenshot of the RGA result, showing the pressure vs. time measurement, is seen in FIGURE 9.5. From the beginning, a significant amount of nitrogen is present, and as time increases and the cryosurfaces warm up, argon starts to appear, followed by helium. This measurement indicates that the trap was primarily filled with nitrogen gas during the nested trap measurements in August 2023.

In November and December 2023, a second campaign of HCI production at AEgIS took place. During this time, a series of measurements was conducted to enhance the understanding of the nested trap procedure and the formation of the TOF signal. It was noticed that the most persistent background in all measurements comes from helium inside the trap. FIGURE 9.6 shows the TOF measurements in the helium background. Left plots show the TOF spectrum measured

[3]These are the gases that were available at AEgIS at the time.

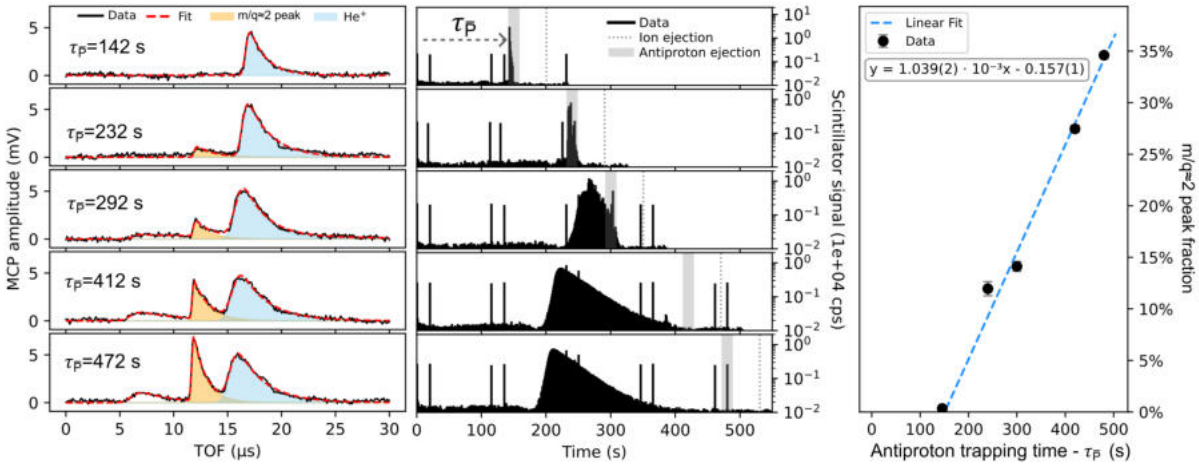

FIGURE 9.6: TOF measurements of the positively charged particles after trapping antiprotons within a Penning-Malmberg trap filled with helium gas (figure from [148]).

for different durations of storing antiprotons inside the trap during nested-trap procedures. One peak can be observed in all runs (shaded blue region), which was identified as He^+ ($\frac{m}{Q} \approx 4$ u/e). With increasing duration of antiproton trapping time, a second peak, with $\frac{m}{Q} \approx 2$ u/e, begins to appear. Middle plots of FIGURE 9.6 show the scintillators' signals monitoring pions from antiproton annihilation in time. The shaded grey area indicates the time when antiprotons are removed from the nested trap, while the dashed line indicates the time at which the TOF measurement of trapped ions was performed. The peak with $\frac{m}{Q} \approx 2$ u/e increases together with observed annihilations inside the nested trap. The size of this peak, as a fraction of He^+ peak, is shown in the right plot of FIGURE 9.6 as a function of the antiproton storage time, together with a linear fit, indicating that the intensity of the $\frac{m}{Q} \approx 2$ u/e peak increases linearly with time. This relation is direct evidence that the ions with $\frac{m}{Q} \approx 2$ u/e trapped inside the nested trap are a result of the annihilations occurring within the trap region.

9.4.2 HCI runs of 2024

After the initial success of the nested trap of 2023, it was planned to improve the control over the environment[4]. A dedicated leak valve was introduced, allowing for controlled leaks between two chambers in the vacuum system. This upgrade enables control over the pressure of incoming gas, which in turn determines the amount of gas in the trap. To avoid contamination of different gases, it was decided to use only argon inside the apparatus in the last two weeks of the winter

[4]Nobody wants to have a random leak into their vacuum.

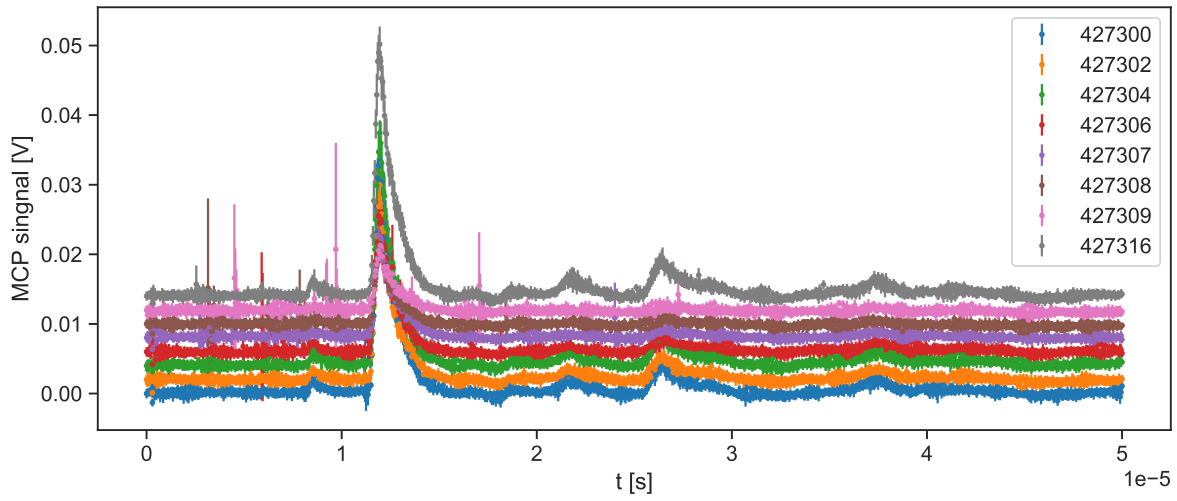

FIGURE 9.7: The time spectra of 8 good runs acquired during the 2024 campaign with argon gas. The spectra are plotted with an offset of 2 mV between the runs to improve readability.

experimental campaign at AE$\bar{g}$IS. This campaign was particularly unlucky, as the first week of the experiment experienced multiple minor system failures (pulser, oscilloscope, trap electrodes), which greatly limited available beam time for HCI studies. Moreover, the last week was shortened by the unexpected stop of AD due to problems with the magnetic horn. Nevertheless, the total of 8 good runs were collected with time-of-flight spectra from the nested trap with argon. FIGURE 9.7 shows full spectra from all 8 runs binned with bin size of 50 ns. The trapping parameters used during the runs are summarised in TABLE 9.1.

TABLE 9.1: Summary of trapping parameters used in good runs from the 2024 campaign with argon gas.

Run	trap floor [V]	trap wall [V]	$\bar{p}$ hot storage [s]	$\bar{p}$ cooling [s]	ion accumulation [s]
427300	180.0	190.0	200.0	170.0	30.0
427302	180.0	190.0	100.0	70.0	30.0
427304	180.0	190.0	300.0	270.0	30.0
427306	180.0	190.0	900.0	870.0	30.0
427307	180.0	190.0	1200.0	1170.0	30.0
427308	180.0	190.0	1500.0	1470.0	30.0
427309	180.0	190.0	1800.0	1770.0	30.0
427316	180.0	190.0	300.0	270.0	30.0

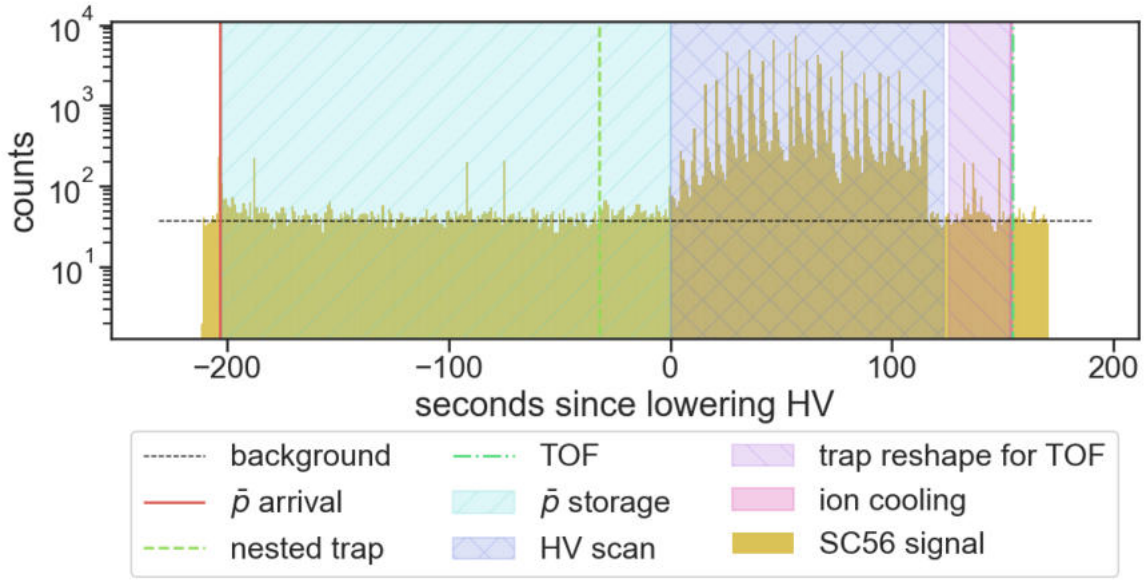

FIGURE 9.8: Example scintillator signal of a nested trap procedure with slow extraction of antiprotons on the main degrader. The light blue region indicates the antiproton storage time. The dark blue highlight indicates the period during which HV electrodes are lowered in steps of 1 kV every 10 s. The green, dashed line indicates when the nested trap is created.

9.4.2.1 Cooling on rest gas

Throughout the HCI campaign, attempts were made to find the optimal trapping condition for creating and trapping the highest number of ions from the annihilations. Crucial roles are played by various delays and durations at different stages in the trapping sequence. The $\overline{p}$ *storage* defines how long antiprotons are kept inside the trap. During that time, antiprotons interact with the gas, which should decrease the energy of antiprotons, increasing the cross section of production of antiprotonic atoms [37]. To test the cooling efficiency of argon, a sequence was designed to release antiprotons from the nested trap at a controlled rate. The release is performed by setting a 1 kV lower potential on the HV1 electrode and waiting for 5 s to ensure that the real potential on the electrode reaches the requested value. This sequence should release all antiprotons with energy higher than the potential set on the electrode onto the main degrader. Following this, the potential on the HV3 electrode is lowered following the same procedure. In total, lowering of both electrodes from −12 kV to 0 kV takes 120 s. FIGURE 9.8 shows the scintillator signal with time windows of different steps of the sequence.

By releasing antiprotons slowly, the average energy of trapped antiprotons can be estimated. This estimate was achieved by fitting a Gaussian function to the scintillator signal within the

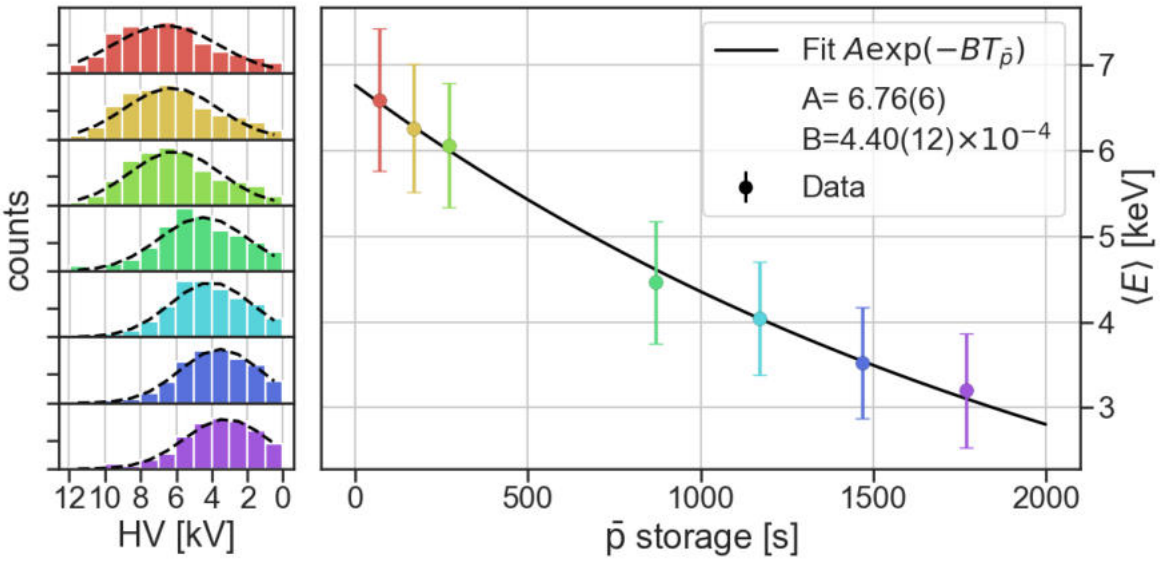

FIGURE 9.9: The average energy of antiprotons as a function of antiproton storage time. The average energy is calculated based on a Gaussian fit of the scintillator data, shown for different runs on the left. The colours correspond to different experimental runs. The average energy is fitted with an exponential function, with the results of the fit shown in the top right corner.

window of HV electrode lowering. The scintillator signal was binned into 12 bins of 10 s (1 bin per lowering by 1 kV both electrodes). Thanks to the binning, it is irrelevant how the potential on the HV electrodes changes inside a window of a single step of the release procedure. The mean of the fit is then used as the average energy of antiprotons trapped with $u\left(\langle E\rangle\right) = \sigma/\sqrt{12}$ used as the uncertainty of the measurement. The fitted scintillator signal, as a function of HV potential, is shown in the left plots of FIGURE 9.9. The main plot in FIGURE 9.9 shows how the average energy depends on the antiproton storage time. The average energy was then fitted with the exponential function of the form

$$\langle E\rangle = Ae^{-BT_{\bar{p}}}, \tag{9.2}$$

where $T_{\bar{p}}$ is the antiproton storage time. The fit demonstrates that antiprotons interacting with the argon gas experience an exponential energy decrease. Parameter A from equation 9.2 is the average energy of antiprotons at the moment of trapping particles inside the Penning-Malmberg trap filled with argon gas. According to simulations performed with GEANT4 for the degrader efficiency studies, antiprotons moderated by the main degrader have an average kinetic energy of 12(3) keV. From the fit, the average energy is equal to 6.76(6) keV. The discrepancy between the

two values proves that argon gas works as a moderator for the antiprotons. The second parameter B in the equation 9.2 is related to the effectiveness of the energy moderation by the argon gas. From the fit, the value of $B = 4.40(12) \times 10^{-4}\ s^{-1}$ was obtained. Knowing that parameter $A = \langle E \rangle_i$, the equation 9.2 can be used to calculate the antiproton storage time $T_{1/2}$ inside the argon gas for the average energy of trapped antiprotons to decrease by a factor of two:

$$\frac{\langle E \rangle_i}{2} = \langle E \rangle_i \exp(-BT_{1/2}) \rightarrow T_{1/2} = \frac{\ln(2)}{B} = 1580(40)\ \text{s}.$$

9.4.2.2 Mass to charge estimation

FIGURE 9.10 shows the average spectrum of 4 runs (427 300, 427 302, 427 304 and 427 316) of antiprotonic atoms formation on the rest gas. The antiprotons were trapped for $\langle \tau_{\bar{p}} \rangle \approx 150$ s. Subsequently, the HCI were moved to a shallow trap with floor potential $V_{floor} = 180$ V and wall potential $V_{wall} = 190$ V to evaporatively cool [149] the trapped particles.

Each peak was fitted with an EMG function individually, as described in section 8.2.2.2. Afterwards, a global fit was repeated with a sum of all the functions. The parameters obtained from the fits of individual peaks were later used as the initial parameters for the global fit. The function obtained from the global fit is shown as the red curve in FIGURE 9.10.

The $\frac{m}{Q}$ for each peak was calculated according to equation 8.4, with the most prominent peak, He^{1+}, used as the reference values. The summary peak positions and estimated $\frac{m}{Q}$ values can be found in TABLE 9.2.

TABLE 9.2: Identified ion peaks from the argon campaign spectrum (FIGURE 9.10). The spectrum was calibrated using TOF of the identified He^{1+} peak, m/Q values are given with statistical uncertainties (parentheses). m/Q of fragments is calculated assuming the complete stripping of nuclear annihilation fragments with masses greater than ^{4}He. The table was copied from [148].

TOF (μs)	$\frac{m}{Q}\Big\|_{exp}$ [u/e]	Ion Candidate(s)	$\frac{m}{Q}\Big\|_{lit}$ [u/e]
		H_2^+	2.01510
8.457(30)	2.018(14)	He^{2+}	2.00075
		HCI frag.	2.0-2.6
11.911(7)	–	He^{1+}	4.00260
16.774(75)	7.94(7)	Ar^{5+}	7.99193
18.698(68)	9.86(7)	Ar^{4+}	9.99005
21.641(56)	13.21(7)	Ar^{3+}	13.32025
26.264(29)	19.46(5)	Ar^{2+}	19.98064
37.378(55)	39.41(12)	Ar^{1+}	39.96183

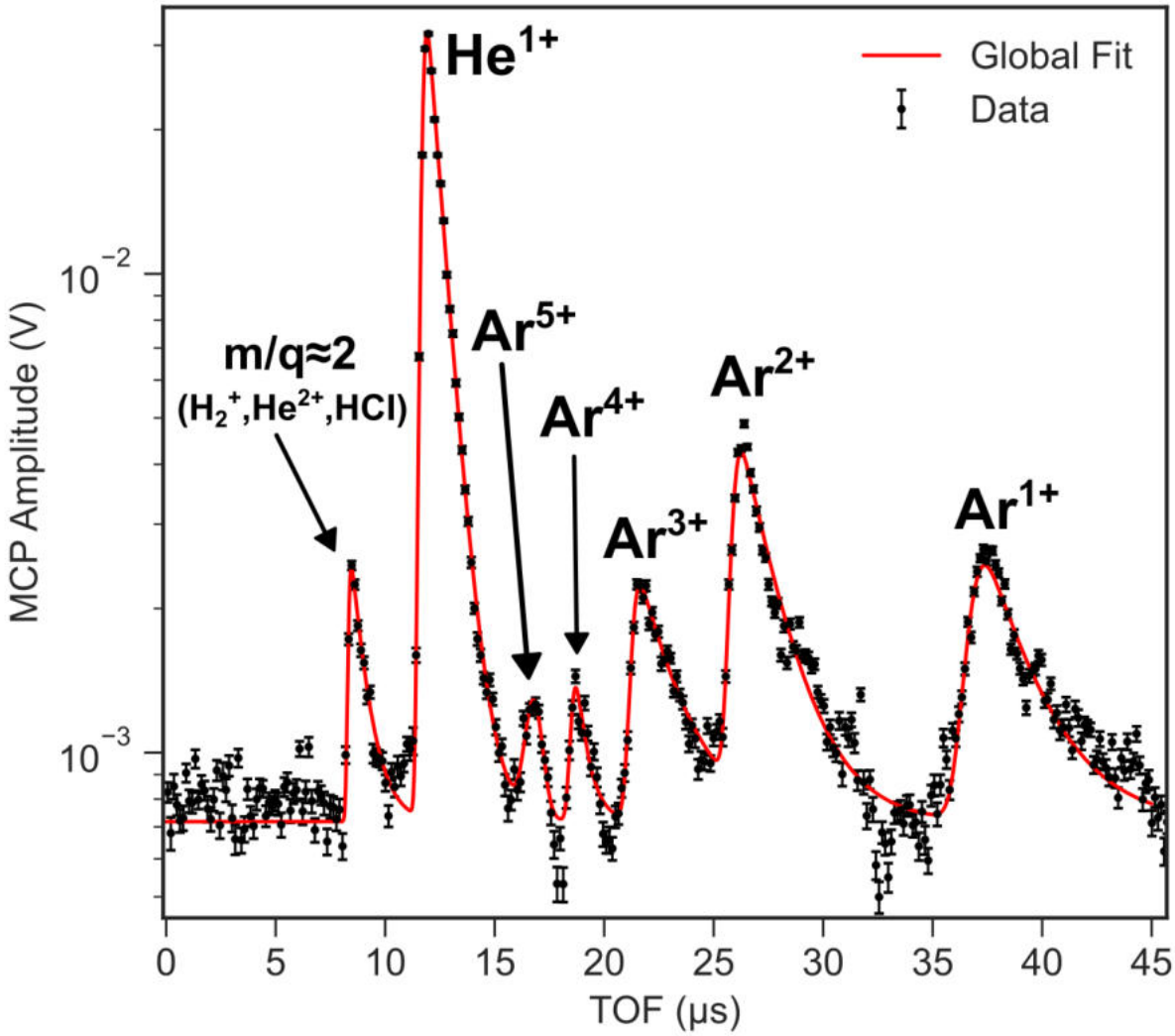

FIGURE 9.10: The fitted TOF spectrum from average of 4 runs of nested trap sequence performed at AE$\bar{g}$IS. The global fit as a combination of multiple exponentially modified Gaussian functions is shown in red. Each peak was identified from m/Q estimated based on the measured TOF for He^{1+} peak.

9.4.3 Comparison with simulated expected signals for fragments created from $\bar{p}^{40}Ar$

As indicated in TABLE 9.2, the first peak at $m/Q \approx 2$ u/e is the expected position of the trappable fragments created from annihilations $\bar{p}^{40}Ar$. A comparison was performed of the expected TOF signals calculated by using different parameters in the model introduced in section 6.3.7.

Firstly, the peak at $m/Q \approx 2$ u/e of all the runs was investigated. The raw signal (offset by the background in each run) is shown in FIGURE 9.11. The shaded area for each run indicates a band

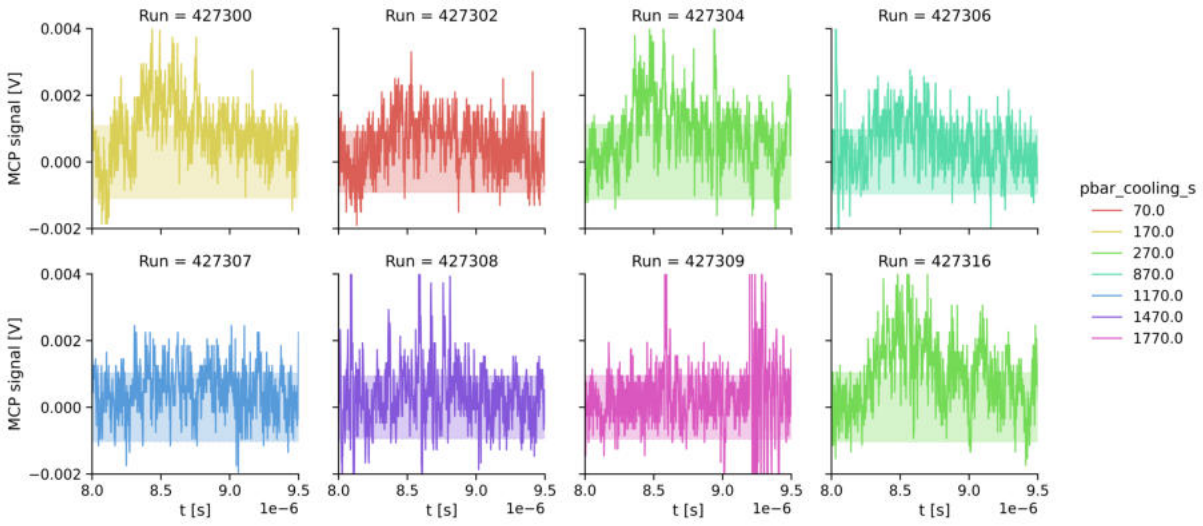

FIGURE 9.11: Experimentally measured signal in good runs of HCI campaign limited to the region where the signal of fragments from annihilations of antiprotonic atoms is expected. Raw signal offset by the background. Bands indicate region of $\pm bcg/\sqrt{2}$ for each run. Colours refer to different durations of antiproton storage time during the nested-trap procedure.

with a width of $bcg/\sqrt{2}$. In all the runs, the ion storage time is constant at 30 s. However, the *pbar_cooling_s* time, which defines a delay between trapping antiprotons and releasing them by opening the HV electrodes, varies. In FIGURE 9.11 it can be seen that the size of the peak fluctuates with *pbar_cooling_s* parameter. This fluctuation is expected with varied storage time for antiprotons from 30 s to 1800 s. The highest yield of fragments is likely to occur around the average lifetime of the antiprotons inside the trap, as it defines the time with the highest annihilation rate. To produce fragments, antiprotons need to cool down to low enough energy so that they can annihilate on the rest gas in the trap. If the nested trap is created too early, only a small fraction of trapped antiprotons have a chance to annihilate. However, if the nested trap is created too late, all the antiprotons annihilate, and the positive fragments aren't trapped in the negative trap used for antiprotons. From FIGURE 9.11 the peak can be seen in 3 runs: 427 300, 427 304 and 427 316. An argument can be made that it can also be seen in runs 427302 and 427306; however, given the low intensity of the peak, it was decided to exclude these runs to keep the expected number of trapped fragments similar across the runs used in the analysis.

After selecting the runs, the signals were averaged and binned into intervals of 10 ns. The binning was repeated for all simulated signals. Data was compared with two different simulated signals: only He^{2+} and combination of He^{2+} with $\overline{p}^{40}Ar$ fragments. Furthermore, I scaled the simulation signal $S_{sim}(t)$ (which is in arbitrary units) to experimental signal $S_{data}(t)$ with

$S_{sim}^{norm}(t) = f_{scale} \cdot f_{norm} \cdot S_{sim}(t)$, where:

$$f_{norm} = \frac{\sum S_{data}(t) \cdot dt}{\sum S_{sim}(t) \cdot dt} \tag{9.3}$$

is the normalisation factor, and f_{scale} is an additional scaling factor that was numerically estimated with the fit.

There are three parameters :

- scaling factor f_{scale}: 0.7 to 1.3 with step of 0.1;
- weight of He^{2+} $W_{He^{2+}}$: 0.005 to 0.030 with step of 0.001;
- minimum spacecharge: 0.0 to 3.78[5] with step of 0.02.

These ranges were selected after some initial exploration. The weight of He^{2+} is used only for the total signal, as the total signal is calculated according to equation 6.17. As there is no good indicator for the ratio of He^{2+} produced from ionisation to fragments produced from the annihilations, the weight $W_{He^{2+}}$ needs to be estimated numerically. For comparing only He^{2+} simulated signals, the weight $W_{He^{2+}}$ can be omitted as normalisation of the signal is done with the simulation of a single species.

FIGURE 9.12 shows simulated TOF signals from He^{2+} without fragments and without additional scaling ($f_{scale} = 1.0$). The rows display different values of minimum spacecharge used in the simulation. At the same time, the columns refer to different spatial distributions used by selecting the *thermalised* flag to either *True* (flatten distribution in the left column) or *False* (Gaussian distribution in the right column). Similarly, FIGURE 9.13 shows a comparison of the data with simulated signals for the combination of signals from He^{2+} and $\overline{p}^{40}Ar$ fragments. The He^{2+}-only signals have a too high maximum, while they can closely describe the tail of the signals. Adding the signal from $\overline{p}^{40}Ar$ fragments improves the description of the maximum. It also has the potential to improve the tail of the distribution. The simulated signal is plotted as a band spanning the region between the upper and lower limits of the signal, calculated with an additional 10 % error due to modelling errors.

I used the least squares method to find the best parameters for the simulated signals, where the parameter set with the minimum LS is considered the best fit. The LS is defined as:

$$LS = \sum_t \frac{\left[S_{data}(t) - S_{sim}^{norm}(t)\right]^2}{err_{data}(t)}, \tag{9.4}$$

[5] This is limited by the depth of the trap that is achievable with $V_{floor} = 180\,\text{V}$ and $V_{wall} = 190\,\text{V}$ set on HV_AMP_8CH modules from Sinara.

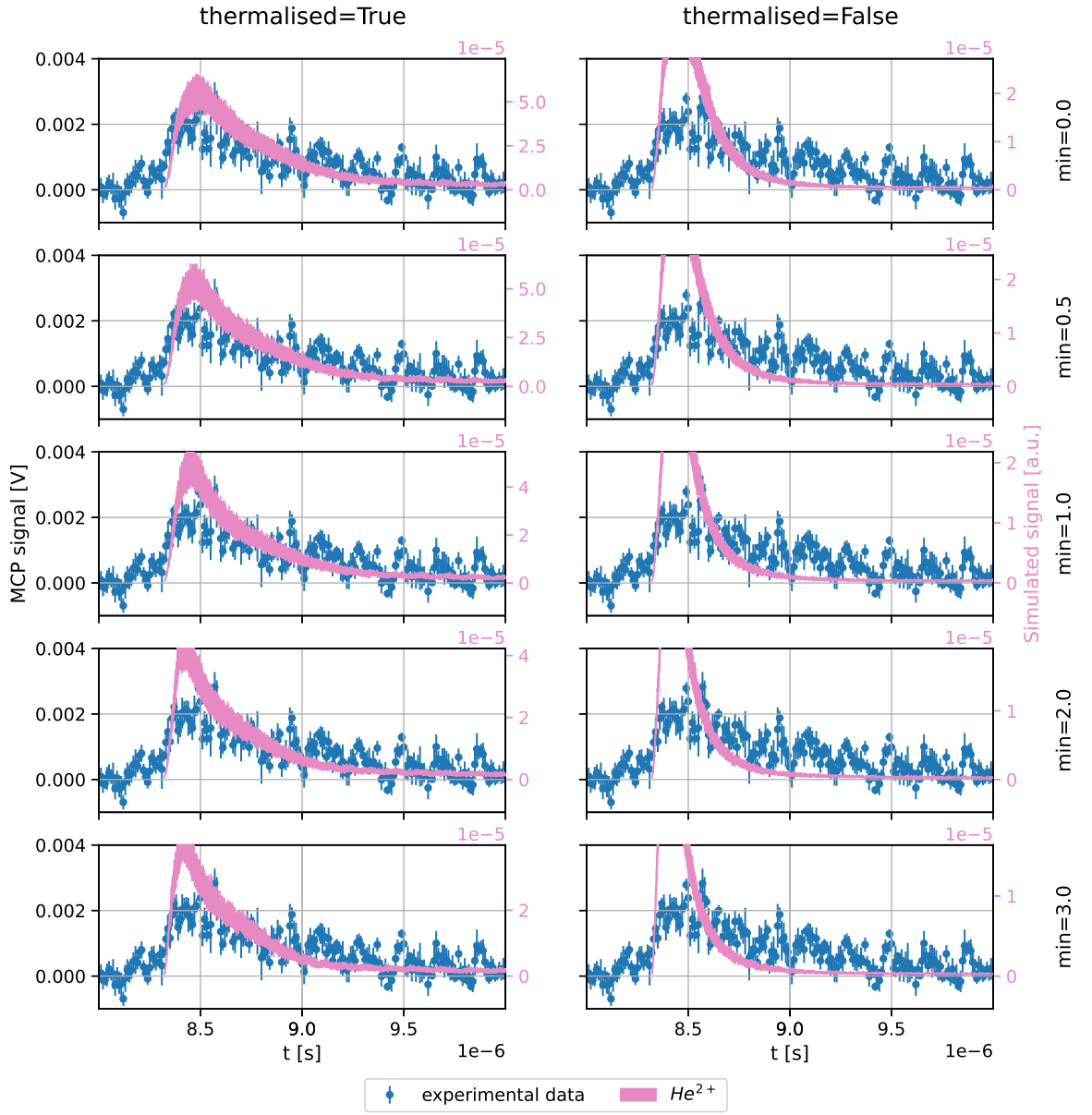

FIGURE 9.12: Simulated TOF signal of He^{2+} (pink line) compared with the average measured signal (blue points). Different signals are shown as obtained with the *thermalised* flag True or False as columns and different minimums of *spacecharge_min* used as rows.

where $err_{data}\,(t)$ is the error of the data point at time t. The best results of fitted simulations to data are summarised in TABLE 9.3.

FIGURE 9.14 and FIGURE 9.15 show the parameters landscape for LS as calculated with *thermalised=True* flag with He^{2+}-only signal and combination of He^{2+}+$\bar{p}^{40}Ar$ signal respectively. For a single species signal, there is a preference for lower *spacecharge_min* values (<1 kV), while the

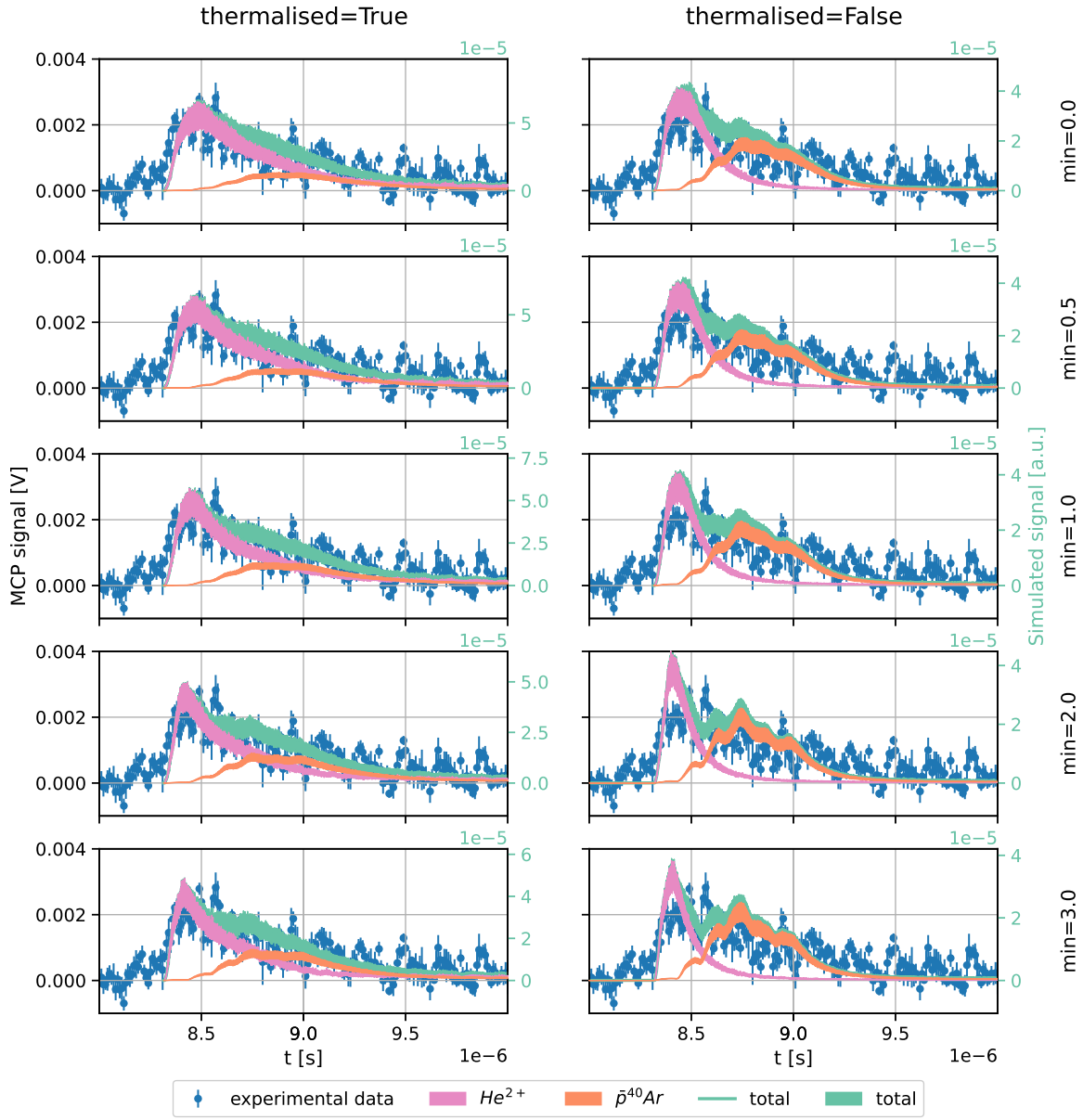

FIGURE 9.13: Sum of simulated signals (teal line) for He^{2+} (pink line) and $\bar{p}^{40}Ar$ (orange line) compared with the average measured signal (blue points). The weight for He^{2+} signal was chosen such that the total signal closely resembles the experimental signal. Different signals are shown as obtained with the *thermalised* flag True or False as columns and different minimums of *spacecharge_min* used as rows.

combined signal has a minimum at much higher values (>3 kV). As the spacecharge generated by particles inside the trap depends on the charge of the constituent particles, it is to be expected that completely stripped fragments will yield a high spacecharge. It is, however, worth noting

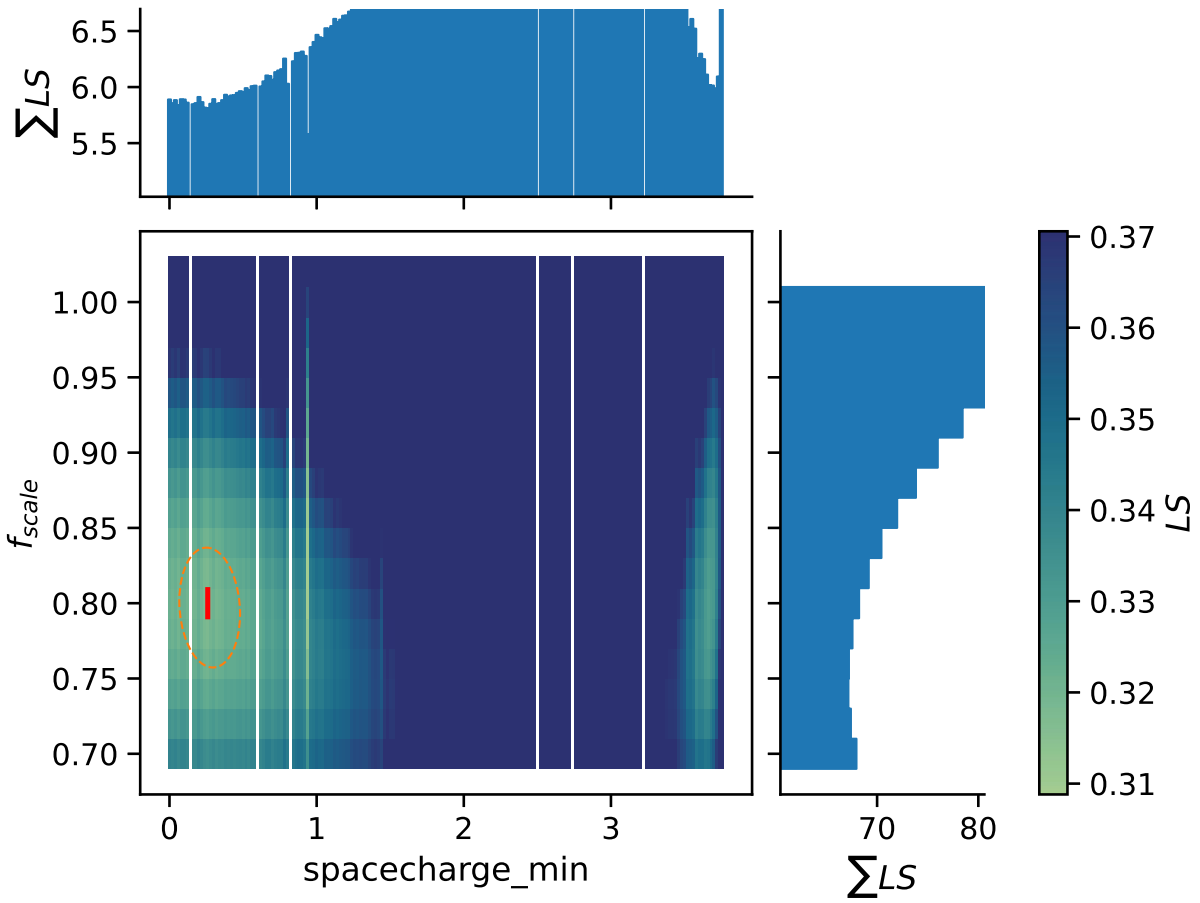

FIGURE 9.14: Least squares (LS) landscape for simulated He^{2+} only signal when using *thermalised=True*. A red rectangle indicates the minimum LS (best fit). Orange ellipse indicates region with $LS < 1.025 \cdot LS_{min}$. Projections of each parameter (scaling factor f_{scale} on right and *spacecharge_min* on top) is shown as the sum of calculated LS over other parameters.

that the simulated signal is based on the model described in section 6.3.7 and relies on weaker assumptions.

Nevertheless, in the context of the model, using a combined signal of He^{2+} with $\bar{p}^{40}Ar$ better describes the experimentally measured signal with calculated LS smaller by $\sim 20\,\%$ than from single species He^{2+} signal. The best weight of He^{2+} $W_{He^{2+}} = 0.017$, which is ~ 1.8 times higher than the total weight of $\bar{p}^{40}Ar$ fragments ($W_T = \sum_i^N W_{X_i}$) and ~ 9.6 times higher than the biggest weight from fragments ($W_{^{39}Ar} \approx 0.0018$ for ^{39}Ar).

FIGURE 9.16 and FIGURE 9.17 shows the simulated signal on top of the data for He^{2+}-only signal and combination of $He^{2+} + \bar{p}^{40}Ar$ respectively. The bottom plot of the figure shows data with subtracted contribution of He^{2+} in the simulated signal. The simulated signals from $\bar{p}^{40}Ar$ are

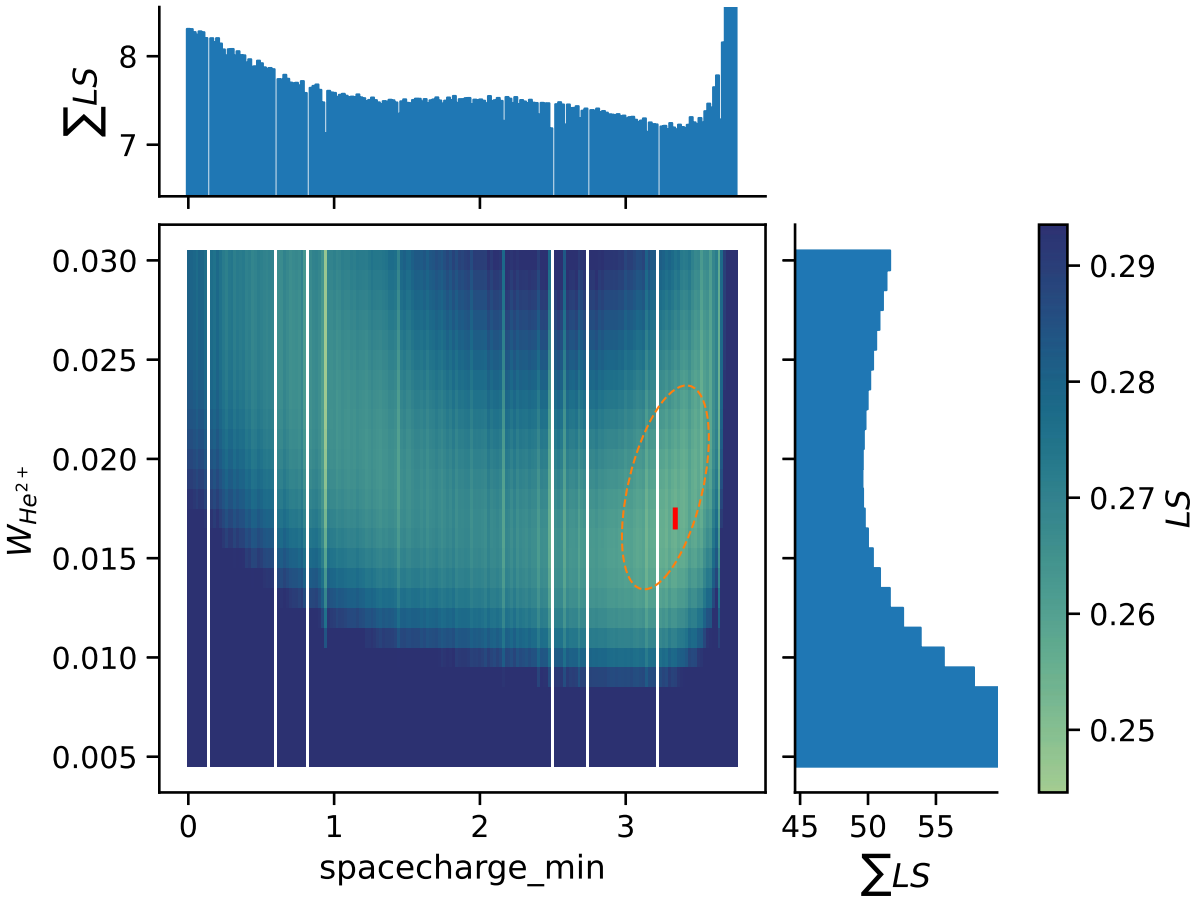

FIGURE 9.15: Least squares (LS) landscape for simulated He^{2+}+$\bar{p}^{40}Ar$ signal when using *thermalised=True*. Because there are three parameters involved in the calculation of LS, the plot shows a slice for $f_{scale} = 0.9$, which contains the global minimum LS. The minimum LS (best fit) is indicated as a red rectangle. Orange ellipse indicates region with $LS < 1.025 \cdot LS_{min}$. Projections of each parameter (weight of He^{2+} $W_{He^{2+}}$ on right and *spacecharge_min* on top) is shown as the sum of calculated LS over other parameters.

shown as an orange band. The expected signal of He^{2+} + $\bar{p}^{40}Ar$ is the best fit to the experimental data; however, due to significant fluctuations of the experimental data and uncertainties due to the simulation model, it is hard to conclusively state that these are indeed trapped fragments.

TABLE 9.3: Results of the best-fitted simulated signals to the experimental data. For simulations with only He^{2+} signals, the weight parameter can be omitted. At the same time, for the combination of He^{2+} + $\bar{p}^{40}Ar$ signals, the weight parameter was also fitted to best match experimental data, assuming all fragments from $\bar{p}^{40}Ar$ have weights calculated based on their yields according to the GEANT4 simulation.

Simulated signal	spacecharge_min	$W_{He^{2+}}$	f_{scale}	LS
Thermalised distribution				
He^{2+}	0.26	-	0.8	0.317
He^{2+} + $\bar{p}^{40}Ar$	3.34	0.017	0.9	0.254
Not thermalised distribution				
He^{2+}	3.72	-	0.7	0.463
He^{2+} + $\bar{p}^{40}Ar$	3.66	0.011	0.82	0.288

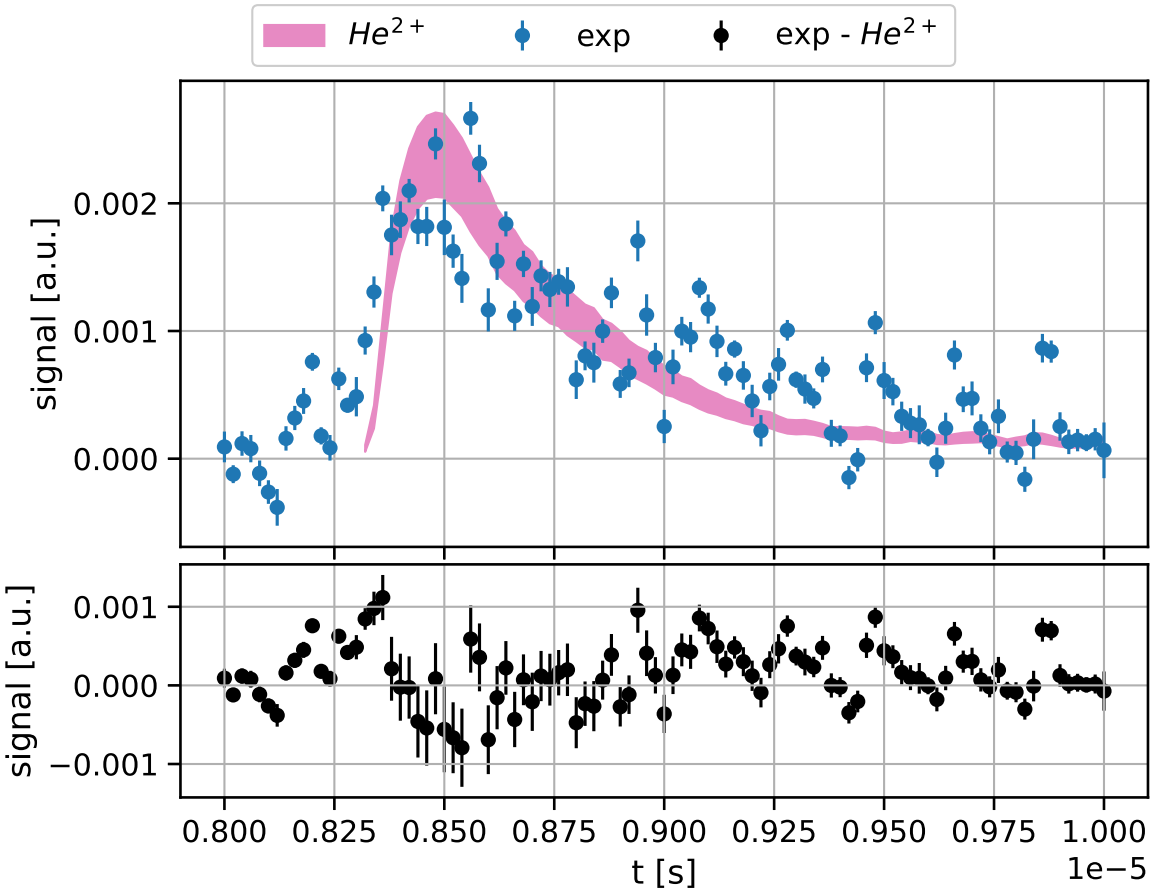

FIGURE 9.16: Simulated signal (shaded regions) on top of experimental data (points) with the best fit for *thermalised=True*, *spacecharge_min_V=0.26* assuming only signal from He^{2+}. The bottom plots show data after removing He^{2+} contribution from the experimental data. Both simulated and experimental signals were binned with a bin size of 20 ns.

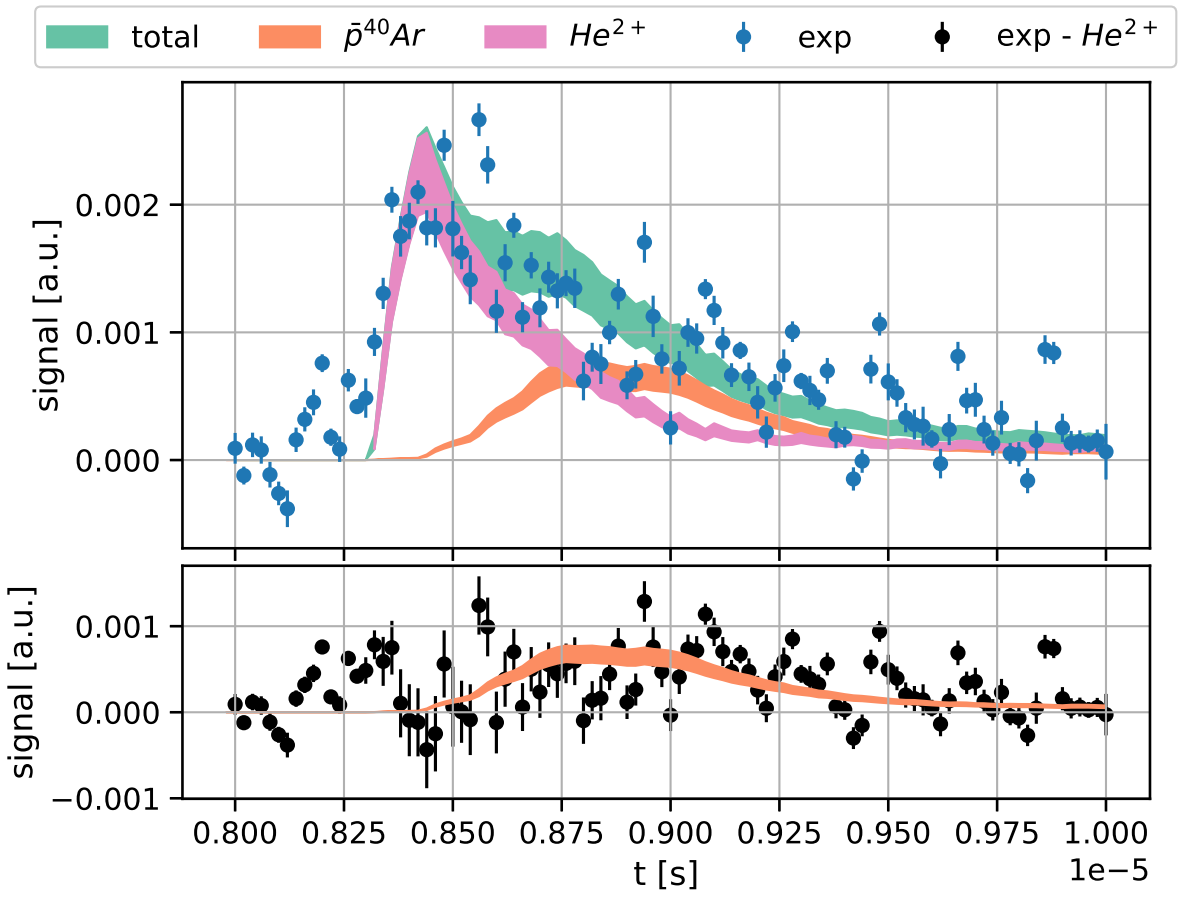

FIGURE 9.17: Simulated signal (shaded regions) on top of experimental data (points) with the best fit for *thermalised=True*, *spacecharge_min_V=3.34*, and the weight for He^{2+} $W_{He^{2+}} = 0.017$. The bottom plots show data after removing He^{2+} contribution from the experimental data. Both simulated and experimental signals were binned with a bin size of 20 ns.

Chapter 10
Discussion and outlook

This thesis presents the initial steps taken towards producing antiprotonic atoms from cold antimatter and subsequently trapping the fragments produced during the annihilation of these exotic systems.

Firstly, the simulations performed indicate that we currently lack experimental data. Various tools and models enable the simulation of interactions between antiprotons and atoms. It is possible to use them to estimate yields of fragments from annihilations; however, different models and toolkits give vastly different results in some cases. The most common toolkits were developed with high-energy physics in mind. They are based on available data from beam-on-target experiments with high-energy antiprotons. As the number of target materials is limited and the fragments produced are usually measured via indirect methods, these models rely on interpolation and extrapolation.

A direct measurement of the yields of fragments could provide additional data to benchmark and improve the models. The models can be further improved by measuring the energy of nuclear remnants. All this can be achieved using the proposed method for directly forming antiprotonic atoms in a Penning-Malmberg trap under UHV conditions. As I showed in this thesis, the yields of fragments can be estimated using available toolkits, and the trapped fraction can be calculated. The energy distribution of fragments can be estimated by varying the parameters of the Penning-Malmberg trap, such as the magnetic field and potential on the endcaps. The species can be differentiated via the TOF measurements. And the preliminary studies I performed for the AEgIS experiment show that this is possible with existing experimental setups.

Furthermore, the trapped fragments can also be used to perform detailed studies on radioactive HCIs. The fragments are expected to be formed in HCI states; however, this is another unknown that can be verified with the proposed experiment. Complete stripping of electrons suggests that some radioactive, short-lived isotopes could be trapped and studied, a process that is currently impossible due to the timescales of existing production schemes.

We have selected the AEgIS experiment as the host for the development of the experimental technique. The main goal of AEgIS is the measurement of gravitational effects on antimatter. For this purpose, it implements the charge exchange reaction between Ps and $\overline{p}$ inside a Penning

trap to form a collimated beam of $\overline{\mathrm{H}}$. As proposed in this thesis, Ps can be replaced by any negative ions, and the same technique can be used to form antiprotonic atoms. By implementing a nested Penning trap, the positive fragments from the annihilation can be subsequently trapped.

The antiprotons are required by both $\overline{\mathrm{H}}$ and antiprotonic atoms programs. I helped design and develop the control system of AEgIS, which is one of the major updates from Phase I to Phase II of AEgIS. The CIRCUS has been used since 2022, with significant data-taking periods being done in complete autonomy. The new control system shows flexibility and reliability with smooth operation of different frontlines at AEgIS. Furthermore, the feedback loop between the control system and the data analysis framework enables the solution of optimisation problems, such as beam steering into the experiment, which significantly accelerates the commissioning of the apparatus after each major update. The novel control system, and in particular the autonomous operation I helped develop, is one of the significant reasons for results like Positronium cooling achieved at AEgIS in 2024.

Thanks to all the updates, AEgIS achieved a record high trapping efficiency for antiprotons, estimating trapping of approximately 70 % of each ELENA bunch. This result was made possible thanks to the degrading stack, the new control system for trapping electrons, and beam steering optimisation, to which I contributed on all fronts. Furthermore, it also led to the development of the stacking procedure and the accumulation of antiprotons, resulting in several hundred million cold antiprotons within a Penning trap.

Lastly, I was able to perform experiments with the nested trap at AEgIS. The nested-trap setup was successfully implemented into the AEgIS control system, which allowed for capturing positively charged particle species. The amount of particles trapped is correlated with the observation of antiproton annihilations inside the trap. This observation leads me to conclude that the trapped particles are a result of annihilation.

The trapped cations were identified as having different ionisation levels of ^{40}Ar, with up to $^{40}Ar^{+5}$, which was used as the rest gas inside the trap. The measured spectra show some signal at $m/Q \approx 2$ u/e, which is where we would expect to observe the fragments produced via the annihilation of $\overline{\mathrm{p}}^{40}$Ar. This signal could also be explained by the presence of the He^{2+} background, which may be due to impurities in the argon gas used for injection or other factors, such as leaks into the apparatus. The experimental data, where $m/Q \approx 2$ u/e, were compared with the simulated signals calculated using the model I created. The best fit to the data is achieved when using a combination of He^{2+} and $\overline{\mathrm{p}}^{40}$Ar fragments. Due to uncertainties in the TOF model and the limited amount of data collected, the results are inconclusive, making it difficult to claim that we have achieved the trapping of fragments produced by the annihilation of antiprotonic atoms.

All the results indicate that the implemented procedure is effective and can serve as a starting point for experiments involving controlled charge-exchange reactions between antiprotons and trapped ions. One of the most significant factors contributing to the uncertainties is the background coming from the residual gas. The amount of trapped ionised gas atoms vastly outnumber the possible trapped fragments, making identification of fragments difficult. This problem can be addressed by implementing a controlled procedure for forming antiprotonic atoms inside the Penning-Malmberg trap by co-trapping single-species ions and antiprotons. Several steps must be taken to achieve this goal.

One of the developments required is the improvement of trapping electrodes for positive species. Currently, the electrodes of traps in AEgIS can be biased to ±200 V. The potential limits significantly reduce the trapping efficiency for positive species. As shown by the simulations, increasing the trapping potential to ∼5 kV can improve the efficiency for trapping heavier fragments to over 80 %. The design of the *1T* trap at AEgIS includes 3 HV (HV4-HV6 in FIGURE 5.7) electrodes that were designed to handle kV potential; however, at the time of running the nested trap procedures, there was no power supply available that could provide the positive HV potential on these electrodes. This power supply was already ordered, and its installation is expected in the near future. Moreover, the nested trap procedure will need to be adapted for a new trapping location, as the currently available procedures utilise only electrodes from the *5T* trap.

As pointed out, the background originates from the ionisation of the reset gas inside the trap. Therefore, ongoing work is being conducted on the implementation of the ion source and the development of ion trapping within the AEgIS traps. Two ion sources are being considered in parallel: the iodine source and the Borealis source. The *Borealis* source was recently successfully integrated into the AEgIS apparatus, and the work on the control sequences for trapping ions is ongoing. It is expected that co-trapping of ions and antiprotons will be achieved at AEgIS before the next long shutdown at CERN in the middle of 2026.

This improvement should address the issue of background present from the rest gas used in the experiment. However, this creates additional challenges that must be addressed. Even after co-trapping of antiprotons and negative ions, some additional procedures might be required for mixing of the plasma due to Coulomb repulsion of like-sign species. Furthermore, to improve the cross section and develop controlled formation of antiprotonic atoms, a laser system for Rydberg excitation of the negative ions needs to be introduced and integrated into the AEgIS apparatus. All the highlighted developments were recently submitted in the long-term plan for the AEgIS Collaboration [80].

Additional studies should be conducted on the simulation front. Especially useful would be to remake the detailed simulation in GEANT4 in other toolkits like FLUKA to better estimate the

uncertainties of the models for comparison with the experimental data. Moreover, other toolkits may be worth investigating, with the possibility of developing a dedicated model for simulating the formation and subsequent fragmentation due to the annihilation of antiprotonic atoms. This model would be instrumental in the context of low-energy physics, a regime where there are limited simulation toolkits.

As pointed out in the thesis, the first steps towards developing a method for the controlled production of antiprotonic atoms inside a Penning-Malmberg trap in a UHV environment were successfully achieved. A significant step is the apparent trapping of cations formed after the annihilation of antiprotons on residual gas inside the trap. This work is a fundamental step towards a better understanding of antiproton interactions with nuclei and provides a reliable method for studying short-lived, radioactive isotopes.

10.1 Conclusions

This thesis is a summary of the last four years of my career. Throughout this time, I was involved in different aspects of experimental physics. I created multiple simulation programs using available toolkits, which enhanced my understanding of these tools. I analysed the results of the simulations for general trends, as well as in the context of specific experiments, to later compare the results with experimental data. I was involved in the development of the control system, for which I needed to learn new concepts and techniques. In this regard, I became an expert on the control system of the AEgIS experiment, often making decisions on the direction of future developments and guiding others on the implementation of various features into the system. I actively provide support and respond to various issues that arise during the experiment's operation. I was also involved in the installation of various hardware subsystems for the experiment, which significantly enhanced my understanding of electronics and vacuum systems. Furthermore, I actively participate in the development of experimental sequences and actual data-taking campaigns. My contributions to the AEgIS experiment were vital for most, if not all, the results achieved by the Collaboration in recent years.

List of Achievements

The author has contributed to the following publications and proceedings:

- ☐ F. P. Gustafsson et al., "Spectrometry of Captured Highly Charged Ions Produced Following Antiproton Annihilations". 2025. [Online]. Available: https://arxiv.org/abs/2510.08440
- ☐ S. Alfaro et al., "Towards metrology with highly charged isomeric ions from antiproton annihilation", Journal of Physics B: Atomic, Molecular and Optical Physics, vol. 58, no. 21, p. 215002, 2025.
- ☐ M. Volponi et al., "TALOS (Total Automation of LabVIEW Operations for Science): A framework for autonomous control systems for complex experiments", Review of Scientific Instruments, vol. 95, no. 8, Aug. 2024, doi: 10.1063/5.0196806.
- ☐ G. Kornakov, G. Cerchiari, J. Zieliński, L. Lappo, G. Sadowski, and M. Doser, "Synthesis of cold and trappable fully stripped highly charged ions via antiproton-induced nuclear fragmentation in traps", Phys. Rev. C, vol. 107, no. 3, p. 034314, Mar. 2023, doi: 10.1103/PhysRevC.107.034314.
- ☐ G. Kornakov, J. Zieliński, and G. Kasprowicz, "THE CONTROL SYSTEM OF THE AEgIS EXPERIMENT AT CERN", Elektronika - kontrukcje, technologie, zastosowania, vol. 64, no. 8, doi: 10.15199/13.2023.8.18.
- ☐ G. Kornakov and J. Zieliński, "FRONTIER SCIENCE IN A QUANTUM EXPERIMENT: AEGIS AT CERN", Elektronika - kontrukcje, technologie, zastosowania, vol. 64, no. 8, doi: 10.15199/13.2023.8.6.

proceedings:

- ☐ L. Lappo, J. Zieliński, F. P. Gustafsson, M. Grosbart, G. Kornakov, and M. Doser, "Antiprotonic Atoms as Gateways to HCI", Atoms, vol. 13, no. 11, p. 93, 2025, doi: 10.3390/atoms13110093.

The author has given the following talks and participated in the following poster sessions:

invited talks on behalf of the AEgIS Collaboration:

- ☐ J. Zieliński (on behalf of AEgIS Collaboration), "Toward Pulsed Production of Antihydrogen and Test of the Weak Equivalence Principle for Antimatter," XII International Conference on New Frontiers in Physics, 10-23.07.2023, OAC, Kolymbari, Crete, Greece

poster sessions:

- ☐ J. Zieliński, G. Kornakov, M. Doser, "New production scheme of HCI using antiprotonic atoms," 14th European Conference on Atoms, Molecules, and Photons, 27.06-01.07.2022, Vilnius, Lithuania
- ☐ J. Zieliński, "Antiproton-induced nuclear fragmentation," International Conference on Exotic Atoms and Related Topics and conference on Low Energy Antiprotons, 25-30.08.2024, Vienna, Austria

The author has co-supervised the following engineering theses:

- ☐ T. Januszek, "Software for the control system of an ion source for the AEgIS experiment at CERN," Warsaw University of Technology, defended on 11.02.2025
- ☐ A. Giszczak, "Development of a physics analysis framework for the AEgIS experiment at CERN," Warsaw University of Technology, defended on 08.02.2024

The author has participated in the following projects:

- ☐ IDUB-POSTDOC, “Konsolidacja programu eksperymentalnego AEgIS na PW,” 01.03.2022–31.07.2023, independent researcher
- ☐ IDUB-QT, “Opracowanie koncepcji adaptacji rozszerzenia biblioteki QisDAX dla systemu pułapki jonowej,” 08.11.2023–15.12.2023, independent researcher
- ☐ NCN SONATA BIS, “Pęsety z antymaterii do edycji nuklearnej,” 01.03.2024-01.09.2026, stipendiary

The author has received the following grants during the PhD:

- ☐ IDUB YoungPW programme. "Can highly-charged ions be produced by interaction of cold antiprotons with a gas? An experimental study towards a better understanding of interactions between antiprotons and the rest gas inside a Penning trap". IDUB/56/Z01/2024. 01.04.2024-31.12.2025

Appendix A
CIRCUS graphics

CIRCUS can update its appearance. It is defined via a parameter in the configuration file called *GUI_Skins* in the *TALOS.ini* file. The parameter defines the suffix of the PNG file, located in *Support VIs/Pictures and skins/* folder, for the specific object. Four objects in CIRCUS are updated:

- CIRCUS logo - picture located in the top centre of the CIRCUS screen. The allocated space for the picture has a width of 598 pixels and a height of 175 pixels. The file should be called *Circus-<GUI_Skins>.png*.
- CIRCUS background - The background of the CIRCUS window. The background picture should have a width of 1920 pixels and a height of 950 pixels for the best effect. The file should be called *Bkg-<GUI_Skins>.png*. By default, a white background is used.
- Monkey icon - picture of the Monkey next to the name of the µService on the front panel. The allocated space for the picture has a width of 64 pixels and a height of 64 pixels. The file should be called *Monkey-<GUI_Skins>.png*.
- Tamer indicator - picture of the Tamer holding a "stage" with Monkey located in the bottom left corner of the µService front panel. The allocated space for the picture has a width of 128 pixels and a height of 128 pixels. The file should be called *Tamer-<GUI_Skins>.png*.

Figure A.1 shows how the CIRCUS window updates with different *<GUI_Skins>* parameters.

Custom skins and graphics were created purely for entertainment and have no impact on the system's performance; however, they add a level of personalisation to the system. The pictures of Tamer and Monkey were created by the author of this thesis alongside most of the custom skins. Marta Zielińska contributed to the creation of "Darth Monkey" (Figure A.3e) skin for the Monkey, while Dr M. Volponi prepared all Halloween skins.

A.1 CIRCUS logo for AEḡIS

The default CIRCUS logo is shown in Figure A.2a. For the AEḡIS experiment, a custom logo was created. The standard CIRCUS logo of AEḡIS is shown in Figure A.2b with a banner with AEḡIS logo and two additional characters of AERIALIST (in the top right corner) and ALPACA (in the bottom right) that reflect other packages integrated into the system. Furthermore, there are different

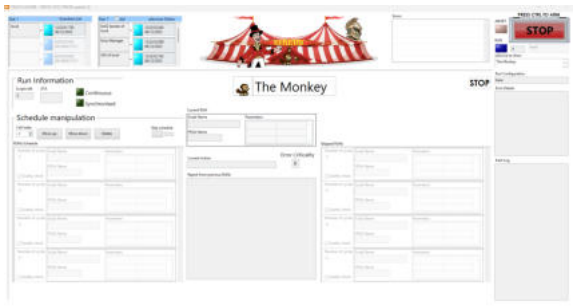

(A) Default.

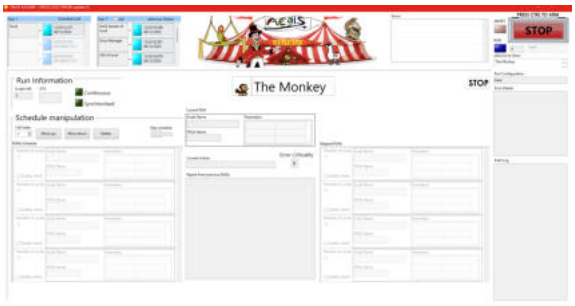

(B) AEGIS.

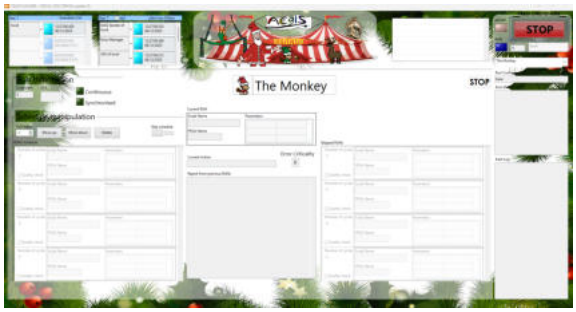

(C) AEGIS during Christmas.

(D) AEGIS during Easter.

(E) AEGIS during Halloween.

FIGURE A.1: Versions of the CIRCUS window with different <*GUI_Skins*> as used in AEGIS experiment.

versions of the logo for Holiday periods (Christmas, Easter, and Halloween), where characters "put on costumes" to match the given period, e.g. ALPACA becoming a reindeer for Christmas. FIGURE A.2c to FIGURE A.2e show how logo is updated for each period. These skins are available in CIRCUS [150] without the custom characters of AEGIS.

A.2 Monkey icon

The Monkey µService is one of the main µService in the autonomous operation of CIRCUS. Therefore, a dedicated icon was created for this µService. Furthermore, some custom skins for the

(A) Default.

(B) AEgIS.

(C) AEgIS during Christmas.

(D) AEgIS during Easter.

(E) AEgIS during Halloween.

FIGURE A.2: Versions of the CIRCUS logo for different periods as created for the AEgIS experiment.

Monkey were created for different periods. All variations of the Monkey icon are shown in FIGURE A.3.

(A) Default Monkey icon.

(B) Monkey as Santa for Christmas.

(C) Monkey as Easter Bunny for Easter.

(D) Monkey in a hula skirt in the summertime.

(E) Monkey as Darth Vader for May the 4th (Star Wars celebration day).

FIGURE A.3: Display of the number of Monkeys controlled by the Tamer.

A.3 Tamer indicator

The Tamer indicator, which is located in the bottom left corner of the µService, updates according to the number of Monkey µServices controlled by the Tamer. The indicator can show between zero and four Monkeys, where four means ≥ 4. Moreover, the picture of the Tamer in the indicator updates based on the *Tamer-<GUI_Skins>.png* parameter. FIGURE A.4 shows how the display graphic updates depending on the number of Monkey µServices, with FIGURE A.4c and FIGURE A.4d showing the skin of the Tamer for Christmas and Halloween.

(A) Zero Monkeys.

(B) One Monkey.

(C) Two Monkeys with the Christmas skin of the Tamer.

(D) Three Monkeys with the Halloween skin of the Tamer.

(E) Four or more Monkeys.

FIGURE A.4: Display of the number of Monkeys controlled by the Tamer.

Appendix B

Custom ARTIQ-based library

The ARTIQ environment provides functions for the hardware operations, which in the context of the bigger experiments can be considered low-level. They are subsequently used within an `EnvExperiment` class, the default ARTIQ parent class for all experiments, that defines a sequence of operations. The experiment consists of four functions: `build()`, `prepare()`, `run()`, and `analyze()`. The environment supports a library-based approach of creating routines of experiments. Therefore, a custom library architecture for the AEgIS experiment was created. The *Antimatter Experiment Real-time Integration of Artiq Libraries and Sinara Technology* (AERIALIST) is the library structure designed by Dr Saiva Huck for AEgIS [63]. The structure of the schematic view of the architecture is shown in FIGURE B.1.

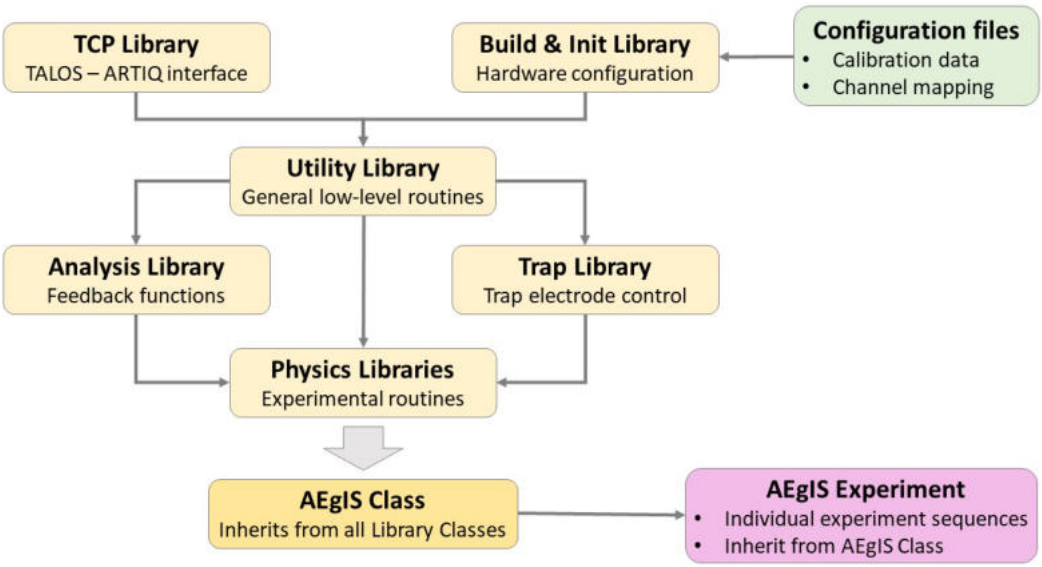

FIGURE B.1: The library structure of the AERIALIST as used at the AEgIS experiment. Each library defines a class, which all the experimental scripts of AEgIS inherit from.

The creation of the AERIALIST greatly simplifies the development of experimental procedures at AEgIS. It adds another level of abstraction, allowing less experienced users to quickly understand the function's goal without needing to delve into the complex implementation of the functionality.

Furthermore, the main experiment class of the ARTIQ was overwritten in the AERIALIST. This is shown in the LISTING B. The implemented AEgIS class overwrites the `run()` function and exposes two new functions to the end User: `experiment()` and `closure()`. This allows for three main improvements to the control code.

Firstly, each experiment is now unified, following the same structure by default. It starts with the `build()` function, which is called by the internal infrastructure of ARTIQ. Each script in AERIALIST in its `build()` function performs the initialisation of the Sinara crate it requires. Following, the `StartRun()` function is executed, which establishes communication between Sinara and TALOS. Then, the `experiment()` function is called, where the User can enter their sequences. Ultimately, the script concludes with the `closure()` function, where the User inserts any code intended to be executed at the end of the experiment. These are safety functions, such as turning off high voltage on crucial devices that were used. Then, the `StopRun()` function is called, which informs TALOS that the script has finished.

Secondly, having a unified `run()` function allowed for the introduction of error handling to all the scripts. This is done with AEgIS defined errors that follow the return code structure of `BANANA` (custom error criticality code defined in TALOS). This makes the system more robust when executing the scripts in autonomous operation. Whenever a `BANANA` is raised, the error is caught, and the `closer()` function is called before TALOS is informed that something was wrong with the `StopRun()` function.

Lastly, the unified `run()` function enabled the implementation of the `TerminationFlag` in the AEgIS system. It allows for running only the `closure()` function to terminate the script properly. With the `TerminationRequested` flag, each script can have a unique set of commands that can be run whenever some problems occur instead of having a global stop script. This is especially important when unexpected errors occur, which can terminate the script without proper error handling. Afterwards, the system can rerun the script with the `TerminationRequested` flag to execute the `closure()`, ensuring that every device was stopped correctly.

```
class _AegisExpOfficial(*Libraries):

    def experiment(self):
        pass

    def closure(self):
        pass

    def build(self):
        pass

```

```
12     def run(self):
13         try:
14             # Start procedure
15             self.Simplified_Init()
16             if self._TerminationRequested:
17                 # termination requested means that the run was closed,
    and we try to run the closure for safety
18                 self.GracefulTermination()
19 
20             self.StartRun()
21             self.core.reset()
22             # Experiment routine
23             self.experiment()
24         # Exception handling and script closure
25         except Banana as error:
26             self.ExceptBanana(error)
27         except RTIOOverflow as error:
28             self.ExceptKernelBanana(error)
29         except Exception as error:
30             self.ExceptException(error)
31         finally:
32             # Closing
33             print("Starting closure procedure...")
34             # Post-measurement cleanup
35             self.closure()
36             self.Send_SyncChecks_to_DAQ()
37             self.StopRun(self.RetCode)
38             return
```

LISTING B.1: The code implementation of the overwrite of the ARTIQ experiment class for AEgIS. The `run()` function is explicitly overwritten, and the two new functions, `experiment()` and `closure()`, are exposed for the end User to overwrite.

Appendix C

TALOS framework

TALOS is the underlying control system framework at AEgIS. Dr Marco Volponi designed its structure. It was extensively described in two publications [60], [61] and a PhD thesis [62]. The following is a short overview of the framework and its main components.

TALOS was designed to address common problems encountered when developing control systems for nuclear, atomic, and quantum experiments. The main requirements of the system are:

- general enough design such that the framework can be considered experiment-agnostic,
- inherently safe to operate under various environments,
- scalable and easily expandable,
- future-proofed and reliable.

The framework addresses these conditions with its modular design, self-checking capabilities, and distributed architecture. TALOS is considered the framework, as it provides the system's inner structure through the implemented classes, while exposing the control system developer to a handful of Virtual Instruments (VIs) to be overwritten, allowing the definition of custom behaviours and actions while maintaining the system's internal logic.

The framework is founded on two main pillars:

1. everything is a MicroService,
2. system follows a distributed architecture.

The MicroService (or µService for short) is an independent, autonomous piece of code with a limited set of responsibilities (for example, controlling a single device or detector, or monitoring a specific environmental parameter). Each µService is run asynchronously side-by-side within the system. They can interact with each other (and with outside systems) through a built-in messaging system. The µServices inherit from the common class defined in TALOS called *Father of All µServices* (FOAM). This adds code uniformity across all µServices and retains the framework's maintainability without affecting user-defined code. According to the first pillar, the entire control system code should be divided into small, easily maintainable parts that can be isolated from the system (misbehaviour of a single µService shouldn't affect the entire system).

The second pillar introduces a single process running on every machine in the system. This is achieved by a Guardian that monitors the state of all other Guardians on the network and the

status of µServices present on the PC. It unifies each PC as a single entity under Guardians and simplifies the communication between computers in the system. Communication is handled via a TCP connection between computers, which is subsequently relayed to specific µService if needed.

To implement all the features, the framework is built on top of the LabVIEW™'s implementation of the Actor model [151]. The Guardian is the root actor on the PC, while all the µServices are nested actors of the Guardian. The structure is shown in FIGURE C.1.

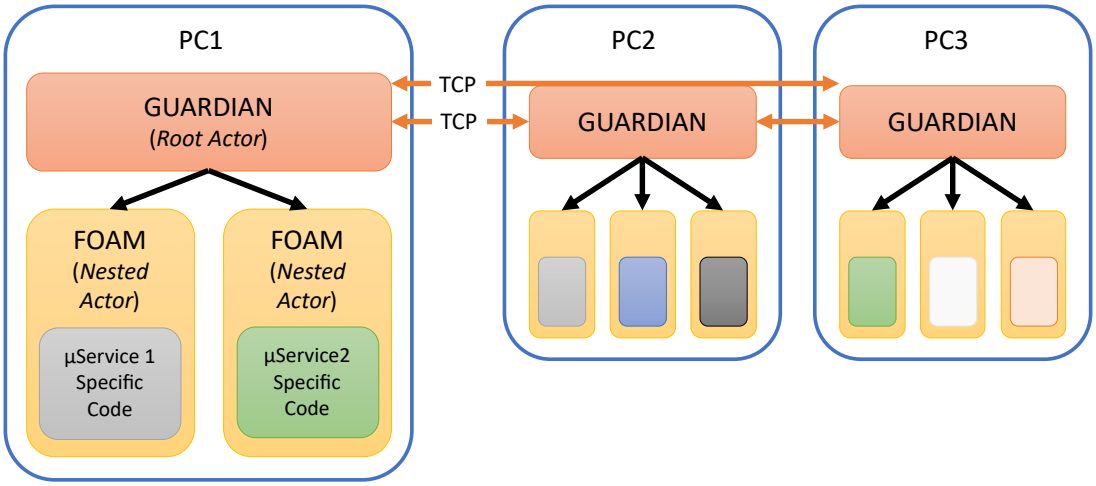

FIGURE C.1: The TALOS framework structure. Each PC has a Guardian running as a root actor and the µServices as the nested actors of the Guardian (taken from [61]). Communication between the computers is via TCP between individual Guardians.

C.1 Guardian

The Guardian is the root actor of all µServices for each PC in the system. The actor hierarchy in the system is flat, which simplifies the interface between µServices and the Guardian without imposing any limitations on the system's development and growth.

The Guardian is the core of the TALOS system. Firstly, it establishes network communication, handling the communication between Guardians and µServices in the distributed system. Secondly, it is responsible for monitoring the system's status, including other Guardians on the network and the µServices present under that Guardian. If any Guardian notice misbehaviour, it can put the system in *Safe Mode*. It is a state which firstly calls all µServices to perform the user-defined action for the *Safe Mode* (for example, turning off high-voltage), after which the system becomes idle and doesn't respond to messages. A manual intervention (pressing *Reset ABORT*

button on the front panel of a Guardian) is required to bring the system back from the *Safe Mode*. The monitoring of the system is implemented with three watchdogs:

- Guardian Watchdog: each Guardian sends a period message to all other Guardians present in the network. The message timestamp is checked against the last-seen timestamp for the Guardian. If the time difference exceeds a specified value (defined in the TALOS configuration file), the Guardian is marked as unresponsive, and the system enters *Safe Mode*.

- µServices Watchdog: each µService sends a message to its Guardian. The Guardian then checks the timestamps in the same way as done in the Guardian Watchdog. If the µService is marked as unresponsive, the system attempts to restart it by first stopping the µService and then starting a new instance. If this operation is successful, the system returns to its normal state, but ensures that any measurement is retaken. Otherwise, the system enters the *Safe Mode*.

- `ABORT` Watchdog: To ensure that the system enters *Safe Mode*, a shared variable (SV) was introduced on the network. Whenever this boolean variable, called `ABORT`, is set, all Guardians are notified about the event, and the *Safe Mode* can be called. This variable should be a singleton on the network; however, it is not a trivial problem. The `ABORT` Watchdog periodically scans the network for the `ABORT` SV. In the absence of the variable, a new instance of the variable is created and set to *True* (putting the system in *Safe Mode*). Suppose more than one `ABORT` SV is present. In that case, all Guardians whose name is later in the alphabet will un-deploy the variable, leaving only a single instance deployed.[1]

A TALOS configuration file defines the list of PCs that make up the distributed system. Furthermore, each Guardian has a list of µServices that it should start during the booting process. These µServices are checked before starting any experimental sequence to make sure that the minimum required µServices are present in the system.

C.2 Father of All Microservices

A µService is a standard building block of the TALOS-based system. It is a small, self-contained program that operates a specific device or performs a specified task. It is a good practice to limit

[1] In the most recent update of the system, the support for shared variables was removed (which is removed in newer versions of LabVIEW™). The `ABORT` is replaced with two boolean flags in Guardian's data. One with the current value of the `ABORT` and the other as the "bearer" flag. The "bearer" flag shows which `ABORT` flag should be considered as the original value, making all the others effectively copies. The `ABORT` Watchdog works similarly, but instead it makes sure that only one Guardian is marked as the "bearer".

µServices to single tasks; however, sometimes it is beneficial to combine some tasks into a more complex µService. Each µService is a child of the parent class called *Father of All Microservices* (FOAM). This class is a nested actor of Guardian, which means that all µServices are automatically a nested actor working asynchronously side-by-side thanks to the class inheritance. Therefore, each µService inherits also the *Queued Message Handler* (QMH) structure, which is at the heart of the Actor Framework. The simplified schematic diagram of the QMH is shown in FIGURE C.2. Thanks to the QMH, the µService can react to internal or external events and messages to the µService via the *Event Handler*. Based on the events, the µService can perform specified tasks which are handled by the *Consumer* part of the QMH structure.

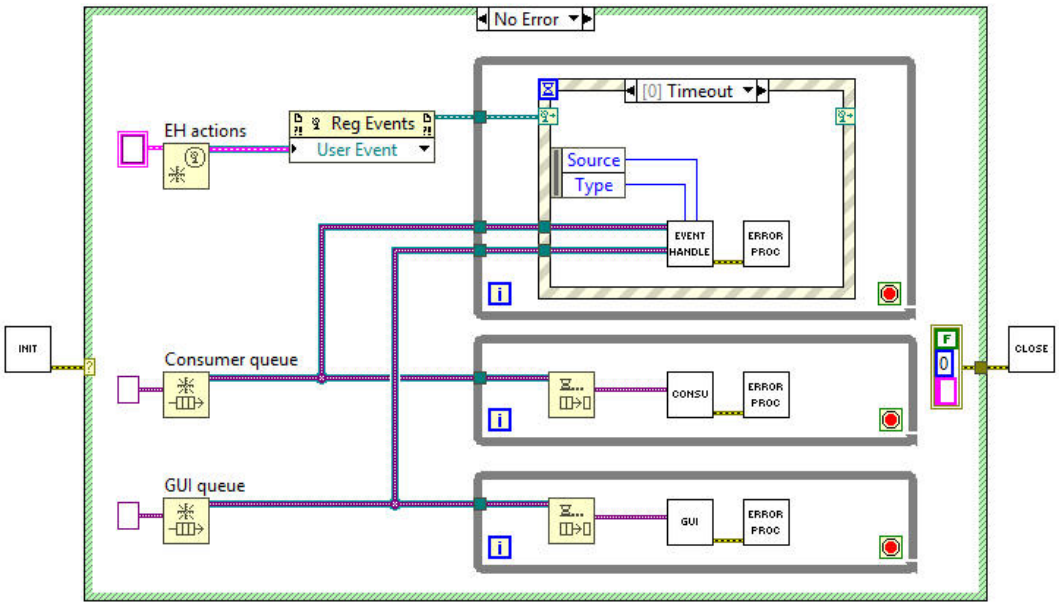

FIGURE C.2: Schematic diagram mimicking the behaviour of the µService (inspired by [62]). It is based on the Queued Message Handler. This architecture requires two parallel while loops that exchange messages. One loop (the top loop) handles events, such as a button being pressed or an external message. This loop enqueues actions executed by the consumer loop (the middle loop). An additional loop (bottom loop) can be used to handle updates of the GUI.

Making all µServices a child of FOAM hides the complexity of the Actor Framework from the end user and makes developing new µServices much simpler. Moreover, it allows for "backend" development without affecting the User's code of the µService.

Each µService has to override several VIs to perform specific tasks. These VIs are:

- <µService Name>.ctl - container for storing the private data of the µService.

- *Init* - This VI is called before the µService starts and can be used to initialise connections or read the configuration file.
- *Close* - This VI is called during the shutdown of the µService. It should be used to close all open connections and related resources.
- *Consumer* - This VI defines the execution processes in the consumer loop of the QMH. Individual cases of the Consumer should take less than the *µService Watchdog Timeout*, or the µService will be marked as unresponsive.
- *Event Handler* - This VI defines the processing of events in the event loop of the QMH. The predefined events that can be called are:
  - Button Pressed: invoked by pressing a button on the µService GUI.
  - Message: invoked by receiving a message, for example, from another µService.
  - Ready to launch?: called at the beginning of each Schedule. This event should perform a self-check of the µService and the response (True/False) should be returned to the control µService (Tamer).
  - Start Run: called at the beginning of a run.
  - Stop Run: called at the end of a run.
  - Safe Mode: called whenever the system enters the *Safe Mode*.
- *µService GUI*: Defines the graphical user interface (GUI) of the µService.
- *Process Error*: This VI is called whenever µService generates an error. It can be used to filter out errors or perform specific actions based on the error code.

The VIs for override can be left untouched if no custom code is needed.

Furthermore, the µService inherits default methods defined for the FOAM class, which significantly simplifies the development process. Inherited methods include, but are not limited to:

- *Send to Consumer* - enqueue a case for the consumer loop,
- *Update GUI* - update the value of the indicator/control on the graphical interface of the µService,
- *Message to µService* - send a message to another µService in the system.

It is often the case that a single hardware device is used for different purposes. For that reason, TALOS provides a simple *Hardware* class that can be used as a parent to any hardware device implementations. It is recommended that the hardware class define the device's low-level control. The specific hardware class can then be used within the private data of the µService and called within the overridden VIs to perform more complex tasks.

C.2.1 Father of All Detectors and Detector Managers

Given the similarity of operation of many detectors, a dedicated hardware class that inherits from the *Hardware Class* was implemented into TALOS. This class, called *Father of All Detectors* (FOAD), provides basic methods for override that are common to detectors:

- *Init* - initialise the device. This method is called at the start of the µService, and can also be called via a button.
- *Set Config* - sets a configuration for the detector.
- *Arm* - ready the device for the acquisition.
- *Acquiring* - polls the status of the acquisition. If the data is present, the program moves to *Save Data*. In the event of a timeout, the program moves to *Stop*.
- *Save Data* - retrieve the data from the device, then format and save it in a specified location (locally and/or on the DAQ).
- *Stop* - stop the acquisition.
- *Close* - shutdown the device. This method is guaranteed to be performed at the shutdown of the µService but can also be called via a button press.

The FOAD is used to define the *Detector Manager* class in TALOS. It is a class that can be used as a parent for any µService that is responsible for a detector. It provides a standardised GUI with a sub-panel area that the User can fill to visualise data from the detector. This approach greatly simplifies implementing µServices for detectors into the system. The User is required to define the device class that inherits from FOAD and then create the *Detector Manager* with the overridden sub-panel.

C.3 Config class

The *Config* class is a part of every µService but can also be used outside the µService. Thanks to the class, each µService (and, by extension, each detector) can use a text-format configuration file. This file can define different configurations as sections, each with its own parameters. This approach is beneficial for the FOAD classes. Detectors often can have multiple configurations, each defined for a different measurement. These configurations can be defined in a single text file and loaded with a single button on the detector's front panel, or via a message to the µService. Configuration files greatly simplify the process of creating new detector setups in FOAD.

C.4 Core µServices

One of the most powerful features of the CIRCUS system is its ability to schedule and autonomously perform experiments. This scheme leverages the advantages of the TALOS framework through a series of specially designed µServices that work in tandem. The following sections explain the role and the design of the main µServices.

C.4.1 Error Manager

A core component of any autonomous system is error handling. TALOS reacts to every error generated in any of its parts (error leaving the VI with the error cluster indicator). Errors that occur in the ARTIQ layer of the system are caught by the internal structure of the AEgIS experiment class implemented in AERIALIST (see Appendix B). These errors are then recognised by the Kasli Wrapper µService (see section C.4.3.1). Furthermore, TALOS can accept errors from external devices via TCP messages. This feature provides a foundation for ensuring the system's safety and security.

During the development, the errors are substituted within the LabVIEW™ code block, with the help of TALOS's *Substitute Error* VI. This VI converts the error that enters the VI into an error that is defined in the *TALOS Errors* and *CIRCUS Errors* files. The files contain a list of error codes, each accompanied by a description of the error and its corresponding criticality level. Error conversion is crucial, as the same error can be interpreted differently depending on the code's context. All the errors are then collected and handled by a specific µService called *Error Manager*. The µService retrieves the information about the error criticality and updates the system accordingly.

Error criticality takes values ranging from 0 to 4. Each criticality code corresponds to the proper action by the autonomous system (see C.4.4). In the event of encountering an error with criticality level 4, the *Error Manager* updates the `ABORT` flag to True, and the system enters *Safe Mode*.

This design proved reliable across multiple unsupervised system sessions. The error implementation at the AEgIS has over 500 user-defined errors.

C.4.2 Class structure of CIRCUS scheduling

A single *run* is an ARTIQ script [2] with parameters. A *run* is implemented in CIRCUS as the *Run Instance* class.

[2] The script can be replaced with any sequence of operations that can be executed by the appropriate *FPGA Wrapper* (see section C.4.3.1)

As is customary in physics experiments, a single *run* with specific parameter values can be executed multiple times in a row, either to collect statistical significance or to mitigate hardware issues. Therefore, CIRCUS implements *Schedule Cell* class, which stores information about the *Run Instance* together with the number of repetitions for this script. Furthermore, a more complicated cell can be defined. For example, the *Optimiser Cell* inherits from the *Schedule Cell* and overrides some of the functionalities. In the *Optimiser Cell*, the number of repetitions defines the maximum number of iterations for the optimiser (see sections C.5.2 for more details). The inheritance allows both *Schedule Cells* and *Optimiser Cells* to be in the same list called *Schedule*.

The *Schedule* class defines a sequence of runs to execute. It is an array of *Schedule Cells*, and it implements methods for manipulation of the schedules, such as:

- *Add Run.vi* - Adds *Run Instance* to the end of the schedule. If the *Run Instance* matches the class instance in the last *Schedule Cell*, the number of iterations in the *Schedule Cell* is increased by a specified number of iterations. Otherwise, a new *Schedule Cell* is created with the specified number of repetitions.

- *Add Cell.vi* - Adds a specified cell to the beginning or the end of the Schedule. The VI compares the *Run Instance* of the new *Schedule Cell* with the existing one and either adds the number of repetitions if the *Run Instances* are the same or appends the cell to the array.

- *Append Schedule.vi* - Combines two *Schedule* classes. The last and first *Schedule Cell* of the first and the second *Schedule* are compared as in the *Add Cell.vi*. The rest of the second *Schedule* is appended to the first.

- *Move Cell.vi* - Moves the specified cell in the *Schedule* one index up or down.

Furthermore, it records whether the Schedule is executed in continuous mode. The continuous mode allows for repeating a specified series of experiments indefinitely.

The *Run Block* class defines the current scope for the autonomous execution of experiments. This object stores the series of experiments to be executed (as the *Schedule* object), the current run (as the *Run Instance* object), and the list of skipped experiments due to errors (as the second *Schedule* object). Furthermore, this class provides all the necessary functionality for managing a series of experiments, allowing for retrying, skipping, or stopping the current script. *Run Blocks* are used by the Monkey µService in its autonomous operation (see sections C.4.4 C.5 for more details).

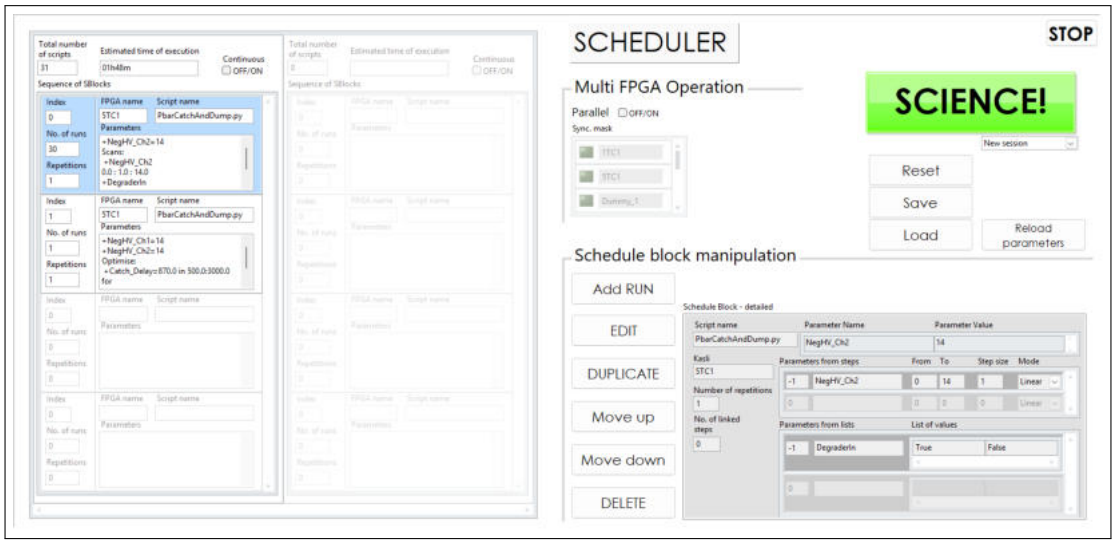

FIGURE C.3: A screenshot of the Scheduler µService GUI. It has five main action buttons in the top-right corner, excluding the "STOP" button. The big, green "SCIENCE!" button can be used to send schedules to the *Tamer* µService for execution of defined runs. The "Reset" button allows the User to clear the currently defined sequences on the GUI. The "Load" and "Save" buttons can be used to load-/save defined sequences from/in a file. The "Reload parameters" updates the list of known parameters which can be selected from the drop-down menu when defining a *Schedule SBlock*. On the left, the sequences of *Schedule SBlocks* are shown. When parallel operation is enabled, the Schedule for each FPGA will appear in separate columns. The control for enabling parallel operation is available in the middle section labelled "Multi FPGA Operation." The "Sync. mask" is populated with FPGAs identified by CIRCUS. All FPGAs which are selected in the "Sync. mask" will have their *Schedules* executed with the same starting time enforced. The "Schedule block manipulation" section allows for adding, updating, re-arranging, or removing *SBlocks* from the scheduled sequence. The *SBlock* for manipulation can be selected by pressing the desired *SBlock* in the defined sequence.

C.4.2.1 Scheduler

To ease the creation of schedules, a µService called Scheduler was created. Interaction with this µService is the first step for every experimental session. The GUI of the Scheduler is shown in FIGURE C.3. The Schedule is created from so-called *schedule blocks* (*SBlocks* for short), which define a small sequence of *Schedule Cells* allowing for easier creation of longer schedules. There are currently two types of *SBlocks* that can be defined: *Scan SBlock* and *Optimiser SBlock*. The *SBlocks* are defined via a pop-up window, shown in FIGURE C.4.

The *Scan SBlock* defines a schedule for a single script, with parameters changed between runs based on the specified combination. The *Scan SBlock* offers multiple options for defining

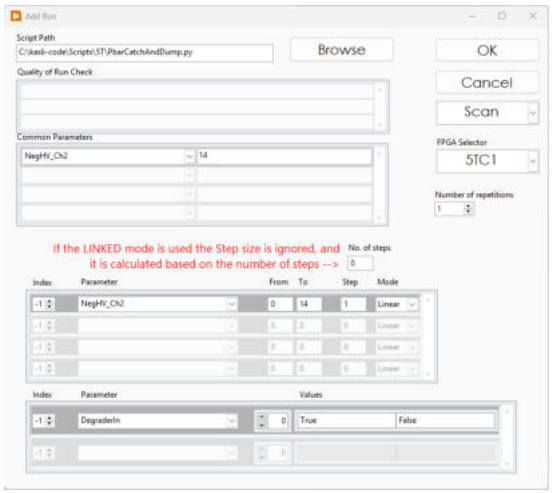

(A) *Scan SBlock*. It creates a series of *Schedule Cells* with parameters changing according to the scan option. It allows for performing scans over multiple parameters (see text for more details).

(B) *Optimiser SBlock*. It creates an *Optimiser Cell* used to perform optimisation tasks (see text for more details).

FIGURE C.4: Screenshots of the pop-up Add Run window used to define a *Schedule Block*.

how the parameter changes: linear, logarithmic, or from a list. After defining which parameters should change and how, the Schedule is created with all possible combinations of those parameters. The value of a numerical parameter (x) is calculated based on the initial value x_0 and final value x_f and the step-size dx. There is also the possibility of linking the numerical parameters to perform a linear scan. This feature creates a schedule that updates m parameters simultaneously in n steps. The calculation of each parameter value is shown in TABLE C.1 along with the number of values created for the scan. This creates a schedule of N *Schedule Cells*

$$N = (n_{link} + 1) * \prod n_k, \tag{C.1}$$

where n_{link} is the number of steps used for the linked parameters and n_k is the number of different values for the k-th parameter.

The *Scan SBlock* also enables ordering of the scanned parameters. This arrangement is done by changing the index of the scan parameter. Lower index values mean a deeper scan level. Let's say we have two parameters to scan *Parameter1*$= [10, 20, 30]$ and *Parameter2*$= [a, b, c]$. Setting index value to 0 for *Parameter1* and to 1 for *Parameter2* will create series:

$$(10, a), (20, a), (30, a), (10, b), (20, b), \ldots, (30, c).$$

TABLE C.1: Calculation of the i-th parameter in different scan options and the restrictions for the values used.

scan option	x_i	restriction	number of values
linear	$x_0 + i \times da$	$dx \neq 0$	$\lfloor \frac{x_f - x_0}{da} \rfloor + 1$
logarithmic	$x_0 \times dx^i$	$dx > 1$ $x_0 > 0$ $x_f > 0$	$\lfloor \log_{dx} \left(\frac{x_f}{x_0} \right) \rfloor + 1$
linked	$x_0 + i \times \frac{x_f - x_0}{n}$	$n \geq 1$ $x_0 \neq x_f$	$n + 1$

Setting index as 1 for *Parameter1* and as 0 for *Parameter2* will create

$$(10, a), (10, b), (10, c), (20, a), (20, b), \ldots, (30, c).$$

The default index value is −1, which means that parameters will be scanned in the order they appear on the Add Run Window. If two parameters have the same, non-default index, they will be scanned in alphabetical order.

The *Optimiser SBlock* defines the optimisation problem for the system. The optimisation is one of the powerful features of the autonomous system, and it is only possible if the system has access to the analysed data at the end of the run. Therefore, it uses the *Analysis Framework* to perform the optimisation. In the AEgIS Collaboration, ALPACA is used as the *Analysis Framework* (see section 5.4). The optimisation problem is defined by specifying the parameters to be optimised. They can be numeric (integers or floating-point numbers, also known as doubles) or categorical (represented as strings). The system will update the parameters based on the *Analysis Framework* 's response. The system is optimised for a specific observable. The problem can be defined as maximisation, minimisation, or convergence to a specified value.

Furthermore, each run can obtain a quality-of-run query. It is defined with a string of the form <*observable name*><*comparison mode*><*value*> (e.g. *antiprotons_count<1000* checks if the observable called "antiproton_count" has a value greater than 1000 at the end of the script). All standard comparison modes are supported ("<", "<=", "=", ">=", ">"). All white spaces will be removed from the quality check query at runtime.

The CIRCUS system supports multiple FPGAs; hence, the Scheduler allows defining numerous schedules. The configuration of the operation mode is done in the "Multi FPGA Operation"

section of the µService GUI. There, it is possible to specify whether the Schedule should be executed in sequential or parallel mode. In parallel mode, the User can define the synchronisation mask, i.e., which FPGAs should synchronise script execution across their schedules. The performance of synchronisation in the parallel mode is presented in section 5.5.5.1. Switching between sequential and parallel mode splits the current Schedule into separate sequences for each FPGA. Switching back to sequential combines all schedules into a single instance by concatenating them.

The Scheduler µService also allows for appending runs to an already running schedule. This action can be done by using the selector below the "SCIENCE!" button:

- *New session* - send the schedule(s) as the main operation.
- *Append to bottom* - add the defined schedule(s) to the end of the current run session.
- *Append to top* - add the defined schedule(s) to the beginning of the current run session. Runs from this Schedule(s) will be executed before continuing the previously scheduled runs.

By default, the *New session* is created. When any of the append options is selected, the "SCIENCE!" button changes to "APPEND." If there is an active run session when using *New session* or there isn't any session when using *Append* option, a warning will be displayed, and the action will be ignored.

C.4.3 FPGA Interface

The control system of a quantum experiment requires a ns-precision for some operations. This requirement is achieved with a Field Programmable Gate Array chips (FPGA). Therefore, CIRCUS needs a way to control an FPGA. *FPGA Interface*, provided by TALOS, can be used to implement control of different FPGA types by any experiment. In the case of the AEgIS experiment, the FPGA is included in the Kasli controller that ARTIQ/Sinara provides.

The *FPGA Interface* declares methods that are used by the system to perform operations. The methods were based on the implementation for ARTIQ's Kasli, but they can be easily adopted for other FPGA systems. Furthermore, a dedicated µService needs to be defined that can execute a submitted *Run Instance*. At the AEgIS experiment, this µService is called the Kasli Wrapper (detailed in the section C.4.3.1).

The declared methods are:

- Check Run Build.vi - VI for checking if the script scheduled for execution is addressed for the currently used FPGA. The method is used by the Monkey µService during autonomous operation (see section C.5). This VI can always return True if the experiment doesn't require

any specific checks before execution. In the case of the AEgIS experiment, the check makes sure that the build function used in the script is the same as the requested device (see Appendix B for details about the ARTIQ code of AEgIS).

- Create Map of Parameter Names.vi - VI for retrieving all the parameters for the specified FPGA. It creates a mapping between the FPGA's name and the parameters defined for its scripts. This VI is used by the Scheduler µService to populate the pop-up window and allow the User to select a parameter from the drop-down menu instead of typing the name. If the VI returns an empty Map, the Scheduler won't provide any parameter suggestions during schedule creation, and all values will need to be entered by the User.

- Find script.vi - This function is used to create a *Run Instance* object without specifying the full path to the script. The Scheduler never uses this option. It was introduced to allow the Kasli Wrapper µService to execute a single script by simply providing the script name.

- Get FPGA Name from Script.vi - This VI returns the name of the FPGA based on the path to the script for the execution. The Scheduler uses it to determine which FPGA to use when creating a schedule. The FPGA can also be selected by the User building the Schedule.

- Get FPGA uService ID.vi - based on the FPGA's name, return the unique ID of the µService that controls the FPGA. This VI is used by the Monkey µService to determine which µService should be called for execution of the script. At the AEgIS experiment, the µService ID is created as FPGA's name + " Kasli Wrapper."

- Get list of Names.vi - This VI returns one list of FPGA names and the second list of FPGA IPs. This VI is called directly by the TALOS at the Guardian init.

- Get Path for Scripts.vi - Returns the path to the directory that stores the scripts for all FPGAs. The Scheduler uses it to open the directory when browsing for the script in the Add Run window.

- Init.vi - This VI is called directly by the TALOS at the Guardian init and is the moment of creation of the FPGA Interface object.

The FPGA Interface is required to utilise all the system's capabilities; therefore, it is necessary to define all the functions for the FPGA being used. The second part required for interfacing between CIRCUS and FPGA is the dedicated µService for executing commands. This µService needs to implement two specific messages, "Submit Script" and "Terminate Script."

The "Submit Script" is sent by the Monkey µService during the autonomous operation. It has the *Run Instance* object and the DAQ control selector (On, Off, External) as the message data. The DAQ control data is used to determine whether the DAQ is controlled by the script (option On), is not used (option Off), or is regulated by the Tamer µService (option External).

The "Terminate Script" message is sent by the Monkey µService after the User requests termination of the currently running script. This message contains only a single boolean field as private data, indicating whether termination should be graceful. In the case of the Kasli Wrapper, graceful termination stops the script and then executes the `closure()` method of the same script.

C.4.3.1 Kasli Wrapper

The Kasli Wrapper µService is an essential component of autonomous operation, as it implements the methods for executing scripts. The execution is performed using the ARTIQ management system. The Kasli Interface defined for the AEgIS experiment is configured with a configuration file. Because the system works with multiple Kasli controllers, the file is divided into sections. The first section, called "ARTIQ," defines the global parameters for all devices: the path to conda (a package and environment management system for Python) [152] for Python environment control, and the name of the conda environment. The other sections are controller-specific, including: the repository path for script execution (the directory containing the device_db.py file for the particular Kasli), the device IP, and the four communication ports (as stated in the ARTIQ documentation [153]).

The Kasli Wrapper µService was written as a general class for controlling any Kasli at the AEgIS experiment. When a new instance of that µService is created, the Kasli is selected based on the µService ID (format is Kasli name + "Kasli Wrapper"). Based on the Kasli name and the configuration file, the µService starts the master shell (which calls *artiq_master* with the necessary arguments) that waits for new scripts to be submitted. With each call of the "Submit Script" message, a new shell is opened that submits a script (calls *artiq_client submit* with necessary arguments). The client and master shell logs are saved and displayed in the GUI.

This µService has information only about the currently running script and the DAQ status. The simple design of it as a wrapper for executing functions on the Kasli allows for easy exchange of Kasli for another FPGA in the system by defining a new µService.

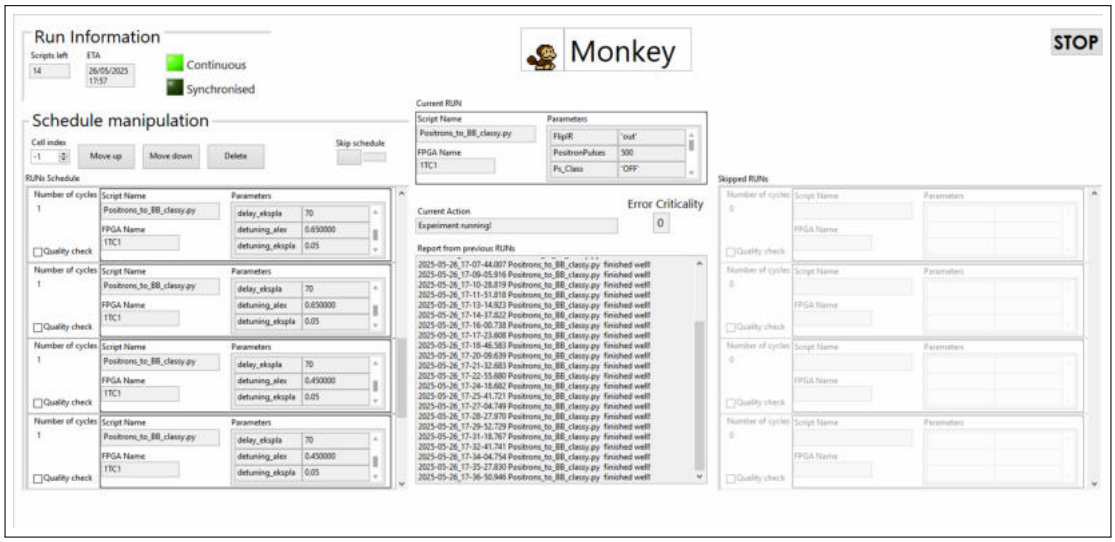

FIGURE C.5: A screenshot of the Monkey µService GUI. The left panel indicates the list of runs remaining in the current run session. In the middle, the currently executed script is displayed, with the history of actions Monkey has taken shown below. On the right, the list of skipped runs is shown. This list is populated whenever a run has finished with a criticality level of >1 or was skipped by the User.

C.4.4 Monkey

The Monkey µService is the core part of the automation process. This µService is responsible for deciding what to do with scripts from the Schedule received from the Scheduler. The Monkey keeps track of the current status of the system thanks to the continuous updates from the Error Manager µService. It saves the highest error criticality level that occurred during the script's execution. At the end of the script, it receives an update from the Kasli Wrapper with a *Basic quAlity Notification After the eNd of an Action*, or `BANANA` for short, which encodes the script's status. The `BANANA` is then recalculated together with the error criticality level according to the equation C.2.

$$\texttt{BANANA} = max(errorcriticality, \texttt{BANANA}) \tag{C.2}$$

The `BANANA` can take one of five possible values:

- 0: *Continue* - Everything finished well. The system will execute the next script.
- 1: *Retry* - There was a minor problem in the execution (e.g., some data was not saved). Since the error is most likely a one-time occurrence, the script will be re-executed to ensure that all scripts in the Schedule finish correctly.

- 2: *Skip* - There was a problem that prevented the completion of the script (e.g. an incorrect configuration for a detector was provided). Since the error is based on the defined operation itself, the script cannot be repeated. It will be skipped, and the following script in the Schedule will be tried.
- 3: *Stop* - There was an error during the operation (e.g., the Kasli controller not responding). This error is a serious problem that the system itself cannot solve, and it isn't script-dependent. Therefore, there is no reason to continue with the Schedule. The Monkey skips the remaining Schedule and is idle.
- 4: *Abort* - A critical error happened (e.g. one of the Guardians is not responding). At this moment, executing any scripts unsupervised is not safe. The system enters the *Safe Mode*. The Monkey skips the Schedule and becomes idle, ignoring any requests to execute scripts.

At the end of the script, with `BANANA` =0, the Monkey can call the analysis framework to perform further actions, such as optimisation or quality checks. The full decision tree is shown in FIGURE C.6.

The µService GUI allows for the inspection of the current operation. It displays the Schedule that Monkey still needs to execute, the current run being executed, and the scripts that were skipped. It also displays the highest error criticality that Monkey encountered and the history of results from all scripts so far. Furthermore, the µService offers the possibility to fine-tune the Schedule by changing the order of the scripts or removing them entirely from the Schedule. The alignment of runs in the schedules in synchronised parallel mode is not assured when the Schedule is modified in a single Monkey. The µService also provides an Estimated Time of Arrival (ETA). It is calculated as an average time of execution (time between submitting the script and receiving the `BANANA`) based on the last 10 scripts. The GUI of the µService is shown in FIGURE C.5.

C.4.5 Tamer

The CIRCUS control system is designed with the operation of multiple, independent FPGA chips in mind. With the Monkey µService, it is possible to operate any FPGA as a single machine. The object-oriented design of the system allows spawning multiple Monkey µServices to operate multiple FPGAs at the same time. To ensure the proper execution of the scripts on each Monkey, another µService called Tamer was created. The Tamer is used as a message distributor. It receives all the `BANANA` messages from the Kasli Wrappers and error criticality codes and forwards them to the appropriate Monkey(s). Furthermore, it serves as the starting point for each

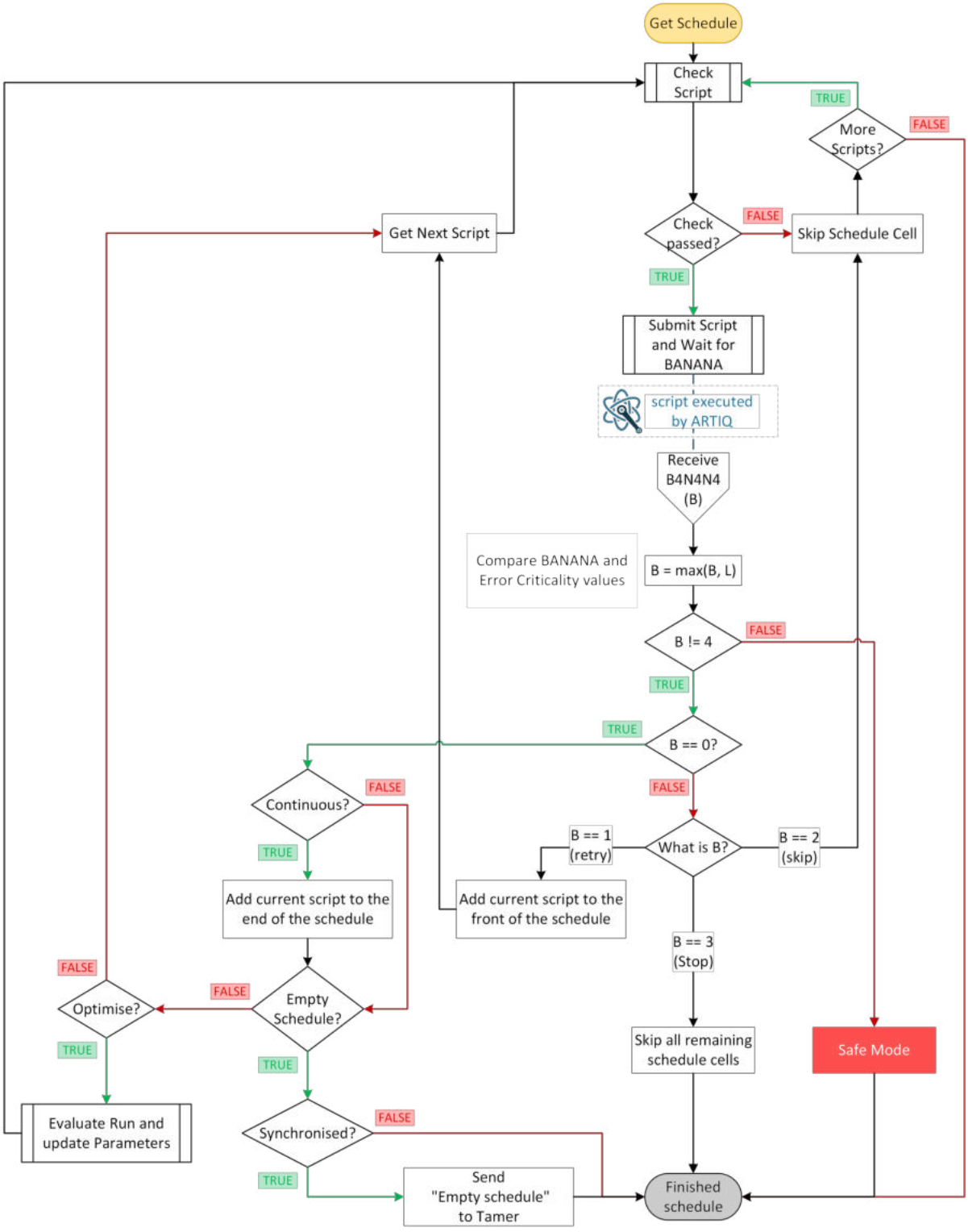

FIGURE C.6: A flow chart depicting the decisions made by the Monkey µService during execution of scripts.

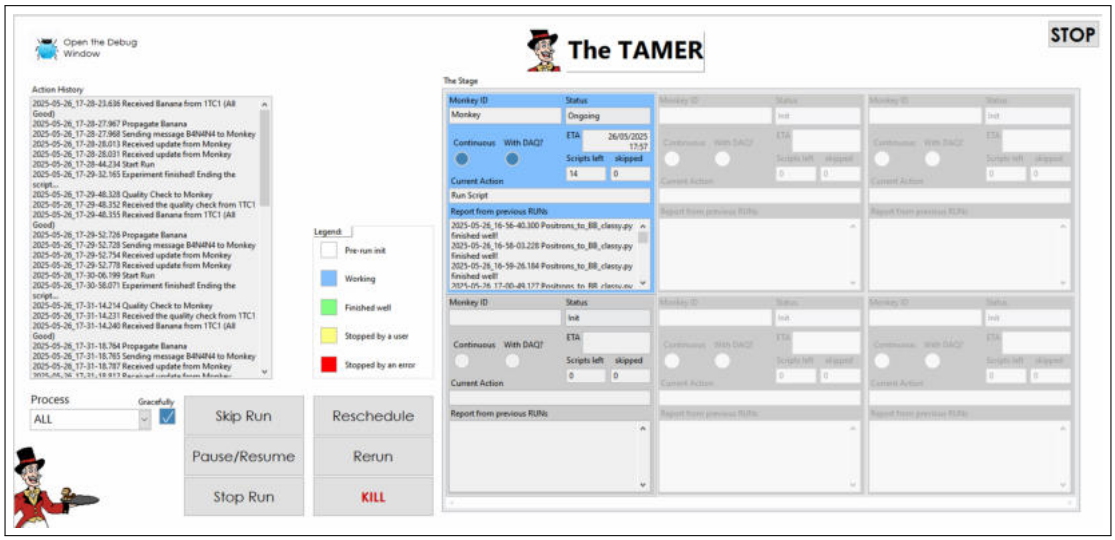

FIGURE C.7: A screenshot of the Tamer µService GUI. It shows the overview of all running Monkey µServices on "The Stage." The history of Tamer's actions is shown on the left. It allows for requesting five actions to Monkey specified with the "Process" selector: "Skip RUN," "Pause/Resume," "Stop Run," "Reschedule," "Rerun." All Monkey and Kasli Wrapper µServices can be stopped with the "KILL" button. In the top left corner, there is an option to "Open the Debug window" for inspecting the internal memory of Tamer.

Schedule. The Scheduler µService sends a schedule message with all the schedules and the synchronisation mask. The Tamer then starts all the necessary system µServices (Monkeys and Kasli Wrappers) and performs necessary checks before starting each Schedule (checking if all Guardian are online and all µServices present are ready to start).

The introduction of the Tamer greatly simplifies communication within the system during operation, as the Tamer is the single recipient of crucial messages. It also allowed for the implementation of synchronised and asynchronous parallel operation of the system. The Tamer groups Monkeys into processes based on the synchronisation mask received from the Scheduler.

The GUI of the µService was created to try to show all the necessary information in compact form. It is shown in FIGURE C.7. There is a panel showing the action history. It is updated when Tamer receives or sends a message from/to µServices. The status of each Monkey currently operating is shown in the middle as a 3x2 grid, allowing up to six Monkeys to be shown at once. The scroll bar below the Monkey status can be used to see the status of additional Monkeys. The µService provides six basic actions:

- *Skip Run* - ask all Monkey(s) to skip the current script. The script is stopped, and the Monkey(s) move to the next cell in the Schedule.

- *Pause/Resume* - ask Monkey(s) to Pause or Resume. Pausing the Schedule means that the Monkey won't send the next script for execution, but it will complete the current script.
- *Stop Run* - ask Monkey(s) to stop the current script and skip the remaining Schedule, effectively halting the entire run session.
- *Reschedule* - ask Monkey(s) to send the list of skipped runs to the Scheduler. This option allows the User to modify the parameters of the skipped runs before repeating them.
- *Rerun* - ask Monkey(s) to use the list of skipped runs as the new Schedule. This action can be helpful when the User has resolved the error that resulted in the skip action, and scripts can be tried again.
- *KILL* - requests the system to stop the Monkey(s) and FPGA Wrappers used.

The action is performed for all the Monkeys in the specified process, or for all the Monkeys currently working in the system.

Furthermore, there is the *Open Debug Window* option. It is a pop-up window that always stays on top. It allows seeing more details of the current status (mapping between Monkeys and FPGAs, received `BANANA` messages, Guardian and µServices checks, and more) without unnecessary visual clutter for the usual operation. This feature is handy at the beginning of the Schedule, when the system performs the "Ready to launch" check. During this process, all Guardians and µServices perform a check and need to respond to Tamer. Guardians check if all µServices from their list of µServices needed are running. Each µService performs a check that the programmer defined. There are three states for the "Ready to launch" messages received by the Tamer as displayed in the *Debug Window*:

- green - check passed;
- red - check failed;
- white - no response.

This information helps to pinpoint what is stopping the system when starting a new schedule. Whenever a check from the Guardian fails, a µService needs to be started on the corresponding PC. The name of µService can be identified by finding µServices that didn't respond.

C.5 Autonomous operation

One of the most valuable features of the CIRCUS is the autonomous operation. The system can execute a predefined series of experiments without any supervision. It is implemented via a

close cooperation of core µServices, that is, Tamer, Monkey, FPGA (Kasli) Wrapper, and the Error Manager together with the Sinara system controlled by ARTIQ. The system operates in a master-slave scheme, where roles are switched throughout the execution.

At the beginning, the role of the master is taken by TALOS. The Schedule(s) are defined in the Scheduler µService. After pressing the *SCIENCE* button, the Tamer µService receives Schedule(s) and performs necessary checks. First, the Tamer analyses the Schedule to determine how many Monkeys and FPGA Wrappers are needed. Next, all Guardians and µServices are asked if they are ready to start a new schedule. Each µService will perform the *self-check* that is defined for each µService (for example, a check if the device is powered on, the connection to the device is correct, etc.). Each Guardian checks if it has all the necessary µServices, as defined in the configuration file, present. They also make sure that they can see all the other Guardians on the network. The Tamer receives all the responses. If any µService or Guardian responds with a "no-go" message, the system will rerun the check, asking Guardians and µServices again. Some problems can be automatically solved by µService or Guardian itself. If the problems persist, the Tamer stops, and an error is shown notifying that Guardians and/or µServices aren't ready to start the Schedule. At this moment, the User needs to intervene.

After all the checks pass, the Schedule is sent to the Monkey(s) to begin the autonomous execution. The Monkey(s) sequentially execute the Schedule. The µService checks the script, then submits it to the FPGA. At this stage, the master role is assigned to the FPGA, and TALOS becomes the slave, waiting for instructions from the FPGA. All µServices can respond to incoming messages received via a TCP connection. The AERIALIST includes a library with the TCP calls for all messages defined by µServices. The messages are usually called in a non-blocking manner from the script. The FPGA is unaware of the system's status and whether the message was executed correctly. TALOS does the system monitoring and error handling throughout the execution of the entire Schedule. The system can terminate the run at any point if an error of sufficiently high criticality is encountered, thereby protecting the system from damage. When the run is finished, the `BANANA` message is sent to the Monkey. At this stage, TALOS regains control once again. The Monkey performs the checks at the end of a run. If the run was completed correctly, the Monkey can then perform the *Quality of run check* and the *optimisation*, if defined in the Schedule. Then the Monkey moves to the next run in the Schedule.

The run can have one of five outcomes, as defined in section C.4.4. The execution of the Schedule continues until it is either empty or an error with a criticality level of at least 3 is encountered. At the end of the Schedule, the Tamer notifies that the Schedule has finished, displaying an appropriate message depending on whether the Schedule was fully or partially executed.

C.5.1 Quality of run check

Each *Run Instance* can define a list of observables to be checked at the end of the script. This feature, called Quality of run check, is performed by the Monkey using the analysis framework. At the end of the script, the Monkey asks the analysis framework to retrieve the necessary observables. The values are then compared according to the rules defined during creation of the Schedule in the Scheduler (less than, less than or equal, equal, greater than or equal, and greater than). For example, "Beam_Intensity*acq_0*value > 1e6" will repeat any run with less than one million $\overline{\text{p}}$ delivered from ELENA. This feature ensures that the system executes the entire Schedule and collects meaningful data while unsupervised.

C.5.2 Optimiser

One of the most powerful capabilities of the CIRCUS system is its ability to solve optimisation problems, all done online with real data, as soon as it becomes available. This process is essential in experiments like AE$\overline{\text{g}}$IS, which perform complex operations, with a changing environment. The optimisation is achieved through the interface between the control system and the *Analysis Framework*.

To perform an optimisation task, a special *Optimisation Cell* must be defined in the Schedule. This cell contains information about the optimisation strategy (maximisation, minimisation, or convergence to a specified value) and the observable. A list of observables could be defined with a weight for which the final target value will be calculated as $\sum w_i x_i$, where w_i is the weight for observable x_i. The *Optimisation Cell* also contains information for the parameter space, including the names of the parameters, their types (integer, floating-point, or categorical), and the possible range (categorical types take a list of acceptable values). Moreover, the cell contains the number of exploration runs (runs in which the optimiser uses randomly chosen parameter values) and the maximum number of optimisation runs.

During the execution of the Schedule, the *Optimiser Cell* is executed with a set of parameter values. At the end of the script, given that `BANANA` =0, the Monkey asks the *Analysis Framework* to calculate the observables of interest for the optimisation. Then it asks the *Analysis Framework* again to suggest a set of new values. These values are inserted into the *Optimiser Cell* and the cell is rerun with the new values. The process repeats until the number of runs exceeds the initially specified limit or the *Analysis Framework* indicates that convergence has been reached.

The history of the optimisation (parameter values and the estimated target value) is stored in a CSV file. This file allows pausing the optimisation and resuming later without losing progress

by reloading previously evaluated points. It is also helpful as a monitoring tool for plotting relationships between parameters and the target value, or the evolution of the target value over iterations.

The optimisation process was tested in the operational environment. One example task performed by the system is the optimisation of the antiproton beam entering the experiment to maximise the number of trapped $\overline{p}$. The $\overline{p}$ beam that ELENA delivers can be steered by regulating 20 correctors, electrostatic devices (12 dipoles and 8 quadrupoles) that can bend the beam of charged particles, which are installed in the beamline between ELENA and AE$\overline{g}$IS. Initially, the correctors were controlled by four parameters (vertical and horizontal offsets and angles). These values are easy for humans to understand; however, the convoluted relationship between these parameters and the voltages set on the correctors creates a complex parameter space: setting specific values on a parameter changes the acceptable range for the other parameters. With the optimiser, the beam steering can be performed by directly controlling the individual correctors. The correctors work in pairs, with the same amplitude but opposite polarity of potentials. Therefore, the optimisation is done with 10 parameters instead of 20. The example of beam steering optimisation is shown in section 9.1.1.

Appendix D
Implementation of relevant hardware µServices

The current control system of AEgIS consists of around 50 unique µServices, from which some operate as stand-alone µServices, while the others are defined as parents for children with different configurations. The total system running consists of around 130 µServices working on six different PCs. In this section, the µServices that were relevant to obtain the physics results are shown.

D.1 Degrader Ladder Manager

The *Degrader Ladder Manager* is a µService that controls the actuator which moves in/out the degrader ladder (see section 5.2.8). A Trinamic TMCM-1311 controller controls the actuator. A dedicated hardware class was created to define simple methods for operating any motor. This class hides the complexity of using the library of the controller by providing simple methods for starting and stopping rotation of the motor, moving motor to a specific position (in microsteps), disabling or enabling the limit switch for the controller, getting the current position (in microsteps) of the motor, setting the current position[1] (in microsteps). The self-check for the device is performed by first verifying that communication between the PC and the controller can be established, and then checking if the required voltage for the motor is supplied (this is a command that can be requested of the controller). This class is then used inside the *Degrader Ladder Manager* to communicate with the device.

The controller operates the motor attached to the linear actuator; therefore, a conversion from rotation to linear displacement is required. This calculation is done by the µService. One complete rotation of the motor corresponds to a movement of 3 mm. One rotation is $360°/0.9° = 400$ motor steps. Each step is split into 256 microsteps, which gives the conversion ratio of 102 400 microsteps per 3 mm. The µService allows the User to specify the desired

[1] This command overwrites the current position of in the controller without moving the motor. It is useful, for example, whenever the controller resets due to a power cut.

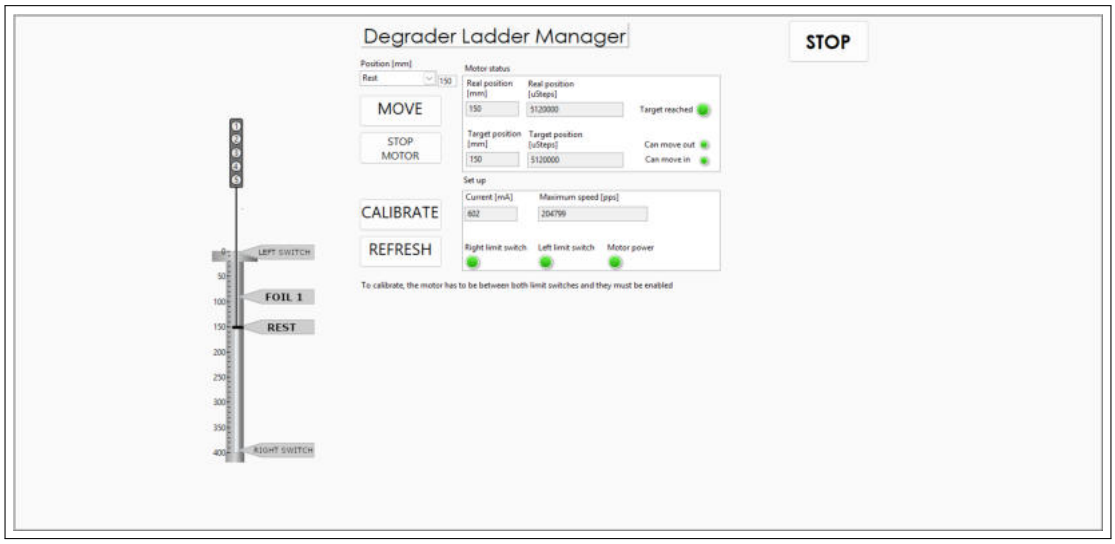

FIGURE D.1: The front panel of the *Degrader Ladder Manager*. The "Motor status" shows information about the current position, the target position, and the state of limit switches. The position can be selected from the predefined values using the "Position [mm]" selector or by entering the desired value in the control. The rotation of the motor can then be started with the "MOVE" button and stopped at any time with the "STOP MOTOR" button. The bottom panel, called "Set up," displays general information about the controller's initialisation. This panel can be updated with the "REFRESH" button. The calibration procedure of the motor can be started with the "CALIBRATE" button.

position in mm. Furthermore, it contains a list of predefined positions, which are summarised in TABLE D.1. There are four types of positions:

- Foil #i - position for inserting the i-th foil in the beamline.
- Rest - the minimum position at which the degrader ladder is entirely out of the $\overline{p}$ beam. This position is defined to minimise the distance required to insert/remove the foils, as the actuator speed is limited to protect the thin foils.
- View #i - position when the i-th foil is placed on the axis of the viewport of the vacuum chamber. This position is used to inspect the state of the foils.
- OUT - position where the actuator is below the vacuum valve. This position is crucial for the system's safety. Whenever the degrader ladder is positioned above this point, the valve cannot be closed, as the actuator physically blocks it.

The current position, in microsteps, is saved in a file. This file is updated every time a position of the motor is read (every 1 s). Whenever the µService is started, that file is used to restore the motor's position, ensuring that calibration isn't required after each reboot of the µService.

The µService provides all the essential information on the front panel (see FIGURE D.1). The

TABLE D.1: Predefined positions of the degrader ladder at AE$\bar{g}$IS. The first 5 positions are defined such that the foil with the corresponding number is inserted into the path of antiprotons. The view positions are used to align the corresponding foil with the viewport.

Position	Value [mm]
Foil 5	7.0
Foil 4	27.0
Foil 3	48.0
Foil 2	69.0
Foil 1	89.0
Rest	150.0
View 5	310.0
View 4	331.0
View 3	351.0
View 2	373.0
View 1	390.0
OUT	395.0

information about the motor status includes current position and the target position (both in mm and in microsteps). The current position is also indicated via a visualisation of the actuator with the degrader ladder. Furthermore, it indicates whether the limit switch has been reached (with two indicators, "Can move out" and "Can move in"), as well as an indicator to show when the target position has been reached. This panel is auto-updated every 5 seconds. The information about the motor's settings includes the limit for the supplied current to the motor. The maximum rotation speed for the motor in microsteps per second (the speed is set to 2 rotations per second, which corresponds to 6 mm s^{-1}). It also has three indicators. Two indicators are used to indicate whether the limit switches are ignored (the indicator is red); otherwise, it is green. The last indicator shows whether the controller receives enough power (this is checked by retrieving information about the supplied voltage, and checking it against the motor requirement: 48 V). This panel is updated after the motor is initialised.

The front panel of the µService has four buttons and one selector for the User to interact with. The selector is used to define the position for the foil. It can be selected from the drop-down list (as defined before), or a user-specified position can be used. To move the actuator to the selected position, the User needs to press the *MOVE* button. The motor can be stopped at any point by pressing the *STOP MOTOR* button. The *REFRESH* button forces the update of all information on the front panel. The last button *CALIBRATE* performs the calibration of the motor position. The calibration is done by slowly moving the actuator out until the limit switch

is tripped. The limit switch stops the motor, and the current position is set to zero microsteps, which corresponds to the position in mm of the limit switch.

The hardware class is general enough to be reused by other devices that can be controlled with the TMCM-1311 controller. Thanks to this approach, the class is utilised by a rotary actuator located inside the beamline to insert the MCP into/out of the beamline. Furthermore, the same controller setup will be used to control the rotation of gratings used in the Moiré deflectometer during gravity measurements at AEgIS. That's why a more generalised version of the µService for operating motors controlled by the TMCM controllers was created. The documentation for this µService is attached to this thesis in Appendix E.

D.2 Captorius Manager

This µService is an example of using the *Detector Manager* and FOAD classes to implement an acquisition of a new detector into the system. "Captorius" is a name used for Teledyne LeCroy oscilloscopes at AEgIS. The *CAPTORIUS* class inherits from FOAD, and it implements all the essential functions for controlling the readout devices of a detector. It utilises low-level functions from the *LeCroy Wave Series* LabVIEW™ library for direct communication with the device, which Teledyne LeCroy provides.

The *Captorius Manager* is the first µService that uses the configuration file approach for defining device settings for different measurements. Thanks to the configuration file, defining a new configuration for the device requires a simple modification of a text file. This approach proved to be a powerful solution, especially relevant when there are parallel developments for measurements on multiple physics fronts. Since then, many more µServices were reworked to use the configuration files, with the goal for all detectors to be based on the configuration files[2].

The *Captorius Manger* is a good example of how FOAD and the class structure defined in TALOS simplifies the development process for new acquisition devices. The AEgIS experiment uses two "Captorius" oscilloscopes. Each of the oscilloscopes has a dedicated µService called *Captorius 1 Manager* and *Captorius 3 Manager*. Each Manager only requires overriding the *Init.vi* in which the VISA resource name, along with the device name for the specific piece of equipment, is specified. With setup, it is possible to easily introduce any new "Captorius" oscilloscopes by solely creating a copy of the existing Manager and changing the two values specified in the *Init.vi*.

The "Captorius" oscilloscope is a crucial device across all fronts of the physics studied at AEgIS. They are often directly connected to the MCP detectors and used as the readout for the

[2] In the newest version of TALOS, each µService and FOAD supports a dedicated configuration file with the name *<class name>.ini*.

currents on the phosphor screen, making them frequently used for measurements in $\overline{\text{H}}$, Ps, and HCI campaigns.

Details about setup and usage of the *CAPTORIUS* and *Captorius Manager* μServices, as well as the usage of the configuration file, are described in the documentation written for the μService attached to this thesis as the Appendix F.

D.2.1 Pulser Manager

Pulser is a device used to quickly open/close traps by applying a potential to an electrode with a pulse. A single pulser contains two cards (top and bottom). Each can control up to four electrodes, which gives a total of eight electrodes. However, a single card can pulse only one electrode at a time. The pulser has two inputs for triggers, and any of the triggers can trigger each card. Therefore, the pulser is capable of pulsing up to four electrodes simultaneously.

The Pulser Manager μService is used to define the signals created by the pulser. These settings include the amplitude of a pulse, the number of pulses (up to 255), the delay after the trigger, the duration of a single pulse, the interval of the pulse, and the electrode that should be pulsed. These settings can be configured using the front panel of the μService or by sending a message via TCP to TALOS. The pulser is triggered from ARTIQ with a TTL line connected between the Sinara crate and the pulser itself.

With the setup, the pulser can be easily prepared and later triggered from the ARTIQ script. Because the triggering is done with a TTL, the pulse can be applied with nanosecond precision, which is crucial for plasma manipulation inside a trap. Moreover, the pulser is an essential device for performing TOF measurements, as a clear definition of the start time (the time of opening the trap) is one of the primary sources of uncertainty in these types of measurements.

D.2.2 Rotating Wall Manager

Another μService that is very important for the plasma manipulation inside a trap is the *Rotating Wall Manager* that controls the waveform synthesiser used to perform the rotating wall (RW) technique for compressing/expanding plasma [86]. The technique uses a sinusoidal electric field applied to a segmented electrode. The waves applied to each segment are shifted by $2\pi / N$ in phase, where N is the number of segments. The applied electric field creates an effect on the plasma as if the entire trap was rotating (hence the name). The plasma experiences additional torque that modifies its angular momentum. By applying the RW technique, it is possible to

counteract the radial expansion of the plasma inside a trap that is a consequence of imperfections in the electric field of the trap.

The RW can also be used to expand the plasma. The final effect of the application of RW depends on the frequency and amplitude of the applied sinusoidal wave f_{RW}. FIGURE D.2 shows examples of the plasma shape achieved with different parameters of the RW. Any plasma inside the trap experiences a radial electric field that leads to the rotation of the plasma inside the Penning-Malmberg trap. The frequency of the rotation of a uniformly dense cylindrical plasma inside a magnetic field B is described by:

$$f_E = \frac{\rho q}{4\pi\epsilon_0 B}, \tag{D.1}$$

where q is the charge of the particle that makes up the plasma and ρ is the density of the plasma; ϵ_0 is the vacuum permittivity. In general, applying the RW on the plasma with $f_{RW} > f_E$ increases the rotation of the plasma, which results in compression. Alternatively, by applying $f_{RW} < f_E$, the rotation of the plasma is slowed down, which expands the plasma inside the trap. In general, the compression of the plasma is a desired effect when working with trapped particles (as expansion may lead to losses); however, there might be cases where expansion is beneficial, like increasing the overlap of two trapped plasmas. Furthermore, by applying the RW to compress the plasma, the plasma's temperature increases (as its angular velocity increases). Because of this, the RW technique is usually coupled with an additional method for cooling the plasma, such as electron cooling.

The RW technique is established with an AD9959 DDS DAC-based custom-made controller that can supply pure sine waves from 0 MHz to 50 MHz. The maximum amplitude of 2.5 V can be achieved. This device is controlled by the *Rotating Wall Manager*. It has 8 channels that can be separately controlled; however, some electrodes of the Penning-Malmberg trap at AEgIS are used in tandem to create a longer RW region. Because of that, the μService defines the electrode type, which is then mapped to the channels of the device. For example, instead of setting the individual values for channels controlling electrodes P7 and P8 in the 5T region, both channels are set up by referring *5T_P7&P8* electrode type when providing the setting[3].

Each channel is capable of performing a sweep over amplitudes and frequencies. As a result, six parameters are available for each channel. Those are: sweep time, phase, amplitude start (starting voltage for the sweep), amplitude stop (final voltage for the sweep), frequency start, and frequency stop. Voltages are provided in V, and frequencies are provided in MHz.

[3]Each electrode can still be set separately with *5T_P7* and *5T_P8* for electrodes P7 and P8 respectively.

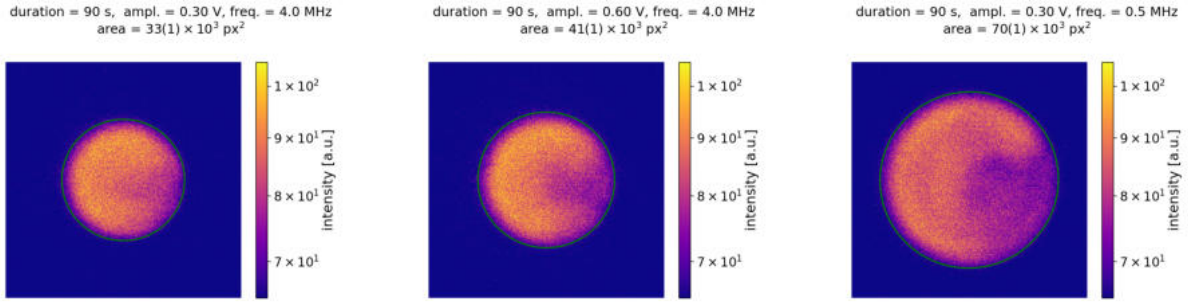

FIGURE D.2: Shape of positron plasma released from a trap after applying the rotating wall technique with different parameters. The left figure shows the best plasma compression achieved. The effects of using higher amplitude or smaller frequency are shown in the middle and right plots, respectively. The green circle indicates the region of the picture identified as the size of the plasma.

Appendix E

TMCM Rotor Manager

This document describes the main aspects of controlling a motor using a TMCM-1311 controller from Trinamic. The example controller setup shown in section E.1 was initially used to control the Degrader Ladder with thin Parylene foils and later refurbished for controlling the rotation of the MCP in the *HedgeHog* region.

E.1 Hardware

The controller used for the rotational motor is a Trinamic TMCM-1311 closed-loop stepper motor controller module. It is a blue colour controller that can be seen in Figure E.1. The controller

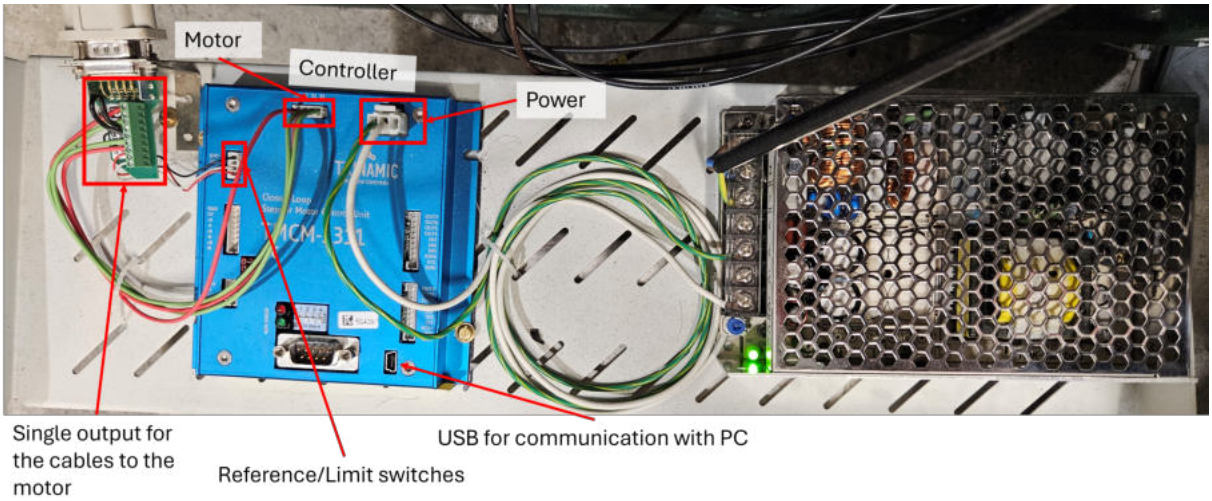

Figure E.1: Example of the TMCM setup used initially for the Degrader Ladder and later for the MCP rotation in the HH region.

allows for 256 microsteps ($\mu Steps$) per complete step of the motor, which, in combination with the Oriental PKP268MD28B stepper motor (used for degrader ladder and MCP rotation in the HH region), provides a minimum rotation of approximately $\sim 0.2°$ per microstep.

The micro-USB connection provides both communication between the controller and a PC, and power to the controller itself. The power for the motor is provided to the controller via the

external power supply. It supports supply voltage of +12 V to +48 V DC and can deliver up to 3 A, which is programmable in the software. The Oriental PKP268MD28B stepper motor requires 48 V at 0.6 A. The power to the motor is transferred via a four-line connection. Additionally, the controller supports directional limit switches, which can be configured to stop movement in one direction (turning right or left) when the switch (right or left, respectively) is tripped.

Figure E.1 illustrates the setup of the controller used for controlling the rotation of the MCP detector in the HH region. All required connections from the controller are collected in a single output, ended with a D-sub 9-pin connector. The layout of the pins and corresponding connector on the TMCM controller is summarised in Table E.1 along with the zoomed-in picture of the D-sub connector from Figure E.1.

Table E.1: Pin layout for the single output from the TMCM controller setup.

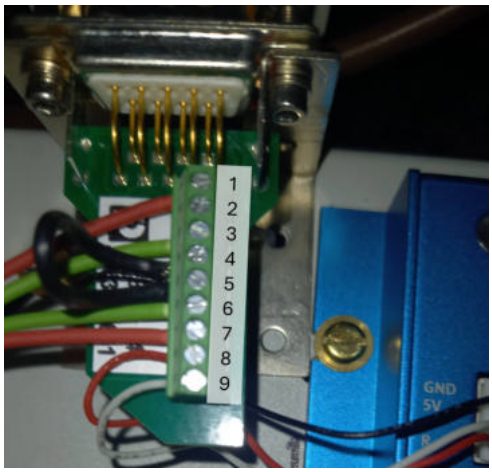

Pin no.	D-sub cable colour	Connection
1	Black	Motor B1
2	Brown	<empty>
3	Red	Motor A2
4	Yellow	Switch Right GND
5	Orange	Switch Left GND
6	Green	Motor B2
7	Blue	Motor A1
8	Purple	Right limit switch
9	White/Grey	Left limit switch

E.2 µService

The *TMCM Rotor Manager* is a general-purpose parent µService for operating motors with the TMCM-1311 controller. The front panel of the µService is shown in Figure E.2. The front panel is divided into three sections. The first section, located at the bottom right, is about the setup of the motor. It has three buttons:

- RECONNECT - Open the connection between the PC and the controller. This button will also reload the configuration file.
- REFRESH - Reads all parameters of the controller and updates all GUI indicators.
- CALIBRATE - Start calibration procedure.

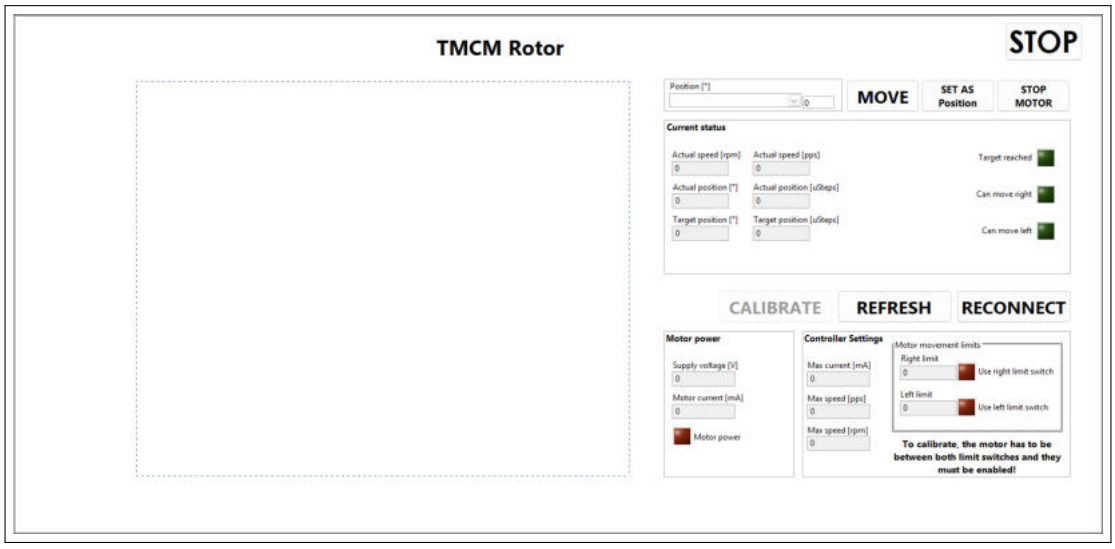

FIGURE E.2: The front panel of the *TMCM Rotor Manager* (a general µService for *TMCM*-based motors). The subpanel window used for visualising the motor position is indicated with dashed lines.

This section provides indicators regarding the motor's status. These values are updated only after a new connection with the controller is established or when the REFRESH button is pressed.

The second section, located in the top right corner, is about motor movement. It has three buttons:

- MOVE - Request motor to move to the angle position which can be selected from the predefined values from the *Position [°]* drop-down selector. The position can also be provided as a value specified in the box next to the selector. The positions are defined as an absolute value. The limit positions in the configuration file define the reference frame for the angles.
- SET AS POSITION - Redefine the current position as the value specified by the *Position [°]* selector.
- STOP MOTOR - Request motor to stop all movement.

Furthermore, it provides indicators about the current position and speed of the motor, as well as the status of the limit switches (whether the motor can rotate to the right/left).

The third section, indicated with the dashed line in FIGURE E.2, can be used to display the visualisation of the motor movement. It uses *Position visualizer.vi* to display a user-defined GUI for giving visual feedback on the movement of the motor.

E.2.1 Configuration file

The controller in the µService is set via a dedicated configuration file for the µService. It is divided into three sections. The first section, called *settings*, is used to define information about the motor/device's parameters. The parameters in this section are summarised in Table E.2. All parameters in this section are required in the configuration file.

Table E.2: Required parameters in the *settings* section of the configuration file for TMCM Rotor Manager

Setting name	Description	Accepted values
com_port	String with the name of the COM port to which the controller is connected to PC	String (e.g. "COM4")
motor_max_rpm	Maximum rotation speed of the motor in rotations per minute. This value is limited by a hard limit coded in the µService. By default, it is limited to 5 RPM of the motor. This can be overwritten in the child class.	Positive double values
motor_max_current_mA	Maximum current provided to the motor by the controller in mA	Positive integer < 3000
motor_steps_per_rotation	Number of steps of the motor to perform rotation by 360°	Positive integers
motor_rot_per_device_rot	Number of rotations of the motor to perform rotation by 360° of the connected device	Double values.

The second section, called *limit_switches*, defines the range of movement of the device controlled by the motor. The parameters in this section are summarised in Table E.3. All parameters in this section are required in the configuration file. By default, the "right" rotation of the motor is defined as positive speed, and the "left" rotation is defined as negative speed. To properly use the limit switches, the User must make sure that the right limit is greater than the left limit.

TABLE E.3: Required parameters in the *limit_switches* section of the configuration file for TMCM Rotor Manager

Setting name	Description	Accepted values
right_limit_switch_disable	Flag if the right limit switch is disabled	0 - enable, 1 - disable
right_limit	Position (in °) of the right limit switch	Any double value
left_limit_switch_disable	Flag if the left limit switch is disabled	0 - enable, 1 - disable
left_limit	Position (in °) of the left limit switch	Any double value

The last section, called *positions*, can be used to define named positions for the selector on the GUI of the µService. Parameters in this section follow the format **label = position**, with position provided in ° of the device.

E.2.2 Position conversion

The controller operates on $\mu Steps$; however, for human readability, the positions on the µService are converted to ° of the device connected to the motor. The position is calculated based on the two values specified in the configuration file: SPR_{motor} (motor steps per rotation) and R^{motor}_{device} (motor to device rotation ratio). The conversion $^{\circ \rightarrow \mu Steps}$ is calculated as:

$$\theta' \left[\mu Steps\right] = \frac{\theta \left[^{\circ}\right]}{360 \left[\frac{^{\circ}}{rotation}\right]} \times SPR_{motor} \left[\frac{Steps}{rotation}\right] \times 256 \left[\frac{\mu Steps}{Steps}\right] \times R^{motor}_{device}.$$

This conversion assumes that one pulse from the controller equals one $\mu Step$, which is a valid assumption in standard operation of a motor. In case of the Oriental PKP268MD28B stepper motor (as used for the rotation of the MCP in the HH region), which has a minimum step size of 0.9°, it has $SPR_{motor} = \frac{360}{0.9} = 400 \left[Steps/rotation\right]$.

With this approach, it is possible to easily define the rotation of the device controlled by the motor, even when a gear ratio exists between the motor and the device. For example, if one full rotation of the device equals 10 complete rotations by the motor, by defining 10 as the *_rot_per_device_rot* in the configuration file.

E.2.3 Calibration

The calibration process is based on the right limit switch. Because of that, there are two requirements for calibration to work:

1. The right limit switch needs to be enabled, which can be done inside the configuration file. If the right limit switch is disabled, the CALIBRATE button is also disabled.

2. The motor needs to be positioned such that when it rotates right, it will encounter the right limit switch.

The calibration is performed by rotating the motor to the right, with a maximum speed of 10 % (which can be defined in the configuration file), until the right limit switch is triggered. The motor is stopped, and the current value is set to µSteps corresponding to the right limit.

E.2.4 Creating children µServices

Thanks to the configuration file, creating a µService for a new motor controlled with the TMCM-1311 requires creating a new class that inherits from the *TMCM Rotor Manager* µService. The µService needs to implement only *Position visualizer.vi*, which is used to visualise the current position of the motor. Additionally, the µService requires a configuration file named as *<µService name>.ini*.

If the device connected to the motor requires a different hard limit for the motor's rotation speed than 5 RPM, the *Get Max Hard Speed Limit.vi* needs to be implemented in the child µService. This VI needs to return the maximum speed limit in pulses per second, which is directly compared with the value retrieved from the TMCM controller.

Appendix F
Captorius Manager

F.1 Hardware

"Captorius" is a name used at AEgIS for Teledyne LeCroy HDO6104 oscilloscopes. The oscilloscope can measure up to four channels simultaneously. Each channel has nine possible settings, and there are additional global settings available for use. These settings are described in section F.1.1. Each setting is defined as a new section in the configuration file. This approach significantly simplifies the use of the detector µService. Furthermore, it allows for updates of the configuration when the µService is in use.

F.1.1 Configuration file

Through the configuration file, users can define various settings for the oscilloscope. The default value is used if the parameter is not specified in the configuration file. Note that there is a single configuration file for the *Captorius.lvclss* hardware class. Below are described all possible available parameters for configuring different scope elements.

F.1.1.1 Configuring channels

The oscilloscope supports four channels. Each can be configured using the parameters described in Table F.1. Each parameter should be preceded by *channel_i_* where *i* is replaced with the channel index. The numbering of channels starts at 0; therefore, configuration parameters for Channel 1 will be preceded by *channel_0_*. The channel is disabled in the scope when no parameters are specified for the channel.

F.1.1.2 Configuring timebase

The time configuration of the scope, or horizontal axis, is common for all channels.

TABLE F.1: Channel configuration settings that can be specified in the configuration file for the "Captorius" detector. Each parameter must be preceded by *channel_i_* prefix, which specifies the addressed channel. Available channel numbers are $0, 1, 2, 3$.

Parameter name	Accepted values	Default value
bandwidth	"FULL", "20MHZ", "25MHZ", "200MHZ", "250MHZ", "1GHZ", "2GHZ", "3GHZ", "4GHZ"	"FULL"
vertical_coupling	"A1M", "D1M", "D50", "Ground", "DC", "AC"	"A1M"
probe_attenuation	All double values	-1.0
vertical_division_V	All double values	0.125
vertical_offset_V	All double values	0.0
interpolation	"Linear", "Sinx/x"	"Linear"
noise_filter	"None","+0.5 bit", "+1 bit", "+1.5 bits", "+2 bits", "+2.5 bits", "+3 bits"	"None"
sweeps_to_average	Positive integers	1
invert	Boolean values (Note that this value needs to be specified as strings "True" or "False")	"False"

F.1.1.3 Configuring trigger

The Captorius scope supports different types of trigger signals. The oscilloscope has multiple types of triggers. Each trigger option has a range of adjustable parameters. Selecting a specific trigger type can be done with the *trigger_type* option. All triggers supported by the oscilloscope: Edge, Width, Glitch, Runt, Interval, Qualify, State, Slew, Dropout, Logic, TV. For now, only the Edge trigger is implemented. If you want different triggers, please get in touch with the Control System Team of AEgIS.

TABLE F.2: Timebase configuration settings that can be specified in the configuration file for the "Captorius" detector.

Parameter name	Accepted values	Default value
timebase_s	All double values	5E-4
position_s	All double values	0.0
maximum_sample_points	50, 100, 250, 500, 1000, 2500, 5K, 10K, 25K, 50K, 100K, 250K, 500K, 1M, 2M, 2.5M, 5M, 10M, 25M, 50M, 100M	500

For external triggers, it is recommended by LeCroy to use the options "Ext" or "Ext10", as "External" is only included for backward compatibility of the software.

TABLE F.3: Trigger configuration settings that can be specified in the configuration file for the "Captorius" detector.

Parameter name	Accepted values	Default value
trigger_type	Edge	There is no default value
trigger_source	"Channel 1", "Channel 2", "Channel 2", "Channel 3", "External", "Line", "EXT", "EXT10"	"Channel 1"
trigger_slope	"Rising", "Falling"	"Rising"
trigger_level_V	All double values	0.0
holdoff_type	"Time", "Events", "None"	"Time"
holdoff_value_by_time_ns	All double values	50
holdoff_value_by_events	Positive integer values	1

F.1.1.4 Other options

Additional options that can be specified include configuring a continuous acquisition mode. If this option is "False", the *auto_trigger_enabled* is ignored.

TABLE F.4: Other configuration settings that can be specified in the configuration file for the "Captorius" detector.

Parameter name	Accepted values	Default value
continuous_acquisition_mode	"True", "False"	"True"
auto_trigger_enabled	"True", "False"	"True"

F.2 µService

At the time of writing this document, there are two Captorius oscilloscopes as summarised in TABLE F.5.

TABLE F.5: List of Captorius oscilloscopes used at AEgIS.

Name	Model	IP	µService
Captorius 1	HDO6104	128.141.59.191	Captorius 1 Manager
Captorius 3	HDO6104A-MS	128.141.59.226	Captorius 3 Manager

F.2.1 Adding new Oscilloscope

Adding the new oscilloscope that uses the same hardware class for communication between a computer and the detector requires creating a copy of one of the existing *Captorius Managers* µServices. In the *Init.vi* set two values for the *CAPTORIUS.lvclass* instance (as shown in FIGURE F.1):

- VISA resource name - name of the VISA line used for communication with the device. When using a remote control, the resource name can be set as **VICP::<ip address>::INSTR** or by using an alias.
- Device Name - a label for the device used in DAQ and errors to identify the specific device.

The alias for the device VISA resource can be set in *NI MAX* application under *My System > Devices and Interfaces > Network Devices* by pressing *Add Network Device*. The scope can be identified by its IP address, and a unique alias can be assigned to each scope.

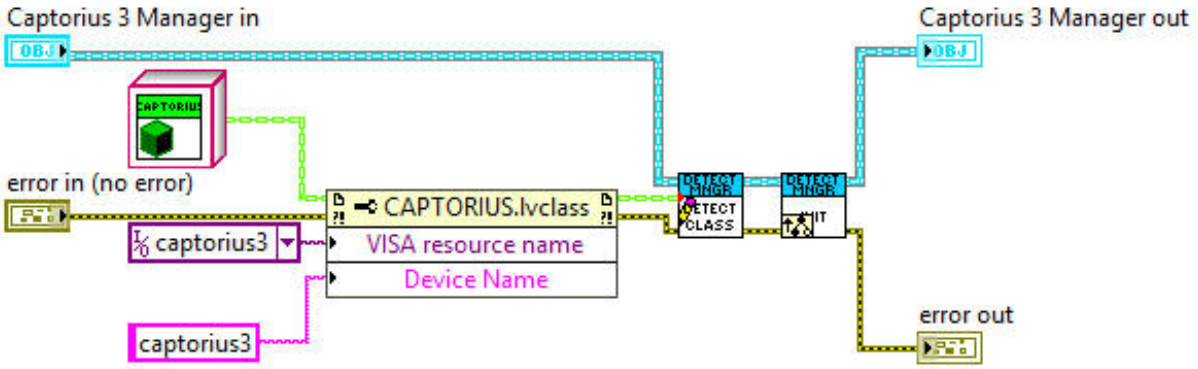

FIGURE F.1: Example *Init.vi* used in *Captorius 3 Manager* µService.

Appendix G

Code used to download data using IAEA-NDS API.

The Python script shown in LISTING G downloads the data from the database. Each isotope is identified by its number of protons (z) and neutrons (n), together with its atomic number. The mass of the isotope is stored in μAMU (atomic mass unit) in the database, which is then converted to AMU upon download.

```
import polars as pl
from urllib.request import Request, urlopen

def load_data(config_str:str):
    url = "https://nds.iaea.org/relnsd/v1/data?" + config_str
    req = Request(url)
    req.add_header('User-Agent', 'Mozilla/5.0 (X11; Ubuntu; Linux x86_64; rv:77.0) Gecko/20100101 Firefox/77.0')
    return pl.read_csv(urlopen(req),ignore_errors=True)

if __name__ == "__main__":
    data = load_data("fields=ground_states&nuclides=all")

    data = (data.select(['z','n','symbol','half_life_sec','atomic_mass','sn'])
             .filter(pl.col('z').is_not_null())
             .rename({'z':'Z','n':'N','sn':'neutron_separation_energy_keV','half_life_sec':'half_life_s'})
             .with_columns(pl.col("atomic_mass").mul(1e-6))
             )
    data.write_parquet("parquet/isotopes_info.parquet")
```

LISTING G.1: The Python script used to downlod the data from IAEA-NDS databases.

Appendix H

Validation of TOF simulation with antiprotons

The model described in section 6.3.7 was validated against electron-cooled antiprotons. The antiprotons were trapped between electrodes with $V_{wall} = -150$ V or $V_{wall} = -190$ V. Then they were launched from different launch potential V_{launch} in range from −100 V to −120 V for $V_{wall} = -150$ V and from −170 V to −180 V for $V_{wall} = -190$ V. For each experimentally measured spectrum, the best parameters for the simulated signals were found by implementing the least squares method:

$$LS = \sum_t \frac{\left[S_{data}\left(t\right) - S_{sim}^{norm}\left(t\right)\right]^2}{err_{data}\left(t\right)}, \tag{H.1}$$

where $err_{data}\left(t\right)$ is the error of the data point at time t. The best results of fitted simulations to the data are summarised in Table H.1. Figure H.1 to Figure H.7 shows the best fitted simulated signal on top of the experimental data. Each TOF plot is accompanied by the heatmap of the calculated LS for all simulated parameters.

Table H.1: Summary of parameters used in the model that simulates the TOF spectrum with the lowest least square (LS) for a given V_{wall} and V_{floor}. The last column gives the LS value calculated for the given parameters.

V_{launch} [V]	V_{wall} [V]	*spacecharge_min* [V]	*spacecharge_max* [V]	LS
-100	-150	0.10	0.14	0.04
-105	-150	0.18	0.32	0.14
-110	-150	0.16	0.24	0.08
-115	-150	0.04	0.14	0.10
-120	-150	0.26	0.32	0.06
-170	-190	0.00	0.08	0.08
-180	-190	0.06	0.26	0.20

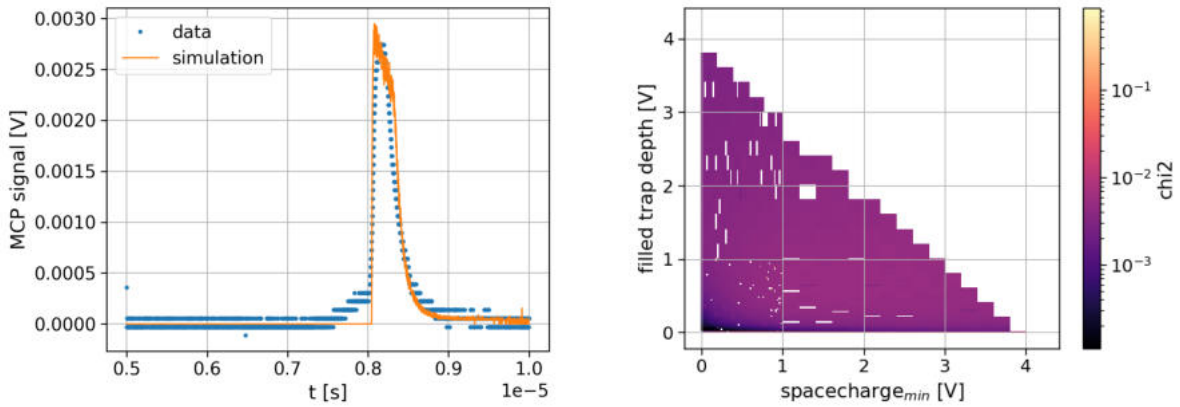

FIGURE H.1: The best fit of the simulated signal (in orange) to experimentally measured data (blue). Antiprotons trapped in $V_{wall} = 150\,\text{V}$ and launched from potential $V_{launch} = 100\,\text{V}$. Calculated LS for all simulated signals are shown as a heatmap (right).

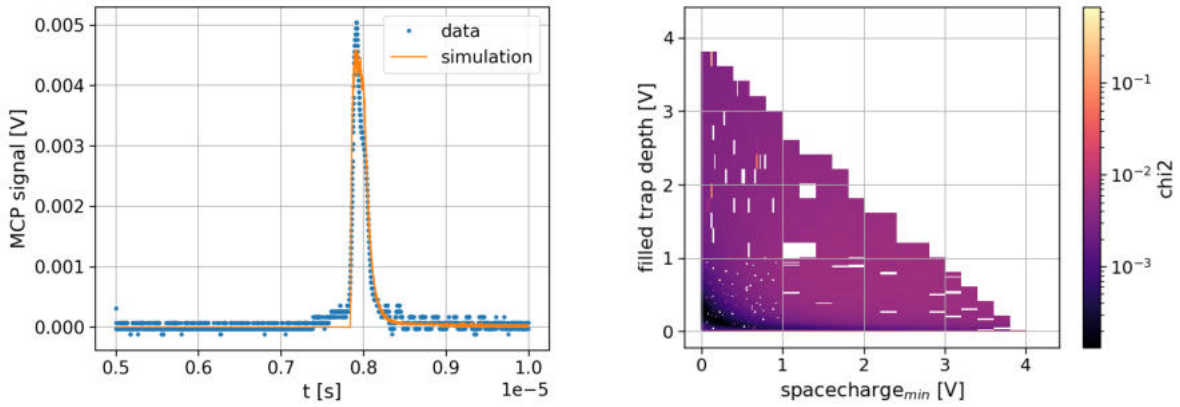

FIGURE H.2: The best fit of the simulated signal (in orange) to experimentally measured data (blue). Antiprotons trapped in $V_{wall} = 150\,\text{V}$ and launched from potential $V_{launch} = 105\,\text{V}$. Calculated LS for all simulated signals are shown as a heatmap (right).

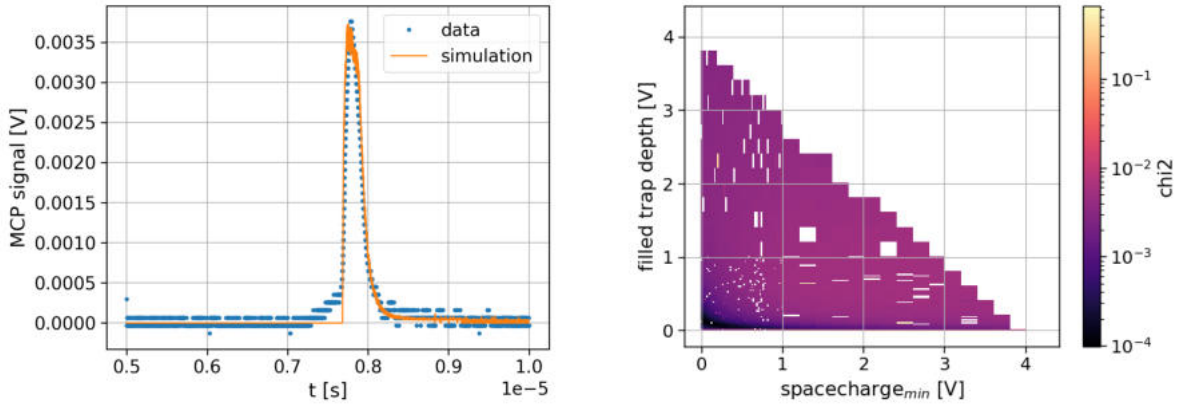

FIGURE H.3: The best fit of the simulated signal (in orange) to experimentally measured data (blue). Antiprotons trapped in $V_{wall} = 150$ V and launched from potential $V_{launch} = 110$ V. Calculated LS for all simulated signals are shown as a heatmap (right).

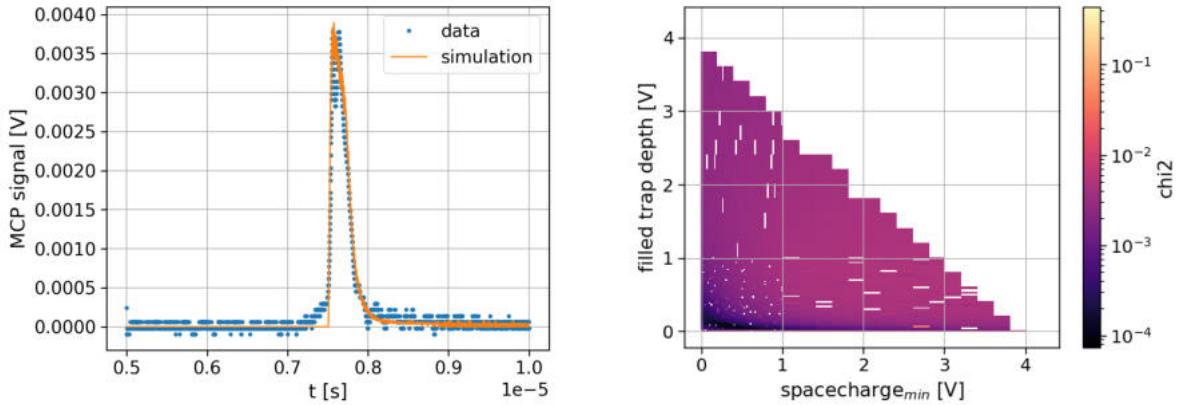

FIGURE H.4: The best fit of the simulated signal (in orange) to experimentally measured data (blue). Antiprotons trapped in $V_{wall} = 150$ V and launched from potential $V_{launch} = 115$ V. Calculated LS for all simulated signals are shown as a heatmap (right).

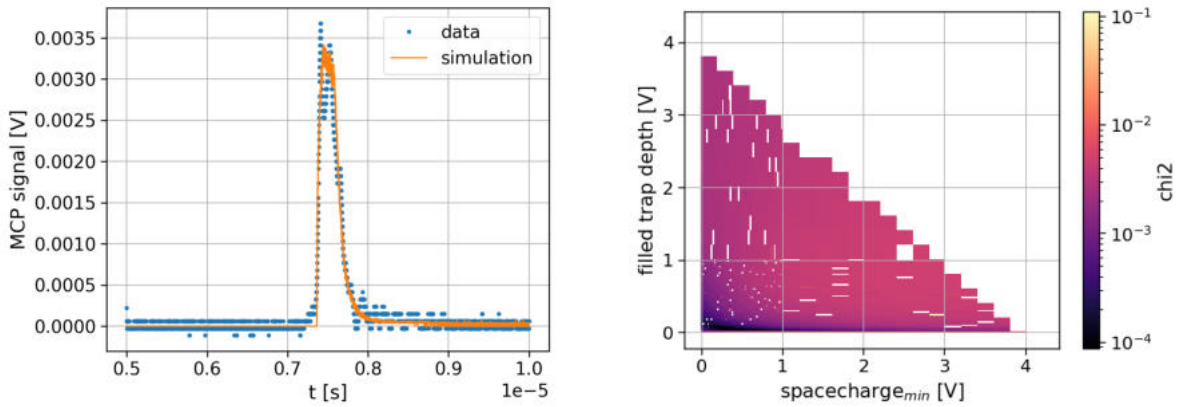

FIGURE H.5: The best fit of the simulated signal (in orange) to experimentally measured data (blue). Antiprotons trapped in $V_{wall} = 150\,\text{V}$ and launched from potential $V_{launch} = 120\,\text{V}$. Calculated LS for all simulated signals are shown as a heatmap (right).

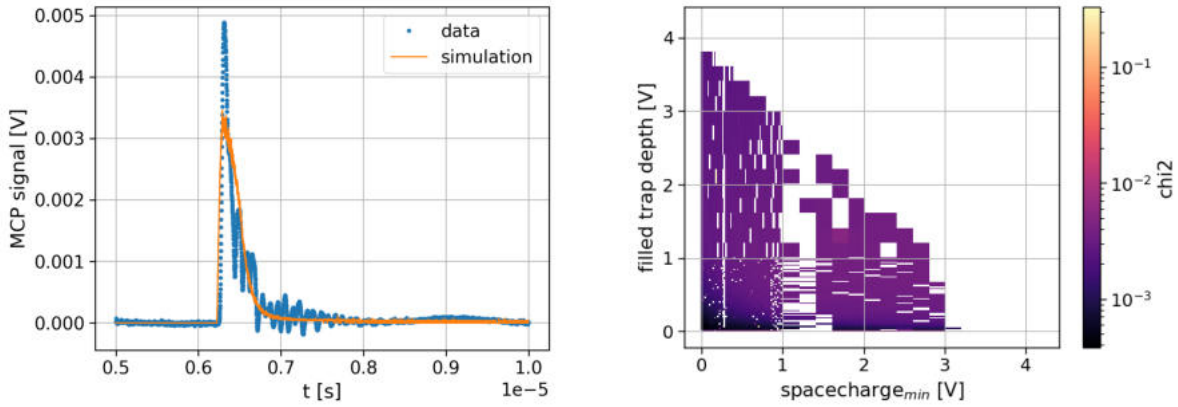

FIGURE H.6: The best fit of the simulated signal (in orange) to experimentally measured data (blue). Antiprotons trapped in $V_{wall} = 190\,\text{V}$ and launched from potential $V_{launch} = 170\,\text{V}$. Calculated LS for all simulated signals are shown as a heatmap (right).

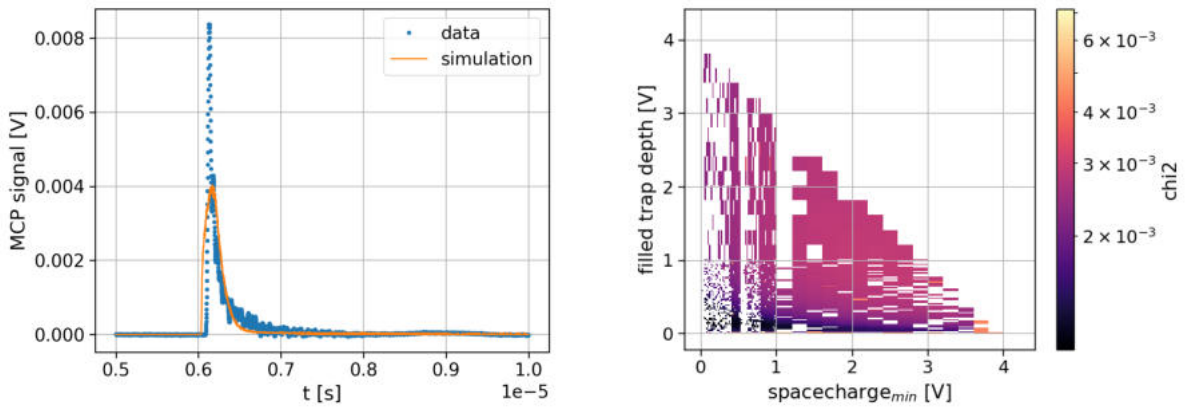

FIGURE H.7: The best fit of the simulated signal (in orange) to experimentally measured data (blue). Antiprotons trapped in $V_{wall} = 190\,\text{V}$ and launched from potential $V_{launch} = 180\,\text{V}$. Calculated LS for all simulated signals are shown as a heatmap (right).

Appendix I

List of experimental runs used in analyses

I.1 The degrader efficiency study

Table I.1: List of runs used in the analyses of scintillator signals in the degrader efficiency studies.

368702	368703	368704	368705	368706	368707	368708	368709	368710
368711	368712	368713	368714	368715	368716	368717	368718	368719
368720	368721	368722	368723	368724	368725	368726	368727	368728
368729	368730	368731	368733	368734	368736	368737	368738	368741
368742	368743	368744	368745	368746	368747	368748	368749	368750
368751	368752	368753	368755	368756	368757	368758	368759	368760
368761	368762	368763	368764	368765	368766	368767	368768	368769
368770	368771	368772	368773	368774	368775	368776	368777	368778
368779	368780	368781	368782	368783	368784	368785	368786	368787
368788	368789	368790	368791	368792	368793	368794	368795	368796
368797	368798	368799	368800	368801	368802	370911	370912	370913
370914	370915	370917	370918	370919	370920	370921	370922	370923
370924	370925	370926	370927	370929	370930	370931	370932	370933
370934	370935	370936	370937	370938	370939	370940	370941	370942
370943	370944	370945	370946	370947	370948	370949	370950	370951
370952	370953	370954	370955	370957	370958	370959	370960	370961
370962	370963	370964	370965	370966	370967	370968	370969	370970
370971	370972	370973	370974	370975	370976	370977	370978	370979
370980	370981	370982	370983					

TABLE I.2: List of runs used in the analyses of MCP signals in the degrader efficiency studies.

424159	424160	424161	424162	424163	424164	424165	424166	424167
424168	424169	424170	424172	424173	424174	424175	424176	424177
424178	424179	424180	424181	424182	424183	424184	424185	424186
424188	424189	424190	424191	424192	424193	424194	424195	424196
424197	424198	424199	424200	424201	424202	424203	424204	424205
424206	424207	424208	424209	424210	424211	424212	424213	424214
424215	424216	424217	424218	424219	424220	424221	424222	424223
424224	424225	424226	424227	424228	424229	424230	424231	424232
424233	424234	424235	424236	424237	424238	424239	424240	424241
424242	424243	424244	424245	424246	424247	424248	424249	424250
424251	424252	424253	424254	424255	424256	424257	424258	424259
424260	424261	424262	424263	424264	424265	424266	424267	424268
424269	424270	424271	424272	424273	424274	424275	424276	424277
424278	424279	424280	424281	424282	424283	424284	424285	424286
424287	424288	424289	424290	424291	424292	424293	424294	424295
424296	424297	424298	424299	424300	424301	424302	424303	424304
424305	424306	424307	424308	424309	424310	424311	424312	424313
424314	424315	424316	424317	424318	424319	424320	424321	424322
424323	424324	424325	424326	424327	424328	424329	424330	424331
424332	424333	424334	424335	424336	424337	424338	424339	424340
424341	424342	424343	424344					

I.2 TOF spectra from antiprotons interaction with ^{40}Ar

TABLE I.3: List of runs used in measurements of TOF signals for fragments from antiprotons interacting with argon gas.

427300	427302	427304	427306	427307	427308	427309	427316

Table I.4: List of runs used in validation of the TOF model with experimental data taken with antiprotons.

400395	400396	400397	400398	400399	400400	400401	400402	400403
400404	400405	400406	400407	400408	400409	400410	400411	400412
400413	400414	400415	400416	400417	400418	400419	400420	400421
400422	400423	400424	400425					

List of Abbreviations

1T	region of the AEgIS experiment inside 1 T magnetic field
5T	region of the AEgIS experiment inside 5 T magnetic field
AD	Antiproton Decelerator
AEgIS	Antimatter Experiment: Gravity, Interferometry, Spectroscopy
AERIALIST	Antimatter Experiment Realtime Integration of Artiq LIbraries and Sinara Technology
ALPACA	All Python Analyses Code of AEgIS
ALPHA	Antihydrogen Laser Physics Apparatus
ARTIQ	Advanced Real-Time Infrastructure for Quantum physics
ASACUSA	Atomic Spectroscopy And Collisions Using Slow Antiprotons
`BANANA`	Basic quAlity Notification After the eNd of an Action
BASE	Baryon Antibaryon Symmetry Experiment
`BERT`	Bertini model
`BIC`	Binary Cascade model
BNL	Brookhaven National Laboratory
CERN	European Organization for Nuclear Research
`CHIPS`	CHiral Invariant Phase Space model
CIRCUS	Computer Interface for Reliably Controlling, in an Unsupervised manner, Scientific experiments
CP	charge-parity symmetry
DAC	Digital-Analog-Converter
DMA	Direct-Memory-Access
EHV	Extremely-High vacuum
ELENA	Extra Low ENergy Antiproton ring
EMG	Exponentially-Modified Gaussian
ESDA	External Scintillating Detector Array
ETA	Estimated Time of Arrival
FOAD	Father of All Detectors
FOAM	Father of All µServices
FPGA	Field Programmable Gate Array
`FTF`	Fritiof model
GBar	Gravitational Behaviour of Antihydrogen at Rest
GR	General Relativity
GUI	Graphical User Interface
$\bar{H}$	antihydrogen
HCI	Highly-Charged Ion
HH	*HedgeHog* chamber in the beamline in AEgIS
HV	High-Voltage

IAEA-NDS	International Atomic Energy Agency - Nuclear Data Service
INCL++	Liège Intranuclear Cascade model
ISOLDE	Isotope mass Separator On-Line facility
LEAR	Low Energy Antiproton Ring
LHC	Large Hadron Collider
lHe	Liquid helium
LS	Long Shutdown at CERN
MCP	Microchannel Plate detector
MIP	Minimal-Ionising particle
OVC	Outer Vacuum Chamber
$\bar{p}$X	antiprotonic atoms
PDG	Particle Data Group
PMT	Photomultiplier Tube
PS	Proton-Synchrotron
Ps	positronium
PUMA	antiProton Unstable Matter Annihilation
QGS	Quark-Gluon String model
QMH	Queued Message Handler
RF	Radiofrequency
RFQD	radiofrequency quadrupole decelerator
RGA	Rest Gas Analysis
RW	Rotating Wall
SBlock	Schedule Block
SM	Standard Model of particle physics
SPC	Scientific Policy Committee
SPS	Super-Proton Synchrotron
SV	Shared Variable
TALOS	Total Automation of LabView Operation for Science
TOF	Time-Of-Flight
UHV	Ultra-High Vacuum
VI	Virtual Instrument

List of Figures

List of Tables

Bibliography

[1] M. Aguilar, L. Ali Cavasonza, B. Alpat, *et al.*, "Antiproton Flux, Antiproton-to-Proton Flux Ratio, and Properties of Elementary Particle Fluxes in Primary Cosmic Rays Measured with the Alpha Magnetic Spectrometer on the International Space Station," *Phys. Rev. Lett.*, vol. 117, no. 9, p. 091 103, Aug. 2016. DOI: 10.1103/PhysRevLett.117.091103.

[2] S. Acharya, D. Adamová, G. Aglieri Rinella, *et al.*, "Measurements of chemical potentials in pb-pb collisions at $\sqrt{s_{NN}} = 5.02\,TeV$," *Phys. Rev. Lett.*, vol. 133, no. 9, p. 092 301, Aug. 2024. DOI: 10.1103/PhysRevLett.133.092301.

[3] Andrei D Sakharov, "Violation of CP invariance, C asymmetry, and baryon asymmetry of the universe," *Soviet Physics Uspekhi*, vol. 34, no. 5, p. 392, May 1991, ISSN: 0038-5670. DOI: 10.1070/PU1991v034n05ABEH002497.

[4] M. Gell-Mann, "A schematic model of baryons and mesons," *Physics Letters B*, vol. 8, pp. 1–4, 1964.

[5] G. Aad, T. Abajyan, B. Abbott, *et al.*, "Observation of a new particle in the search for the Standard Model Higgs boson with the ATLAS detector at the LHC," *Physics Letters B*, vol. 716, no. 1, pp. 1–29, Sep. 2012, ISSN: 0370-2693. DOI: 10.1016/j.physletb.2012.08.020.

[6] S. Chatrchyan, V. Khachatryan, A. Sirunyan, *et al.*, "Observation of a new boson at a mass of 125 GeV with the CMS experiment at the LHC," *Physics Letters B*, vol. 716, no. 1, pp. 30–61, Sep. 2012, ISSN: 0370-2693. DOI: 10.1016/j.physletb.2012.08.021.

[7] Q.-Y. Shou, Y.-G. Ma, S. Zhang, *et al.*, "Properties of QCD matter: A review of selected results from ALICE experiment," *Nuclear Science and Techniques*, vol. 35, no. 12, p. 219, Dec. 2024, ISSN: 2210-3147. DOI: 10.1007/s41365-024-01583-2.

[8] C. Weinheimer and K. Zuber, "Neutrino masses," *Annalen der Physik*, vol. 525, no. 8-9, pp. 565–575, Sep. 2013, ISSN: 0003-3804. DOI: 10.1002/andp.201300063. (visited on 01/20/2026).

[9] T. von Egidy, "Interaction and annihilation of antiprotons and nuclei," *Nature*, vol. 328, no. 6133, pp. 773–778, Aug. 1987, ISSN: 1476-4687. DOI: 10.1038/328773a0.

[10] E. Klempt, C. Batty, and J.-M. Richard, "The antinucleon–nucleon interaction at low energy: Annihilation dynamics," *Physics Reports*, vol. 413, no. 4, pp. 197–317, Jul. 2005, ISSN: 0370-1573. DOI: 10.1016/j.physrep.2005.03.002.

[11] M. Dine, L. Randall, and S. Thomas, "Baryogenesis from flat directions of the supersymmetric standard model," *Nuclear Physics B*, vol. 458, no. 1-2, pp. 291–323, 1996, ISSN: 0550-3213.

[12] E. W. Kolb, A. Linde, and A. Riotto, "Grand-unified-theory baryogenesis after preheating," *Physical Review Letters*, vol. 77, no. 21, p. 4290, 1996.

[13] T. Matsuda, "Baryon number violation, baryogenesis, and defects with extra dimensions," *Physical Review D*, vol. 66, no. 2, p. 023 508, 2002.

[14] R. Aaij, A. S. W. Abdelmotteleb, C. A. Beteta, *et al.*, "Observation of charge–parity symmetry breaking in baryon decays," *Nature*, Jul. 2025, ISSN: 1476-4687. DOI: 10.1038/s41586-025-09119-3.

[15] N. BOHR, "Atomic Structure," *Nature*, vol. 107, no. 2682, pp. 104–107, Mar. 1921, ISSN: 1476-4687. DOI: 10.1038/107104a0.

[16] P. A. M. Dirac, "The quantum theory of the electron," *Proceedings of the Royal Society of London. Series A, Containing Papers of a Mathematical and Physical Character*, vol. 117, no. 778, pp. 610–624, 1928. DOI: 10.1098/rspa.1928.0023.

[17] C. F. v. Weizsäcker, "Zur Theorie der Kernmassen," *Zeitschrift für Physik*, vol. 96, no. 7, pp. 431–458, Jul. 1935, ISSN: 0044-3328. DOI: 10.1007/BF01337700.

[18] M. G. Mayer, "THE STRUCTURE OF THE NUCLEUS," *Scientific American*, vol. 184, no. 3, pp. 22–27, 1951, ISSN: 00368733, 19467087. JSTOR: 24945113. (visited on 07/13/2025).

[19] K. L. G. Heyde, "The Nuclear Shell Model," in *The Nuclear Shell Model: Study Edition*, K. L. G. Heyde, Ed., Berlin, Heidelberg: Springer Berlin Heidelberg, 1994, pp. 58–154, ISBN: 978-3-642-79052-2. DOI: 10.1007/978-3-642-79052-2_4.

[20] C. Baglin, *93MO EC Decay (6.85 H) to 93NB*, 2011.

[21] M. Kowalska, "Global properties of atomic nuclei," *The European Physical Journal Plus*, vol. 131, no. 8, p. 294, Aug. 2016, ISSN: 2190-5444. DOI: 10.1140/epjp/i2016-16294-0.

[22] G. Fricke and K. Heilig, *Nuclear Charge Radii* (Landolt-Börnstein - Group I Elementary Particles, Nuclei and Atoms). Berlin, Heidelberg: Springer-Verlag, 2004, vol. 20.

[23] E. Rutherford, "LXXIX. the scattering of α and β particles by matter and the structure of the atom," *The London, Edinburgh, and Dublin Philosophical Magazine and Journal of Science*, vol. 21, no. 125, pp. 669–688, May 1911, ISSN: 1941-5982. DOI: 10.1080/14786440508637080.

[24] B. Alex Brown, "Neutron Radii in Nuclei and the Neutron Equation of State," *Phys. Rev. Lett.*, vol. 85, no. 25, pp. 5296–5299, Dec. 2000. DOI: 10.1103/PhysRevLett.85.5296.

[25] B. Hu, W. Jiang, T. Miyagi, *et al.*, "Ab initio predictions link the neutron skin of ^{208}pb to nuclear forces," *Nature Physics*, vol. 18, no. 10, pp. 1196–1200, Oct. 2022, ISSN: 1745-2481. DOI: 10.1038/s41567-022-01715-8.

[26] J. Jastrzębski, H. Daniel, T. v. Egidy, *et al.*, "Signature of a neutron halo in ^{232}Th from antiproton absorption," *Nuclear Physics A*, vol. 558, pp. 405–414, 1993, ISSN: 0375-9474. DOI: 10.1016/0375-9474(93)90409-Q.

[27] P. Lubiński, J. Jastrzębski, A. Grochulska, *et al.*, "Neutron Halo in Heavy Nuclei from Antiproton Absorption," *Phys. Rev. Lett.*, vol. 73, no. 24, pp. 3199–3202, Dec. 1994. DOI: 10.1103/PhysRevLett.73.3199.

[28] S. Ajimura, H. Asano, G. Beer, *et al.*, ""K^-pp", a $\overline{K}$-meson nuclear bound state, observed in $^3He(K^-,\lambda p)n$ reactions," *Physics Letters B*, vol. 789, pp. 620–625, Feb. 2019, ISSN: 0370-2693. DOI: 10.1016/j.physletb.2018.12.058.

[29] J.-P. E. Collaboration, T. Yamaga, S. Ajimura, *et al.*, "Observation of a $\overline{K}NN$ bound state in the $^3\mathrm{He}(K^-,\Lambda p)n$ reaction," *Physical Review C*, vol. 102, no. 4, p. 044 002, Oct. 2020. DOI: 10.1103/PhysRevC.102.044002.

[30] G. Backenstoss, "Exotic Atoms," in *Progress in Atomic Spectroscopy: Part B*, W. Hanle and H. Kleinpoppen, Eds., Boston, MA: Springer US, 1979, pp. 1385–1426, ISBN: 978-1-4613-3935-9. DOI: 10.1007/978-1-4613-3935-9_16.

[31] G. Backenstoss, "Pionic atoms," *Annual Review of Nuclear Science*, vol. 20, no. 1, pp. 467–508, 1970.

[32] R. Seki and C. E. Wigand, "Kaonic and other exotic atoms," *Annu. Rev. Nucl. Sci., v. 25, pp. 241-281*, 1975.

[33] C. Curceanu, C. Guaraldo, M. Iliescu, *et al.*, "The modern era of light kaonic atom experiments," *Reviews of Modern Physics*, vol. 91, no. 2, p. 025 006, Jun. 2019. DOI: 10.1103/RevModPhys.91.025006.

[34] G. Backenstoss, "Antiprotonic atoms," *Contemporary Physics*, vol. 30, no. 6, pp. 433–448, Nov. 1989, ISSN: 0010-7514. DOI: 10.1080/00107518908221991.

[35] G. Backenstoss and J. Zakrzewski, "Exotic bound states of strange hadrons," *Contemporary Physics*, vol. 15, no. 3, pp. 197–225, 1974.

[36] D. B. Cassidy and S. D. Hogan, "Atom control and gravity measurements using Rydberg positronium," *International Journal of Modern Physics: Conference Series*, vol. 30, p. 1 460 259, Jan. 2014. DOI: 10.1142/S2010194514602592. (visited on 11/20/2025).

[37] M. Doser, "Antiprotonic bound systems," *Progress in Particle and Nuclear Physics*, vol. 125, p. 103 964, Jul. 2022, ISSN: 0146-6410. DOI: 10.1016/j.ppnp.2022.103964.

[38] S. Navas *et al.*, "Review of particle physics," *Phys. Rev. D*, vol. 110, no. 3, p. 030 001, 2024. DOI: 10.1103/PhysRevD.110.030001.

[39] RJ Hughes, "New light on antiprotonic atoms," *Nature*, vol. 368, pp. 813–814, 1994, ISSN: 0028-0836.

[40] J. S. Cohen and N. T. Padial, "Initial distributions, cascade, and annihilation of $\bar{p}$p atoms formed in $\bar{p}$ + H and $\bar{p}$ + H^- collisions in near vacuum," *Physical Review A*, vol. 41, no. 7, pp. 3460–3468, Apr. 1990. DOI: 10.1103/PhysRevA.41.3460.

[41] N. Paul, G. Bian, T. Azuma, S. Okada, and P. Indelicato, "Testing Quantum Electrodynamics with Exotic Atoms," *Physical Review Letters*, vol. 126, no. 17, p. 173 001, Apr. 2021. DOI: 10.1103/PhysRevLett.126.173001.

[42] W. M. Bugg, G. T. Condo, E. L. Hart, H. O. Cohn, and R. D. McCulloch, "Evidence for a Neutron Halo in Heavy Nuclei from Antiproton Absorption," *Phys. Rev. Lett.*, vol. 31, no. 7, pp. 475–478, Aug. 1973. DOI: 10.1103/PhysRevLett.31.475.

[43] M. Leon and R. Seki, "Determination of the neutron halo from antiproton absorption," *Physics Letters B*, vol. 48, no. 3, pp. 173–175, Feb. 1974, ISSN: 0370-2693. DOI: 10.1016/0370-2693(74)90001-X.

[44] G. Kornakov, G. Cerchiari, J. Zieliński, L. Lappo, G. Sadowski, and M. Doser, "Synthesis of cold and trappable fully stripped highly charged ions via antiproton-induced nuclear fragmentation in traps," *Physical Review C*, vol. 107, no. 3, p. 034 314, Mar. 2023. DOI: 10.1103/PhysRevC.107.034314.

[45] R. S. Hayano, "Antiprotonic Helium Atoms," *Nuclear Physics News*, vol. 19, no. 2, pp. 18–24, Jun. 2009, ISSN: 1061-9127. DOI: 10.1080/10506890902958463.

[46] F. G. Major, V. N. Gheorghe, and G. Werth, *Charged Particle Traps: Physics and Techniques of Charged Particle Field Confinement*. Springer Science & Business Media, 2005, vol. 37, ISBN: 3-540-22043-7.

[47] K. Blaum, Yu. N. Novikov, and G. Werth, "Penning traps as a versatile tool for precise experiments in fundamental physics," *Contemporary Physics*, vol. 51, no. 2, pp. 149–175, Mar. 2010, ISSN: 0010-7514. DOI: 10.1080/00107510903387652.

[48] W. Quint and M. Vogel, *Fundamental Physics in Particle Traps*. Springer, 2014, vol. 1, ISBN: 3-642-45200-0.

[49] R. S. Hayano, "Precision spectroscopy of antiprotonic atoms," *Low Energy Positron and Positronium Physics*, vol. 171, no. 1, pp. 145–152, Aug. 2000, ISSN: 0168-583X. DOI: 10.1016/S0168-583X(00)00309-8.

[50] M. Charlton, "Antihydrogen production in collisions of antiprotons with excited states of positronium," *Physics Letters A*, vol. 143, no. 3, pp. 143–146, Jan. 1990, ISSN: 0375-9601. DOI: 10.1016/0375-9601(90)90665-B.

[51] D. Krasnický, R. Caravita, C. Canali, and G. Testera, "Cross section for Rydberg antihydrogen production via charge exchange between Rydberg positroniums and antiprotons in a magnetic field," *Physical Review A*, vol. 94, no. 2, p. 022 714, Aug. 2016. DOI: 10.1103/PhysRevA.94.022714.

[52] A. Iljinov, V. Nazaruk, and S. Chigrinov, "Nuclear absorption of stopped antiprotons: Multipion-nucleus interactions," *Nuclear Physics A*, vol. 382, no. 3, pp. 378–400, Jul. 1982, ISSN: 0375-9474. DOI: 10.1016/0375-9474(82)90352-9.

[53] E. R. Badman and R. G. Cooks, "Cylindrical Ion Trap Array with Mass Selection by Variation in Trap Dimensions," *Analytical Chemistry*, vol. 72, no. 20, pp. 5079–5086, Oct. 2000, ISSN: 0003-2700. DOI: 10.1021/ac000377n.

[54] A. N. Verenchikov, S. N. Kirillov, A. V. Vorobyev, *et al.*, "Multi reflecting TOF MS approaching resolution of 1,000,000 in a wide mass range," *International Journal of Mass Spectrometry*, vol. 508, p. 117 395, Feb. 2025, ISSN: 1387-3806. DOI: 10.1016/j.ijms.2024.117395.

[55] F. M. Maier, C. M. Ireland, G. Bollen, *et al.*, *A high-voltage MR-ToF mass spectrometer and separator for the study of exotic isotopes at FRIB*, 2025.

[56] M Doser, "AEgIS / AD-6 annual report 2021," CERN, Geneva, Tech. Rep., 2022.

[57] R Caravita, "AEgIS/AD-6 annual report 2022," CERN, Geneva, Tech. Rep., 2023.

[58] R. Caravita, "AEgIS/AD-6 annual report 2023," CERN, Geneva, Tech. Rep., 2024.

[59] R Caravita, "Progress report of the AEgIS experiment (2024)," CERN, Geneva, Tech. Rep., 2025.

[60] M. Volponi, S. Huck, R. Caravita, *et al.*, "CIRCUS: An autonomous control system for antimatter, atomic and quantum physics experiments," *EPJ Quantum Technology*, vol. 11, no. 1, p. 10, 2024. DOI: 10.1140/epjqt/s40507-024-00220-6.

[61] M. Volponi, J. Zieliński, T. Rauschendorfer, *et al.*, "TALOS (Total Automation of LabVIEW Operations for Science): A framework for autonomous control systems for complex experiments," *Review of Scientific Instruments*, vol. 95, no. 8, Aug. 2024, ISSN: 1089-7623. DOI: 10.1063/5.0196806.

[62] M. Volponi, "Towards the formation of a forward-boosted beam of neutral antihydrogen for gravitational studies," Ph.D. dissertation, Trento U., 2024.

[63] S. H. R. Huck, "From the efficient trapping and accumulation of cooled antiprotons towards the formation of a pulsed beam of antihydrogen atoms," Ph.D. dissertation, Staats- und Universitätsbibliothek Hamburg Carl von Ossietzky, 2025.

[64] E. Lopienska, "The CERN accelerator complex, layout in 2022. Complexe des accélérateurs du CERN en janvier 2022," 2022.

[65] N Abgrall, O Andreeva, A Aduszkiewicz, *et al.*, "NA61/SHINE facility at the CERN SPS: Beams and detector system," *Journal of Instrumentation*, vol. 9, no. 06, P06005, Jun. 2014, ISSN: 1748-0221. DOI: 10.1088/1748-0221/9/06/P06005.

[66] E. C. Gil, E. M. Albarrán, E. Minucci, *et al.*, "The beam and detector of the NA62 experiment at CERN," *Journal of Instrumentation*, vol. 12, no. 05, P05025, May 2017, ISSN: 1748-0221. DOI: 10.1088/1748-0221/12/05/P05025.

[67] E. Kugler, D. Fiander, B. Johnson, *et al.*, "The new CERN-ISOLDE on-line mass-separator facility at the PS-Booster," *Nuclear Instruments and Methods in Physics Research Section B: Beam Interactions with Materials and Atoms*, vol. 70, no. 1, pp. 41–49, Aug. 1992, ISSN: 0168-583X. DOI: 10.1016/0168-583X(92)95907-9.

[68] P. Scampoli and J. Storey, "The AEgIS experiment at CERN for the measurement of antihydrogen gravity acceleration," *Modern Physics Letters A*, vol. 29, no. 17, p. 1 430 017, Jun. 2014, ISSN: 0217-7323. DOI: 10.1142/S0217732314300171. (visited on 11/20/2025).

[69] C. L. Cesar, G. B. Andresen, W. Bertsche, *et al.*, "Antihydrogen Physics at ALPHA," *Canadian Journal of Physics*, vol. 87, no. 7, pp. 791–797, Jul. 2009, ISSN: 0008-4204. DOI: 10.1139/P08-148. (visited on 11/20/2025).

[70] N. Kuroda, S. Ulmer, D. J. Murtagh, *et al.*, "The ASACUSA CUSP: An antihydrogen experiment," *Hyperfine Interactions*, vol. 235, no. 1, pp. 13–20, Nov. 2015, ISSN: 1572-9540. DOI: 10.1007/s10751-015-1205-1.

[71] C. Smorra, K. Blaum, L. Bojtar, *et al.*, "BASE – The Baryon Antibaryon Symmetry Experiment," *The European Physical Journal Special Topics*, vol. 224, no. 16, pp. 3055–3108, Nov. 2015, ISSN: 1951-6401. DOI: 10.1140/epjst/e2015-02607-4.

[72] D. P. van der Werf, "The GBAR experiment," *International Journal of Modern Physics: Conference Series*, vol. 30, p. 1 460 263, Jan. 2014. DOI: 10.1142/S2010194514602634. (visited on 11/20/2025).

[73] Aumann, T., Bartmann, W., Boine-Frankenheim, O., *et al.*, "PUMA, antiProton unstable matter annihilation - PUMA collaboration," *Eur. Phys. J. A*, vol. 58, no. 5, p. 88, 2022. DOI: 10.1140/epja/s10050-022-00713-x.

[74] J. Hémery and S. Maury, "The Antiproton Decelerator: Overview," *Proceedings of the Fifth Biennial Conference on Low-Energy Antiproton Physics*, vol. 655, no. 1, pp. c345–c352, Aug. 1999, ISSN: 0375-9474. DOI: 10.1016/S0375-9474(99)00223-7.

[75] M. Hori and J. Walz, "Physics at CERN's Antiproton Decelerator," *Progress in Particle and Nuclear Physics*, vol. 72, pp. 206–253, Sep. 2013, ISSN: 0146-6410. DOI: 10.1016/j.ppnp.2013.02.004.

[76] V. e. "Chohan, C. "Alanzeau, M. E. "Angoletta, *et al.*, "Extra Low ENergy Antiproton (ELENA) ring and its Transfer Lines: Design Report," CERN, Tech. Rep., Jul. 2014.

[77] D. Gamba, M. E. Angoletta, P Belochitskii, *et al.*, "ELENA Commissioning," pp. 626–631, 2020. DOI: 10.18429/JACoW-NAPAC2019-WEYBB1.

[78] G. Y. Drobychev, P Nédélec, D Sillou, *et al.*, "Proposal for the AEGIS experiment at the CERN antiproton decelerator (Antimatter Experiment: Gravity, Interferometry, Spectroscopy)," CERN, Geneva, Tech. Rep., 2007.

[79] C. Amsler, M. Antonello, A. Belov, *et al.*, "Pulsed production of antihydrogen," *Communications Physics*, vol. 4, no. 1, p. 19, Feb. 2021, ISSN: 2399-3650. DOI: 10.1038/s42005-020-00494-z.

[80] R Caravita, "Long-term outlook for the AEgIS experimental program," CERN, Geneva, Tech. Rep., 2025.

[81] L. T. Glöggler, N. Gusakova, B. Rienäcker, *et al.*, "Positronium laser cooling via the 1^3s-2^3p transition with a broadband laser pulse," *Phys. Rev. Lett.*, vol. 132, no. 8, p. 083 402, Feb. 2024. DOI: 10.1103/PhysRevLett.132.083402.

[82] V. Rodin, G. Cerchiari, M. Doser, *et al.*, "Low-Energy Negative Ion Injection Beamline for Experiments with Antiprotonic Atoms at AEgIS," F. Zimmermann, H. Tanaka, P. Sudmuang, *et al.*, Eds., 4 pages, 4.188 MB, 2022, ISSN: 2673-5490. DOI: 10.18429/JACOW-IPAC2022-WEPOTK031. (visited on 04/04/2025).

[83] P. Yzombard, M. Hamamda, S. Gerber, M. Doser, and D. Comparat, "Laser cooling of molecular anions," *Physical review letters*, vol. 114, no. 21, p. 213 001, 2015.

[84] U. Even, "Pulsed Supersonic Beams from High Pressure Source: Simulation Results and Experimental Measurements," *Advances in Chemistry*, vol. 2014, no. 1, p. 636 042, Jan. 2014, ISSN: 2356-6612. DOI: 10.1155/2014/636042. (visited on 12/06/2025).

[85] V. Baglin, "Cryopumping and Vacuum Systems," Tech. Rep., 2020.

[86] X.-P. Huang, F. Anderegg, E. M. Hollmann, C. F. Driscoll, and T. M. O'Neil, "Steady-State Confinement of Non-neutral Plasmas by Rotating Electric Fields," *Physical Review Letters*, vol. 78, no. 5, pp. 875–878, Feb. 1997. DOI: 10.1103/PhysRevLett.78.875.

[87] G. Gabrielse, "Comparing the antiproton and proton, and opening the way to cold antihydrogen," in *Advances In Atomic, Molecular, and Optical Physics*, B. Bederson and H. Walther, Eds., vol. 45, Academic Press, Jan. 2001, pp. 1–39, ISBN: 1049-250X. DOI: 10.1016/S1049-250X(01)80037-9.

[88] A. M. Lombardi, W. Pirkl, and Y. Bylinsky, "First operating experience with the CERN decelerating RFQ for antiprotons," in *PACS2001. Proceedings of the 2001 Particle Accelerator Conference (Cat. No.01CH37268)*, vol. 1, Jun. 2001, 585–587 vol.1. DOI: 10.1109/PAC.2001.987575.

[89] J. R. Danielson, D. H. E. Dubin, R. G. Greaves, and C. M. Surko, "Plasma and trap-based techniques for science with positrons," *Reviews of Modern Physics*, vol. 87, no. 1, pp. 247–306, Mar. 2015. DOI: 10.1103/RevModPhys.87.247.

[90] N. Zurlo, C Amsler, M Antonello, *et al.*, "Calibration and equalisation of plastic scintillator detectors for antiproton annihilation identification over positron/positronium background," *Acta Physica Polonica B*, vol. 51, no. 1, pp. 213–223, 2020, ISSN: 0587-4254.

[91] W. Commons, *File:PhotoMultiplierTubeAndScintillator.svg — Wikimedia Commons, the free media repository*, 2025.

[92] T. Gys, "Micro-channel plates and vacuum detectors," *New Developments in Photodetection NDIP14*, vol. 787, pp. 254–260, Jul. 2015, ISSN: 0168-9002. DOI: 10.1016/j.nima.2014.12.044.

[93] J. Ladislas Wiza, "Microchannel plate detectors," *Nuclear Instruments and Methods*, vol. 162, no. 1, pp. 587–601, Jun. 1979, ISSN: 0029-554X. DOI: 10.1016/0029-554X(79)90734-1.

[94] R. Garnett, *Bayesian Optimization*. Cambridge University Press, 2023.

[95] J. Mockus, "The Bayesian approach to local optimization," in *Bayesian Approach to Global Optimization: Theory and Applications*, Springer, 1989, pp. 125–156.

[96] M. Malu, G. Dasarathy, and A. Spanias, "Bayesian Optimization in High-Dimensional Spaces: A Brief Survey," in *2021 12th International Conference on Information, Intelligence, Systems & Applications (IISA)*, 2021, pp. 1–8. DOI: 10.1109/IISA52424.2021.9555522.

[97] T. Head, M. Kumar, H. Nahrstaedt, G. Louppe, and I. Shcherbatyi, *Holgern/scikit-optimize*, Zenodo, Jun. 2024. DOI: 10.5281/zenodo.11478072.

[98] S. Bourdeauducq, R. Jördens, P. Zotov, *et al.*, *ARTIQ 1.0*, Zenodo, May 2016. DOI: 10.5281/zenodo.51303.

[99] G. Kasprowicz, P. Kulik, M. Gaska, *et al.*, "ARTIQ and Sinara: Open Software and Hardware Stacks for Quantum Physics," in *OSA Quantum 2.0 Conference*, Optica Publishing Group, 2020, QTu8B.14. DOI: 10.1364/QUANTUM.2020.QTu8B.14.

[100] Sinara, *HW Wiki*, https://github.com/sinara-hw/meta/wiki, GItHub Repository, 2023.

[101] Sinara, *HVAMP8CH*, https://github.com/sinara-hw/HV_AMP_8CH/wiki, GItHub Repository, 2023.

[102] J. Zieliński, *Degrader efficiency simulation*, https://github.com/jzielins97/degraderMC, GItHub Repository.

[103] J. Zieliński, *Antiproton–induced fragmentation*, https://github.com/jzielins97/antiproton_annihilation, GItHub Repository.

[104] J. Zieliński, *Tof model*, https://github.com/jzielins97/tof_simulation, GItHub Repository.

[105] S. Agostinelli, J. Allison, K. Amako, *et al.*, "Geant4—a simulation toolkit," *Nuclear Instruments and Methods in Physics Research Section A: Accelerators, Spectrometers, Detectors and Associated Equipment*, vol. 506, no. 3, pp. 250–303, Jul. 2003, ISSN: 0168-9002. DOI: 10.1016/S0168-9002(03)01368-8.

[106] J. Allison, K. Amako, J. Apostolakis, *et al.*, "Geant4 developments and applications," *IEEE Transactions on Nuclear Science*, vol. 53, no. 1, pp. 270–278, Feb. 2006, ISSN: 1558-1578. DOI: 10.1109/TNS.2006.869826.

[107] J. Allison, K. Amako, J. Apostolakis, *et al.*, "Recent developments in Geant4," *Nuclear Instruments and Methods in Physics Research Section A: Accelerators, Spectrometers, Detectors and Associated Equipment*, vol. 835, pp. 186–225, Nov. 2016, ISSN: 0168-9002. DOI: 10.1016/j.nima.2016.06.125.

[108] G. Battistoni, T. Boehlen, F. Cerutti, *et al.*, "Overview of the FLUKA code," *Joint International Conference on Supercomputing in Nuclear Applications and Monte Carlo 2013, SNA + MC 2013. Pluri- and Trans-disciplinarity, Towards New Modeling and Numerical Simulation Paradigms*, vol. 82, pp. 10–18, Aug. 2015, ISSN: 0306-4549. DOI: 10.1016/j.anucene.2014.11.007.

[109] C. Ahdida, D. Bozzato, D. Calzolari, *et al.*, "New capabilities of the FLUKA multi-purpose code," *Frontiers in Physics*, vol. 9, p. 788 253, 2022, ISSN: 2296-424X.

[110] Geant4 Collaboration, *Physics Reference Manual, Release 11.3*, Dec. 2024.

[111] B. Andersson, G. Gustafson, and B. Nilsson-Almqvist, "A model for low-p_T hadronic reactions with generalizations to hadron-nucleus and nucleus-nucleus collisions," *Nuclear Physics B*, vol. 281, no. 1, pp. 289–309, Jan. 1987, ISSN: 0550-3213. DOI: 10.1016/0550-3213(87)90257-4.

[112] H. W. Bertini, "MONTE CARLO CALCULATIONS ON INTRANUCLEAR CASCADES (thesis)," United States, Tech. Rep., May 1963. DOI: 10.2172/4692927.

[113] A. B. Botvina, Y. S. Golubeva, A. S. Iljinov, and I. A. Pshenichnov, "Intranuclear-cascade mechanism in antinucleon-nucleus interactions," *Physics of Atomic Nuclei (English Translation); (United States)*, vol. 55:5, 1.

[114] G. Folger, V. N. Ivanchenko, and J. P. Wellisch, "The Binary Cascade," *The European Physical Journal A - Hadrons and Nuclei*, vol. 21, no. 3, pp. 407–417, Sep. 2004, ISSN: 1434-601X. DOI: 10.1140/epja/i2003-10219-7.

[115] D. R. F. Cochran, P. N. Dean, P. A. M. Gram, *et al.*, "Production of Charged Pions by 730-MeV Protons from Hydrogen and Selected Nuclei," *Phys. Rev. D*, vol. 6, no. 11, pp. 3085–3116, Dec. 1972. DOI: 10.1103/PhysRevD.6.3085.

[116] J. Cugnon, C. Volant, and S. Vuillier, "Improved intranuclear cascade model for nucleon-nucleus interactions," *Nuclear Physics A*, vol. 620, no. 4, pp. 475–509, Jul. 1997, ISSN: 0375-9474. DOI: 10.1016/S0375-9474(97)00186-3.

[117] D. Mancusi, A. Boudard, J. Cugnon, J.-C. David, P. Kaitaniemi, and S. Leray, "Extension of the Liège intranuclear-cascade model to reactions induced by light nuclei," *Physical Review C*, vol. 90, no. 5, p. 054 602, Nov. 2014. DOI: 10.1103/PhysRevC.90.054602.

[118] A. Kelić, M. V. Ricciardi, and K.-H. Schmidt, "ABLA07 - Towards a Complete Description of the Decay Channels of a Nuclear System from Spontaneous Fission to Multifragmentation," in *Joint ICTP-IAEA Advanced Workshop on Model Codes for Spallation Reactions*, International Centre for Theoretical Physics, Trieste, Italy, Aug. 2008, pp. 181–221. DOI: 10.61092/iaea.jnhr-bxb3.

[119] J. L. Rodríguez-Sánchez, J. Cugnon, J.-C. David, J. Hirtz, A. Kelić, and S. Leray, "Hypernuclei formation in spallation reactions by coupling the Liège intranuclear cascade model to the deexcitation code ABLA," *Phys. Rev. C*, vol. 105, no. 1, p. 014 623, Jan. 2022. DOI: 10.1103/PhysRevC.105.014623.

[120] S. Leray, J. C. David, M. Khandaker, *et al.*, "Results from the IAEA benchmark of spallation models," *Journal of the Korean Physical Society*, vol. 59, no. 2, pp. 791–796, 2011.

[121] Geant4 Collaboration, "Geant4 10.0 Release Notes," Tech. Rep., Dec. 2013.

[122] Geant4 Collaboration, "Geant4 11.2 Release Notes," Tech. Rep., Dec. 2023.

[123] CERN, *FLUKA website*.

[124] A. Donadon, G. Hugo, C. Theis, and V. Vlachoudis, "FLAIR3 – recasting simulation experiences with the Advanced Interface for FLUKA and other Monte Carlo codes," *EPJ Web Conf.*, vol. 302, 2024. DOI: 10.1051/epjconf/202430211005.

[125] CERN, *Fluka manual – 2.1.1. hadron inelastic nuclear interactions*, https://flukafiles.web.cern.ch/manual/chapters/quick_look/physics/hadron_inelastic.html.

[126] A. Ferrari, J. Ranft, S. Roesler, and P. Sala, "Cascade particles, nuclear evaporation, and residual nuclei in high energy hadron-nucleus interactions," *Zeitschrift für Physik C Particles and Fields*, vol. 70, no. 3, pp. 413–426, Sep. 1996, ISSN: 1431-5858. DOI: 10.1007/s002880050119.

[127] C. Amsler, H. Breuker, M. Bumbar, *et al.*, "Antiproton annihilation at rest in thin solid targets and comparison with Monte Carlo simulations," *The European Physical Journal A*, vol. 60, no. 11, p. 225, Nov. 2024, ISSN: 1434-601X. DOI: 10.1140/epja/s10050-024-01428-x.

[128] R. Bacher, P. Blüm, D. Gotta, *et al.*, "Degree of ionization in antiprotonic noble gases," *Physical Review A*, vol. 38, no. 9, pp. 4395–4404, Nov. 1988. DOI: 10.1103/PhysRevA.38.4395.

[129] D. Gotta, K. Rashid, B. Fricke, P. Indelicato, and L. M. Simons, "X-ray transitions from antiprotonic noble gases," *The European Physical Journal D*, vol. 47, no. 1, pp. 11–26, Apr. 2008, ISSN: 1434-6079. DOI: 10.1140/epjd/e2008-00025-3.

[130] B. M. Pontecorvo, "One-meson and zero-meson annihilation of antinucleons," *Zh. Eksp. Teor. Fiz*, vol. 30, p. 947, 1956.

[131] Y. A. Batusov, S. A. Bunyatov, and I. V. Falomkin, "Production of λ-hyperons and k_s^0 mesons in annihilation of antiprotons in ^{4}he nuclei at 600 mev/c," Joint Inst. for Nuclear Research, Dubna (USSR). Lab. of Nuclear Problems, Tech. Rep., 1989.

[132] J. Cugnon and J. Vandermeulen, "Antiproton and antilambda annihilations on several nucleons," *Physical Review C*, vol. 39, no. 1, pp. 181–191, Jan. 1989. DOI: 10.1103/PhysRevC.39.181.

[133] S. Alfaro, L. Panzl, T. Faorlin, *et al.*, "Towards metrology with highly charged isomeric ions from antiproton annihilation," *Journal of Physics B: Atomic, Molecular and Optical Physics*, vol. 58, no. 21, p. 215 002, 2025.

[134] P. Mohr, "Nucleosynthesis of ^{92}nb and the relevance of the low-lying isomer at 135.5 kev," *Physical Review C*, vol. 93, no. 6, p. 065 804, Jun. 2016. DOI: 10.1103/PhysRevC.93.065804.

[135] T. M. O'Neil and C. F. Driscoll, "Transport to thermal equilibrium of a pure electron plasma," *The Physics of Fluids*, vol. 22, no. 2, pp. 266–277, 1979.

[136] S. A. Prasad and T. M. O'Neil, "Finite length thermal equilibria of a pure electron plasma column," *The Physics of Fluids*, vol. 22, no. 2, pp. 278–281, 1979.

[137] R. Caravita, "Towards measuring gravity on neutral antimatter," Ph.D. dissertation, 2017.

[138] J. R. Haack, C. D. Hauck, and M. S. Murillo, "A conservative, entropic multispecies BGK model," *Journal of Statistical Physics*, vol. 168, no. 4, pp. 826–856, 2017.

[139] B. M. Haines, "Charged particle transport coefficient challenges in high energy density plasmas," *Physics of Plasmas*, vol. 31, no. 5, 2024.

[140] S. L. Rolston and G. Gabrielse, "Cooling antiprotons in an ion trap," *Hyperfine Interactions*, vol. 44, no. 1, pp. 233–245, Mar. 1989, ISSN: 1572-9540. DOI: 10.1007/BF02398673.

[141] R. Brun and F. Rademakers, "ROOT: An object oriented data analysis framework," *Nucl. Instrum. Meth. A*, vol. 389, M. Werlen and D. Perret-Gallix, Eds., pp. 81–86, 1997. DOI: 10.1016/S0168-9002(97)00048-X.

[142] M. L. Waskom, "Seaborn: Statistical data visualization," *Journal of Open Source Software*, vol. 6, no. 60, p. 3021, 2021. DOI: 10.21105/joss.03021.

[143] P. Virtanen, R. Gommers, T. E. Oliphant, *et al.*, "SciPy 1.0: Fundamental Algorithms for Scientific Computing in Python," *Nature Methods*, vol. 17, pp. 261–272, 2020. DOI: 10.1038/s41592-019-0686-2.

[144] R. Vink, S. de Gooijer, A. Beedie, *et al.*, *Pola-rs/polars: Rust Polars 0.52.0*, Zenodo, Nov. 2025. DOI: 10.5281/zenodo.17514842.

[145] A. Bianconi, M. Corradini, A. Cristiano, *et al.*, "Experimental evidence of antiproton reflection by a solid surface," *Physical Review A*, vol. 78, no. 2, p. 022 506, Aug. 2008. DOI: 10.1103/PhysRevA.78.022506.

[146] The International Atomic Energy Agency, *Livechart Data Download API*, https://www-nds.iaea.org/relnsd/vcharthtml/api_v0_guide.html.

[147] H. Johnston, *Top 10 Breakthroughs of the Year in physics for 2024 revealed*, https://physicsworld.com/a/top-10-breakthroughs-of-the-year-in-physics-for-2024-revealed/, Physicsworld.Com, Dec. 2024.

[148] F. P. Gustafsson, M. Volponi, J. Zieliński, *et al.*, *Spectrometry of Captured Highly Charged Ions Produced Following Antiproton Annihilations*, 2025.

[149] ALPHA Collaboration, G. B. Andresen, M. D. Ashkezari, *et al.*, "Evaporative Cooling of Antiprotons to Cryogenic Temperatures," *Physical Review Letters*, vol. 105, no. 1, p. 013 003, Jul. 2010. DOI: 10.1103/PhysRevLett.105.013003.

[150] M. Volponi and J. Zieliński, *CIRCUS*, https://github.com/drvolpe/CIRCUS.git, GItHub Repository.

[151] C. Hewitt, P. Bishop, and R. Steiger, "Session 8 formalisms for artificial intelligence a universal modular actor formalism for artificial intelligence," in *Advance Papers of the Conference*, vol. 3, Stanford Research Institute Menlo Park, CA, 1973, p. 235.

[152] c.-f. community, *The conda-forge Project: Community-based Software Distribution Built on the conda Package Format and Ecosystem*, Zenodo, Jul. 2015. DOI: 10.5281/zenodo.4774217.

[153] M-Labs, *ARTIQ v7 Documentation*, https://m-labs.hk/artiq/manual-legacy/introduction.html, 2025.